# Plasma-based Decomposition of Per- and Polyfluoroalkyl Substances in Water: Plasma Source Exploration, Batch Kinetics, Effects of Water Conductivity, and an Architecture for Continuous Flow Processing

by

Joseph R. Groele

A dissertation submitted in partial fulfillment
of the requirements for the degree of
Doctor of Philosophy
(Mechanical Engineering)
in the University of Michigan
2023

Doctoral Committee:

Professor John Foster, Co-Chair
Professor Volker Sick, Co-Chair
Professor Eric Johnsen
Professor Terese Olson

Joseph R. Groele

jrgroele@umich.edu

ORCID iD:  0000-0003-2470-7273

© Joseph R. Groele 2023

## Dedication

This dissertation is dedicated to my family for their unconditional love and support.

**Acknowledgements**

First, I would like to thank my advisor, Professor John Foster, for his continued mentorship throughout my entire graduate school research experience. This work would not have been possible without his support and encouragement. I'd also like to thank Professor Terese Olson for her critical work and support around the PFAS data collection and analysis, as well as for her role in the continuous flow processing architecture presented in this thesis. I want to thank Professor Volker Sick for being my co-advisor and Professor Eric Johnsen for serving on my committee. All my committee members provided valuable feedback at key times throughout my doctoral research experience and helped me make it through the process.

I'd also like to recognize the late Dr. Isaiah Blankson who was originally one of my committee members. Dr. Blankson sadly passed away in November 2021, but it was an honor and a privilege to have worked with him. It was especially fun to spend the summer of 2017 with him at the NASA Glenn Research Center. He was a true pioneer in the field of non-equilibrium plasmas for water purification, as well as hypersonic research. He will be missed.

Next, I would like to acknowledge the funding sources that supported this work including the National Science Foundation Industry-University Cooperative Research Center for High Pressure Plasma, Energy, Agriculture, and Biomedical Technologies (PEAB), Revitalizing Auto Communities Environmental Response (RACER) Trust, the Anthropocene Institute, and the National Aeronautics and Space Administration (NASA). This work was made possible through their funding.

I'd also like to thank my fellow Plasma Science and Technology Lab mates, both past and current for being a welcoming and helpful group of people. The conferences that we attended together are particularly memorable thanks to all of you. There are many more people that helped support my research projects in various ways: Tom Yavaraski for his training and assistance with PFAS analysis, Kent Pruss and David Carter for their machine shop support, and the graduate coordinators in both mechanical and nuclear engineering for helping me navigate the various degree requirements along the way. There are many more that I won't be able to thank personally here, but I am sincerely thankful for everyone who has helped me along the way.

Finally, I would like to give a special thanks to my friends and family, especially my parents and sister, who have made my life so wonderful and meaningful; and, to my partner, Ilka. Without her love and support throughout the final stretch of the thesis writing and defense, I would probably not have made it through. I am truly grateful for her.

## Table of Contents

Dedication ..... ii

Acknowledgements ..... iii

List of Tables ..... ix

List of Figures ..... xi

Abstract ..... xvi

Chapter 1 Introduction ..... 1

1.1 Water Resources and Contaminants of Emerging Concern ..... 1

1.2 The Per- and Polyfluoroalkyl Substance Problem ..... 4

1.3 PFAS Treatment Technologies ..... 7

1.4 Motivation ..... 11

1.5 Scope of Work ..... 13

Chapter 2 Plasma-water Reactors: Theory and State of the Art ..... 17

2.1 Introduction to Plasmas ..... 17

2.2 Plasmas in Contact with Liquids ..... 18

2.3 Configurations for Plasma-liquid Interaction ..... 21

2.4 Towards Pilot-scale Plasma-water Reactors ..... 29

2.4.1 Early Pilot-scale Plasma-based Advanced Oxidation (AquaPure Ltd.) ..... 30

2.4.2 Underwater Dielectric Barrier Discharge Plasma Jet (NASA) ..... 32

2.4.3 Enhanced Contact Reactor (Clarkson University) ..... 38

2.4.4 Packed-bed Reactor (University of Michigan) ..... 41

Chapter 3 Experimental Methods for Evaluating Plasma-based Water Treatment ..... 45

3.1 Contaminant Removal Assessments ..... 47
3.1.1 Spectrophotometry ..... 48
3.1.2 Total Organic Carbon ..... 50
3.1.3 Biochemical/Chemical Oxygen Demand ..... 51
3.2 Hydrogen Peroxide Interference in COD Assessments of Plasma Treated Waters ..... 52
3.2.1 Materials and Methods ..... 53
3.2.2 Results and Discussion ..... 56
3.3 PFAS Concentration Measurements by LC-MS/MS ..... 61
3.4 Water Property Measurements ..... 64
3.4.1 Electrical Conductivity ..... 64
3.4.2 pH ..... 66
3.4.3 Temperature ..... 68
3.5 Reactive Species Measurements ..... 68
3.5.1 Hydrogen Peroxide ..... 70
3.5.2 Ozone ..... 71
3.5.3 Nitrite and Nitrate ..... 71
3.5.4 Metals ..... 71
3.6 Optical Emission Spectroscopy ..... 73
Chapter 4 Exploring the Efficacy of Plasma Reactors for PFAS Decomposition ..... 77
4.1 Reactors ..... 78
4.1.1 Dielectric Barrier Discharge Plasma Jet Reactor ..... 80
4.1.2 Packed-bed Reactor with Water Dielectrics ..... 82
4.2 Power Supplies ..... 84
4.2.1 Alternating Current Power Supply ..... 85
4.2.2 Nanosecond Pulsed Power Supply ..... 86

4.2.3 Voltage-Current Waveform Analysis ..... 88
4.3 Results and Discussion ..... 89
4.4 Conclusions ..... 95
Chapter 5 Time-resolved PFAS Decomposition: Batch Kinetics ..... 97
5.1 Packed-bed Reactor High Concentration PFOA Decomposition ..... 98
5.2 Plasma Jet Groundwater Decomposition Kinetics ..... 102
5.3 Packed-bed Reactor Long Duration Groundwater Treatment ..... 107
5.3.1 PFAS Decomposition ..... 109
5.3.2 pH and Electrical Conductivity ..... 114
5.3.3 Discharge Voltage, Current, and Power ..... 115
5.4 Highlighting the Issue of PFOA Ubiquity ..... 117
5.5 Conclusions ..... 124
Chapter 6 Influence of Water Electrical Conductivity on Plasma Discharge Properties ..... 126
6.1 Voltage-Current Waveform Analysis ..... 128
6.2 Discharge Power Analysis ..... 135
6.3 Optical Emission Spectroscopy ..... 137
6.3.1 Gas Temperature ..... 141
6.3.2 Plasma Density ..... 144
6.4 Water Heating ..... 148
6.5 Conclusions ..... 150
Chapter 7 Packed-bed Reactor Scale-up Analysis ..... 153
7.1 Continuous Flow Architecture and Model ..... 155
7.2 Energy Cost Assessment ..... 162
Chapter 8 Summary and Future Work ..... 168
8.1 Summary ..... 168

8.2 Future Work ..... 173
8.2.1 Understanding the Different Discharge Modes ..... 173
8.2.2 Scale-up Approach Validation ..... 175
8.3 Concluding Remarks ..... 176
Bibliography ..... 181

## List of Tables

Table 2.1 Comparison of different advanced oxidation technologies including the AquaPure plasma-based advanced oxidation process for removal of MTBE, TCE, NDMA, and 1,4-dioxane. Data compiled from Even-Ezra et al. and Malik.[57], [60] ..... 31

Table 3.1 Measured COD values for untreated and treated samples of MB. MB-A samples (left) contain initial MB concentration of 5 mg/L while MB-B samples (right) start with 1000 mg/L MB. ..... 57

Table 3.2 EPA method development analyte list showing the 24 compounds to be quantified.. 62

Table 3.3 Summary of calibration standards used for PFAS quantification. [a] 1000x denotes a dilution factor of 1000 of PFAC-24PAR standard solution. [b] 100x denotes dilution factor of 100. [c] 10x denotes dilution factor of 10. ..... 63

Table 4.1 PFAS concentrations (ppt) in the raw groundwater samples, measured in-house at University of Michigan (UM) and by an independent test laboratory. Boldface denotes the two most abundant compounds measured in the water samples. [a] Independent diluted Site 1 samples 2× and UM did not dilute Site 1 samples, with reporting limits of ±10 and ±1 ppt, respectively. [b] Independent diluted Site 2 samples 20× and UM diluted Site 2 samples 200×, with reporting limits of ±100 and ±200 ppt respectively. [c] NM = Not measured, UM did not have standard curves for PFBA an PFPeA. ..... 91

Table 4.2 PFOS and PFHxS removal data for Site 1 experiments using the single jet DBD-PJ reactor. [a] Initial concentrations of PFOS and PFHxS were 255 and 205 ppt, respectively. [b] Negative values indicate an increase in concentration. ..... 92

Table 4.3 PFOS and PFHxS removal data for Site 2 experiments. [a] Initial concentrations of PFOS and PFHxS were 33,000 and 16,500 ppt, respectively. [b] Negative values indicate an increase in concentration..... 93

Table 5.1 Perfluoroalkyl sulfonic acid (PFSA) concentrations vs. treatment time for the DBD plasma jet reactor treatment of Site 1 groundwater. The water temperature was maintained between 20 and 30 °C. The uncertainty for these concentrations is estimated at ±10%. The maximum concentration in each column is denoted by boldface. ..... 104

Table 5.2 Perfluoroalkyl carboxylic acid (PFCA) concentrations vs. treatment time for the DBD plasma jet reactor treatment of Site 1 groundwater. The water temperature was maintained between 20 and 30 °C. The uncertainty for these concentrations is estimated at ±10%. The maximum concentration in each column is denoted by boldface. ..... 104

Table 5.3 State of Michigan MCLs for six specific PFAS. ..... 108

Table 5.4 Packed-bed reactor Source Isolation (PBSI) test sample summary. Deionized (DI) water from the Engineering Research Building (ERB) was tested first to ensure that the starting water was not contaminated with PFOA. Samples PBSI-1, -2, and -3 involved flowing water through the packed-bed section (including the "showerhead" nozzle and the electrodes and housing), but the reactor reservoir, plumbing, and pump were replaced by a peristaltic pump with silicone tubing. [a] PBSI-4 included the same components as PBSI-3 except the heat shrink tubing covering the central electrode upstream of the discharge region was removed. [b] PBSI-5 did not include the nozzle or the electrodes. [c] PBSI-6 included the nozzle and central electrode, but not the outer electrode or the discharge region housing. Note that DI water rinsing occurred between samples PBSI-3 and PBSI-4. PBSI-HB confirmed that the silicone tubing did not leach PFOA. In all tests, 500 mL of DI water were circulated through the system. ..... 119

Table 5.5 Packed-bed reactor electrode insulation replacement (EIR) and printed nozzle replacement (PNR) test sample summary. Deionized (DI) water from the Engineering Research Building (ERB) was tested first to ensure that the starting water was not contaminated with PFOA. [a] The same batch of water was used for samples EIR-2 and -2. [b] The same batch of water was used for EIR-3 and -4. [c] The same batch of water was used for PNR-2, -3, and -4. Note that DI water rinsing occurred between samples EIR-4 and PNR-1. In all tests, 500 mL of DI water were circulated through the system. ..... 121

Table 6.1 Total energy over 4 min and energy per pulse added to the water as heat at varying water EC. The EC values listed in the tables are the average EC values over the treatment time. ..... 149

Table 7.1 The required value of $k\tau$ and $\tau$, as well as the required volume per tank, $V_{tank}$, and total tank volume $V_{total}$ calculated using Equation (7.2) for varying values of concentration factor (CF) and number of plasma stages ($n$). Here, $q$ is the flow rate through an individual plasma stage unit, where $q = Q_{process}/(i \times \mathrm{CF})$ and $i = 2$ for all cases. The row in boldface (CF = 4, $n$ = 3) denotes the configuration depicted in Figure 7.3. ..... 159

Table 7.2 Energy cost estimates for powering the plasma heads ($E_{plasma}$), the recirculation pumps ($E_{pump}$), and the membrane concentration stage ($E_{membrane}$), along with the sum of these, $E_{total}$. Here, $Q_{recirc}$ is the recirculation flow rate for a single tank, and $q_{recirc}$ is the recirculation flow rate through a single plasma head. ..... 163

## List of Figures

Figure 1.1 Proposed mechanism for the hydroxyl-driven oxidation of benzene.[11] ..... 3

Figure 1.2 Overview of PFAS exposure pathways for different human populations outside of occupational settings, including AFFF (aqueous film forming foams –firefighting foams) from Sunderland et al.[12] ..... 5

Figure 1.3 Examples of PFAS structures, including PFOA and PFOS from Bentel et al[16]. Here, *n* indicates the variable length of $C_nF_{2n+1}$. Surfactant structures are from Barzen-Hanson et al. and D'Agostino et al.[17], [18] ..... 6

Figure 1.4 Treatment technologies for the remediation of PFAS in water from Ross et al.[21] Absorptive/separative technologies are outlined in black, and destruction technologies are outlined in blue. ..... 8

Figure 2.1 Schematic overview of some important species and transfer processes at the plasma-liquid interface from Samukawa et al.[44] The topical review by Bruggeman and Leys provides more details regarding the complex processes at the plasma-liquid interface.[45] ..... 20

Figure 2.2 (top) Plasma-liquid configuration diagram and (bottom) typical image of the discharge for (a) direct filamentary discharge in water (microsecond pulse width), (b) DC glow discharge in air with water cathode, and (c) nanosecond pulsed discharge in argon bubbles in water from Samukawa et al.[44] ..... 22

Figure 2.3 Experimental setup of a DBD plasma used to study the physicochemical processes in an indirect plasma discharge above deionized water, from Liu et al. [48] ..... 23

Figure 2.4 (a) Time integrated emission intensity of a plasma discharge propagating along the plasma-water interface in a bubble discharge from Lai et al, and (b) time integrated emission intensity simulated in plasma discharges sustained in He, Ar, and $N_2$ bubbles from Tian et al., with the maximum values of total emission and OH emission provided in each frame.[49], [50] Surface hugging discharges are caused by the gradient in dielectric constant between the gas and water leading to electric field enhancement, as well as increased OH production at the interface. ..... 25

Figure 2.5 Schematic of some different discharge configurations used to generate plasma-liquid interactions: (a) direct discharge in liquid, (b) indirect gas-phase discharge above liquid, (c and d) gas-phase discharge making direct contact with liquid surface, (e) gas-phase plasma with dispersed liquid phase (i.e., aerosols), and (f) discharges in bubbles, from Bruggeman et al.[55]

Blue represents the liquid, pink indicates plasma, green is for dielectric materials, and black represents the metal electrodes. ..... 27

Figure 2.6 AquaPure discharge configuration for generating plasma in contact with thin water sheets (water sheet thickness is approximately 5 mm). The discharge takes place in ambient air.[40]..... 31

Figure 2.7 Schematic of the DBD plasma jet for plasma-liquid interaction, from Foster et al.[61] ..... 34

Figure 2.8 (a) Electrostatic simulation predicting downstream electric field enhancement at the air-water interface and (b) various components of the plasma discharge observed in the underwater DBD plasma jet operation, from Foster et al.[61], [62]..... 35

Figure 2.9 (a) Implementation concept for large-scale water treatment using the DBD plasma jet apparatus as a plasma applicator, and (b) schematic of treatment dynamics of a water slug flowing past a plasma jet applicator, from Foster et al.[40] The thickness of the plasma activated annulus is dependent on diffusion and induced fluid dynamical flow effects. ..... 37

Figure 2.10 Side view and top view schematics of the enhanced contact reactor, from Singh et al.[24] ..... 39

Figure 2.11 (a) Percent removal of PFAS after a single cycle through the reactor and (b) image of the enhanced contact reactor in operation, from Nau-Hix et al.[23] ..... 40

Figure 2.12 Cylindrical embodiment of the packed-bed reactor showing the central rod electrode and outer mesh electrode. The aggregate of water jets forming the “packed-bed” is shown by the blue cylinders. Plasma is generated in the spaces between the water jets, from Foster et al.[40]42

Figure 2.13 (a) Photograph of the packed-bed reactor showing a closed loop configuration, including the water reservoir, pump, and system plumbing. (b) Schematic of the discharge section of the packed-bed reactor in which water is disposed into thin jet streams and a plasma is generated in the spaces between the water jets, essentially coating the surfaces of the water jets in plasma, from Foster et al.[40], [63] ..... 43

Figure 3.1 Schematic diagram of a spectrophotometer.[70]..... 49

Figure 3.2 (a) Schematic of the DBD plasma jet experimental set-up used in this work. (b) Schematic and image of the DBD plasma jet apparatus operating in steam-mode discharge in deionized water. ..... 54

Figure 3.3 Discharge voltage and current signals measured during operation of the underwater DBD plasma jet operating in steam-mode at 5 kHz. ..... 55

Figure 3.4 (a) Images of samples starting with 5 mg/L MB showing decrease in color indicating destruction of the MB dye. (b) Image of untreated sample with 1000 mg/L MB and sample after 40 minutes of plasma treatment showing MB precipitates and mostly clear supernatant. ..... 57

Figure 3.5 (a) COD vs. $H_2O_2$ concentration, where $H_2O_2$ is added to samples by a solution of 30% $H_2O_2$. (b) COD vs. $H_2O_2$ concentration, where $H_2O_2$ is added to samples by exposure to the underwater DBD plasma jet. ..... 60

Figure 3.6 Relative speciation (%) of carbon dioxide ($CO_2$), bicarbonate ($HCO_3^-$), and carbonate ($CO_3^{2-}$) in water as a function of pH.[81] For this example, the water temperature is 20 °C and the electrical conductivity is 250 µS/cm. ..... 67

Figure 3.7 Experimental setup of the Monochromator spectrometer system with photomultiplier tube (PMT). ..... 74

Figure 4.1 (a) Schematic of the DBD plasma jet reactor setup, capable of being powered by AC or ns-pulsed power supplies. (b) Image of the DBD plasma jet reactor operating in single-jet mode under ns-pulsed excitation. ..... 82

Figure 4.2 (a) Schematic depiction of barrier discharge with water dielectrics. The top drawing is a cross-section perpendicular to the flow of the water jets, and the bottom drawing is a cross-section parallel to the flow of the water jets. (b) Water circulation system with plasma discharge inset. The arrows indicate the direction of water flow. ..... 84

Figure 4.3 Basic system diagram for the Eagle Harbor Technologies Rapid Capacitor Charging System (NSP-5000). ..... 87

Figure 4.4 Typical voltage and current waveforms for (a) the low-frequency sinusoidal AC power supply operating at 5 kHz and (b) the ns-pulsed voltage source operating at 2 kHz. ..... 89

Figure 5.1 PFOA removal (%) vs. treatment time using the packed-bed reactor with the ns-pulsed power supply and ambient air as the working gas. The initial concentration of PFOA is 5.7 ppm. ..... 99

Figure 5.2 Advanced oxidation of PFOA from Trojanowicz et al.[114] ..... 100

Figure 5.3 (a) PFOS concentration and (b) $\ln([PFOS]/[PFOS]_0)$ vs. treatment time with exponential decay trendlines (dashed gray lines). ..... 106

Figure 5.4 (a) PFNA concentration and (b) $\ln([PFNA]/[PFNA]_0)$ vs. treatment time with exponential decay trendlines (dashed gray lines). ..... 107

Figure 5.5 (a) PFOS concentration and (b) $\ln([PFOS]/[PFOS]_0)$ vs. treatment time with exponential decay trendlines (dashed gray lines). ..... 110

Figure 5.6 (a) PFHxS concentration and (b) $\ln([PFHxS]/[PFHxS]_0)$ vs. treatment time with exponential decay trendlines (dashed gray lines). The orange solid line in (a) crossing through the last three data points is an exponential curve for that omits the initial concentration ($[PFHxS]_0$). ..... 111

Figure 5.7 (a) PFBS concentration and (b) PFHxA concentration vs. treatment time. ..... 112

Figure 5.8 (a) PFNA concentration and (b) PFOA concentration vs. treatment time. ..... 113

Figure 5.9 (a) Water pH and (b) electrical conductivity measured over the duration of the treatment time. ..... 114

Figure 5.10 Discharge voltage and discharge current vs. time for (a) EC = 800 µS/cm, and (b) EC = 4,000 µS/cm. ..... 115

Figure 5.11 (a) Maximum discharge voltage vs. water EC, and (b) maximum discharge current vs. water EC. ..... 116

Figure 5.12 (a) Discharge power and (b) energy per pulse vs. water EC. ..... 117

Figure 5.13 (a) The 3-D printed "showerhead" nozzle that disperses the water into thin jet streams in the packed-bed reactor was found to be a significant source of PFOA contamination. (b) A PVC on/off valve for drinking water from McMaster-Carr with a polytetrafluoroethylene (PTFE) plastic seat. ..... 123

Figure 6.1 Discharge voltage and discharge current vs. time for (a) EC = 4 µS/cm, and (b) EC = 4,350 µS/cm. ..... 129

Figure 6.2 (a) Maximum discharge voltage vs. water EC, and (b) maximum discharge current vs. water EC. ..... 130

Figure 6.3 Discharge voltage and discharge current vs. time for (a) EC = 390 µS/cm, and (b) also EC = 390 µS/cm, showing the variation in voltage-current waveforms that can occur pulse-to-pulse for a given water EC and power supply inputs. ..... 130

Figure 6.4 Discharge voltage and discharge current vs. time for (a) EC = 4,350 µS/cm, and (b) also EC = 4,350 µS/cm, showing the only small variations in peak voltage and peak current at around 9 kV and 100 A, respectively. ..... 131

Figure 6.5 Discharge voltage and discharge current vs. time for (a) EC = 390 µS/cm, and (b) EC = 390 µS/cm, demonstrating two different discharge modes that can occur for a given water EC and power supply inputs; however, the narrow voltage pulse and high current waveform shown in (b) was observed to occur infrequently compared to the more stable and wider voltage pulse shown in (a). ..... 132

Figure 6.6 Discharge voltage and discharge current vs. time for (a) EC = 15,800 µS/cm, and (b) also EC = 15,800 µS/cm, demonstrating pulse-to-pulse variation that can occur for a given water EC and power supply inputs. In this case, the voltage waveform in (b) appears to almost transition into the spark type mode (large voltage drop), but the voltage increases again after the first drop and results in a similar pulse width overall as in (a). This may indicate a sort of hybrid discharge mode. ..... 134

Figure 6.7 (a) Discharge power and (b) energy per pulse vs. water EC. ..... 135

Figure 6.8 Experimental setup for optical emission spectroscopy using the packed-bed reactor. ..... 138

Figure 6.9 Sample emission spectrum from 200 to 900 nm collected from the plasma discharge in contact with water at EC = 200 µS/cm. The shaded region represents ultraviolet light (200 – 400 nm), with the high energy UVC light to the left of the dotted vertical line (200 – 280 nm). The wavelength range collected for analyzing the nitrogen second positive band (290 – 310 nm) is indicated, as well as the hydrogen alpha Balmer line (656.28 nm) used for the plasma density calculation. The oxygen line (777 nm) is also labeled..... 139

Figure 6.10 Emission spectra for (a) water EC = 4 µS/cm showing high intensity UVC emission (200 – 280 nm), and for (b) water EC = 8,140 µS/cm in which the emission is dominated by nitrogen in the 300 – 400 nm range. ..... 141

Figure 6.11 Specair simulated nitrogen second positive band (green) compared to the experimental data (black) at water EC = 15,800 µS/cm. The best fit (smallest residual) was found for the wavelength range of 325 – 365 nm. In this case, the gas temperature was estimated at 700 K..... 142

Figure 6.12 Experimentally determined gas temperatures vs. water EC. ..... 144

Figure 6.13 An example of a Voigt fit to experimentally measured data, in this case for a water EC = 4,350 µS/cm..... 147

Figure 6.14 Experimentally determined plasma densities vs. water EC..... 148

Figure 7.1 Comparison of (a) conventional continuous flow reactor and (b) the proposed plasma micro-reactor with internal recirculation. ..... 156

Figure 7.2 Schematic diagram of a continuous flow plasma treatment process with a membrane concentration stage (from T. Olson, personal communication)..... 157

Figure 7.3 Schematic diagram of a continuous flow plasma treatment process with a membrane concentration stage for $Q_{process}$ = 170 L/min, CF = 4, $n$ = 3, $i$ = 2, and $C_{des}$ = 12 ppt PFOS. ..... 160

Figure 7.4 Concentration of PFOS exiting each stage of the plasma treatment process based on the model conditions described in Figure 7.3. ..... 160

Figure 7.5 Schematic diagram of the 3-stage plasma treatment process with two parallel process lines based on the model configuration from Figure 7.3. Each tank has a volume of 826 L with 6 recirculating plasma heads per tank. ..... 161

Figure 8.1 Example of a suggested planning and design process that connects engineering (outer loop) with sustained stakeholder participation (inner loop) from Guest et al.[138] The double-headed arrows connecting the technical design process with stakeholder participation represent workshops and engagement throughout the planning and design of a water treatment system. 179

## Abstract

Demand for freshwater is rapidly rising due to expanding agriculture and industrialization, further exacerbated by population growth, changing climate, accidental spills, and deteriorating infrastructure. Meanwhile, providing access to safe drinking water around the globe remains a grand challenge of the 21st century. A significant part of the solution is to recycle and re-use water; however, wastewaters contain contaminants of emerging concern which are not adequately addressed by conventional water treatment technologies.

Per- and polyfluoroalkyl substances (PFAS), for example, have received attention lately after being detected in >98% of the US population's blood. Meanwhile, most municipal water treatment plants are not equipped to remove these compounds. Furthermore, human exposure to PFAS has been linked to a multitude of health problems including endocrine system disruption and cancers. These chemicals are found in a wide range of industrial and consumer products including non-stick coatings for cookware, food packaging, and firefighting foams. The high strength of the carbon-fluorine bonds found in PFAS are both the source of their industrial appeal and the reason for their persistence in the environment. While activated carbon filtration has shown efficacy for removing long-chain PFAS from water, the compounds are not decomposed, but simply stored in different media that must be dealt with, thus leading to high overall costs and concerns about reintroducing the contamination back into the environment.

Non-thermal plasmas are a promising emerging technology for the destruction of PFAS in water owing to their ability to drive multiple decomposition mechanisms including advanced oxidation and reduction. This thesis explores two plasma-water reactor configurations for the

decomposition of PFAS in contaminated groundwaters collected from legacy sites. The reactors included an underwater plasma jet and a barrier discharge with water dielectrics. Based on the removal percent of perfluorooctanesulfonic acid (PFOS), air was found to be a suitable working gas alternative to argon, and both AC and ns-pulsed power supplies could generate the plasmas for these reactors with similar performance. Plasma-water contact area was a critical variable governing the decomposition performance. Furthermore, it was found that the mass removal efficiency was higher when treating higher PFAS concentrations, suggesting that a concentration step followed by plasma treatment can improve the cost-effectiveness of the treatment process.

Batch processing of the groundwater revealed that long-chain PFAS followed empirical first-order decay, and notably, the two most prevalent PFAS in the groundwater were removed to below Michigan EPA regulatory limits within 90 minutes of treatment. Throughout the treatment duration, the water conductivity increased approximately fourfold; however, a separate experiment indicated that the plasma discharge properties did not change significantly with increasing water conductivity. Specifically, plasma density, gas temperature, and discharge power were approximately constant around $(9 \pm 2) \times 10^{16}$ $cm^{-3}$, 700 ± 250 K, and 120 ± 20 W, respectively. Low water conductivities (<200 μS/cm) were associated with higher peak discharge voltages, higher electron densities and gas temperatures, and more intense UV emission, which is thought to be associated with a spark-type discharge that forms due to longer charge relaxation times and streamer propagation lengths, thus enabling a transient conductive channel between electrodes.

Finally, an architecture for converting the batch-mode plasma treatment into a scalable continuous flow configuration is proposed, along with a model for estimating the system size and performance based on the batch reactor kinetics. This architecture features membrane

concentration of PFAS followed by a staged plasma micro-reactor treatment, each with internal water recirculation. The treatment cost for removing PFOS to below Michigan EPA limits from an initial concentration of 200 ppt is estimated at 1.30 USD per thousand liters at a continuous flow rate of 170 L/min.

# Chapter 1 Introduction

In this chapter, a brief introduction to water resources and the issues of emerging contaminants are presented in the context of water re-use. Specifically, this thesis will focus on the class of contaminants known as per- and polyfluoroalkyl substances which have been accumulating in the environment and in groundwaters for the past several decades. Recently, human exposure to these chemicals has been linked to health concerns.

Currently, there is no cost-effective solution for removing or decomposing this category of contaminants. Several technologies are being developed, including those based on the application of non-thermal plasmas. Indeed, thus far, plasma-based remediation of per- and polyfluoroalkyl substances in water appears to be one of the most promising of these emerging technologies, but the barrier of scaling up to relevant processing flow rates still must be addressed.

## 1.1 Water Resources and Contaminants of Emerging Concern

Providing access to safe drinking water amidst rapidly growing global demand remains a grand challenge of the 21st century. Water-related diseases continue to be a major cause of death worldwide, especially among children. Meanwhile, threats from emerging contaminants such as pesticides and pharmaceuticals, along with accidental spills, changing climate, and deteriorating infrastructure further exacerbate the concern of freshwater scarcity.

In 2016, it was found that four billion people experience severe water scarcity for at least one month per year, while half a billion people face severe water scarcity year-round.[1] More

recently, the 2018 edition of the United Nations World Water Development Report (WWDR) estimated that close to six billion people will lack reliable access to clean water by 2050.[2] However, a 2019 reassessment of this WWDR suggests that this value of six billion people facing severe water scarcity by 2050 may be an underestimation.[3]

A significant part of the solution must involve recycling and re-using the water that is available; however, wastewaters contain contaminants of emerging concern (CECs) which are currently not adequately addressed by conventional water treatment technologies. Specifically, pharmaceuticals such as pain relievers, hormones, and antibiotics, industrial products such as dyes and other volatile organic compounds, as well as agricultural pesticides and microcystins can pass through wastewater treatment plants without significant reductions in the concentrations of these unwanted chemicals.[4]–[8]

As a result, these contaminants can show up in measurable quantities at commercial and residential taps leading to a host of problems including antibiotic resistant bacteria. In some cases, wide-spread drinking bans have been issued in order to preserve public health.[9] Albeit, the concentrations of these contaminants are frequently considered miniscule, sometimes in the parts per trillion (ppt or ng/L) range. Regardless, the effects of consuming trace amounts of contaminates over extended periods of time is not well understood, and with the large volumes of water that humans consume daily to support life functions, it is best to proceed with caution.

In this way, contaminants of emerging concern represent a barrier to water re-use because traditional wastewater plants do not typically possess the advanced treatment technologies to remove these chemical and biological contaminants. Versatile on-demand remediation is urgently needed to protect and preserve our freshwater resources. Fortunately, most contaminants of emerging concern can be removed with advanced oxidations processes.[10]

Advanced oxidation processes (AOPs) typically involve the injection of externally supplied chemicals, such as ozone or hydrogen peroxide, driving reactions in the water being treated. Often performed in conjunction with ultraviolet radiation, a primary goal of advanced oxidation processes is the production of hydroxyl radicals which aggressively attack organic contaminants through a series of chain reactions, reducing the organics to carbon dioxide, water and salts in a process called mineralization. For example, a proposed mechanism for the hydroxyl-driven oxidation of benzene is shown in Figure 1.1. Continued oxidation by hydroxyl radicals can lead to mineralization of the benzene.

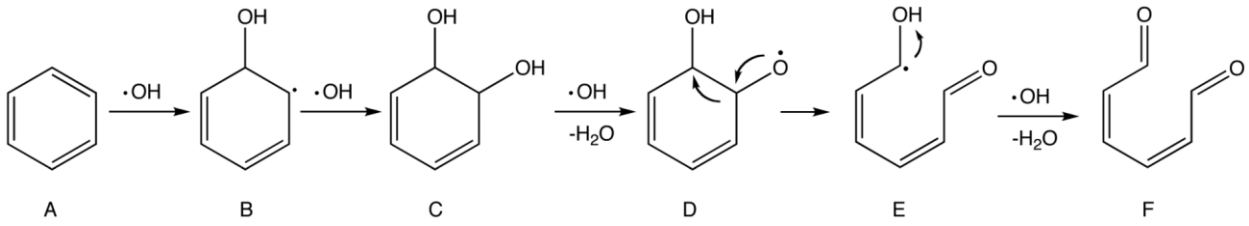


Figure 1.1 Proposed mechanism for the hydroxyl-driven oxidation of benzene.[11]

Unfortunately, not all CECs can be easily decomposed by advanced oxidation processes. For example, per- and polyfluoroalkyl substances are a category of chemicals which typically feature a multitude of carbon-fluorine bonds. The strength of these bonds allows them to remain stable even in the presence of hydroxyl radicals. As such, it is not surprising that these chemicals do not readily biodegrade in the environment, but rather tend to bioaccumulate. The next section provides some background on these chemicals and the problems that are associated with their accumulation in the environment, particularly in groundwaters.

## 1.2 The Per- and Polyfluoroalkyl Substance Problem

Per-and polyfluoroalkyl substances (PFAS) are fluorinated organic compounds that are extensively used in industrial and public settings, including in items such as water and oil repellant surfaces, non-stick cooking surfaces, food packaging, and firefighting foams.[12] Many of the applications of these chemicals leverage the fact that they are heat resistant, hydrophobic, and highly stable. In the case of the firefighting foams, PFAS floats on the surface of burning liquid fuel, thus smothering the flames and reducing heat transfer from the fire. Since PFAS coatings resist the formation of oil stains, its use has proliferated for packaging in the fast-food arena, for example pizza boxes.

These substances' relative stability to decomposition, though an advantage for various commercial applications, is however particularly problematic from an environmental standpoint. This stability is derived from the strength of the carbon-fluorine bond, the strongest bond in organic chemistry.[13] This stability combined with its high hydrophobicity makes it incredibly difficult to decompose by conventional means. The substances therefore have the capacity to accumulate in the environment such as groundwater and have been colloquially referred to as "forever chemicals" owing to their resistance to biodegradation and conventional treatments.

Invariably, uptake by humans is a consequence of ingesting contaminated water or seafood. Indeed, over 98 percent of all Americans have detectable levels of PFAS in their blood stream.[12] Accumulation pathways are illustrated in Figure 1.2 as discussed by Sunderland et al. PFAS compounds can bioaccumulate in human tissue and typically have a long half-life in the body leading to long-term health effects such as diabetes, cancer, thyroid hormone disruption, and low sperm activity to name a few.[14], [15]

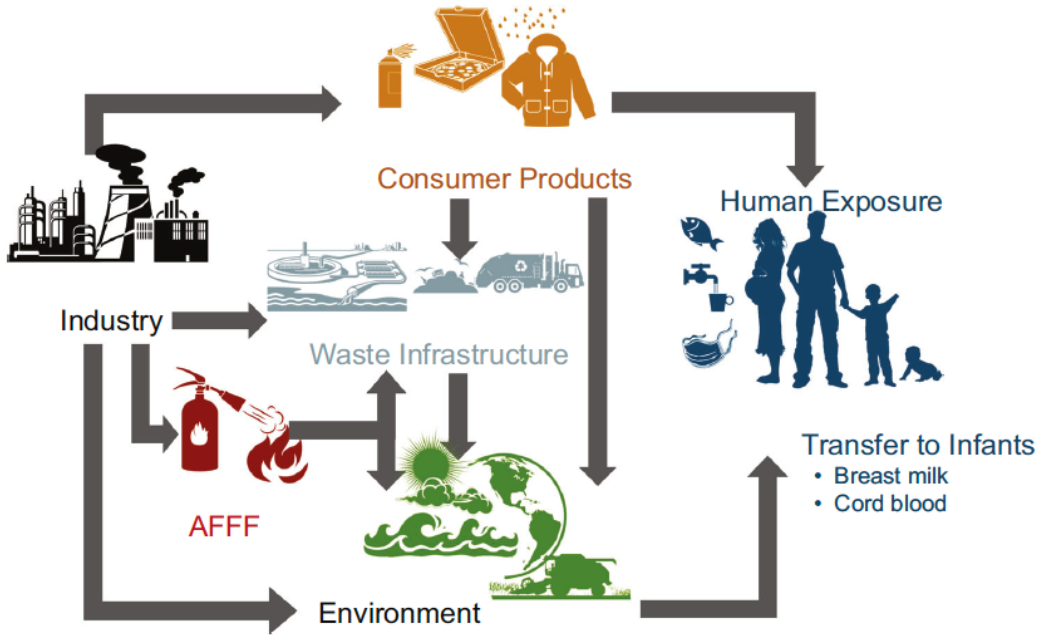


Figure 1.2 Overview of PFAS exposure pathways for different human populations outside of occupational settings, including AFFF (aqueous film forming foams –firefighting foams) from Sunderland et al.[12]

Since being introduced in the 1940s, it was not until recently that a comprehensive plan was formulated to address PFAS proliferation in the environment, particularly in groundwaters. The number of actual PFAS compounds numbers well over 4,000, thus giving some appreciation of the diversity of these recalcitrant compounds that have been introduced into the environment.[14] A chemical depiction of selected PFAS compounds found in contaminated groundwaters, including perfluorooctanoic acid (PFOA) and perfluorooctanesulfonic acid (PFOS), are shown in Figure 1.3. Which specific PFAS compounds are most prevalent in the groundwater of a given region is highly dependent upon the nature of chemical exposure, such as whether it is derived from industrial chemical processing, landfill leachates, or regions near air bases where contamination is derived from extensive use of firefighting foam products.

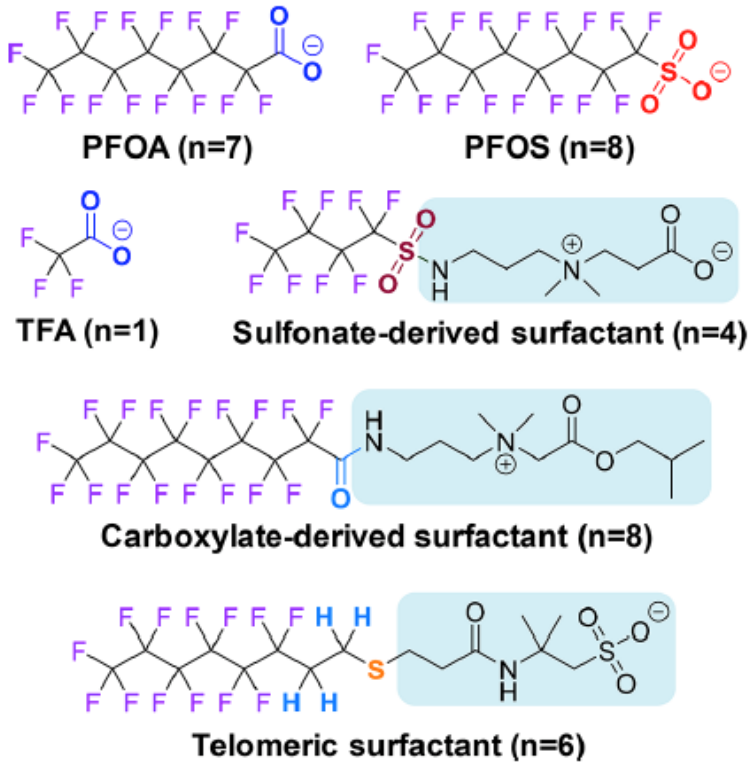


Figure 1.3 Examples of PFAS structures, including PFOA and PFOS from Bentel et al[16]. Here, *n* indicates the variable length of $C_nF_{2n+1}$. Surfactant structures are from Barzen-Hanson et al. and D'Agostino et al.[17], [18]

The primary issue with novel compounds is inadequate study of the full chemical lifecycle. A comprehensive picture of how the substances enter the environment and are ultimately remediated is lacking. The United States Environmental Protection Agency (US EPA) is currently reviewing alternatives to a class of PFAS compounds as well as developing a plan for stewardship and eventual elimination of these chemicals. While regulatory pressures will ultimately determine the trajectory of the phase out of these chemicals, their presence in the environment owing to extensive use needs to be addressed.

The US EPA's guidance from 2020 on PFAS where remediation action is recommended is 70 ppt.[19] Recently, state laws have also been passed with considerably lower remediation action concentration levels.[20] Since state laws have now established maximum contamination

levels of PFAS compounds in wastewaters, the substance is officially regulated and compliance requires that treatment technologies be capable of removing PFAS to adequate levels. Unfortunately, the recalcitrant nature of these compounds makes removal and destruction difficult. The decomposition of PFAS to less harmful compounds represents an important opportunity, particularly for the introduction of new water treatment technologies, such as non-thermal plasmas in contact with water. Indeed, the low concentration of the regulatory limits (ppt levels) and widespread contamination presents the need for treating large dilute volumes of water. As will be discussed later in this thesis, concentrating PFAS prior to destruction can improve the non-thermal plasma treatment process efficiency.

### 1.3 PFAS Treatment Technologies

Treatment technologies for the remediation of PFAS contamination generally fall into two categories: (1) absorptive/separative and (2) destruction technologies, illustrated in Figure 1.4. Absorptive/separative technologies tend to be at a more mature stage of development and are more practically feasible for dealing with relevant throughputs, although these technologies are not actually capable of decomposing the PFAS contaminants; rather, they simply concentrate the compounds in the filter material or a waste steam, which then needs to be addressed.

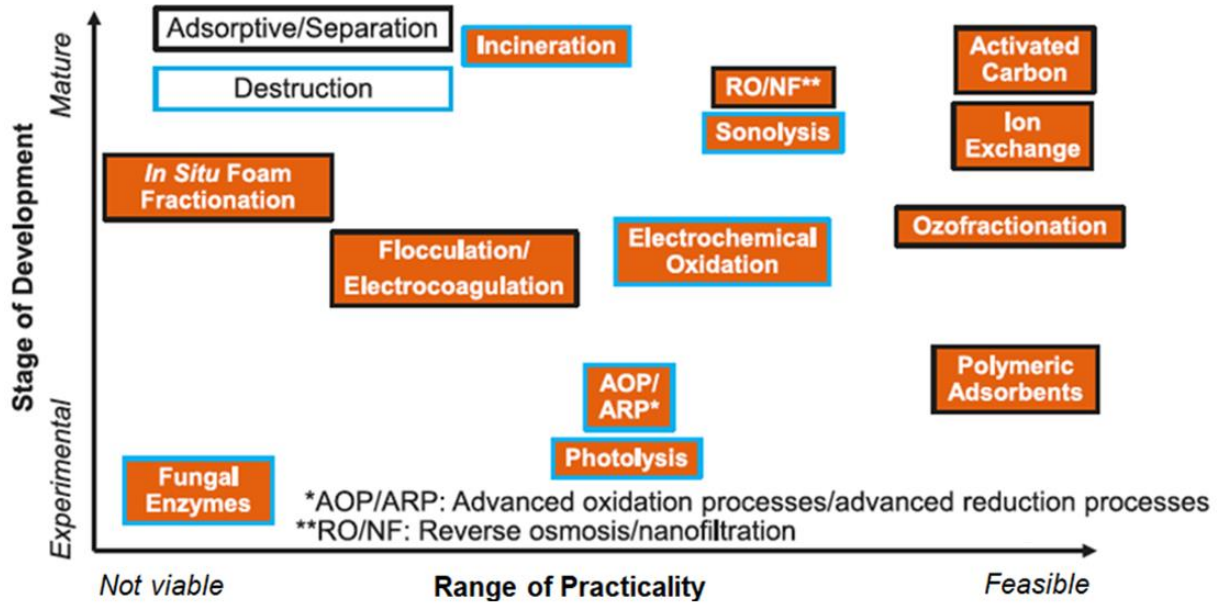


Figure 1.4 Treatment technologies for the remediation of PFAS in water from Ross et al.[21] Absorptive/separative technologies are outlined in black, and destruction technologies are outlined in blue.

Currently, the predominant approach to dealing with PFAS contamination in water is filtering it out with activated carbon (powder or granular—PAC or GAC) and subsequently regenerating the media at high temperature for reuse or incinerating the media once it has been loaded to capacity. Both thermal regeneration and incineration are expensive options. While activated carbon appears to be the most practically feasible approach at the present, several issues remain to be resolved.

For example, GAC filters are not effective at removing the shorter chain PFAS, which may still be problematic from a public health standpoint. Furthermore, the incineration of spent GAC filters has been under increasing scrutiny, not only due to the high energy costs involved but also the potentially harmful byproducts which can form and escape back into the environment generating secondary contamination. The reality is that there is no existing solution that has proven to adequately address the problem of PFAS in the environment.

Several emerging PFAS decomposition technologies are being studied to evaluate their potential roles in the remediation of PFAS contamination, in part to complement the more mature absorptive/separative methods such as GAC, ion exchange, and reverse osmosis. These decomposition technologies include electrochemical, sonochemical, photolysis/photocatalysis, persulfate, thermolysis, and zero-valent iron to name a few.

Additionally, treatment train approaches are being considered involving combinations of these technologies, including both tandem treatment trains involving concentration then destruction of PFAS like the GAC filtering followed by incineration, and parallel destructive treatment train approaches such as hydrogen peroxide combined with persulfate or thermolysis with parallel photolysis.[22] Unfortunately, to date all these emerging technologies have faced significant problems with scale-up: namely, the high cost of chemicals and/or energy required.

In this respect, plasma-based methods for PFAS remediation show great promise for scale-up since the process does not require the use of chemicals. The plasma generates the necessary chemicals via the electrical energy input. Furthermore, plasma-based treatment methods have the potential to operate with excellent energy efficiency thanks to the development of power supplies capable of high-voltage pulses with pulse widths on the order of nanoseconds which can be operated at low duty cycles to save power while still achieving necessary electron excitation to drive PFAS decomposition.

Plasma also represents a unique treatment technology in that it can drive multiple PFAS destruction processes in parallel such as advanced reduction, advanced oxidation, photolysis and thermolysis, using a single power input and no added chemicals. When plasma is used after a concentration stage, such as reverse osmosis, this combination is effectively a tandem and

parallel treatment train approach using just two technologies that can be highly modular for scale-up.

Though plasma technologies also face challenges with scale-up to high throughput processing, Thagard and colleagues at Clarkson University have successfully decomposed PFAS from groundwaters collected from contaminated wells in a pilot-scale reactor, the "enhanced contact reactor" which features argon bubbling and plasma discharge over the surface of the water.[23] This reactor represents the state of the art in regard to demonstrated large-scale plasma batch reactors for the decomposition of PFAS. The large batch reactor has been successful in reducing PFAS below the US EPA maximum contaminant levels (MCLs) using groundwater from a contaminated site at an Air Force base.

The energy requirements for the enhanced contact reactor as determined using the Electrical Energy per Order (EE/O), which represents the amount of energy necessary to degrade a contaminant by an order of magnitude in unit volume ($m^3$) of contaminated water, ranged between 1.7-56 kWh/$m^3$ for combined PFOA and PFOS depending on the source well of the groundwater and the treatment time required.[24] It will be noted in Chapter 5 that the packed-bed batch reactor presented in this thesis has achieved EE/O values of similar magnitude for PFOA and PFOS removal.

For reference, the EE/O for PFOA removal is ~5,000 kWh/$m^3$ for persulfate, photolysis, and sonolytic methods using prepared PFOA- and PFOS-contaminated samples.[25]–[27] Meanwhile, sonochemical removal of PFOS can cost more than 20,000 kWh/$m^3$.[27] Electrochemical treatments can be less energy intensive with EE/O values between 130-500 kWh/$m^3$, with PFOS being more costly to remove than PFOA.[28] Photochemical oxidation processes have achieved EE/O values of about 380 kWh/$m^3$, which is within the range of

electrochemical treatments, but is still not particularly competitive.[29] The EE/O values for these competing PFAS remediation technologies would likely be even higher for treatments of actual groundwaters containing a complex matrix of contaminants, and thus illustrates the problem of high energy costs associated with PFAS treatment while strengthening the argument that plasma-based methods can offer cost-effective solutions. Indeed, it appears that plasma discharges are currently among the most energy efficient PFAS remediation technologies, particularly for the decomposition of PFOA and PFOS.

The enhanced contact reactor, developed at Clarkson University and described in Section 2.4.3, has demonstrated capability to decompose PFAS via plasma action in a batch reactor with a 4 L recirculating volume at competitive energy costs. The proposed staged flow-through system, described in Chapter 7, featuring recirculation at each stage through a packed-bed reactor seeks to extend upon the successes of Thagard and colleagues. By studying the transition from batch processing to flow-through (i.e., continuous flow) processing using the principle of optimizing the plasma-liquid contact area.

### 1.4 Motivation

The reality is that currently, there is no cost-effective method for the removal and destruction of PFAS from water supplies. Activated carbon filtration is presently the most widely used technology, but this is still an expensive solution. Furthermore, issues related to dealing with spent filter media makes this treatment method far from ideal, and thus the need for technologies that can decompose PFAS to safer compounds is significant and pressing.

Plasma-based treatments have thus far shown great promise for the destruction of PFAS, as demonstrated in small batch reactors. However, it is highly desirable for a water treatment technology to have the capability of processing water in a once-through or continuous flow

fashion. A key question that remains to be answered is if this can be done with a plasma system. After all, plasma-based processing of liquids has been demonstrated at laboratory scales with promising results for a number of applications including industrial processing, nanomaterial synthesis, material functionalization, and cooling water management, to name a few.[30]–[33] The primary impediments to commercialization of these plasma-based liquid processing technologies include the scalability (i.e., capability to process commercially relevant flow rates) and the overall cost of the system, including equipment and operating costs.

In this work, non-thermal plasma is investigated for the treatment of groundwaters containing PFAS contamination. While plasma treatment is often thought of as an advanced oxidation method, it has been shown that oxidation is not particularly effective in decomposing short-chain PFAS compounds.[34] This is largely due the relative strength of the carbon-fluorine bond and the high electronegativity of fluorine. The oxidation potential of fluorine is larger than that of hydroxyl, the chief radical involved in advanced oxidation processes.

On the other hand, reduction methods have shown success at defluorinating and ultimately decomposing PFAS compounds.[35] These methods feature solvated electrons—a short-lived, highly reactive complex that destabilizes PFAS compounds. Solvated electron destruction of PFAS compounds is facilitated by hydrogen-fluorine exchange and by chain shortening via bond breaking of carbon-carbon along with the cleaving of carbon-fluorine bonds.[36]

The exact decay paths for the complete decomposition of PFAS compounds via advanced reduction are still not well understood. What is known however is that advanced reduction of PFAS is most efficient in water at neutral to elevated pH to minimize hydrogen scavenging of the solvated electron, low nitrate concentration (another solvated electron scavenger), reduced

dissolved organic media which competes with PFAS molecules for reactions with solvated electrons, and elevated temperature which increases the collision frequency for reactions.[36]

Plasmas are also a source of free electrons which solvate when in contact with water and have been explored as a means to remove organic contaminants.[37] As previously mentioned, plasmas have already shown success at decomposing PFAS.[24], [38], [39] Here, the effects of plasma and associated plasma-derived solvated electrons on PFAS compounds found in contaminated well water are investigated. The reactor featured in this work is the barrier discharge with liquid dielectrics, referred to as the packed-bed reactor.[40] This reactor separates the water stream in to narrow jets, between which plasma is generated. The geometry maximizes plasma to liquid contact area, a key consideration in treating surfactant compounds like PFAS which tend to collect at the boundary of the gas-liquid interface.

The overarching goal is to transition from batch-mode processing to treatment on a continuous flow basis. In this thesis, a new architecture is proposed to treat water in a flow-through configuration while preserving the batch-mode kinetics from the laboratory-scale experiments. To do this, a comprehensive understanding of the batch-mode kinetics is needed. This thesis seeks to characterize the batch-mode kinetics of plasma-driven decomposition of PFAS to inform the scale-up into a flow-through treatment system that is capable of processing relevant flow rates.

### 1.5 Scope of Work

So far, Chapter 1 has provided a brief introduction to water resources and CECs, including PFAS which represents a category of industrial chemicals featuring carbon-fluorine bonds, often used for their surfactant properties. Unlike many CECs, PFAS have proven recalcitrant to most advanced oxidation processes. An overview of treatment technologies for

the remediation of PFAS contamination in water was presented, and plasma-driven decomposition of PFAS was introduced as a promising emerging technology for the cost-effective destruction of PFAS in waters.

Chapter 2 will provide a brief introduction to plasmas, particularly non-thermal plasmas in contact with water for the purpose of decomposing contaminants. Some of the physical and chemical processes occurring at the plasma-liquid interface will be mentioned, along with a description of some of the various electrode configurations for bringing plasmas in contact with liquids. While many plasma-water reactor configurations have been conceived and have shown promise at laboratory scales, only a few have demonstrated capability to treat volumes or flow rates nearing relevant pilot scales.

Chapter 3 will give an overview of the experimental methods used for evaluating plasma-based water treatment, starting with the assessment of contaminant removal from waters and wastewaters. A case study highlighting the interference of hydrogen peroxide in standard chemical oxygen demand assessments is presented to notify the plasma community that residual hydrogen peroxide from plasma treatment can affect the interpretation of this standard water quality metric. Next, the quantification of PFAS concentrations in water samples by liquid chromatography – tandem mass spectrometry will be discussed. The equipment used for water property measurements such as electrical conductivity, pH, and temperature are provided, and titration and spectrophotometric techniques for the quantification of chemical species derived from the plasma treatment process are also discussed. Lastly, an overview optical emission spectroscopy as a gas/plasma phase diagnostic is given, which will be used to estimate properties of the plasma discharge.

In Chapter 4, two different plasma reactors are investigated for the decomposition of PFAS in groundwaters collected from two legacy sites. Furthermore, the effects of various reactor control variables are assessed, including the power source (either AC or ns-pulsed), feed gas (air or argon), the starting concentration of PFAS (coming from two different legacy sites), and the reactor configuration (packed-bed reactor vs. dielectric barrier discharge plasma jet, which will be discussed later). The two reactors feature different plasma discharges and different plasma-water contact areas. Additionally, two different treatment times will be tested, thus providing some initial insight into the PFAS decay behavior.

The batch-mode kinetics of PFAS decay are explored further in Chapter 5, starting with a high concentration PFOA treatment in which the PFOA concentration is measured at varying times throughout a 60 min treatment duration. Next, two time-resolved groundwater treatment tests are presented for the two reactors configurations explored in Chapter 4, both intended to gain insight into the batch kinetics of these reactors. The treatment test using the packed-bed reactor is run for a long duration with the goal of removing PFAS to below the Michigan EPA regulatory limits. The electrical energy efficiencies associated with these treatments are also commented on. Lastly, a discussion regarding the ubiquity of PFAS, and PFOA in particular, is presented.

Since the electrical conductivity of the water increases throughout the duration of a batch treatment, Chapter 6 investigates the influence of water conductivity on the plasma discharge properties. First, the effects of water conductivity on the voltage-current waveforms are addressed, followed by the discharge power calculated from integrating the voltage-current waveforms. Next, optical emission spectroscopy is used to evaluate the gas temperature and plasma density of the discharge at varying water electrical conductivities.

Chapter 7 proposes an architecture for converting the batch-mode treatment of the laboratory-scale packed-bed reactor with the purpose of scaling up to commercially relevant processing flow rates. A corresponding model is presented to predict the system size and performance based on the kinetics from the batch-mode treatment presented in Chapter 5. An energy cost assessment is also provided including the costs associated with powering the plasma, the pumps, and a proposed upstream concentration stage which helps to reduce the overall system size.

Finally, a summary of the thesis is provided in Chapter 8. Perspectives on future work are provided along with some concluding remarks.

# Chapter 2 Plasma-water Reactors: Theory and State of the Art

This chapter first presents a brief introduction to plasmas, followed by a background on plasmas in contact with liquids, primarily for the purpose of generating reactive species which can react with contaminants in water. Applying a sufficient treatment dose, or appropriate concentration reactive species via the plasma, leads to the mineralization of organic contaminants, including those of emerging concern such as 1,4-dioxane and PFAS. An overview of configurations for bringing plasmas into contact with liquids is presented, along with a selection of plasma-water reactors that show promise for achieving pilot-scale processing flow rates. Included among these is the enhanced contact reactor developed by Thagard and colleagues which represents the current state of the art in PFAS decomposition.

## 2.1 Introduction to Plasmas

Plasma, also known as the fourth state of matter, is a collection of ionized gas that exhibits collective behavior. Plasmas are composed of charged species including electrons and positive and/or negative ions, and overall, these collections of charged species are quasi-neutral (i.e., charge neutral when averaged over time and space). This state of matter can span a tremendously wide parameter space, ranging over 30 orders of magnitude in density and over 6 orders of magnitude in temperature. Additionally, the ionization fraction can range from the parts per million or less all the way to fully or multiply ionized plasmas.

This work will focus on non-thermal plasmas, also referred to as non-equilibrium, low temperature, or cold plasmas, owing to the differences in temperatures between the electrons and

neutral gas particles. Non-thermal plasmas can have gas temperatures close to 300 K (0.025 eV) while the electron temperatures can be significantly higher, often ranging from 1 – 20 eV. The low gas temperature is generally advantageous for chemical processing applications since relatively small amounts of energy can accelerate electrons to high energies which can drive complex chemistry without excessive energy wasted on gas heating.[41] High voltage, short pulse (i.e., on the order of nanoseconds) excitation is often used to generate non-thermal plasmas. While the electrons can be quickly accelerated to high energies on these timescales due to their low mass, the more massive particles do not have time to respond; thus, most of the applied power goes into heating the electrons and the resulting chemistry is largely associated with these energetic electron interactions.[42]

Furthermore, the plasmas featured in this work are generated at atmospheric pressure, and thus are generally filamentary in nature. The four most commonly used non-thermal atmospheric pressure plasma discharges are the corona (or pulsed corona), dielectric barrier, gliding arc, and spark discharges. The typical properties of these discharges along with the breakdown phenomena associated with each are described by Fridman et al.[43] Indeed, the discharges in this thesis are predominantly pulsed corona and dielectric barrier discharges, although a spark-type discharge is observed to occur at low water conductivities, as discussed in Chapter 6.

## 2.2 Plasmas in Contact with Liquids

Here, plasma-liquid interactions are discussed primarily in the context of an alternative advanced oxidation process (AOP); however, when it comes to the decomposition of PFAS, the ability of plasmas to generate solvated electrons is thought to represent an important mechanism involved in breaking the carbon-fluorine bond (i.e., solvated electron mediated reduction). Aside

from PFAS remediation, most plasmas in contact with water are intended for the advanced oxidation of organic contaminants.

A significant disadvantage of traditional AOPs is the required transport and storage of chemicals, such as ozone and hydrogen peroxide. In many cases, this disadvantage complicates the operation, incurs additional costs, and introduces new safety concerns. Other times, it can render traditional advanced oxidation processes uneconomical or unsuitable for the specific application. Due to the cost requisite to acquire the chemical reagents used in AOPs, the quantity of which being proportional to the amount of contaminants that are oxidized, it is currently not economical to use advanced oxidation processes alone to treat high volumes of wastewater without pretreatment. Rather, AOP treatment is typically utilized as a final stage after many contaminants have been removed via primary and secondary treatment stages, in order to minimize the amount of AOP chemicals required while still decomposing contaminants to a suitable concentration for the water to be consumed or transported to a drinking water treatment plant for further processing.

The problem of chemical transport and storage may be solved by producing the reactive oxidative species from the liquid being processed itself. A plasma may be generated in or above the liquid to be processed by applying a high voltage, typically pulsed or sinusoidal (AC). The energy of the applied electric field is deposited preferentially into electrons, which then undergo collisions with water molecules to produce multiple AOP species. Some of the important species and transport processes that occur at the plasma-liquid interface are depicted in Figure 2.1. For example, hydrogen peroxide and ozone can be produced from this plasma-liquid interaction, along with highly reactive hydroxyl radicals. Many of these reactive species have higher

oxidation potentials than chlorine, which is the conventional chemical used in the disinfection stage of water treatment trains.

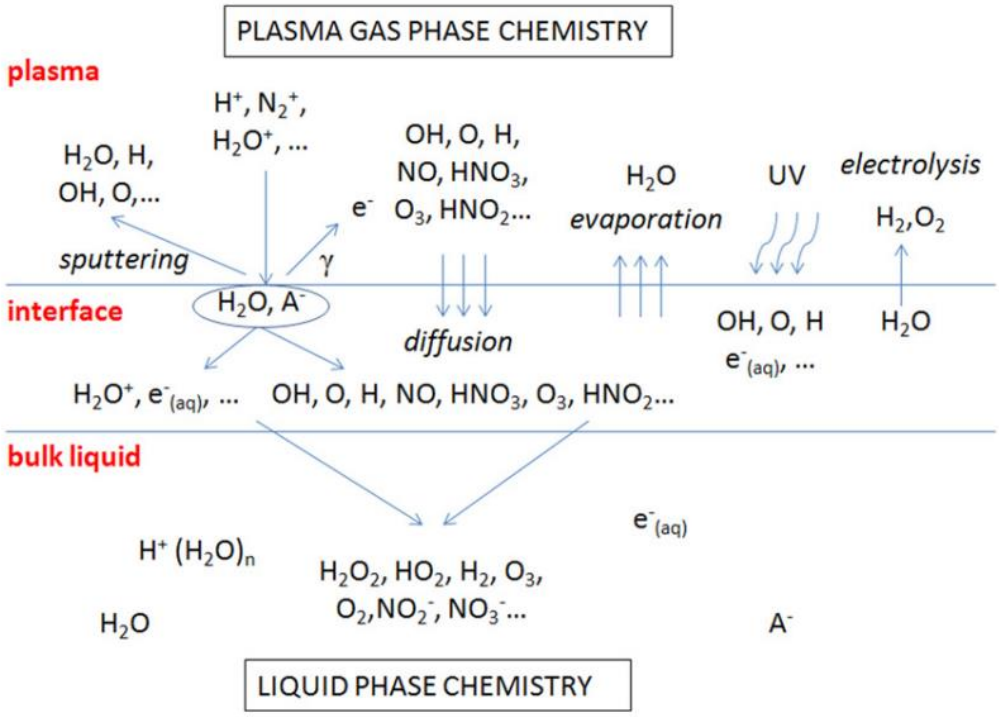


Figure 2.1 Schematic overview of some important species and transfer processes at the plasma-liquid interface from Samukawa et al.[44] The topical review by Bruggeman and Leys provides more details regarding the complex processes at the plasma-liquid interface.[45]

These reactive species can be formed directly from the liquid that is being processed or may utilize some gas injection. Air is a potential feedstock gas for plasma-based water treatment, as it can produce abundant reactive oxygen species (ROS) and reactive nitrogen species (RNS), including hydroxyl radicals, hydrogen peroxide, and ozone to facilitate advanced oxidation. Air is readily available and does not require chemical storage, thus addressing a critical disadvantage of conventional advanced oxidation processes.

However, caution must be taken when using air-plasma-liquid interaction since reactive nitrogen species can lead to production of nitrates in the water which can be dangerous to human

health. These nitrates can be removed from waters for an additional cost via reverse osmosis, anion exchange membranes, electro-dialysis, or by biological processes.[46] Regardless, in applications where nitrate production must be avoided, plasma-liquid interaction allows for potential control of the liquid chemistry through the injected gas composition and discharge geometry. For example, it is possible to use steam as the vapor phase in which plasma is produced in order to prevent the nitrate production from reactive nitrogen species. Indeed, the steam discharge is used in Section 3.2 to avoid the RNS interference in the titration method for quantifying hydrogen peroxide concentration.

Overall, plasma-liquid interactions can decontaminate volatile organic compounds, deactivate microorganisms, and decolor synthetic organic dyes by inducing intense ultraviolet radiation, high electric fields, shock waves, charged particles, and reactive species such as hydroxyl, hydrogen peroxide, and ozone, thus representing the combination of multiple advanced oxidation processes while avoiding the need for chemical transport and storage.[30] The chemical reactivity originates from an electrical power applied to produce the plasma and the accompanying reactive species. The electrical and conversion efficiencies associated with plasma-based liquid processing depend largely on the discharge configuration and operating parameters.

### 2.3 Configurations for Plasma-liquid Interaction

Over recent years, a myriad of discharge configurations have been developed by groups around the world for bringing plasmas into contact with liquids. Despite their specific differences, most of these configurations fall into three main categories: direct, indirect, and multiphase or bubble discharges. Basic schematics of these three discharge categories are provided in Figure 2.2.[44]

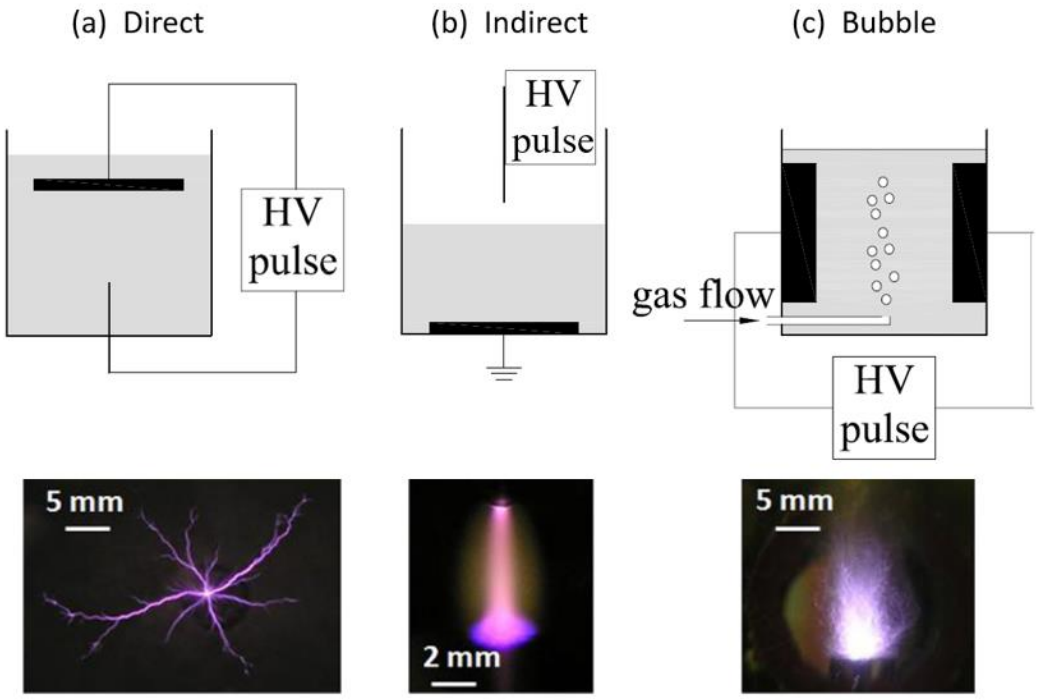


Figure 2.2 (top) Plasma-liquid configuration diagram and (bottom) typical image of the discharge for (a) direct filamentary discharge in water (microsecond pulse width), (b) DC glow discharge in air with water cathode, and (c) nanosecond pulsed discharge in argon bubbles in water from Samukawa et al.[44]

Direct discharges feature electrodes fully submerged in the liquid. Typically, the powered electrode is pointed to take advantage of the electric field enhancement created by the sharp radius of curvature. The grounded electrode is frequently planar, as this helps to distribute the electric field more uniformly across the electrode gap; however, a multitude of electrode geometries have been used, including point-to-point and plane-to plane.[47]

Direct discharges require high applied voltages on the order of 1 MV/cm to achieve breakdown. This is because the density of the liquid is about 1,000 times the density of air, which results in a significant reduction in the electron mean free path between collisions. The electrons must be rapidly accelerated to ionization energies in the short time before colliding with another particle to have a chance of initiating breakdown, hence the electric field required for direct plasma ignition in liquid is much higher compared to gas phase breakdown.

Indirect discharges involve a high voltage electrode in the gas phase adjacent to the liquid surface, allowing reactive species from the plasma to diffuse into the liquid without the plasma directly making contact with the liquid. One approach is to use dielectric barrier discharge (DBD) configurations to generate indirect discharge configurations for plasma-liquid interaction. An example of a DBD reactor experimental set-up that was used to study the physicochemical processes in an indirect plasma discharge above deionized water is shown in Figure 2.3.

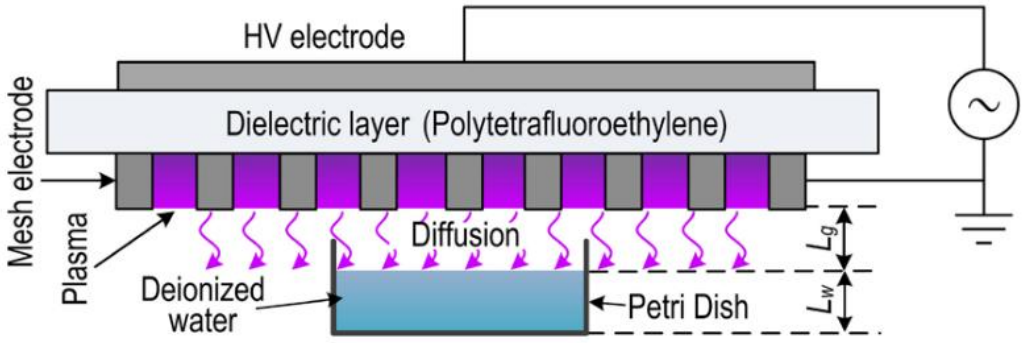


Figure 2.3 Experimental setup of a DBD plasma used to study the physicochemical processes in an indirect plasma discharge above deionized water, from Liu et al. [48]

A general advantage of indirect discharges lies in the reduced density medium for plasma formation – the gas phase. The electron mean free path is longer in gases than in liquids due to the neutral density difference, allowing the electrons a longer distance to accelerate over, thus reducing the magnitude of the applied electric field required to accelerate electrons to ionization energies. In air, the breakdown electric field is on the order of 30 kV/cm.

However, indirect discharge configurations often suffer from low reactivity since the reactive species produced by the plasma must diffuse into the liquid through the gas-liquid interface. This diffusion is typically influenced by a variety of physical and chemical processes that occur at the interface, and the extremely reactive hydroxyl radical may not survive long

enough to make its way into the bulk liquid phase. Instead, the short lifetime of the hydroxyl radical makes it prone to reacting before being delivered to the bulk liquid, often dimerizing with another hydroxyl radical to form hydrogen peroxide.

The limited plasma-liquid surface area along with the diffusion distance that must be traveled by reactive species limits the reactivity of indirect discharges, in comparison with direct discharges which feature radical production directly in the liquid, or within a small gas phase cavity surrounded by liquid if the direct discharge produces enough local evaporation to generate the gas phase. As for direct discharge configurations, the reactive species are usually produced in immediate proximity to the gas-liquid interface, promoting the rapid diffusion of species, including the short-lived hydroxyl radical, directly into the bulk liquid for inducing aqueous phase chemistry. Clearly, there are trade-offs to be considered when it comes to selecting a direct or indirect discharge configuration. The third option, multiphase or bubble discharges, can be considered an indirect discharge that is formed at the gas-liquid interface and takes advantage of the reduced breakdown voltage gas-phase while still generating radical species directly at the gas-liquid interface.

Even in direct discharges, the theory of plasma formation in liquid relies on the existence and formation of microscopic gas bubbles, and since direct immersion of pulsed high-voltage electrodes in liquid results in localized evaporation and subsequent gas-phase ionization, externally injecting bubbles into high electric field can induce breakdown at lower applied voltages while avoiding excessive power dissipation to the liquid. Furthermore, plasma streamer propagation, which is associated with abundant production of radicals, occurs mainly along the air-water interface due to local electric field enhancement caused by the gradient in dielectric constant as seen in Figure 4, and fluid dynamical effects induced by the plasma at the boundary

can lead to enhanced liquid mixing. The submerged gas bubble plasma system offers a reduced breakdown voltage medium and increased gas-liquid interface area for diffusing reactive products into the bulk liquid volume.

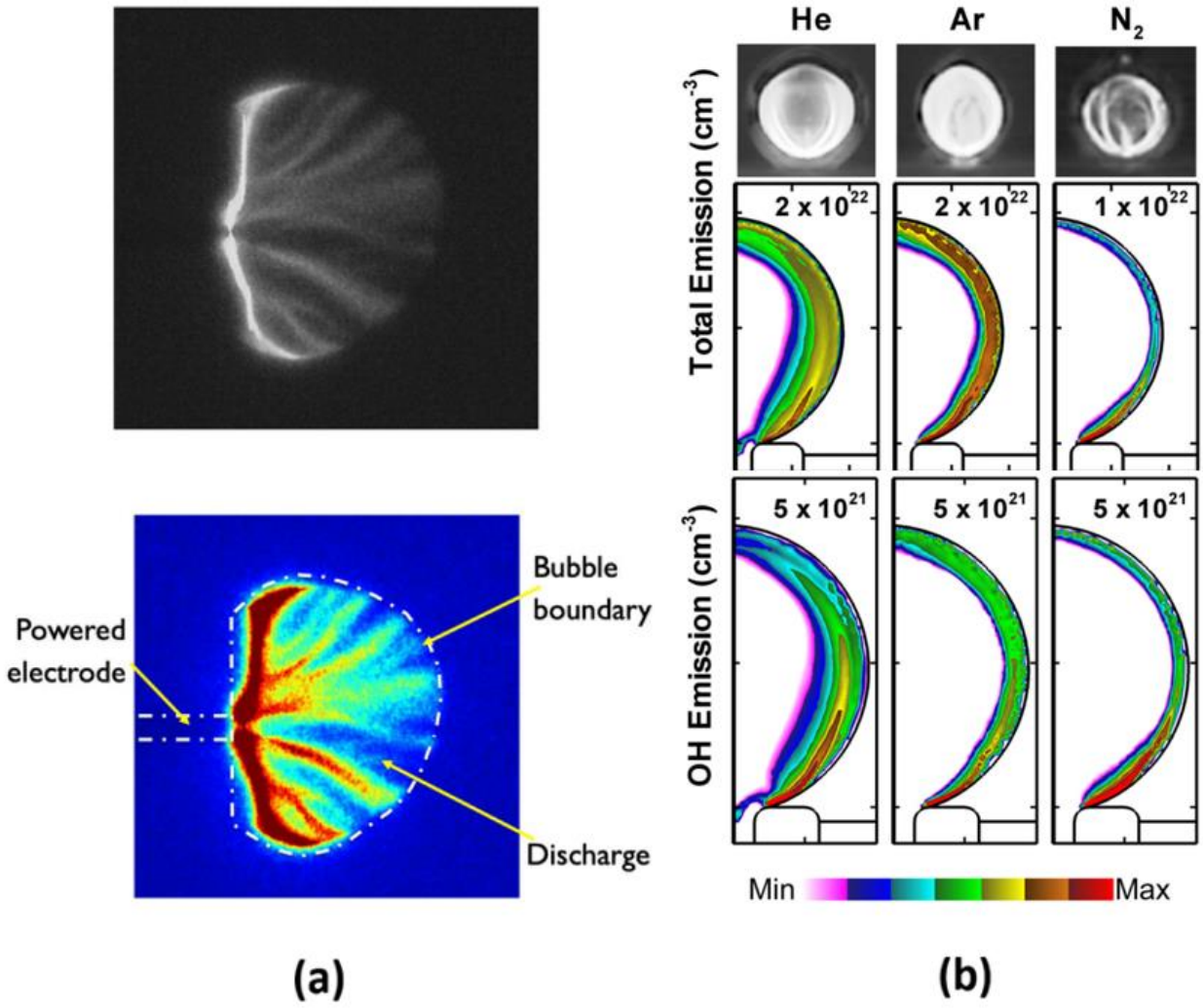


Figure 2.4 (a) Time integrated emission intensity of a plasma discharge propagating along the plasma-water interface in a bubble discharge from Lai et al, and (b) time integrated emission intensity simulated in plasma discharges sustained in He, Ar, and $N_2$ bubbles from Tian et al., with the maximum values of total emission and OH emission provided in each frame.[49], [50] Surface hugging discharges are caused by the gradient in dielectric constant between the gas and water leading to electric field enhancement, as well as increased OH production at the interface.

Thus far, practical realizations of bubble plasma discharges have been mostly limited to configurations involving electrode-attached bubbles and have not shown improved processing rates over other direct or indirect discharge configurations that have demonstrated effective liquid treatment of small laboratory volumes.[51] To solve the throughput problem, reactor configurations that optimize plasma-water contact area to water volume must be realized. This is potentially achieved through the breakdown of isolated gas bubbles distributed throughout the liquid volume to produce the reactive species and deliver those products to the bulk though the gas-liquid interfaces. The other problems that must be addressed are the scalability, electrical efficiency, and conversion efficiency of electrical discharges for inducing chemistry in liquids (i.e., yield of reactive chemicals such as ozone).

Direct plasma-liquid interactions result in a complex combination of physical and chemical processes that take place at the interface. In this case, physical processes occurring at the plasma-liquid interface include diffusion, advection, local heating, surface tension, charge deposition, and secondary emission. Meanwhile, chemical processes can include surface electrolysis, charge transfer, hydrolysis, electron-ion recombination, ion-ion recombination, Penning ionization, collisional relaxation, as well as reduction and oxidation reactions. Indirect plasma-liquid interaction is somewhat simpler, in that diffusion is the primary physical process taking place at the interface; however, chemical processes such as charge transfer, hydrolysis, ion-ion recombination, and reduction/oxidation reactions can still occur.[48]

Based on these basic configurations for brining plasmas in contact with liquids, a myriad of specific discharge configurations may be conceived each with their own advantages and disadvantages, depending on the intended application. A selection of some of these discharge configuration variations are provided in Figure 2.5. As an example, for plasma medicine

applications, indirect discharges are often preferred (i.e., Figure 2.5b) since the flux of reactive species is more predictable and controllable as the main transport process is diffusion.[52]–[54] On the other hand, the added reactivity and transport mechanisms afforded by direct discharges is generally advantageous for water treatment applications. Furthermore, the plasma-water contact area is important for maximizing transport of reactive species, thus a configuration involving a gas-phase plasma with a dispersed liquid phase, shown in Figure 2.5e, is often advantageous.

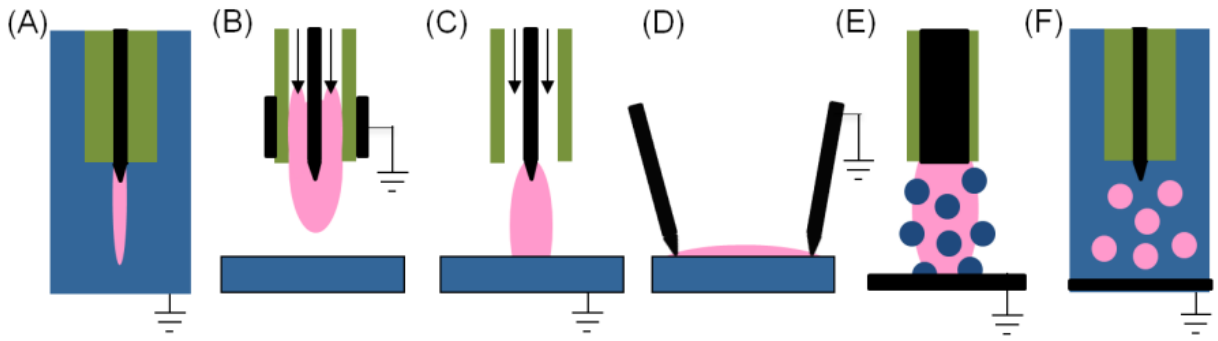


Figure 2.5 Schematic of some different discharge configurations used to generate plasma-liquid interactions: (a) direct discharge in liquid, (b) indirect gas-phase discharge above liquid, (c and d) gas-phase discharge making direct contact with liquid surface, (e) gas-phase plasma with dispersed liquid phase (i.e., aerosols), and (f) discharges in bubbles, from Bruggeman et al.[55] Blue represents the liquid, pink indicates plasma, green is for dielectric materials, and black represents the metal electrodes.

Indeed, many of the reactor configurations being used for water treatment applications are gas-liquid reactors, in which the plasma is generated in the gas-phase and is directly in contact with the liquid as opposed to indirect gas-phase discharges or direct in-liquid discharges. These configurations have been leveraged in a variety of ways to bring plasmas in contact with liquids for the purpose of decomposing contaminants in water. However, most of these reactors have only been demonstrated at laboratory scales, typically on the order of mL to L process volumes.

Several investigations of non-thermal plasmas applied to the decomposition of PFAS have been conducted over the recent years. It can be difficult to make comparisons between them due to the differences in reactor types, sizes, feed gases, flow rates or volumes, and the quality of the water being treated (i.e., initial concentrations of PFAS and existence of co-contaminants/scavengers).

A study by Saleem et al. investigated the performance of three different types of reactors for the degradation of PFOA.[38] These three reactors were referred to as the "7-wires" DC plasma reactor, the "hollow electrode" AC plasma reactor, and the "self-pulsing discharge" reactor, which were used to treat 15 mL of deionized water spiked with PFOA at a concentration of 41.4 ppm. The self-pulsing discharge reactor was designed specifically for the decomposition of PFOA; meanwhile, the 7-wires DC plasma and the hollow electrode AC plasma reactor had been designed for the treatment of other organic contaminants. Synthetic air, ambient air, and argon were tested as the feed gases for these reactors.

The best PFOA degradation performance was achieved using argon as the feed gas. Of the three reactors investigated, the self-pulsing discharge performed the best in terms of energy efficiency and PFOA decomposition rate. This improved performance was attributed to the extended plasma-water interface allowing for increased interaction between the plasma discharge and PFOA molecules in the water. Indeed, the plasma-water contact area has been established to be an important variable impacting the performance of plasma-based water treatments.

A study by Lewis et al. investigated the use of a reverse vortex flow gliding arc plasma for the decomposition of several different PFAS using air, nitrogen, and oxygen as the feed gasses in a 1 L batch treatment of deionized water spiked with PFOA at a concentration of 100 ppm.[56] Air was found to achieve better PFAS degradation performance than nitrogen or

oxygen alone, suggesting that reactive oxygen and reactive nitrogen species can contribute to PFAS decomposition. The best electrical energy efficiencies documented for this investigation ranged from an EE/O of 23.2 kWh/$m^3$ for PFOS to 213.4 kWh/$m^3$ for PFOA.

While these investigations suggest that non-thermal plasmas may represent a cost-effective technology for the remediation of PFAS contaminated waters, they were both batch processes at low volumes (1 L or less). For non-thermal plasmas to make a meaningful contribution to the problem of PFAS contamination in groundwaters, the processing volumes will need to be scaled up considerably. Furthermore, for practical implementation, a continuous flow architecture capable of processing tens of L/min or more would be highly desirable. The next section describes some plasma-water reactors that were either deployed at pilot-scale or considered for reaching pilot-scale processing flow rates.

### 2.4 Towards Pilot-scale Plasma-water Reactors

One of the main challenges facing plasma-based water treatment is scaling up to relevant treatment throughputs. An important consideration related to this throughput problem is maximizing the plasma-water contact area. Once this is achieved for a given system, it will be possible to develop scaling laws that inform the optimization of parameters such as discharge characteristics, electrode dimensions, and the gas and liquid flow rates.

A range of plasma reactor configuration approaches was surveyed by Malik in 2010 to assess the efficiency of the various implementation approaches.[57] The survey reported that reactor configurations involving plasma exposure to thin layers or small droplets of water were the most energy efficient. That is, those geometries maximized the dose of plasma-derived reactive species delivered to the liquid for a given input energy.

The issue is that these reactor configurations and electrode geometries which maximize the efficiency of reactive species transfer to the liquid are also inherently low throughput processes, involving either thin streams or small droplets of water. Scaling these types of reactors to high throughputs would typically require the generation of large volume plasmas, which is particularly challenging at atmospheric pressures.[58] In 2015, Stratton et al. published a study on the development of general principles for plasma-water reactor design which highlighted the importance of optimizing plasma-water contact area as a way to maximize radical species transport to the water.[59]

By now, the importance of maximized plasma-water contact area for improving reactor efficiency has been well established, and results from this work also support this reactor design principle. Still, there are very few plasma reactors for water treatment that are capable of treating pilot-scale throughputs. The following sections discuss a few plasma-water reactors that have been developed with the goal of treating pilot-scale volumes or flow rates.

### *2.4.1 Early Pilot-scale Plasma-based Advanced Oxidation (AquaPure Ltd.)*

To date, there have been few commercial ventures involving plasma-based water treatment that attempt to increase the processing flow rate to amounts nearing pilot-scale throughputs. Perhaps the most well-known early commercialization attempt of a plasma-based water treatment process was the reactor developed by the company AquaPure Ltd. Basing their design off the guidelines proposed by Malik, the AquaPure reactor featured thin sheets of water that flow past a non-thermal plasma at atmospheric pressure. A schematic of the basic reactor configuration is shown in Figure 2.6. The plasma is generated using a brush array of carbon electrodes positioned above the thin flowing water sheet.

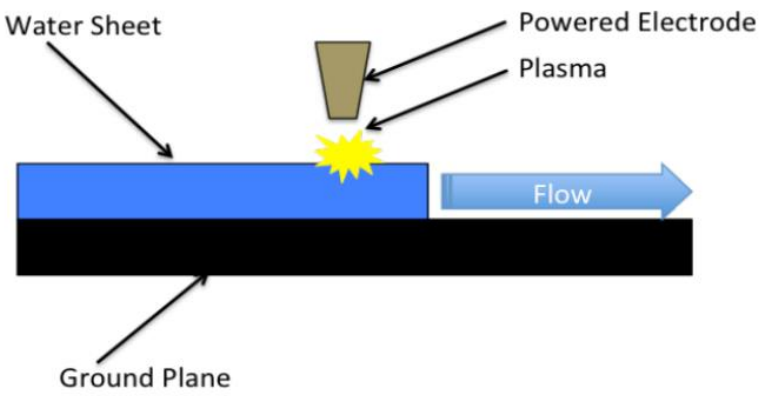


Figure 2.6 AquaPure discharge configuration for generating plasma in contact with thin water sheets (water sheet thickness is approximately 5 mm). The discharge takes place in ambient air.[40]

The AquaPure reactor was successful at decomposing trichloroethylene (TCE) and n-nitrosodimethylamine (NDMA) with electrical efficiencies exceeding that of the conventional advanced oxidation process involving ultraviolet radiation coupled with hydrogen peroxide injection ($UV/H_2O_2$), as seen in Table 2.1. This represents a significant accomplishment for plasma-based water treatment technologies; however, the processing flow rates achieved by the AquaPure reactor were still relatively low, approximately 10 L/min. Consider a typical residential household may require flow rates starting at 20 L/min.

Table 2.1 Comparison of different advanced oxidation technologies including the AquaPure plasma-based advanced oxidation process for removal of MTBE, TCE, NDMA, and 1,4-dioxane. Data compiled from Even-Ezra et al. and Malik.[57], [60]

| **Technology** | **Contaminant** | $E_{EO}$ **(kW h/m$^3$)** |
|---|---|---|
| $O_3/H_2O_2$ | MTBE | 0.1 |
| $HDC/H_2O_2$ | MTBE | 0.3 |
| $UV/TiO_2$ | MTBE | 0.8 |
| $UV/H_2O_2$ | MTBE | 0.7 |
| | TCE | 1.7 |
| | NDMA | 0.7 |
| | 1,4-dioxane | 0.7 |
| Pulsed air/$H_2O_{(\ell)}$ DBD (AquaPure) | MTBE | 0.8 |
| | TCE | 1.2 |
| | NDMA | 0.5 |
| | 1,4-dioxane | 2.0 |

The other advanced oxidation technologies compared in Table 2.1 include ozone/peroxide ($O_3/H_2O_2$), hydrodynamic cavitation/peroxide ($HDC/H_2O_2$), ultraviolet radiation/titanium dioxide ($UV/TiO_2$), and ultraviolet radiation/peroxide ($UV/H_2O_2$). The Electrical Energy per Order ($E_{EO}$ or EE/O) is a figure of merit for comparing the electrical energy costs of treatment across different advanced oxidation processes and will discussed further in Section 5.1 (see Equation (5.1)). Essentially, lower $E_{EO}$ values indicate less energy costs required for removing a target contaminant by one-$\log_{10}$ (90% removal).

While the plasma-based advanced oxidation process by AquaPure represents one of the earliest examples of a plasma-water reactor nearing pilot-scale processing flow rates with degradation efficiencies competitive with conventional advanced oxidation processes, the throughputs demonstrated by Evan-Ezra et al. are still too low to be considered commercially viable for most applications.

The next section will discuss a reactor configuration that has shown promise for treating a variety of waters including wastewaters from food manufacturing and very high salinity produced waters from hydraulic fracturing. While this reactor has yet to be demonstrated at pilot-scale throughputs, the concept is theoretically scalable to commercially relevant flow rates.

### *2.4.2 Underwater Dielectric Barrier Discharge Plasma Jet (NASA)*

The DBD plasma jet represents a class of plasma discharge configurations for achieving plasma-liquid interaction that was developed at the NASA Glenn Research Center in collaboration with the University of Michigan. A dielectric barrier discharge (DBD) is an electrical discharge that forms when a voltage is applied across electrodes separated by a dielectric barrier material. The dielectric material prevents an arc from forming an electrical

connection between the powered and grounded electrodes in order to avoid formation of a thermal plasma. For water treatment, non-thermal plasma discharges are preferred because the formation of radicals takes place without significant power being deposited into gas and liquid heating.

As seen in Figure 2.7, the DBD plasma jet features a central electrode encased in a dielectric tube that is submerged into the liquid. A ground electrode is coiled around the outside of the dielectric to form the dielectric barrier discharge configuration. A key feature of this design is that a gas input flows through the dielectric tube and across the central electrode. As long as there is sufficient gas flow, the liquid will be blown off of the central electrode as continuous bubbles are emitted from the submerged dielectric tube orifice. This prevents the high conductivity wastewaters such as, hydraulic fracturing fluid, from creating a short circuit between the central electrode and the external ground coil

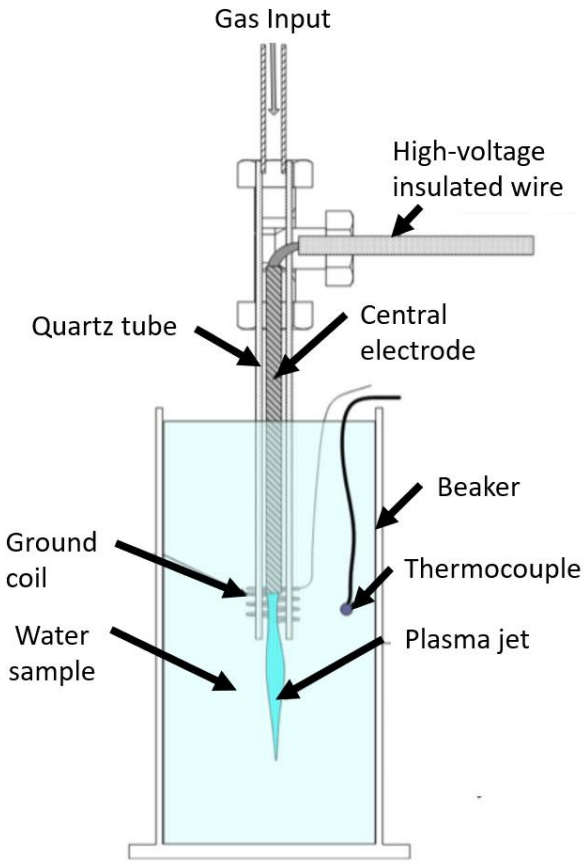


Figure 2.7 Schematic of the DBD plasma jet for plasma-liquid interaction, from Foster et al.[61]

Microsecond, nanosecond, or AC high voltage is applied to the central electrode to initiate the plasma formation inside the dielectric tube. An image of the discharge is provided in Figure 2.8b, and shows micro-discharge jets forming along the interior of the dielectric tube. A diffuse glow and exiting streamer form at the opening of the dielectric tube. The exiting streamer propagates to the gas-liquid boundary. Electric field enhancement at the phase interface due to the local gradient in dielectric permittivity promotes the streamer propagation to this boundary and is responsible for allowing the discharge initiation to occur at lower applied voltages than would be required in the absence of the gas-liquid interface.[61] Simulation results

provided in Figure 2.8b support this theory of electric field enhancement downstream of central electrode tip.

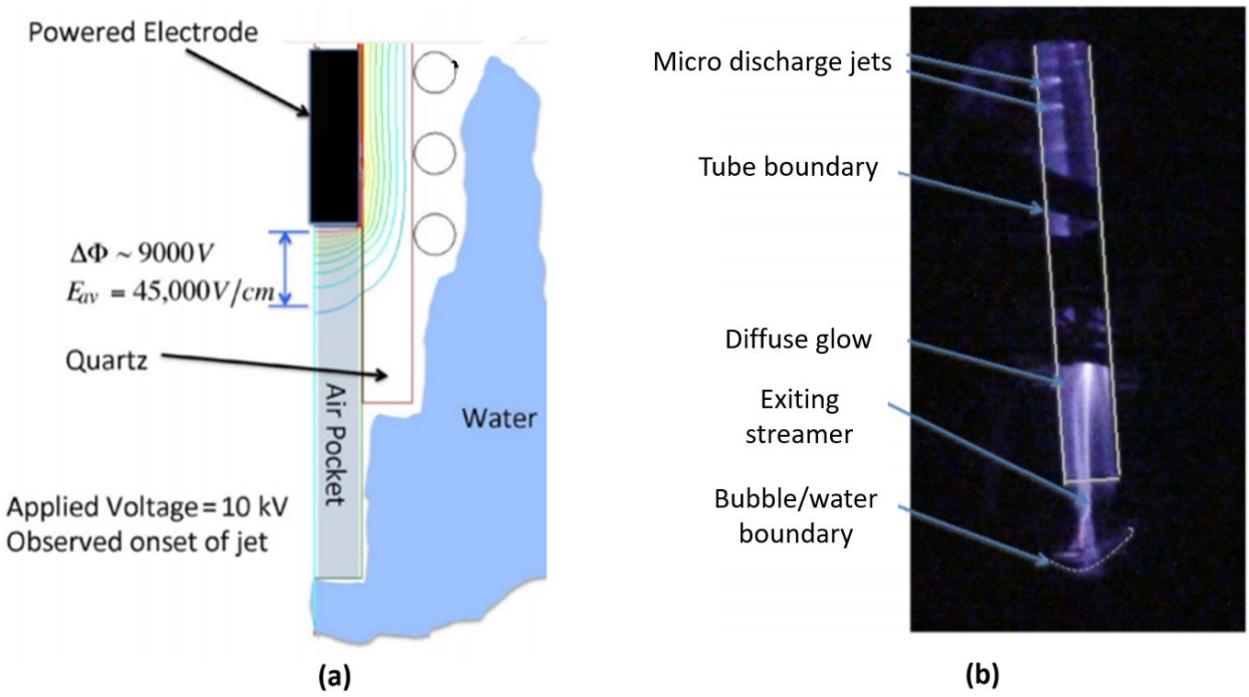


Figure 2.8 (a) Electrostatic simulation predicting downstream electric field enhancement at the air-water interface and (b) various components of the plasma discharge observed in the underwater DBD plasma jet operation, from Foster et al.[61], [62]

Throughput is an issue for all plasma-based liquid processing at the current time because it is difficult for plasma to be applied within the bulk of the liquid; however, the DBD plasma jet offers scalability though the use of multiple plasma jet applicators positioned throughout the volume of the liquid to be processed. The dielectric tubes can be constructed to different geometries, and it could be possible to apply plasma jets deep within the bulk liquid or at varying depths within the liquid in order reach a larger portion of the bulk liquid. Meanwhile, gas flow from each jet helps to mix the liquid.

The underwater DBD plasma jet can also be excited by nanosecond or microsecond pulses at frequencies up to 100 kHz. The advantage to these short pulses is that the power is deposited quickly such that the large inertia of gas particles prevents them from gaining much energy over the pulse period. As a result, the gas temperature remains close to room temperature and minimal power goes into heating the liquid. Highly transient applied electric fields are generally considered more efficient for water treatment; however, power supplies that can produce these short pulses are more complicated to manufacture and more expensive than the sinusoidal AC applied voltage option.

Electron temperatures found in DBD plasma jets interacting with water are usually around 1 – 2 eV and the plasma density generally falls in the range of $10^{14}$ – $10^{16}$ $cm^{-3}$. The highly transient nanosecond pulses generally do not heat the gas particles much above room temperature, while low frequency alternating current applied voltage can result in gas heating to temperatures around 2,000 – 3,000 K. This is still much lower than the electron temperature, indicating that the plasma is still non-equilibrium.

Thus far, water treatments using the DBD plasma jet have been limited to laboratory-scale volumes on the order of liters in batch-mode. However, the reactor configuration allows for modular scaling by simply increasing the number of plasma jets. Here, jets may be added in series to achieve the desired treatment dose (i.e., concentration of reactive species transferred from plasma to liquid); meanwhile, parallel process lines may be added to accommodate the desired flow rate. In this way, a single DBD plasma jet applicator is used as a building block of a large-scale system capable of treating large volumes of water, as depicted in Figure 2.9.

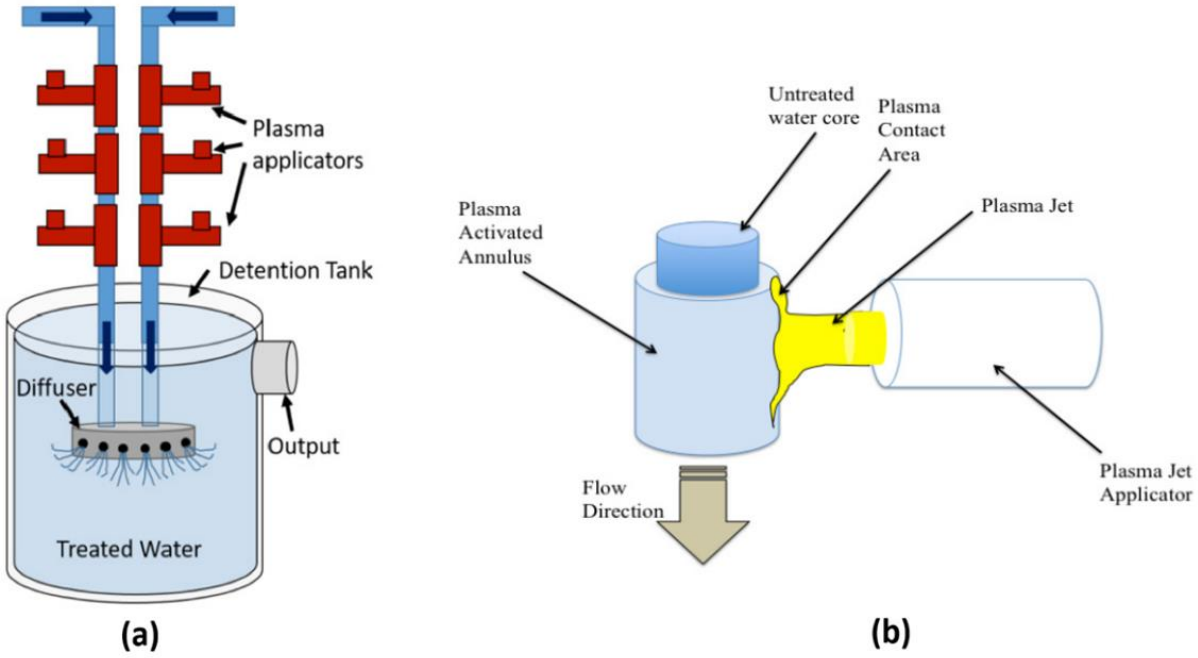


Figure 2.9 (a) Implementation concept for large-scale water treatment using the DBD plasma jet apparatus as a plasma applicator, and (b) schematic of treatment dynamics of a water slug flowing past a plasma jet applicator, from Foster et al.[40] The thickness of the plasma activated annulus is dependent on diffusion and induced fluid dynamical flow effects.

This modular DBD plasma jet reactor configuration was originally conceived as an advanced oxidation alternative. More specifically, water is forced to pass through the highly reactive plasma applicator sections in which organics are directly oxidized by hydroxyl radicals generated at the plasma-water interface. In the process, longer lived species such as ozone and hydrogen peroxide are also generated which can react via the peroxone process (i.e., conventional advanced oxidation involving the injection of ozone and hydrogen peroxide) to produce additional hydroxyl radicals in the volume of the detention tank. In that sense, this concept achieves two-step advanced oxidation (i.e., at the plasma application sites and within the detention tank).

Since the reactive species are generated by the plasma-liquid interaction, the need for injecting external chemicals as consumables is negated. These reactive chemicals are generated

from the energetic electron interactions with water molecules. As such, this implementation concept represents an appealing alternative to conventional advanced oxidation processes which do require external chemical storge and transport. However, this concept has yet to be demonstrated at pilot scales, let alone the large scales that have been theoretically conceived.

The next section discusses a plasma-water reactor that has demonstrated results in a pilot-scale test for the decomposition of PFAS. Adhering to the design recommendations outlined in the Malik study, this reactor design features multiple plasma discharges that spread across the surface of the water layer being treated.

### *2.4.3 Enhanced Contact Reactor (Clarkson University)*

DMax Plasma LLC, a startup company based out of Clarkson University, is currently developing a pilot-scale plasma-water reactor for the purpose of removing PFAS from water, referred to as the enhanced contact reactor. To address the issue of plasma-water contact area, this reactor features an array of pulsed corona discharges to treat liquid layers in batches, as depicted in Figure 2.10. Furthermore, the reactor design takes advantage of the affinity that PFAS has for gas-liquid interfaces by bubbling argon gas through the liquid layer. In the process, PFAS is accumulated in the bubbles and transported to the surface where the array of plasma discharges generates reactive species, such as solvated electrons and excited argon ions to facilitate the decomposition of PFAS. An image of the enhanced contact reactor operating is provided in Figure 2.11b.

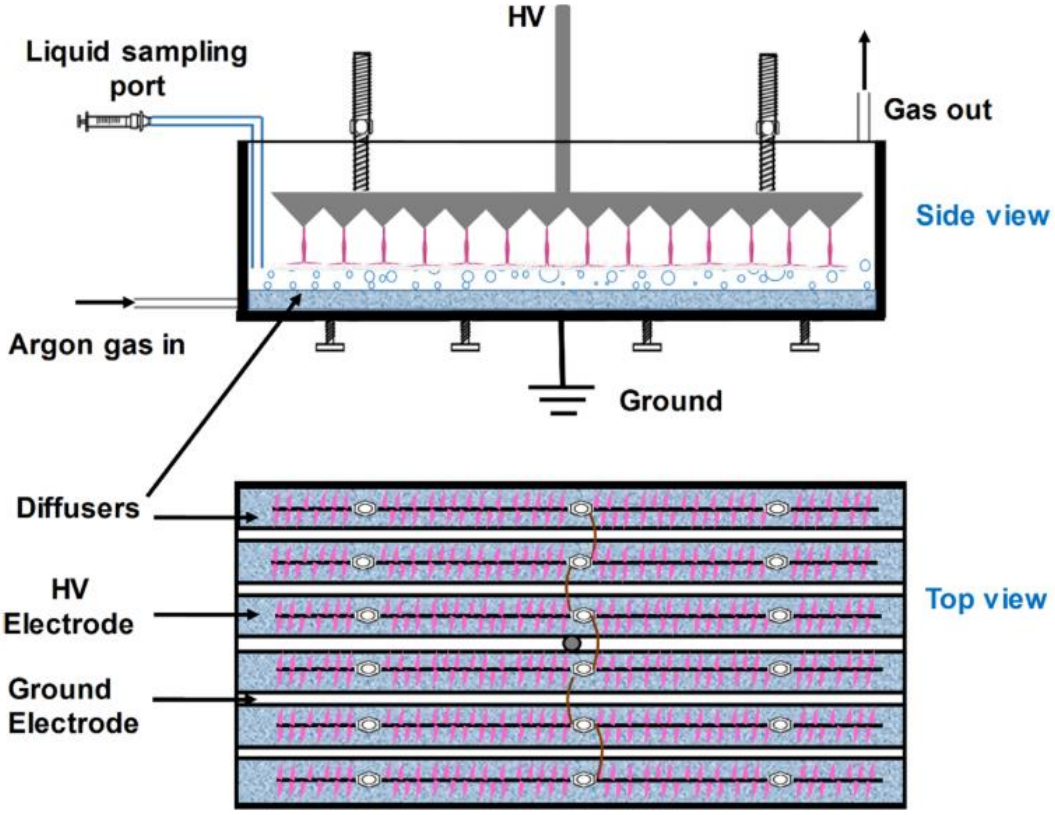


Figure 2.10 Side view and top view schematics of the enhanced contact reactor, from Singh et al.[24]

In this reactor, the water is batch processed to allow for the recycling of the argon gas. Without the ability to recycle the argon, the consumption of argon could become a considerable expense, especially for large scale treatment operations. Though a batch process, the water is cycled through to ensure exposure to the plasma. In the pilot-scale experiment, groundwater derived from a PFAS contaminated Air Force site is treated in batch volumes ranging from 23 – 68 L with water recycling flow rates between 1.2 and 4.2 L/min.

The initial concentrations of PFAS in the groundwater at the Air Force remediation site depended on which well the water was collected from, with the highest concentration being PFOS at approximately 4,000 ppt. The measured concentrations of other PFAS found in the groundwater is provided in Nau-Hix et al.[23] The percent removal of a range of PFAS and

PFAS precursors after a single cycle through the reactor is shown in Figure 2.11a. The time required for a single cycle through the reactor depends on the total treatment volume and the recycling flow rate, and was generally in the range of 8 – 20 min.

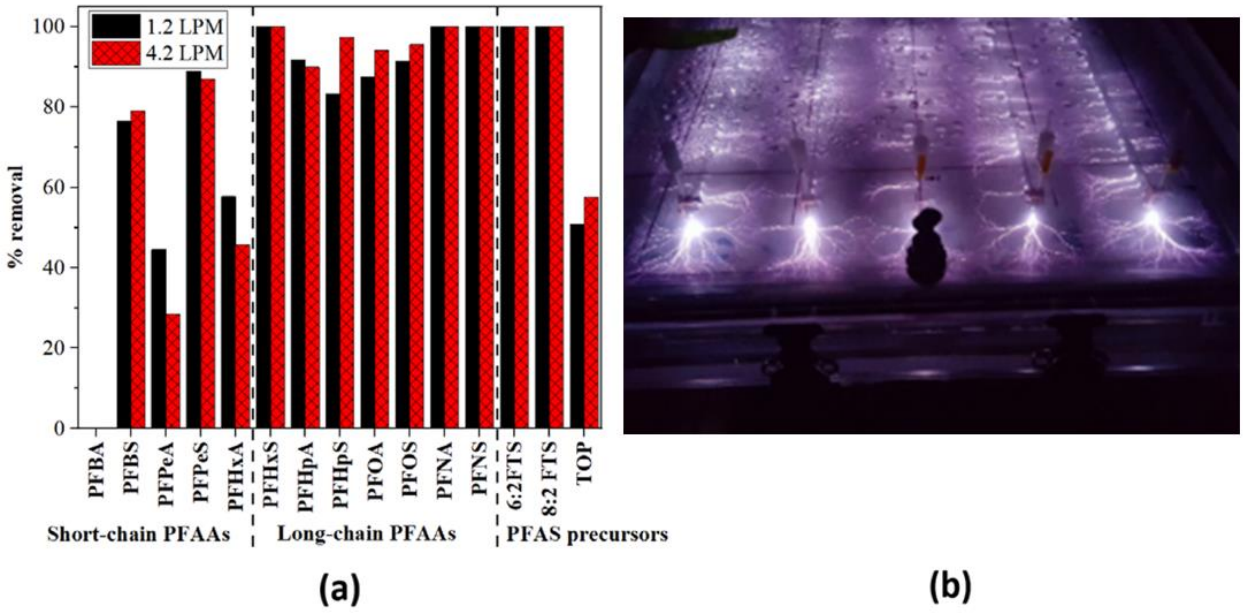


Figure 2.11 (a) Percent removal of PFAS after a single cycle through the reactor and (b) image of the enhanced contact reactor in operation, from Nau-Hix et al.[23]

Notably, the short-chain PFAS were not removed to the same extent as the long-chain PFAS. This is partly due to the generation of short-chain PFAS as a byproduct of long-chain PFAS decomposition throughout the treatment, but also it has been found that the short-chain PFAS do not accumulate as readily at the gas/plasma-liquid interface compared to their long-chain counterparts. Nau-Hix et al. reported that the addition of a cetrimonium bromide (CTAB), which is a cationic surfactant, increased the level of short-chain PFAS accumulation at the interface. With the addition of CTAB, 88% off all short-chain PFAS were removed within 120 min of treatment.

The energy efficiency (EE/O) of this pilot-scale treatment was calculated to range between 9.2 – 31 kWh/$m^3$. This includes the energy consumed by the high-voltage power supplies, the rotating spark gap, and the gas and liquid pumps. The authors report that the approximate cost to treat 1,000 gal to below the US EPA health advisory limits (i.e., 70 ppt combined PFOA and PFOS) would be 7.30 USD/kgal. The enhanced contact reactor represents the first pilot-scale field demonstration of a technology that decomposes PFAS in contaminated groundwaters. Furthermore, based on the cost assessment, plasma-based treatment, particularly of PFOA and PFOS, appears to be one of the most effective options reported to date.

Seeking to extend upon the successes of the enhanced contact reactor, another approach to scaling up plasma-water reactors is being developed at the University of Michigan. Rather than spreading water into thin sheets for treatment, this reactor disposes water into thin cylindrical jet streams around which a plasma discharge is generated. This reactor is referred to as the packed-bed reactor.

### *2.4.4 Packed-bed Reactor (University of Michigan)*

The packed-bed reactor was originally developed according to a geometric approach for optimizing the plasma-water contact area. Originally envisioned for the advanced oxidation of CECs, such as 1,4-dioxane, the high plasma-water contact area of the configuration is also considered promising for the decomposition of PFAS, which will be explored further later in this thesis. The approach involves generating a close-packed array of water jets that pass through a pair of electrodes which generate an electric field of sufficient strength form a plasma discharge in the spaces between the water jets. A cutaway drawing of the electrode and water jet configuration is shown in Figure 2.12.

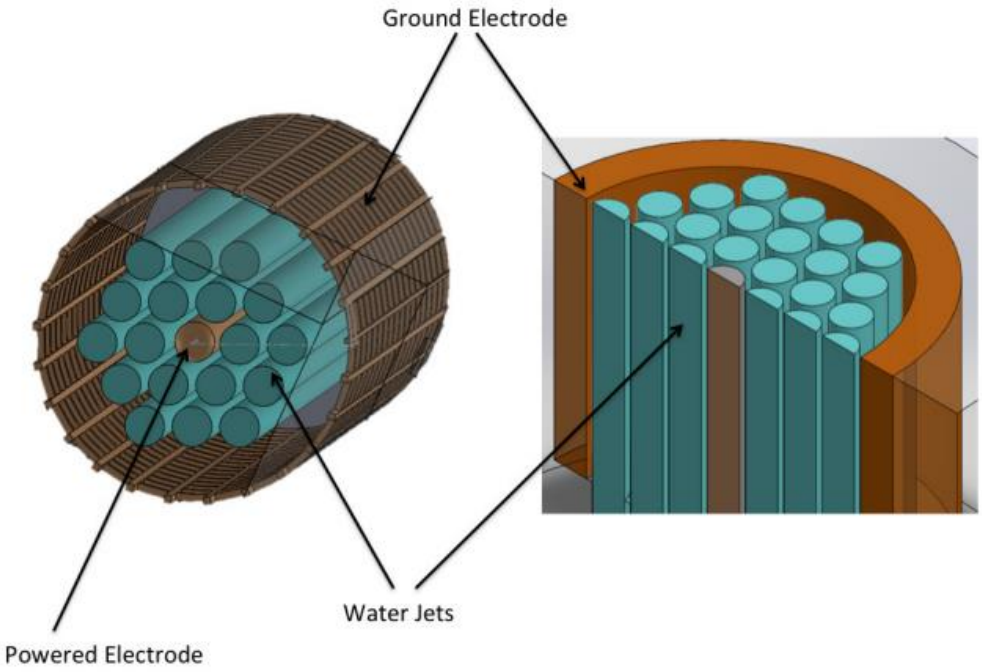


Figure 2.12 Cylindrical embodiment of the packed-bed reactor showing the central rod electrode and outer mesh electrode. The aggregate of water jets forming the "packed-bed" is shown by the blue cylinders. Plasma is generated in the spaces between the water jets, from Foster et al.[40]

A schematic of this cylindrically configured packed-bed of water jets being exposed to plasma is shown in Figure 2.13b. When high voltage is applied across the electrodes, the resulting plasma propagates along the surface of the water jets, taking advantage of the high surface area to volume of the configuration to enhance transport of reactive species to the water jets. This is similar to the configuration illustrated in Figure 2.5e. The discharge is generated in ambient air, although the option for feeding another gas, such as argon, to the discharge section is an option.

Furthermore, the packed-bed reactor may be operated in a flow-through or recirculating batch mode. A photograph of the reactor in a closed loop recirculating configuration is shown in Figure 2.13a. While the packed-bed reactor has not yet been demonstrated at pilot scales, the advantages afforded by this configuration (i.e., high plasma-water surface area to volume ratio

and opportunity for flow-through treatment), make this reactor configuration a promising candidate for scaling up to higher flow rate treatment processes. As such, the packed-bed reactor will be featured throughout the experiments presented in this thesis, with a focus on its performance for the decomposition of PFAS in contaminated groundwaters and its potential for scaling up to a continuous flow system capable of processing pilot-scale and commercially relevant flow rates.

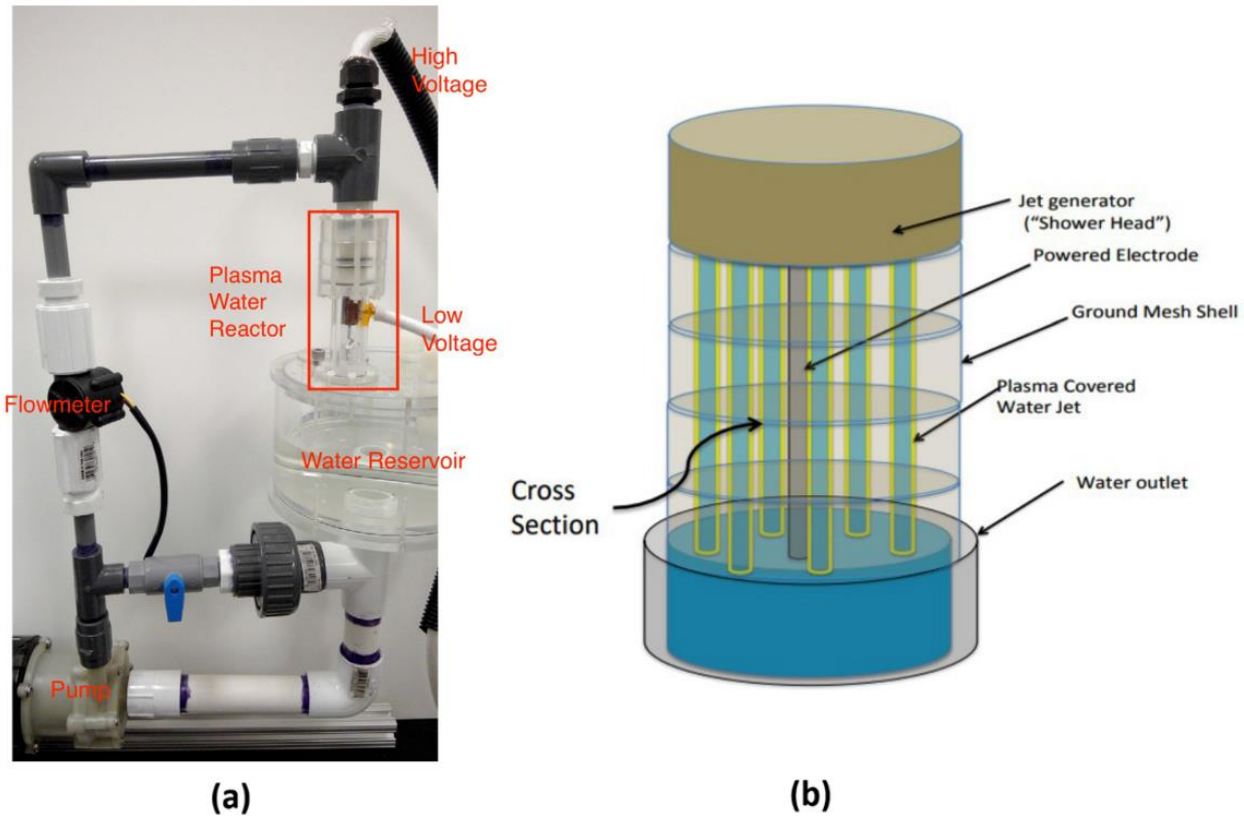


Figure 2.13 (a) Photograph of the packed-bed reactor showing a closed loop configuration, including the water reservoir, pump, and system plumbing. (b) Schematic of the discharge section of the packed-bed reactor in which water is disposed into thin jet streams and a plasma is generated in the spaces between the water jets, essentially coating the surfaces of the water jets in plasma, from Foster et al.[40], [63]

The next chapter will discuss the experimental approach used in this thesis, including methods for assessing contaminant removal effectiveness, including the decomposition of PFAS,

as well as water property measurements, aqueous-phase reactive species measurements, and optical emission spectroscopy as a diagnostic for plasma discharge properties such as plasma density and gas temperature.

## Chapter 3 Experimental Methods for Evaluating Plasma-based Water Treatment

This chapter provides an overview of the experimental methods used in this work starting with a brief review of techniques for assessing contaminant removal. For instance, spectrophotometry can be used to measure the concentrations of specific aqueous species using reagents but can also provide some non-specific information about the quality of waters and wastewaters. Meanwhile, liquid chromatography – mass spectrometry can provide highly specific and sensitive measurements of compounds' concentrations by separating the compounds in time with a chromatography column and then sorting the column effluent by the mass-to-charge ratio of the specific compounds.

On the other hand, non-specific water quality metrics including total organic carbon, biochemical oxygen demand, and chemical oxygen demand are widely used to monitor water and wastewater treatment processes due to their relatively simple procedures and straightforward interpretation. Chemical oxygen demand, in particular, is regarded as the industry standard for monitoring water and wastewater quality in the United States; however, it was discovered throughout the course of this work that residual hydrogen peroxide generated during plasma treatment of waters can cause an interference in the standard chemical oxygen demand assessment.

Indeed, this interference effect has been observed for other advanced oxidation processes that generate residual hydrogen peroxide, but it had not yet been widely discussed in the plasma community. Section 3.2 provides a case study investigating the hydrogen peroxide interference

in chemical oxygen demand assessments of plasma treated waters, thus demonstrating how the interference effect may be masked when treating waters with high chemical oxygen demands. Meanwhile, for waters that have a low chemical oxygen demand, the residual hydrogen peroxide form plasma treatment can significantly impact the interpretation of results, sometimes making it appear as if the plasma treatment has increased the chemical oxygen demand of the water, which would suggest that the treatment was unsuccessful. Ultimately, the results from this case study indicate that the magnitude of this interference approximately follows the theoretical value calculated using Equation (3.3).

Critical to this work, liquid chromatography – tandem mass spectrometry (LC-MS/MS) is used for the quantification of PFAS in water, and a brief description of this measurement technique is provided in Section 3.3. The procedure used here is capable of distinguishing and measuring the concentrations of 24 different PFAS at concentrations as low as 2 ppt. Further details regarding the quantification of PFAS concentrations in water may be found in the EPA Method 537.1.[64]

Next, water property measurements including electrical conductivity, pH, and temperature are discussed in Section 3.4. These water properties will be monitored throughout the treatment of PFAS contaminated waters to gain insights into the effects of plasma treatment; for example, how much of the plasma discharge power goes into heating the water at various water electrical conductivities? Additionally, the methods used for measuring long-lived reactive species, such as hydrogen peroxide and nitrite/nitrate, are discussed in Section 3.5.

Lastly, the basics of optical emission spectroscopy as a plasma/gas phase diagnostic will be discussed. This non-invasive technique uses light emitted from the plasma to glean information about the plasma discharge properties and will be used in Chapter 6 to estimate the

gas temperature and electron density at varying water electrical conductivities in a plasma-water reactor that is being studied for the decomposition of PFAS (i.e., the packed-bed reactor, introduced in Section 2.4.4 and described in further detail in Section 4.1.2).

### 3.1 Contaminant Removal Assessments

As the primary goal of plasma-water reactors for wastewater treatment and water treatment processes in general is the removal or mineralization of contaminants, it is essential to understand the methods that are used to quantify the concentrations of these contaminants before and after treatment, which allows for an assessment of the contaminant removal. The five most prominent methods for assessing contaminant removal from waters are spectrophotometry, liquid chromatography – mass spectrometry (LC-MS), total organic carbon (TOC), biochemical oxygen demand (BOD), and chemical oxygen demand (COD).[65]–[68]

Spectrophotometry and LC-MS allow for the determination of specific species concentrations, whereas TOC, BOD, and COD are non-specific water quality parameters that provide a measurement of the overall pollution potential of a water sample. A disadvantage of spectrophotometry and LC-MS analyses is that they require more specialized training and equipment (particularly in the case of LC-MS), but this additional cost offers the opportunity to measure a myriad of specific compounds in waters at a wide range of concentrations. Section 3.1.1 discusses the principles of spectrophotometry as it pertains to concentration measurements in water samples, while Section 3.5 describes some spectrophotometric measurements of plasma-derived reactive species in water. A description of how LC-MS is used for the measurement of PFAS concentrations in water is given in Section 3.3.

When initially investigating the performance of AOPs, or other water treatment processes, for the removal of contaminants from wastewaters, LC-MS should be used to validate

results from other methods; however, for general monitoring of effluent quality in water and wastewater treatment processes, TOC, BOD, and COD are more commonly used due to the simplicity of the test procedure and easily interpreted results. Spectrophotometry, on the other hand, can be used for both specific chemical concentration measurements as well as more general wastewater quality estimation.[69]

### *3.1.1 Spectrophotometry*

When it comes to concentration measurements of chemical species in water, spectrophotometry is one of the most prevalent techniques and has rightly been referred to as the workhorse of the modern laboratory for its versatility and widespread use. This measurement technique uses an instrument called a spectrophotometer that measures the intensity of light (number of photons) that is absorbed after being transmitted through a sample of solution. The process typically involves a white light source of radiation which is passed through a lens to generate a collimated beam of photons that pass through a monochromator dispersing device (i.e., diffraction grating or prism).

After the monochromator selects the desired wavelength of light for the absorbance measurement, the light is then focused through an exit slit and passes through the liquid sample contained within a cell, or cuvette, made from plastic, quartz, or glass depending on the sample constituents of interest and the wavelength of light being used for the measurement. The portion of light that is not absorbed by the sample is detected and converted to an electrical signal commensurate with the transmitted light intensity. A schematic diagram of a spectrophotometer is provided in Figure 3.1.

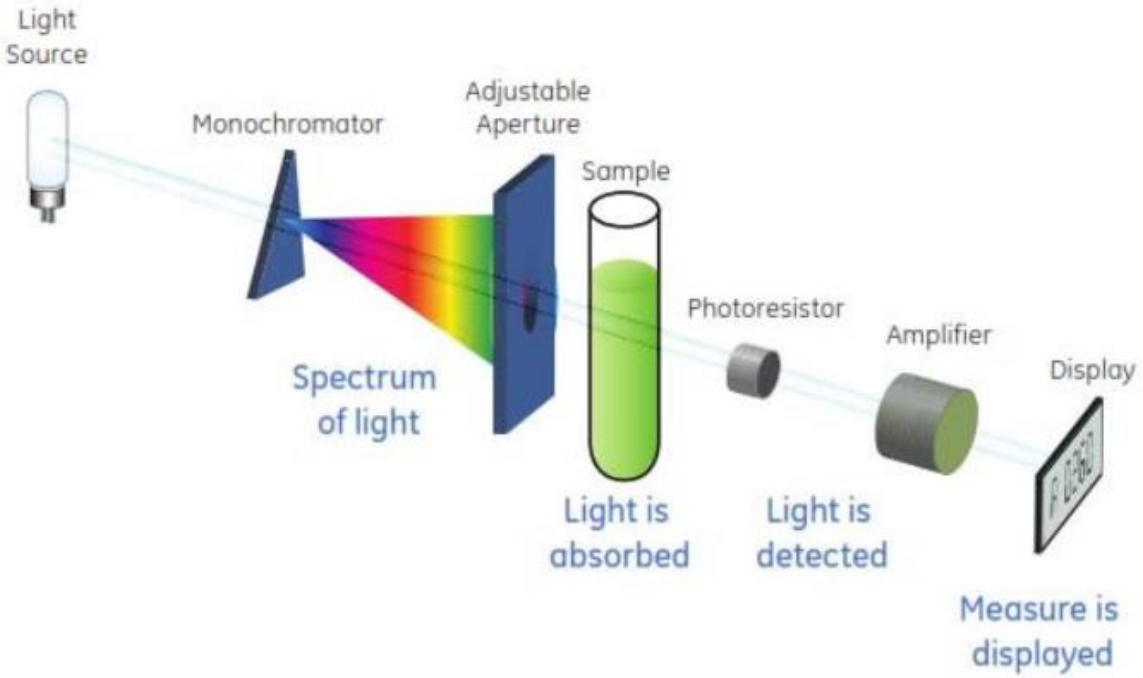


Figure 3.1 Schematic diagram of a spectrophotometer.[70]

Spectrophotometers can be categorized both by the wavelength range of their light source and by the beam of light. As the names suggest, UV-visible spectrophotometers use light in the ultraviolet range (185 – 400 nm) and in the visible range (400 – 700 nm), while IR spectrophotometers use light in the infrared range (700 – 15,000 nm). A double beam spectrophotometer uses two light paths with one passing through a test cell and the other passing through a reference cell, while a single beam spectrophotometer compares the relative light intensity of a single path with and without the sample.[70]

Regardless of the category of spectrophotometer, the basic working principle is based on the Beer-Lambert law, which relates the amount of light attenuation, or light absorbed by a sample, to the concentration of a substance in the sample for a given path length through the sample. The Beer-Lambert equation expresses this mathematically in Equation (3.1).

$$I(x) = I_0 \cdot 10^{\theta x c} \tag{3.1}$$

Where $I$ is the intensity of light transmitted through the solution as a function of the optical pathlength through the sample, $x$, and $I_0$ or $I(x = 0)$ is the intensity of the incident light at a given wavelength. Additionally, $\theta$ is the proportionality constant or molar absorption coefficient for a particular substance and wavelength (e.g., for methylene blue dye $\theta = 3.67 \times 10^4$ L/mol-cm at 609 nm), and $c$ is the concentration of the measured substance in the sample.[71] The ratio of $I$ to $I_0$ gives the fraction of light that is transmitted through the sample, also known as the transmissivity, $T$, and is related to the relative absorbance, $A$, according to Equation (3.2).

$$A = -\log_{10} T = \theta x c - \log_{10} \frac{I(x)}{I_0} \tag{3.2}$$

In this way, the concentration of a substance may be measured. The spectrophotometer used in this work is the HI83399 Hanna Instruments photometer (Hanna Instruments, Woonsocket, RI, USA). As will be described in the following sections, spectrophotometry will also be used to measure the chemical oxygen demand and the concentration of methylene blue dye in waters, as well as the concentrations of certain aqueous phase species, such as nitrite, nitrate, ozone, and copper ions, thus making for an extremely useful benchtop measurement tool. However, total organic carbon assessment will require a different measurement technique.

### *3.1.2 Total Organic Carbon*

As the name suggests, TOC is a measure of the total organic carbon contained in a water sample. This measurement involves two stages: total carbon (TC) and inorganic carbon (IC) measurements, with the difference providing the TOC of the sample. First, combustion catalytic oxidation of the sample converts the organic carbon to carbon dioxide, which is then cooled and

humidified before being detected by an infrared gas analyzer to measure the TC content of the sample. The second step involves acidifying the sample to pH < 4, making bicarbonate and carbonate unstable.[65], [72] Thus, the IC in the sample is converted to carbon dioxide, either free $CO_{2(aq)}$ or in the form of carbonic acid, that can be purged with a $CO_2$-free gas to isolate the carbon dioxide, which is subsequently cooled, humidified, and detected by the gas analyzer as the IC measurement.

### *3.1.3 Biochemical/Chemical Oxygen Demand*

While TOC measurements focus on the carbon content of a sample directly, BOD and COD are measurements of the amount of oxygen consumed in the complete oxidation of organics to carbon dioxide, water, and mineral salts. As such, BOD and COD are particularly well suited for monitoring water treatment processes involving oxidation of organics and for informing the design of the water treatment process (e.g., how much oxidant must be used to remove the contaminants present in the waste stream).[66]

More specifically, BOD is a measure of the oxygen consumed by bacteria in the oxidation of organics and is representative of contaminant decomposition in the natural environment, making this method most suitable for predicting the effects of the organic contaminants on the dissolved oxygen levels of receiving waters. In contrast, COD is a measure of the oxygen consumed in the chemical oxidation of organics.[73] The BOD test typically takes five days to get results, meanwhile the COD test can provide results in less than three hours.

Due to the short analysis time and ability to correlate with BOD, the COD test has become the industry standard for rapid and frequent monitoring of water treatment process efficiency and effluent quality. The most common method is the closed reflux, colorimetric method with potassium dichromate oxidizing agent.[66] Pre-formulated commercial reagent

mixtures are available for rapid COD analysis and provide consistent results between different laboratories.

The assessment of COD in this work was performed using the EPA method 4.10.4 approved method, which is the closed reflux, colorimetric method with potassium dichromate oxidizer. Pre-formulated reagent was purchased from Hanna Instruments (HI9375A-25 COD reagent low range: 0 to 150 mg/L as $O_2$, accuracy: ±5 mg/L or ±4% of reading at 25 °C, resolution: 1 mg/L) along with a HI83399 Hanna Instruments photometer for measuring sample absorbance using an LED light source with narrow band interference filter at 420 nm.

The problem with COD assessments of plasma treated wastewaters is that residual peroxide interferes with the measurement. Indeed, this interference is an issue for any AOP involving residual peroxide.[74] The next section presents a study in which this peroxide interference is demonstrated for a plasma discharge in water using methylene blue as a model contaminant.

### 3.2 Hydrogen Peroxide Interference in COD Assessments of Plasma Treated Waters[1]

Wastewater treatment plants use COD to measure treatment process efficiency and quality of treated water. Plasma-water interaction produces residual peroxide which interferes with the COD measurement. As a result, COD assessments of plasma treated waters will show incomplete removal of oxygen demand and may be viewed as a disadvantage of plasma-based advanced oxidation for municipal wastewater treatment plants and companies looking to treat their wastewater streams.

[1] The results presented and portion of the text in this section have been previously published by Groele and Foster in the journal *Plasma*.[139]

Indeed, when researching new wastewater treatment technologies, LC-MS should be used to determine residual organic content before applying standard water quality diagnostics. This section therefore describes precautions necessary for plasma practitioners to consider so as to yield credible contaminant decomposition measurements. Plasma in contact with water produces a host of reactive oxygen species, and so caution is necessary when interpreting the results.

### *3.2.1 Materials and Methods*

The plasma-liquid discharge configuration used to bring non-equilibrium plasma in contact with water in this investigation is an underwater DBD plasma jet that has been described in Section 2.4.2. The central high-voltage electrode is excited with a 5 kHz sinusoidal voltage at 4 $kV_{p-p}$, provided by an AC power supply, the Elgar model 501SL power supply with a step-up transformer described in Section 4.2.1. The voltage and current are monitored with a high-voltage probe and Pearson coil, respectively, as described in Section 4.2.3. In this case, a 2 GHz Wavepro 7200a oscilloscope (Teledyne LeCroy, Chestnut Ridge, NY, USA) was used to monitor and record the voltage-current waveforms. The experimental set-up is shown in Figure 3.2.

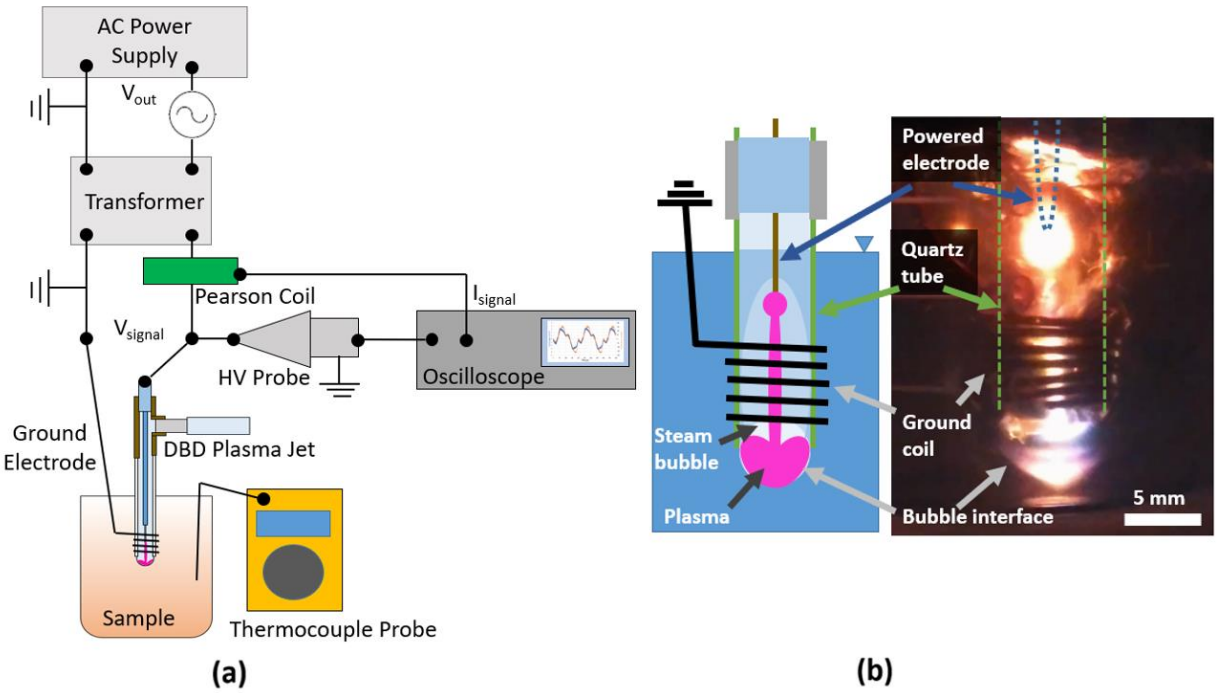


Figure 3.2 (a) Schematic of the DBD plasma jet experimental set-up used in this work. (b) Schematic and image of the DBD plasma jet apparatus operating in steam-mode discharge in deionized water.

Typical voltage and current data are shown in Figure 3.3. Data from previous Lissajous experiments by Garcia et al. with the DBD plasma jet operating in steam-mode at these power supply conditions indicate that about 56 W of power are deposited in the discharge, with peak steam temperatures around 2800 K, as determined from comparing theoretical simulation of OH(A-X) spectra with experimental optical emission spectra.[10]

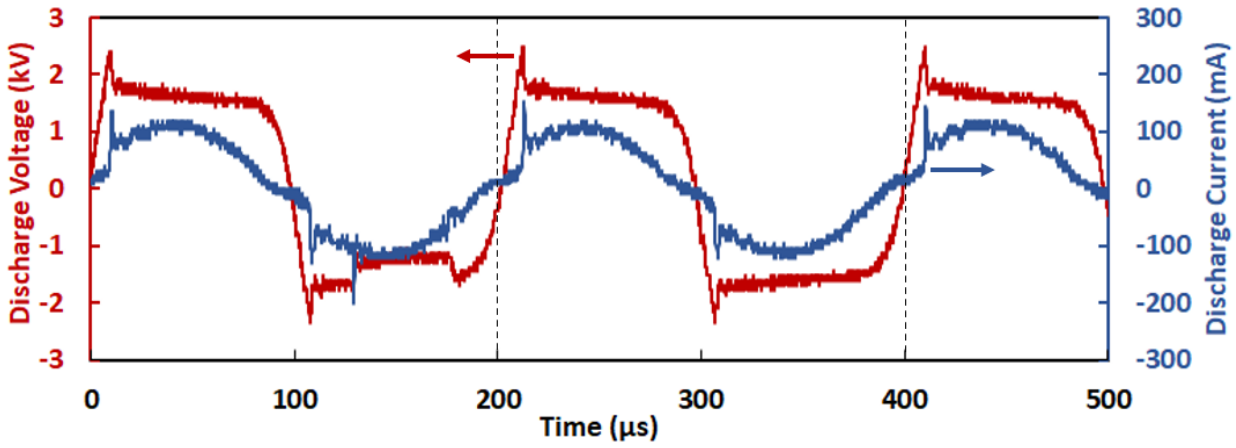


Figure 3.3 Discharge voltage and current signals measured during operation of the underwater DBD plasma jet operating in steam-mode at 5 kHz.

The DBD plasma jet can be operated with or without gas flow. In this work, the plasma jet operates without any input gas. This so-called "steam mode" discharge relies on local evaporation near the tip of the high-voltage electrode to form a vapor bubble that acts as the low-density region for plasma formation. Although a portion of the deposited power goes into heating and evaporating water, operating in steam-mode requires no consumables and minimizes the production of $NO_x$ (i.e., nitrite and nitrate), as evidenced from optical emission spectroscopy.[75], [76] Since the discharge gas contains primarily water vapor and only trace amounts of air bubbles, the amount of hydrogen peroxide that is generated in the water far exceeds the amount of nitrite and nitrate generated. In this case, the iodometric titration method for quantifying hydrogen peroxide concentration discussed in Section 3.5.1 is suitable.

Samples of deionized water (Milli-Q EMD Millipore, Burlington, MA, USA, electrical conductivity ≈ 3 µS/cm) are dosed with hydrogen peroxide either by solution (30%, Fisher Chemical, Hampton, NH, USA) using a variable volume sampler pipette (Thermo Fisher Scientific, Waltham, MA, USA, resolution: 1 µL) or by underwater DBD plasma jet. When dosing with the DBD plasma jet, the opening of the quartz tube is placed approximately in the

center of a 50 mL sample of deionized water and power is provided to the central high-voltage electrode. Approximately one second is required for the vapor bubble to form at the electrode tip in which the plasma discharge subsequently develops.

Plasma is applied to the sample via the DBD plasma jet for 30 s at a time, and the increase in sample temperature throughout the treatment duration is measured using a Fluke 87V true RMS multimeter with a type-K thermocouple (Fluke Corporation, Everett, WA, USA, resolution: 0.1 °C, accuracy: 0.5%). After 30 s of treatment, the sample is placed in an ice bath to cool down to room temperature before further treatment. The objective was to keep the bulk liquid sample below 60 °C. After treatment, the samples are stored in a dark cabinet for approximately 20 h before the hydrogen peroxide concentration and COD are measured to allow post-discharge reactions to take place while mitigating hydrogen peroxide photo-dissociation.

Samples of methylene blue (MB) are prepared by dissolving solid MB powder (M291-25 Fisher Chemical) in deionized water (Milli-Q EMD Millipore). A low concentration sample of 5 mg/L and a high concentration sample of 1000 mg/L are prepared and treated with the underwater DBD plasma jet to demonstrate the hydrogen peroxide interference problem, discussed in Section 3.2.2. Plasma treatment of the MB samples follows the same procedure as described for dosing deionized water samples with hydrogen peroxide by DBD plasma jet, including monitoring the temperature to keep the sample below 60 °C. Again, treated MB samples were stored in a dark cabinet for 20 h before assessing the COD.

### *3.2.2 Results and Discussion*

To illustrate a picture of the hydrogen peroxide interference problem, a 100 mL sample of 5 mg/L MB is prepared, and the COD is assessed before and after steam-mode plasma jet treatment. The results are shown in Table 3.1. In general, the COD is expected to decrease with

plasma treatment time as the MB molecules are mineralized. Indeed, the color of the dye disappears after 15 min of treatment indicating the destruction of MB, as seen in Figure 3.4a; yet, the measured COD actually increases with treatment time. No additional organics are being added to the solution by the plasma; thus, one of the plasma-derived species being transported to the liquid during treatment must be contributing to the measured COD of the sample.

Table 3.1 Measured COD values for untreated and treated samples of MB. MB-A samples (left) contain initial MB concentration of 5 mg/L while MB-B samples (right) start with 1000 mg/L MB.

| MB-A Sample | COD (mg/L) | MB-B Sample | COD (mg/L) |
|---|---|---|---|
| Untreated (5 mg/L) | 6 ± 5 | Untreated (1000 mg/L) | 1680 ± 75 |
| Treated for 7 min | 16 ± 5 | Treated for 40 min | 99 ± 5 |
| Treated for 15 min | 30 ± 5 | Treated for 120 min | 62 ± 5 |

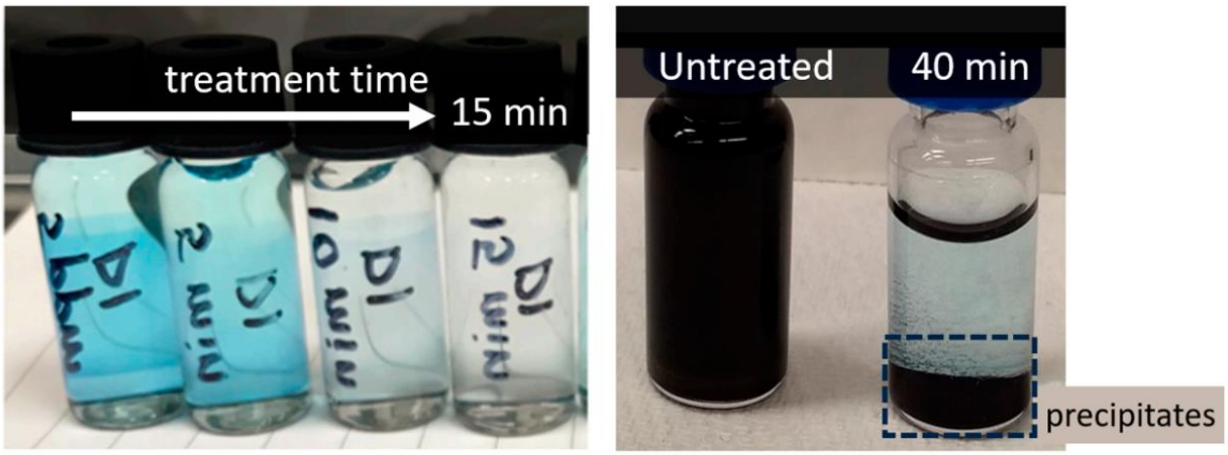


Figure 3.4 (a) Images of samples starting with 5 mg/L MB showing decrease in color indicating destruction of the MB dye. (b) Image of untreated sample with 1000 mg/L MB and sample after 40 minutes of plasma treatment showing MB precipitates and mostly clear supernatant.

The two primary long-lived plasma-derived species that could be present in the sample after plasma treatment are hydrogen peroxide and ozone, since nitrates and nitrites should not be

generated under steam-mode operation. Of these species, hydrogen peroxide has been found to interfere with the standard COD assessment by reducing the potassium dichromate oxidizing agent according to the overall oxidation reaction given in Equation (3.3).[77] From this equation, the theoretical magnitude of the hydrogen peroxide interference is calculated to be 470.6 mg of COD as $O_2$ per 1000 mg $H_2O_2$.

$$K_2Cr_2O_7 + 3H_2O_2 + 4H_2SO_4 \rightarrow K_2SO_4 + Cr_2(SO_4)_3 + 7H_2O + 3O_2 \quad (3.3)$$

Researchers investigating plasma treatment of wastewaters must be particularly careful when interpreting COD results because the interference from residual hydrogen peroxide may not be evident. For example, two 100 mL samples of 1000 mg/L MB were prepared and treated with the underwater DBD plasma jet. After treatment, the COD decreased from the initial value of 1680 ± 75 mg/L, as shown in Table 3.1, and the supernatant becomes transparent as oxidized MB precipitates out of the solution, as shown in Figure 3.4b. This case of high initial COD relative to the residual peroxide concentration masks the peroxide interference effect. Still, any residual peroxide left in the sample after treatment will contribute to the COD. Hence, the COD contribution from organics should be less than the 99 mg/L after 40 min of treatment indicated in Table 3.1, since there is some contribution from residual peroxide.

In this case of high initial dye concentration (MB-B Sample, Table 3.1), the residual peroxide contribution to the COD may have been up 99 mg/L, but since the COD decreases from 1680 mg/L to 99 mg/L, it appears that the process is working as intended (COD decreases as MB is oxidized). In this case, the COD of the residual peroxide is at least 17 times less than the COD of the organics present in the sample before treatment, thus the interference effect is not immediately apparent. In reality, the treatment process is likely working better (faster organic

removal rate) than would be indicated by the COD test because of the interference from residual peroxide.

However, in the case of low initial dye concentration (MB-A Sample, Table 3.1), the measured COD increases with plasma treatment time because the COD contribution from residual peroxide after treatment is greater than the COD of the organics present in the sample before treatment. By simply looking at the measured COD before and after treatment, it would appear as if the process did not work (i.e., organics were not removed), because the peroxide interference has not been corrected for.

To investigate the magnitude of hydrogen peroxide interference in COD assessments, deionized water was dosed with hydrogen peroxide both by solution and by DBD plasma jet according to the procedure described in Section 3.2.1. The hydrogen peroxide concentration is measured immediately before COD assessment. In both cases, the COD increases with increasing hydrogen peroxide concentration, as shown in Figure 4, even though there were no organics present in the samples. This proportional relationship was also found by Lee et al. for conventional advanced oxidation processes, although the interference magnitude varied depending on the water quality and treatment process.[74]

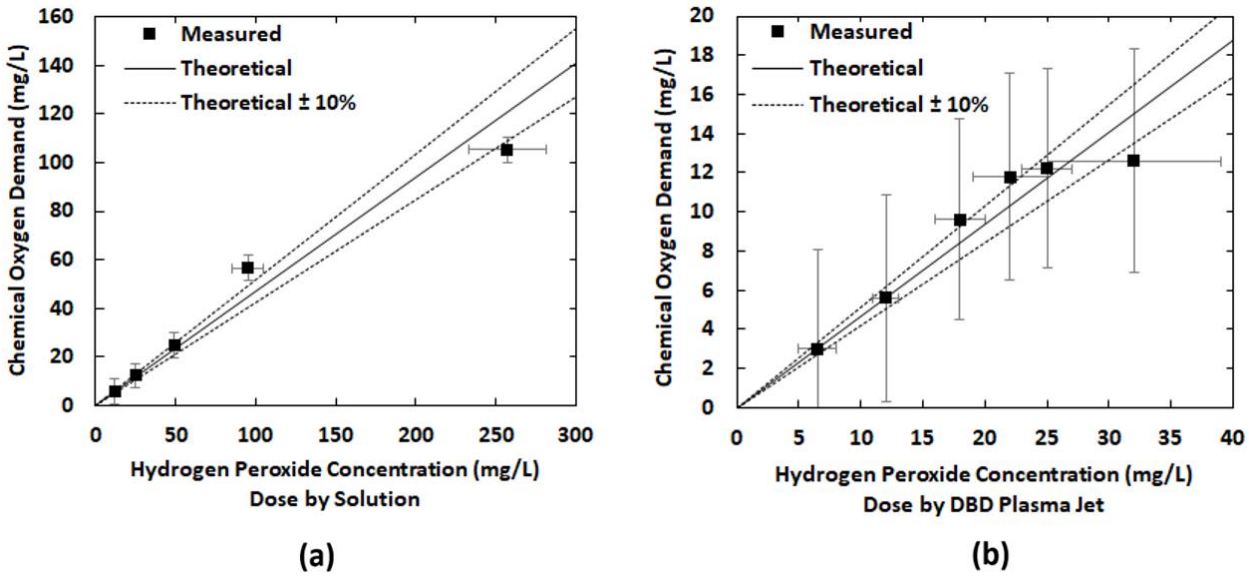


Figure 3.5 (a) COD vs. $H_2O_2$ concentration, where $H_2O_2$ is added to samples by a solution of 30% $H_2O_2$. (b) COD vs. $H_2O_2$ concentration, where $H_2O_2$ is added to samples by exposure to the underwater DBD plasma jet.

These results seem to confirm that the measured COD results from residual peroxide reacting with the potassium dichromate oxidizing agent during the COD assessment. The magnitude of the interference found in this experiment is approximately equal to the theoretical value from Equation 4, but this value can vary in practice by up to 16% percent depending on the specific organic compounds and oxidizing species that are present in the sample being assessed, particularly in real wastewaters.[74]

When AOPs are used to remove trace levels of contaminants from relatively low COD waters, as can occur at final disinfection stages of drinking water treatment plants, the uncertainty in the actual interference magnitude can lead to misinterpretation of results. While reagents may be used to quench residual hydrogen peroxide in attempt to remove this interference, these reagents often introduce their own interferences with the COD assessment.[77] More research is needed to investigate how the residual oxidants and other

long-lived species from plasma treatment affect the COD measurement in various synthetic and real wastewaters in order to develop correction methods for appropriate interpretation of results.

Even though COD measurements are considered the industry standard for monitoring water quality and water treatment performance, this contaminant removal assessment will not be featured prominently in the rest of this thesis. Rather, contaminant removal assessments in much of this work will focus on the highly selective liquid chromatography – tandem mass spectrometry (LC-MS/MS) technique which allows for determination of individual compounds' concentrations, in this case PFAS concentrations, as will be discussed in the next section. Nevertheless, reporting on this interference to the plasma science community for the specific case of plasma treated waters remains an important contribution of this work, as this interference effect was not previously being discussed in the community.

### 3.3 PFAS Concentration Measurements by LC-MS/MS

Since one of the primary goals of this thesis is to evaluate plasma reactors for the decomposition of PFAS, the measurement of concentrations for various PFAS before and after treatment is essential. This task is quite complicated, and requires special training and expensive equipment to perform, particularly when measuring low concentrations of PFAS (in the parts per trillion, ppt, range), as will be done in this thesis. Most of the PFAS concentration measurements included within this work were performed with the help and supervision of Mr. Thomas Yavaraski at the University of Michigan Environmental and Water Resources Engineering Laboratory. The first PFAS concentration measurement results were compared with those from an independent laboratory for comparison purposes, as noted in Section 4.3, and were found to be in general agreement.

First, samples are prepared by adding 8 mL of each test solution to 10 mL amber glass vials (Sigma Aldrich, St. Louis, MO, USA). Calibration standards are formulated using native per- and polyfluoroalkyl substance precision and recovery standard solution PFAC-24PAR (Wellington Laboratories Inc., Guelph, ON, Canada) which has an expanded maximum combined percent relative uncertainty of ±5% and contains the 24 compounds to be quantified (EPA Method Development Analyte List) listed in Table 3.2.

Table 3.2 EPA method development analyte list showing the 24 compounds to be quantified.

| Analytes |
|---|
| Perfluorobutanoic Acid (PFBA) |
| Perfluoropentanoic Acid (PFPeA) |
| Perfluorohexanoic Acid (PFHxA) |
| Perdluorobutane sulfonic Acid (PFBS) |
| Perfluoroheptanoic Acid (PFHpA) |
| Perfluoropentane Sulfonic Acid (PFPeS) |
| Perfluoroocatanoic Acid (PFOA) |
| Perflourohexane Sulfonic Acid (PFHxS) |
| 6:2 Fluorotelomer Sulfonic Acid (6:2FTS) |
| Perdluorononanoic Acid (PFNA) |
| Perflourooctane Sulfonic Acid (PFOS) |
| 4:2 Fluorotelomer Sulfonic Acid (4:2FTS) |
| Perfluoroheptane Sulfonic Acid (PFHpS) |
| Perfluoroctane Sulfonamide (FOSA) |
| Perfluorodecanoic Acid (PFDA) |
| 8:2 Fluorotelomer Sulfonic Acid (8:2FTS) |
| Perfluoroundecanoic Acid (PFUndA) |
| Perfluorononane Sulfonic Acid (PFNS) |
| N-Methyl perfluorooctanesuldonamidoacetic acid (N-MeFOSAA) |
| N-Ethyl perfluorooctanesuldonamidoacetic acid (N-EtFOSAA) |
| Perfluorododecanoic Acid (PFDodA) |
| Perfluorordecane Sulfonic Acid (PFDS) |
| Perfluorotridecanoic Acid (PFTrDA) |
| Perfluorotetradecanoic Acid (PFTeDA) |

Calibration standards of 2, 20, 50, 200, and 600 ppt were generated by adding varying amounts of the PFAC-24PAR standard solution to 8 mL of deionized water, as seen in Table 3.3.

All samples had the same total volume of deionized water (8 mL), and both the calibration standards and test samples were spiked with 8 µL of internal standard (IS), also seen in Table 3.3. The IS contains isotope forms of certain PFAS such that their mass-to-charge ratios are distinct from the rest of the analytes. Additionally, two "blank" samples of deionized water, one with IS and one without, are also run intermittently between test samples to confirm that there is not a carryover effect of contamination between the samples.

Table 3.3 Summary of calibration standards used for PFAS quantification. [a] 1000x denotes a dilution factor of 1000 of PFAC-24PAR standard solution. [b] 100x denotes dilution factor of 100. [c] 10x denotes dilution factor of 10.

| Cal. Std. (ppt) | Volume of PFAC-24PAR | Volume of IS (µL) | $H_2O$ Volume (mL) |
|---|---|---|---|
| 2 | 8 µL of 1000x[a] | 8 | 8 |
| 20 | 8 µL of 100x[b] | 8 | 8 |
| 50 | 2 µL of 10x[c] | 8 | 8 |
| 200 | 8 µL of 10x[c] | 8 | 8 |
| 600 | 24 µL of 10x[c] | 8 | 8 |

PFAS compound analysis is conducted using a modified EPA Method 537.1.[64] Briefly, samples are concentrated using solid phase extraction, and quantified using a liquid chromatography – high-resolution Q-Exactive Plus Hybrid Quadrupole-Orbitrap Mass Spectrometer (Thermo Scientific, Waltham, MA, USA) using negative-mode electrospray ionization. The chromatography column is the Hypersil Gold (1.9 µL, 2.1 x 100 mm, Thermo Scientific).

The PFAS present in the samples are separated based on their retention times in the chromatography column (i.e., transit time through the column) in the liquid chromatography stage, and then the compounds are identified by their mass-to-charge ratio (m/z) in the tandem mass spectrometry stage. The amount of a compound with a particular m/z and retention time can be quantified and calculated as a concentration using the calibration curve generated from

the calibration standards. In addition to quantifying the 24 compounds listed in Table 3.2, the high-resolution mass spectrometer enables the qualitative assessment of unknown PFAS compounds in samples, and the effects of plasma treatment on PFAS speciation within the same analysis.

## 3.4 Water Property Measurements

This section covers the measurements of some basic water property measurements; namely, the electrical conductivity, the pH, and the temperature of the water. While these measurements are comparatively rather simple to perform using probes, they are important measurements for monitoring the plasma treatment process of waters. For example, the rates of some aqueous-phase chemical reactions can be dependent on temperature and the reaction mechanisms can be pH dependent. The electrical conductivity of the water may impact the plasma discharge properties, and the charged species responsible for the electrical conductivity can also affect the water chemistry.

### *3.4.1 Electrical Conductivity*

The electrical conductivity (EC) of water is a measure of the water's ionic activity in terms of its ability to conduct electrical charge as a result of the concentration of dissolved constituents, typically given in units of µS/cm.[78] Essentially, EC can be considered a measure of a water's salinity. While pure water is not a good conductor, most real waters contain varying concentrations of ionic species that can contribute to the EC of the water, and the EC generally increases with increased concentration of ionic species. For example, in Chapter 6, sodium chloride (NaCl) is dissolved in deionized water, thus forming $Na^+$ and $Cl^-$ ions. The more NaCl that is dissolved, the higher the EC of the water.

The EC of water is related to the total dissolved solids (TDS), another important water quality parameter which is also a measure of the total ions dissolved in solution. TDS is measured by filtering out suspended solids, evaporating the remaining filtrate, and weighing the resulting residue, thus making it a more involved and time-intensive measurement compared to using a conductivity probe to measure EC.[78] The relationship between TDS and EC is described using a conversion factor, *k*, such that TDS (mg/L) = $k \times$ EC (µS/cm). However, the value of *k* is not constant, and can vary depending on the activity of the specific ions that are present in the water.[79] For natural waters, the value for *k* can range from 0.55 to 0.75.[80] Future research should investigate this *k* factor for plasma treated waters to determine the range of expected values.

In plasma-liquid systems, the EC tends to increase with plasma exposure as charged species from the plasma-phase are transferred to the liquid. If the electrodes are not insulated from the liquid, metal ions from the electrodes can also be transferred to the liquid and further contribute to the conductivity increase.

Another feature of water conductivity that impacts plasma-water systems is the charge relaxation time, which is the ratio of material permittivity, $\varepsilon$, to electrical conductivity, $\sigma$, and is expressed by Equation (3.4). Here, $\sigma$ is the EC of the water, and the permittivity is the dielectric constant of water (80.2, unitless) multiplied by the free space permittivity ($8.85 \times 10^{-14}$ F/cm); therefore, $\varepsilon = 7.1 \times 10^{-12}$ F/cm, and the charge relaxation time is essentially a function of the EC.

$$\tau_{cr} = \frac{\varepsilon}{\sigma} \tag{3.4}$$

Highly conductive materials, such as copper, have charge relaxation times on the order of $10^{-19}$ s, while an insulator such as silica is on the order of $10^{3}$ s. Meanwhile, groundwater tested

in later chapters started with an EC around 800 µS/cm which corresponds to a charge relaxation time of about 9 ns, while plasma treated waters in Chapter 5 reach an EC up to 4,000 µS/cm (charge relaxation time of about 2 ns). The implication is that higher water EC results in faster charge relaxation times and may reduce the span of surface ionization waves and electron energy relaxation lengths, thus reducing the spreading of plasma over the water (i.e., plasma-water contact area).[50] More research is needed to assess how the EC and charge relaxation time affect the plasma-water contact area and the associated treatment performance for specific discharge configurations and target contaminants.

In this work, the EC is measured using the Orion Star A329 Portable Multiparameter Meter (Thermo Fisher Scientific, Waltham, MA, USA) which is capable of measuring pH, electrical conductivity, and dissolved oxygen. The EC measurement is enabled using the Thermo Orion 013010MD 4-electrode DuraProbe conductivity cell (Thermo Fisher Scientific) which has a conductivity range of 1 µS/cm – 200 mS/cm with a minimum resolution of 0.001 µS/cm and an accuracy of ±1 µS/cm.

### *3.4.2 pH*

In chemistry, the pH of water refers to the hydrogen ion ($H^+$) concentration, specifically the negative common logarithm of the $H^+$ concentration in an aqueous solution, expressed as Equation (3.5). The pH ("potential of hydrogen" or "power of hydrogen") is a scale used to quantify how acidic or basic an aqueous solution is with more acidic solutions containing higher concentrations of hydrogen ions and lower pH values compared to basic solutions.

$$\mathrm{pH} = -\log_{10}([\mathrm{H}^+]) \tag{3.5}$$

At 25°C, solutions with a pH of 7 are considered neutral, with those below 7 being acidic and those above 7 being basic. While a pH of 7 is associated with pure water, in practice even

deionized water will typically vary from this value. Often, the pH will be less than 7, as carbon dioxide gas from the air dissolves in the water to produce carbonic acid.

The pH of water can be important as it affects the relative speciation of certain chemical systems and resulting chemistry.[81], [82] For example, carbon dioxide may appear in different relative amounts depending on the pH, as seen in Figure 3.6. At pH of 4 or less, the dominant form of inorganic carbon is carbonic acid, which exists as aqueous carbon dioxide in water. Recall, that this behavior is leveraged in the TOC measurement, as lowering the pH to below 4 results in the conversion of the other inorganic carbon forms (bicarbonate and carbonate) to aqueous carbon dioxide, which can be purged from the sample and analyzed. Meanwhile, at pH > 12, carbonate is the dominate inorganic carbon species.

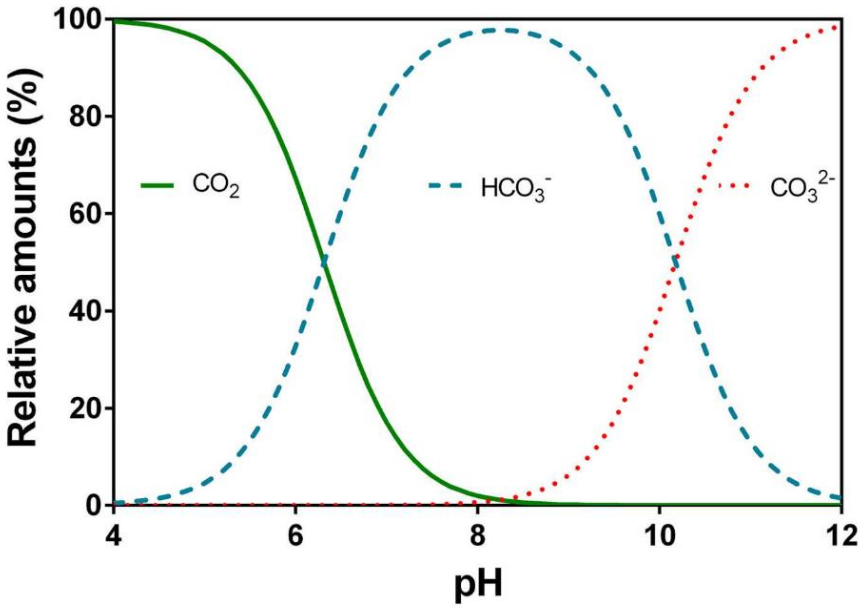


Figure 3.6 Relative speciation (%) of carbon dioxide ($CO_2$), bicarbonate ($HCO_3^-$), and carbonate ($CO_3^{2-}$) in water as a function of pH.[81] For this example, the water temperature is 20 °C and the electrical conductivity is 250 µS/cm.

The pH is measured using the same Orion Star A329 Portable Multiparameter Meter that is used to measure the EC. The pH measurement is enabled using the Orion ROSS Ultra Low

Maintenance pH/ATC Triode Combination Electrodes (Cat. No. 8107UWMMD, Thermo Fisher Scientific), which has a pH range from 0 to 14, a resolution of 0.01, and an accuracy of 0.03, as well as automatic temperature compensation (ATC).

### *3.4.3 Temperature*

Water temperature is an important property since it affects many other properties such as density, viscosity, specific heat capacity, surface tension, vapor pressure, and solubility. Furthermore, rate constants for many chemical, biochemical, and biological reactions in liquids are temperature dependent. In general, as the water temperature increases, the rate of chemical reactions increases while the amount of dissolved gasses, such as oxygen, decreases.[78] Water temperature can also affect the EC of water, such that a given water at a higher temperature will have a higher EC.[83] Temperature is measured using both the Fluke 87V true RMS multimeter with a type-K thermocouple (Fluke Corporation) and the ATC built into the pH probe used with the Orion Star A329 Portable Multiparameter Meter, which has a resolution of 0.1 °C and an accuracy of ±0.1 °C.

## 3.5 Reactive Species Measurements

Aqueous-phase reactive species generated by plasma-liquid interaction can be measured by a variety of analytical methods, each with different sensitivity, precision, and selectivity. Some of the most convenient methods for quick estimation of long-lived species include semi-quantitative test strips which can provide concentration estimates for species such as hydrogen peroxide, nitrite, and nitrate. Fluorescence methods, which are usually based on fluorescein dyes, can be more sensitive, but are not necessarily specific; however, they can be useful for measuring certain species such as peroxynitrate.[84]

Measurement of short-lived species, such as radical species, require fast *in situ* measurements due to the high reaction rates and short lifetimes (e.g., the reaction rate of hydroxyl radicals with L-histidine is around $4.8 \times 10^{-14}$ $M^{-1}s^{-1}$), thus presenting challenges.[85] The paramagnetic nature of radicals owing to their unpaired electrons allows for the determination of radical densities and identification of species using electron paramagnetic resonance (EPR), also referred to as electron spin resonance (ESR).

However, most plasma-liquid systems are not amenable to direct observation of radicals using this EPR alone, so spin trapping techniques are leveraged to extend the lifetime of the plasma generated radicals, as was first reported by Bullock et al. for hydroxyl and hydrogen radicals generated in an aqueous solution by glow-discharge electrolysis.[86] The radical-spin-trap-adducts produce characteristic EPR spectral signatures allowing for quantitative analysis.[87], [88] Still, significant care must be taken to perform these types measurements of short-lived reactive species including appropriate calibration, accounting for reactions of spin traps with other species in the sample, and controlling for the effects of time delay between treatment and measurement.[89]

Measurements of short-lived species will not be included in this work; however, some long-lived reactive species will be considered, including hydrogen peroxide, nitrite, and nitrate. While these species have significantly longer lifetimes than radical species such as hydroxyl radicals, reactions can still occur in the minutes and hours after the sample has been treated with plasma. These post-discharge reactions include catalytic reactions and pH dependent reactions, such as hydrogen peroxide reacting with metal impurities from electrodes and with nitrites, to name a few.[90]–[92]

The long-lived reactive species measurements in this work are done primarily with titration and spectrophotometric techniques, although semi-quantitative test strips were used to gauge the concentrations of hydrogen peroxide, nitrite, and nitrate in preliminary experiments. Note that for all the measurement techniques discussed here, the upper bound of the range can be extended by diluting the sample; however, the uncertainty in the measurement will be increased accordingly.

### *3.5.1 Hydrogen Peroxide*

The concentration of hydrogen peroxide in the sample is quantified using the iodometric titration method (Hach test kit model HYP-1, Hach Company, Loveland, CO, USA, resolution: 1 mg/L $H_2O_2$) immediately prior to COD assessment. The titration method involves the oxidation of iodide to iodine (Equation (3.6)) in the presence of a molybdate catalyst and a starch indicator. The starch indicator forms a dark blue complex with iodine. Subsequent titration with thiosulfate under acidic conditions (approximate pH of 4) converts the iodine back to iodide (Equation (3.7)), and the color change from blue to transparent indicates the titration endpoint.

$$H_2O_2 + 2KI + H_2SO_4 \rightarrow I_2 + K_2SO_4 + 2H_2O \quad (3.6)$$

$$I_2 + 2Na_2S_2O_3 \rightarrow Na_2S_4O_6 + 2NaI \quad (3.7)$$

$$2I^- + 2NO_2^- + 4H^+ \rightarrow I_2 + 2NO + 2H_2O \quad (3.8)$$

This iodometric titration method is subject to interference from nitrite ions (Equation (3.8)); thus, nitrogen species from air plasma discharges will interfere with this measurement. To mitigate the generation of reactive nitrogen species that could result in aqueous nitrite, the DBD plasma jet is operated in steam mode, as discussed in Section 3.2.1. For future studies, colorimetric assay by titanyl sulfate reagent with azide for elimination of nitrite interference is a preferred method of hydrogen peroxide quantification due to superior selectivity, making it

suitable for hydrogen peroxide concentration measurements in waters treated with air plasmas.[93], [94]

### *3.5.2 Ozone*

The concentration of ozone in the water samples is measured using the colorimetric diethyl-p-phenylene diamine (DPD) method along with the HI83399 Hanna Instruments photometer which uses an LED with a narrow band interference filter at 525 nm. This method is capable of measuring ozone concentrations from 0.00 to 2.00 mg/L (as $O_3$) with a resolution of 0.01 mg/L and an accuracy of ±0.02 mg/L ±3% of the reading at 25 °C.

### *3.5.3 Nitrite and Nitrate*

Nitrite concentrations in plasma treated samples are measured using an adaptation of the ferrous sulfite method along with a photometer which uses a LED with a narrow band interference filter at 575 nm. The range for this method is from 0 to 150 mg/L (as NO2-) with a resolution of 1 mg/L ad an accuracy of ±4 mg/L ±4% of the reading at 25 °C.

Nitrate concentrations are measured using an adaptation of the cadmium reduction method along with the photometer which uses a LED with a narrow band interference filter at 525 nm. This method can measure nitrate concentrations from 0.0 to 30.0 mg/L (as $NO_3^-$-N) with a resolution of 0.1 mg/L and an accuracy of ±0.5 mg/L ±10% of the reading at 25 °C.

### *3.5.4 Metals*

While metals and metal ions may not typically be considered plasma-derived reactive species, they can be transferred to the water and contribute to the electrical conductivity, as well as influence the aqueous-phase chemistry. The two metal ions of interest in this work are iron and copper. Since the electrodes used are either stainless steel or copper and these electrodes can

be in contact with the water, some of the electrode material can sputter and be transferred to the water.

Additionally, for some of the longer duration treatments, a copper coiling coil is used to maintain the water temperature within a narrow range and minimize the influence of water temperature on the PFAS decomposition kinetics. Indeed, when copper is exposed to the acidic air-plasma activated water the copper can corrode and release copper ions into the water.[95] The $Cu^{+}$ ions dissolved in water are unstable and are readily oxidized to $Cu^{2+}$ (either as $Cu^{2+}$ ions or as $Cu(OH)^{+}$ at low pH), which can give the water a greenish color. Fortunately, copper can be removed, and even recovered, from waters using techniques such as adsorption, membrane filtration, cementation, and electrodialysis.[96]–[98]

Copper ion concentrations are measured using the spectrophotometer with a LED and a narrow band interference filter at 575 nm. This gives a range from 0.000 to 1.500 mg/L (as $Cu^{2+}$) with a resolution of ±0.001 mg/L and an accuracy of ±0.010 mg/L ±5% of reading at 25 °C. Similarly, iron concentrations can be measured using spectrophotometry. In this case, a LED with a narrow band interference filter at 525 nm is used as an adaptation of the EPA Phenanthroline method 315B, for natural and treated waters, which has a range from 0.00 to 5.00 mg/L (as Fe) with a resolution of 0.01 mg/L and an accuracy of ±0.04 mg/L ±2% of reading at 25 °C.

Unfortunately, high copper ion concentrations can interfere with this spectrophotometric method of iron concentration measurement. For more specific measurements of metal ions, such as iron and copper, inductively coupled plasma mass spectrometry (ICP-MS) is recommended and is available at the Mass Spectrometry Center (University of Michigan, Department of Chemistry). Furthermore, anions such as nitrite and nitrate can be measured using electrospray

ionization mass spectrometry (ESI-MS) in negative ion mode electrospray, which is available at the Biological Mass Spectrometry Laboratory (University of Michigan, Department of Chemistry). While these techniques require more expensive equipment and usually require the supervision of a trained analytical chemist, these techniques overcome the issues of interference from co-existing compounds in water matrices that can impact the more readily accessible spectrophotometric techniques.

Switching focus from aqueous-phase diagnostics to gas/plasma phase diagnostics, emission spectroscopy is an extremely useful technique for assessing plasma discharge properties, such as gas temperature and electron density. The next section introduces this technique.

### 3.6 Optical Emission Spectroscopy

Spectroscopy refers to the study of the interaction between electromagnetic radiation and matter. Optical emission spectroscopy (OES) involves collecting light emitted from a source and separating that light based on its wavelengths. In this case, the light source is the plasma discharge being investigated. The number of photons at a given wavelength can be detected, and this information can provide insight into the relative concentrations of certain species in the plasma. OES is a useful tool both for the quantity of information that can gleaned from the collected spectra and for its non-invasive nature.

The basic experimental setup of an OES system is illustrated in Figure 3.7. Light is collected from the source by a lens and transferred with a fiber optic cable to an opening in the spectrometer. The light is directed into mirrors that redirect the light into a grating which is operated by a controller connected to a computer. The grating separates the light based on wavelength as it reflects the light into another mirror. The light then passes through an exit slit

where it enters a photomultiplier tube (PMT) which uses a photocathode, focus electrode, and a series of dynodes to amplify the photon signal of the individual frequencies at a collector to collect the intensity of each wavelength in counts.

An alternative to the PMT for amplifying the photon signal is an intensified charge-coupled device (ICCD) camera, which also has the advantage of achieving very fast gate times on the order of nanoseconds. When coupled with a signal/delay generator, the spectrometer gating (controlled via the ICCD camera) can be synchronized with ns-pulsed plasma discharges to collect light emitted from the plasma, thus enabling time-resolved or time-averaged OES diagnosis of the discharges' optical emissions.

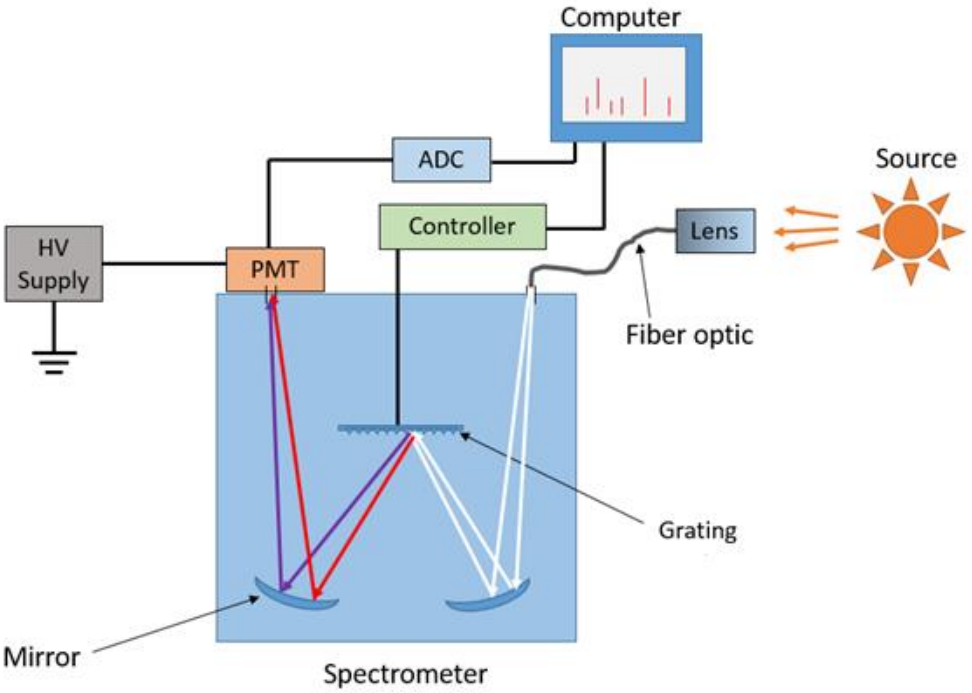


Figure 3.7 Experimental setup of the Monochromator spectrometer system with photomultiplier tube (PMT).

The spectrometer used in this work is a Czerny-Turner type spectrometer, the Acton Series SP-2300i (Princeton Instruments, Trenton, NJ, USA), which has a 0.3 m focal length and an 1800-grooves/mm holographic grating. The photon signals are amplified and detected by a

PI-MAX3 fast ICCD camera (Princeton Instruments). The ICCD gating is synchronized with the power supply generating the plasma discharge using a BNC Model 565 multichannel pulse/delay generator (Berkely Nucleonics Corp., San Rafael, CA). The equipment is controlled, and data is collected using *WinSpec32* software.

The line broadening contributions from instrumental, Doppler, van der Waals, and Stark broadening are considered in the data analysis. Briefly, Doppler broadening is the result of the velocity distribution of atoms or molecules which results in a distribution of doppler shifts. Van der Waals broadening is caused by the dipolar interaction between excited atoms and the induced dipoles from neutral perturbing species (i.e., the van der Waals effect), while the Stark broadening is due to the emitter atoms colliding with surrounding charged particles that generate local electric fields, known as the Stark effect.[99] Instrumental broadening is related to the spectrometer components, including the entrance slit, and must be measured experimentally.

Wavelength dispersion, axial divergence, and non-ideal optics can all contribute to the instrumental broadening. For these experiments, the instrumental broadening, $\Delta\lambda_I$, was measured using a 30 mW He-Ne laser directed into the fiber transmitting light to the spectrometer. A gaussian distribution was fit to the recorded Ne I line at 632.8 nm to determine the instrumental function. From the full width at half maximum (FWHM) of this line, the instrumental broadening was found to be $\Delta\lambda_I = 0.44$ nm.

Recall that the value for $\Delta\lambda_I$ depends on the slit width of the spectrometer, which can be adjusted. In this case, the slit width was set to 1 mm. By narrowing the slit width, the instrumental broadening can be reduced, allowing for higher resolution structures in the collected spectra to be observed. Here, the instrumental broadening was deemed acceptable for the measurements conducted since the calculations do not require high spectral resolution and this

broadening is accounted and corrected for; however, for future studies, narrowing the slit width to 25 microns, which is commensurate with the pixel size of the ICCD camera, is recommended. This will also help to reduce the uncertainty in the measurements related to the spectrometer resolution.

In this work, OES will be primarily used as a diagnostic to estimate the gas temperature and electron density of the plasma discharge at varying water electrical conductivities. These analyses will require a deconvolution of the of the Lorentzian and Gaussian contributions to the overall line broadening, in which the van der Waals and Stark effects contribute to the Lorentzian part of the spectral line profile, while the Doppler and instrumental broadenings contribute to the Gaussian portion. This deconvolution is achieved using a Voigt profile and is discussed further in Section 6.3, with specific details relating to the estimation of the gas temperature and electron density of the plasma discharge.

The next section will discuss some preliminary experiments that explore the efficacy of two types of plasma reactors for the decomposition of PFAS, as well as some of the reactor control variables that impact this decomposition efficacy such as power supply type, working gas, and initial concentration of PFAS.

## Chapter 4 Exploring the Efficacy of Plasma Reactors for PFAS Decomposition[2]

In this chapter, the performances of two types of plasma reactors are investigated for the decomposition of PFAS in groundwaters sampled from two contaminated sites, and the impacts of various reactor operating conditions are assessed based on the removal percentages of the most prevalent PFAS compounds found in these groundwaters. The purpose of this study is to glean insights into the relative importance of the various operating conditions, such as reactor configuration, power source, feed gas, and initial PFAS concentration. In the two groundwaters tested, PFOS was the most prevalent long-chain PFAS compound and was thus selected as the target contaminant for assessing removal performance.

The two reactors investigated in this chapter are the underwater dielectric barrier discharge (DBD) plasma jet reactor and the packed-bed reactor (PBR) which features a packed-bed array of hexagonally spaced dielectric water jets. These two reactor configurations will first be described. Next, two different power supplies used to generate the voltage difference across the electrodes to facilitate the plasma generation will be discussed. One is a low-frequency (50 – 5,000 Hz) alternating current (AC) power supply, while the other is a nanosecond pulsed (ns-pulsed) power supply capable of programmable pulse repetition frequencies up to 30 kHz.

Typical voltage-current waveforms will be provided in Section 4.2.3 to further illustrate the differences between the two power supplies investigated in this study. The voltage-current diagnostics will be explained along with the method for estimating the power deposited in the

[2] The results presented and portion of the text in this chapter have been previously published by Groele et al. in the *Journal of Applied Physics*.[140]

discharge. The estimated power is an important parameter, as it informs the energy efficiency of the treatment process, as well as the expected energy costs that would be associated with the plasma-driven decomposition of PFAS in contaminated waters.

Aside from the reactor configuration (DBD plasma jet or PBR) and type of power source (AC or nanosecond pulsed), the working gas was varied between air and argon, and the starting concentration of PFOS was varied depending on which site the groundwater was collected from. Additionally, the performance of a single DBD plasma jet was compared to that of a dual-DBD plasma jet reactor configuration, which provides roughly double the plasma-water contact area. Lastly, two different treatment times were tested for one set of experimental conditions to gain some preliminary insight into the PFOS decay behavior, prior to conducting a more detailed time-resolved decomposition study, discussed in Chapter 5.

It is worth noting two aspects of this study that are novel compared to most contemporary research in the field of emerging PFAS remediation technologies. First, this study involves the treatment of raw contaminated groundwaters with complex water matrices and reactive species scavengers, while most studies thus far have focused on synthetically derived waters, typically involving deionized water spiked with one or more PFAS compounds.[38], [56], [100]–[103] Secondly, this study involves waters with PFAS concentrations on the order of 100 – 10,000 ppt depending on the groundwater collection site, which is significantly lower than many studies which treat PFAS concentrations in the ppm range.[23], [38], [100], [103]

### 4.1 Reactors

The two reactor configurations considered in this plasma source exploration study are the DBD plasma jet reactor, capable of operating in a single-jet mode or dual-jet mode, and the PBR with water dielectrics. The DBD plasma jet reactor, described in Section 4.1.1, was a promising

candidate for PFAS decomposition owing to its ability to generate plasmas with relatively high gas temperatures which can exceed 2,000 K (>1725 °C) when excited by the AC power supply.

For reference, thermal decomposition of perfluoroalkyl carboxylic acids (PFCAs) such as PFOA can be initiated at temperatures as low as 200 °C, while perfluoroalkyl sulfonic acids (PFSAs) such as PFOS require higher temperatures of ≥450 °C for thermal decomposition. Xiao et al. found that both PFOA and PFOS were nearly completely decomposed (>99.9%) on granular activated carbon media at temperatures of 700 °C or higher, and proposed thermal decomposition pathways of PFOA.[104] Thus, thermal decomposition could possibly be an important and useful decomposition mechanism initiated by the DBD plasma jet reactor, particularly when excited by the AC power supply. However, thermal decomposition may not be the dominant or most efficient method of decomposing PFAS using plasmas.

On the other hand, the plasma-water contact area is also an important variable affecting the decomposition of PFAS in water. Since many PFAS, including the two substances currently of highest concern, PFOA and PFOS, act as surfactants, they have a natural affinity for the gas-liquid interface. In the case of gas-liquid plasma discharge configurations, this interface happens to be the plasma-water interface. Thus, these contaminants tend to accumulate in the region where the plasma reactivity is the highest. In the case of PFOA adsorbing to the gas-water interface, it has been observed that a significant portion of its hydrophobic tail (5-6 carbons of the 8 carbon chain) extends into the gas/plasma phase, where it may react with high energy ions and other reactive plasma species.[59], [105]

Prior work on PFOA decomposition has suggested that solvated electrons ($e_{aq}^-$) are the primary reactant driving PFOA transformation in reduction-based PFAS remediation technologies, although ions and excited species can contribute to PFAS decomposition as

well.[100] Indeed, solvated electrons, also sometimes referred to as hydrated electrons, have a standard reduction potential of -2.9 V, thus making for a potent reducing agent.[106] However, the short lifetimes of solvated electrons means that they do not penetrate far into the bulk liquid, but rather react in a thin layer just below the gas-liquid interface, with penetration depths on the order of 10s of nm.[107], [108]

As a result, optimizing the plasma-water interfacial area is thought to be a key design parameter for improving the decomposition performance of plasma-water reactors. The packed-bed reactor described in Section 4.1.2 was designed based on a geometric approach to maximizing this plasma-water contact area and is thus also considered a promising reactor configuration. Although this study does not fully elucidate the relative importance of each PFAS decomposition mechanism, it does provide insight into which reactor variables are related to improved PFAS removal percentage while also considering the practicality of each variable from an implementation standpoint.

### *4.1.1 Dielectric Barrier Discharge Plasma Jet Reactor*

The first reactor is the underwater DBD plasma jet based on the configuration and construction by Foster et al.[109] Early versions of the DBD plasma jet are described in Section 2.4.2 and were mostly operated in beakers to treat volumes ranging from 100 – 500 mL. The DBD plasma jet reactor investigated here consisted of a 1 L wide-mouth glass jar with a lid that was adapted to allow three individual DBD plasma jets to be mounted with a common central ground electrode feedthrough. The lid was fitted with an exhaust port through which evolved gases could escape. The port was also used as a conduit to pass a thermocouple probe for monitoring the water temperature.

The individual DBD plasma jets act as plasma applicators and each consisted of an 18-gauge tin-plated copper high-voltage wire centered coaxially within a quartz tube with 4 mm ID, 6.35 mm OD, and 150 mm length. A tin-plated copper wire coil wrapped around the outside of the quartz tube to serve as the grounded electrode. In this case, the quartz tube, along with the water that the tube is submerged in, act as the dielectric barriers preventing a thermal arc from forming. Compression fitting tees are attached to the top of each quartz tube to allow for the passage of feed gas and the connection to the high voltage electrode.

All three jets could be powered at once to increase the plasma contact area; however, it was found that with increasing input power, it was difficult to maintain the same intensity of discharge to each tube simultaneously. To minimize the uncertainty in the plasma contact area due to discharge competition between the jets, this study reports on single and dual plasma jet configurations. The dual jet configuration was found to be more stable than the triple jet with discharge intensity similar for each when powered by a single power supply. Regardless of the number of tubes operated, the total gas flow was constant at 35 ± 2 SCFH air. Gas was sent through unpowered tubes to facilitate mixing.

A schematic of the single jet configuration is shown in Figure 4.1a which could be powered by either the AC power supply with a 50:1 step-up transformer that will be described in Section 4.2.1, or with a ns-pulsed power supply that will be described in Section 4.2.2. An image of the DBD plasma jet reactor operating in single-jet mode under ns-pulsed excitation is shown in Figure 4.1b, where the two jets not being excited by the power supply are providing gas flow to promote fluid mixing within the reactor volume.

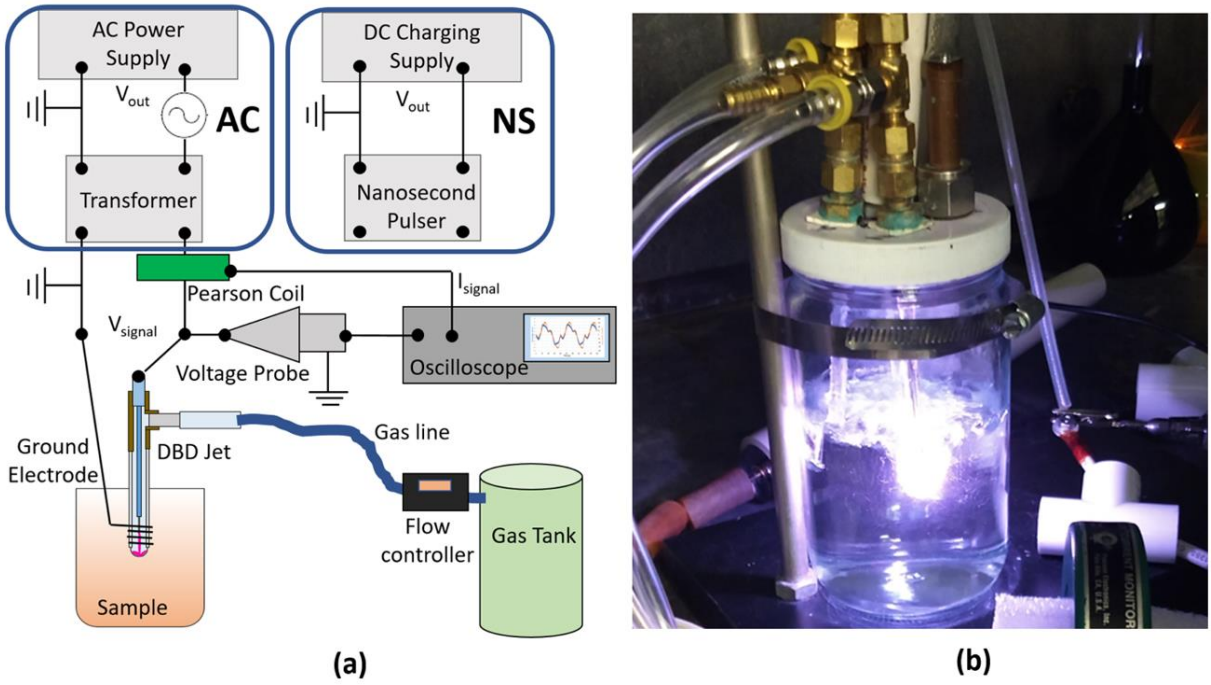


Figure 4.1 (a) Schematic of the DBD plasma jet reactor setup, capable of being powered by AC or ns-pulsed power supplies. (b) Image of the DBD plasma jet reactor operating in single-jet mode under ns-pulsed excitation.

### *4.1.2 Packed-bed Reactor with Water Dielectrics*

The second reactor investigated in this work was a DBD discharge with water dielectrics. Here the input water is delivered as a multitude of thin water jets symmetrically positioned about a centrally powered electrode, as can be seen in Figure 4a. Application of voltage to the central electrode leads to plasma formation between the interstitial spaces of the water jets as well as the propagation of an ionization wave or surface plasma on the water jet.[40] Because the water acts as a barrier to appreciable current conduction – either as an insulator in the case of deionized water or as a resistive layer as in the case of water with finite conductivity, the arrangement is essentially a barrier discharge.[110] The water jets prevent the discharge from transitioning into a spark or arc discharge.

The appeal of this arrangement is that it puts the liquid water in direct contact with high surface area to volume water streams. Since PFAS compounds are hydrophobic, this reactor arrangement assures plasma contact over a large surface area (associated with the water jets) and thereby circumvents the volume effect where treatment in the bulk would otherwise rely on the slow process of diffusion.

As can be seen in Figure 4b, contaminated liquid from the reservoir is circulated through the plasma reactor, which functions to separate the liquid into thin spatially dispersed jet streams using a "showerhead" type applicator and bring the resulting streams into direct contact with plasma so that the solution is batch processed, though the reactor can be operated in a flow-through or once-through mode as well. By separating the water into thin streams, the approach is effectively a quasi- in-volume treatment approach in that the reactivity occurs primarily at the water surfaces while diffusion allows for reactions throughout the volume of the water jets. This reactor is referred to as a packed-bed water reactor (PBR) owing to similarities between the water jets and the dielectric aggregate of a packed-bed reactor.

The water is recirculated through the plasma discharge region using an AC-2CP-MD magnetic drive pump (March Manufacturing, Inc., Glenview, IL, USA) that has a maximum flow of 5 gal/min, a maximum head of 13 ft, and a power of 0.025 HP. The flow rate was measured using a Digiten G1/2" Water Flow Hall Sensor (ShenZhen Huimai Technology co., Ltd., ShenZen City, China) with a flow rate range of 1 – 30 L/min, and was found to be 4.2±0.2 L/min for the system, with a total batch volume of 0.5 L. Separate tests were performed to determine the flow rate through the system. During plasma treatment experiments, the flow meter was disconnected from the LCD display and its power cable was disconnected to prevent the chance

of current passing through the water and reaching ground through the flow meter power cable, which could potentially distort the current-voltage waveforms.

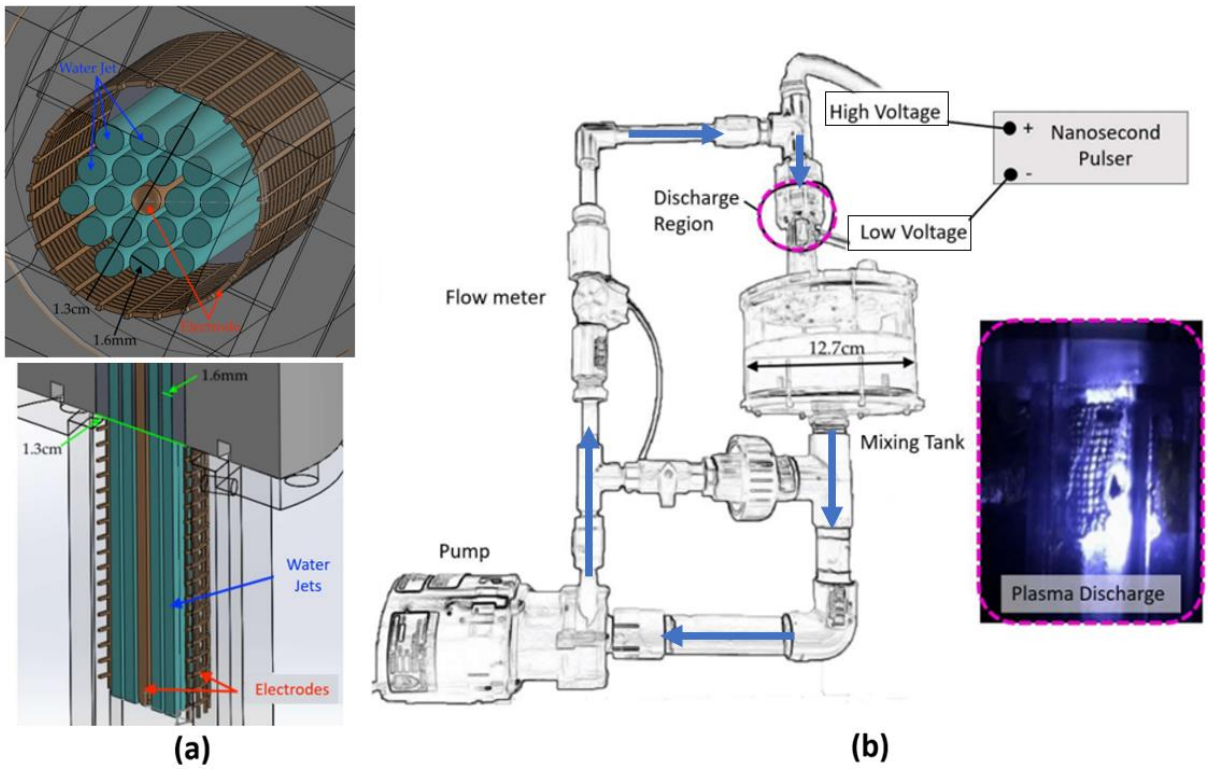


Figure 4.2 (a) Schematic depiction of barrier discharge with water dielectrics. The top drawing is a cross-section perpendicular to the flow of the water jets, and the bottom drawing is a cross-section parallel to the flow of the water jets. (b) Water circulation system with plasma discharge inset. The arrows indicate the direction of water flow.

## 4.2 Power Supplies

The two high-voltage sources were chosen to understand the role of localized heating. Plasma gas temperatures can reach over 2,000 K when excited with the low frequency AC voltage source, whereas the gas generally remains close to room temperature in the ns-pulsed plasma.[111] Gas heating is related to the pulse width and charge relaxation time. At longer pulse widths, such as those associated with the AC power source, the ionization avalanche can

build leading to greater heating and ultimately thermal runaway, owing to increased electron collisions with the background gas. The nanosecond discharge arrests avalanche build-up thus circumventing this ionization/thermal instability.

For the groundwater samples, the charge relaxation time is on the order of 1 to 10 ns, depending on the electrical conductivity of the water during treatment. The rise time of the ns-pulser is about 100 ns, while the rise time for the AC supply is about 10,000 ns. In this respect, the pulse rise time is long compared to the relaxation time, so current can build almost quasi arc-like since the liquid acts more like a conductor over these time scales. This effect can also be observed in ns-pulsed discharges in salty solutions.[49]

Since it has been shown that pyrolysis can be effective in the treatment of PFAS, the higher temperature plasma generated by the AC power source is of potential interest as an additional pathway leading to decomposition.[112] Generally speaking, owing to Arrhenius behavior of typical chemical reactions, the decomposition rate may also be higher at the elevation solution temperatures. The assumption therefore is that this higher temperature discharge may have some benefit over the cooler ns-pulsed discharges.

### *4.2.1 Alternating Current Power Supply*

The AC power supply used in this study was an Elgar model 501SL power supply (AMETEK, Inc., Berwyn, PA, USA) with a step-up transformer (SP-225 Plasma Technics, Inc., Racine, WI, USA). The Elgar model 501SL alone can generate AC signals up to 250 V at frequencies ranging from 50 – 5,000 Hz, while the step-up transformer could amplify the voltage to a maximum voltage of ±5 kV at an upper current limit of ±200 mA. At frequencies below 400 Hz, significant distortion to the applied sinusoidal signal occurs due to limitations of the step-up transformer. For this study, the AC frequency generated by the power supply was kept constant

at 5 kHz. Note that the Elgar power supply has one grounded lead and one powered lead, or hot lead, that carries the high-voltage or low-voltage relative to ground, as opposed to the ns-pulsed power supply described in the next section which is a floating power supply.

### *4.2.2 Nanosecond Pulsed Power Supply*

The ns-pulsed power supply used in this study was the Rapid Capacitor Charging (RCC) System NSP-5000 Series (Eagle Harbor Technologies, Inc., Seattle, WA, USA). This power supply can generate a maximum load voltage of 30 kV at a maximum pulse frequency of 30 kHz, and the maximum load capacitance is 200 pF. The voltage pulse width produced depends on the load capacitance and was found to generally fall within the range of 70 – 180 ns for the tests performed in this study.

The basic system diagram is shown in Figure 4.3. The RCC System is composed of three primary components: the DC charging supply, the nanosecond pulser (NSP), and the resistive output stage (ROS). The DC charging supply used in this setup is a Magna Power-TSA600-8/208 power supply (Magna Power Electronics, Inc., Flemington, NJ, USA), which has a maximum output voltage of 600 V DC and a maximum output power of 5 kW. This limits the maximum output power of the RCC System to 5 kW.

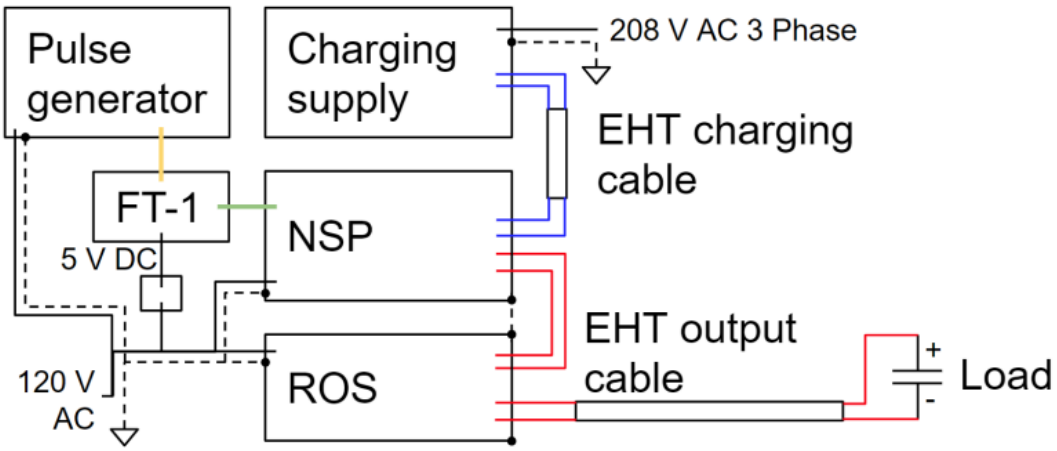


Figure 4.3 Basic system diagram for the Eagle Harbor Technologies Rapid Capacitor Charging System (NSP-5000).

The NSP component of the RCC system conditions the DC power supplied by the DC charging supply into ns-scale pulses and steps up the voltage significantly in the process. The output voltage from the RCC system that is supplied to the load is directly proportional to the voltage output from the DC charging supply, although the proportionality constant can vary somewhat depending on the load capacitance. Additionally, the output voltage measured across the load may be reduced when a plasma is generated, which is indeed intended in these studies. Thus, the voltage across the load must be monitored using high-voltage probes as discussed in Section 4.2.3.

The front panel of the NSP has switches to turn the power and voltage output on/off, as well as a switch to operate the pulser in internal or external mode. Internal mode means that the pulse repetition frequency is controlled by knobs on the front panel of the NSP. External mode allows for the NSP to be triggered remotely using the fiber-optic transmitter (FT-1 in Figure 4.3), which receives a 5 V DC signal from a pulse generator. This is useful for syncing the output voltage pulses to other equipment, such as a spectrometer, as will be done in Chapter 6.

The ROS discharges the load capacitor between each pulse, acting as a passive dump system for the user's load, but is not capable of dumping significant load energy during the short charging period (150 ns), so operating within the maximum allowable operating pulse frequency (30 kHz), DC charging voltage (600 V), and load capacitance (200 pF) is critical to preventing damage to the system and the user's load. In this study, the load is the plasma reactor – either the DBD plasma jet or the packed-bed reactor.

### *4.2.3 Voltage-Current Waveform Analysis*

Voltage and current diagnostics allow for calculation of the estimated power deposited into the plasma, and thus represent important measurements for assessing the energy efficiency of contaminant removal, in this case PFAS decomposition. In this work the voltage was measured using a P6015A high-voltage probe (Tektronix, Beaverton, OR, USA) which has an attenuation factor of 1000, a rise time of 4.0 ns, and a maximum input voltage of 20 kV. The discharge current was measured with a 6600 Pearson coil current monitor (Pearson Electronics, Inc., Palo Alto, CA, USA) which has a resolution of 0.1 V/A and an accuracy of ±1%. Waveforms were recorded and analyzed using a Tektronix MDO3024 oscilloscope (Tektronix, Beaverton, OR, USA) with a bandwidth of 200 MHz. Typical current and voltage waveforms are provided in Figure 4.4 for both the AC and ns-pulsed power supplies. Using the time dependence of the voltage, *V(t)*, and the current, *I(t)*, the average power was obtained using Equation (4.1):

$$P = \frac{1}{\tau} \times \int_0^{\tau_w} I(t) \times V(t) dt \tag{4.1}$$

Where $\tau$ is the reciprocal of the pulse frequency and $\tau_w$ is the pulse width.

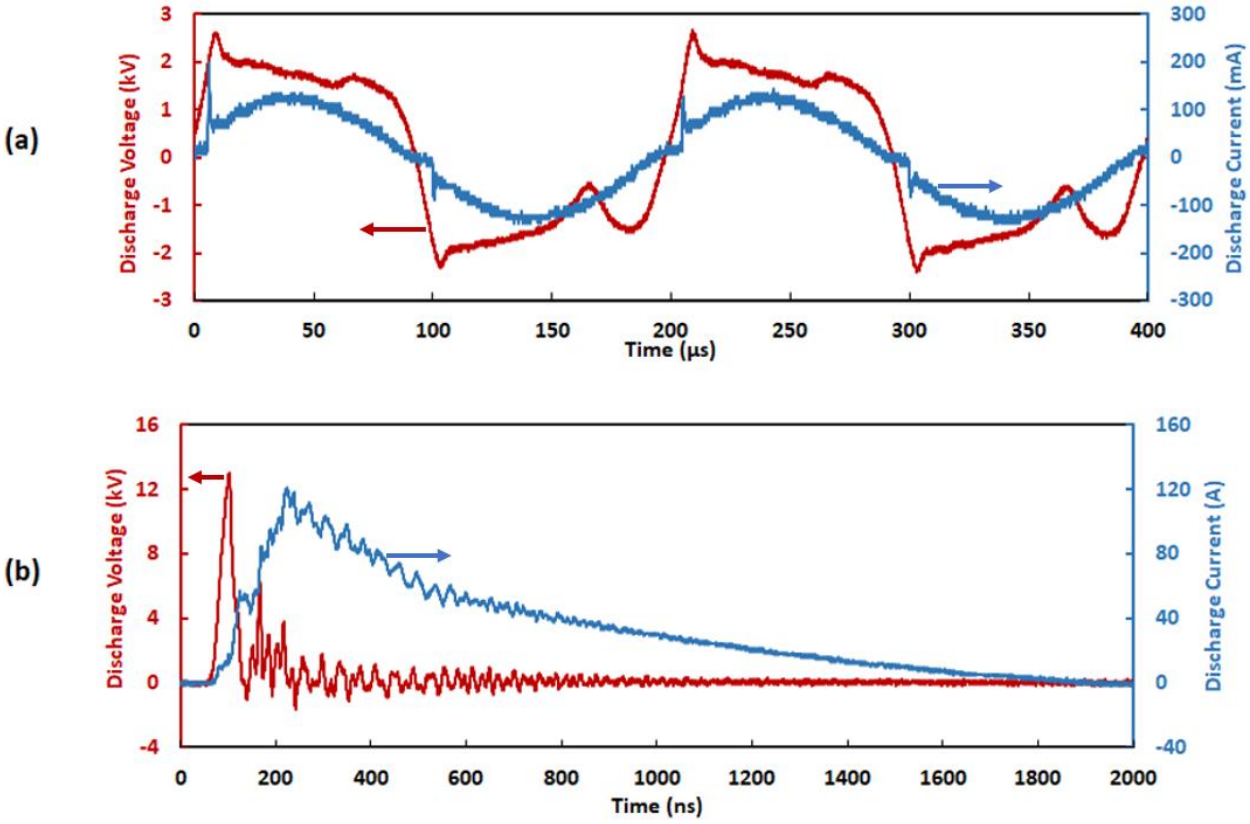


Figure 4.4 Typical voltage and current waveforms for (a) the low-frequency sinusoidal AC power supply operating at 5 kHz and (b) the ns-pulsed voltage source operating at 2 kHz.

### 4.3 Results and Discussion

A goal of this work was to explore the efficacy of the aforementioned plasma sources for decomposing PFAS contaminants. The water samples tested in this work were derived from two legacy sites containing heavily PFAS-contaminated groundwater at levels well above the regulatory limit. Site 2 had contamination levels ~100× that of Site 1. This water is currently being treated by conventional methods. For this work, untreated samples as extracted from the groundwater site used; that is, no pretreatment was carried out before plasma testing.

The concentrations of the contaminants were measured both at UM and at an independent chemical analysis laboratory. Both labs used the EPA Method 537.1 to determine concentration

using Liquid Chromatography – Tandem Mass Spectrometry (LC-MS/MS).[64] For each experimental run, 500 mL of the sample groundwater was treated. Post-test treated solution temperature, pH and conductivity were measured. To assess potential leaching of PFAS from the reactor itself, test runs with deionized water were carried out. The concentrations of PFOS and PFHxS in these sample runs were non-detectable, suggesting no measurable contamination is derived from the apparatus itself in these experiments.

The pre-test PFAS analysis of groundwater samples from Site 1 and Site 2 are provided in Table 4.1. The concentrations of 24 different PFAS compounds were quantified in duplicate using an independent test laboratory and an in-house analytical mass spectrometer. This was done to validate measurements made in-house at the University of Michigan. The results were found to be in general agreement between both labs, with PFOS and PFHxS being the most prevalent PFAS compounds found at both sites. Although the concentrations of PFAS found in the groundwater at Site 2 is much higher than those found in Site 1, the groundwaters from Site 1 and Site 2 are both heavily contaminated compared to regulatory guidelines. For reference, the Michigan Department of Environment, Great Lakes, and Energy has set maximum concentration limits for PFHxS and PFOS at 51 ng/L and 16 ng/L, respectively.[20] It should be emphasized that the extracted groundwater samples were not modified, but rather collected from actual contaminated sites, thus demonstrating treatment of representative water matrices.

Table 4.1 PFAS concentrations (ppt) in the raw groundwater samples, measured in-house at University of Michigan (UM) and by an independent test laboratory. Boldface denotes the two most abundant compounds measured in the water samples. [a] Independent diluted Site 1 samples 2× and UM did not dilute Site 1 samples, with reporting limits of ±10 and ±1 ppt, respectively. [b] Independent diluted Site 2 samples 20× and UM diluted Site 2 samples 200×, with reporting limits of ±100 and ±200 ppt respectively. [c] NM = Not measured, UM did not have standard curves for PFBA an PFPeA.

| | Site 1 concentration (ppt) | | Site 2 concentration (ppt) | |
|---|---|---|---|---|
| Compound | UM[a] | Independent[a] | UM[b] | Independent[b] |
| PFBA | NM[c] | 54 | NM | <100 |
| PFPeA | NM | 91 | NM | 280 |
| PFHxA | 40 | 74 | <200 | 1500 |
| PFBS | 46 | 12 | 370 | 220 |
| 4:2FTS | <1 | <10 | <200 | <100 |
| PFHpA | 22 | 18 | <200 | 250 |
| PFPeS | 51 | 18 | 630 | 450 |
| PFOA | 26 | 30 | 560 | 690 |
| **PFHxS** | **240** | **180** | **16 000** | **10 000** |
| 6:2FTS | 11 | 46 | <200 | <100 |
| PFNA | 84 | 52 | <200 | <100 |
| PFHpS | 8 | <10 | 620 | 470 |
| FOSA | <1 | <10 | <200 | <100 |
| PFDA | <1 | <10 | <200 | <100 |
| **PFOS** | **270** | **330** | **33 000** | **43 000** |
| 8:2FTS | <1 | <10 | <200 | <100 |
| PFUdA | <1 | <10 | <200 | <100 |
| PFNS | <1 | <10 | <200 | <100 |
| N-MeFOSAA | <1 | <10 | <200 | <100 |
| N-EtFOSAA | <1 | <10 | 430 | <100 |
| PFDoA | <1 | <10 | <200 | <100 |
| PFDS | <1 | <10 | <200 | <100 |
| PFTrDA | <1 | <10 | <200 | <100 |
| PFTeDA | <1 | <10 | <200 | <100 |

Water samples from each site were processed by the plasma reactors and the concentrations of PFAS were quantified as described in Section 3.3. Results from the Site 1

PFAS degradation experiments are listed in Table 4.2. Since PFOS and PFHxS were identified to have the highest initial concentrations in the groundwater samples, these two compounds were used to assess the contaminant removal. Four experiments were performed for the Site 1 groundwater using the single-jet DBD plasma jet reactor operating for half an hour. The feed gas was varied between air and argon, and two different power supplies were tested with each feed gas. PFOS removal percentage was slightly greater for argon compared to air, with an additional 15% removal using the AC power source and an additional 11% removal using the ns-pulsed source.

The difference between applying AC power versus ns-pulsed was even less, as the AC source yielded an additional 8% for argon feed gas and 4% for air, although considering the uncertainty, these differences may be negligible. The negative percent removal values observed for PFHxS indicate an increase in concentration. This result suggests that the longer chain PFOS is being decomposed into smaller chain PFAS, including PFHxS in agreement with Singh et al.[113] In this regard, additional treatment time is necessary to fully process these smaller chain compounds.

Table 4.2 PFOS and PFHxS removal data for Site 1 experiments using the single jet DBD-PJ reactor. [a] Initial concentrations of PFOS and PFHxS were 255 and 205 ppt, respectively. [b] Negative values indicate an increase in concentration.

| | | | | PFOS[a] | | PFHxS[a] | |
|---|---|---|---|---|---|---|---|
| Reactor | Power source | Feed gas | Reaction time (h) | ppt | Removal %[b] | ppt | Removal %[b] |
| Single jet | Alternating current | Air | 0.5 | 200 | 22 | 260 | −27 |
| Single jet | Alternating current | Argon | 0.5 | 160 | 37 | 270 | −32 |
| Single jet | Nanosecond pulse | Air | 0.5 | 210 | 18 | 310 | −51 |
| Single jet | Nanosecond pulse | Argon | 0.5 | 180 | 29 | 330 | −61 |

The same set of experiments were conducted for the Site 2 groundwater, along with two tests with the dual-jet reactor, and one test with the packed-bed reactor. The results are shown in Table 4.3, and the same trends can be seen as in Table 4.2 regarding the effect of feed gas and power source for the single-jet experiments. Using argon as the feed gas provides a slight increase in percent removal of PFOS over air, as does using the AC power source compared to the ns-pulsed source. The increase in performance with the AC source is attributed to the higher overall gas temperature which can lead to thermal decomposition in contrast to the reduced gas temperature associated with ns-pulsed operation; however, the AC power source is also associated with higher deposited power and associated energy costs. The advantage of argon over air is most likely due to the increased plasma density owing to the lack of electron loss mechanisms such as attachment and inelastic losses that would otherwise be incurred in air via the excitation of vibro-rotational modes, thus leading to higher plasma densities in argon plasmas.

Table 4.3 PFOS and PFHxS removal data for Site 2 experiments. [a] Initial concentrations of PFOS and PFHxS were 33,000 and 16,500 ppt, respectively. [b] Negative values indicate an increase in concentration.

| | | | | PFOS[a] | | PFHxS[a] | |
|---|---|---|---|---|---|---|---|
| Reactor | Power source | Feed gas | Reaction time (h) | ppt | Removal %[b] | ppt | Removal %[b] |
| Single jet | Alternating current | Air | 0.5 | 26 000 | 21 | 14 000 | 15 |
| Single jet | Alternating current | Argon | 0.5 | 22 000 | 33 | 13 000 | 21 |
| Single jet | Nanosecond pulse | Air | 0.5 | 27 000 | 18 | 15 000 | 9 |
| Single jet | Nanosecond pulse | Argon | 0.5 | 26 000 | 21 | 15 000 | 9 |
| Dual jet | Nanosecond pulse | Argon | 0.5 | 18 000 | 45 | 18 000 | −9 |
| Dual jet | Nanosecond pulse | Argon | 2 | 5 900 | 82 | 7 200 | 56 |
| Packed bed | Nanosecond pulse | Air | 1.5 | 1 200 | 96 | 9 200 | 44 |

The dual-jet experiments were both performed with the ns-pulsed power source and argon as the feed gas. When comparing the half hour treatment time to the single-jet ns-pulsed argon test, the dual-jet doubles the percent removal of PFOS. This is attributed to the

approximately doubled plasma contact area (surface area for electron reduction activity) that the dual-jet reactor provides. When the reaction time for the dual-jet is increased to two hours, the reduction is consistent with exponential decay with a decay constant of 0.85 $hr^{-1}$ ($R^2 = 0.97$), although more data points are needed to properly evaluate the decay behavior.

Finally, the packed-bed reactor demonstrated 96% removal of PFOS for a 1.5-hour treatment time with water circulating at a flow rate of 4.3 ± 0.2 L/min, while the dual-jet achieved 82% removal over a 2-hour treatment time. In both cases, significant decomposition of PFHxS was observed suggesting serial degradation proceeding from the precursor to the daughter byproducts. Although PFHxS may increase in the early stages of treatment, it is ultimately decomposed given sufficient treatment time. It should be noted that the average power and treatment time for the packed bed reactor was less than the dual-jet reactor operating on argon (70 W for 1.5 hours vs. 90 W for 2 hours, respectively), suggesting greater energy efficiency for the packed-bed reactor. This greater efficiency is attributed to the higher plasma-liquid contact area which occurs along the entire length of the water stream in contrast to the localized plasma attachments of the jets. In either case, it is clear at least at these power levels that the level of contaminant removal is dependent on treatment time. These plasma reactors should be capable of breaking down most, if not all the remaining PFAS, but the energy requirements to do so must be investigated.

Notably, despite Site 2 containing significantly higher initial concentrations of PFOS, the percent removal achieved is roughly the same for both sites' waters. For example, the single-jet with ns-pulsed argon yielded 18% removal for both Site 1 and Site 2 waters. In this case, 45 ng/L were removed from the Site 1 groundwater, whereas 6,000 ng/L was removed from Site 2 groundwater. Since the volume in these experiments was 500 mL, that means about 23 ng PFOS

was removed at Site 1 compared to 3,000 ng PFOS at Site 2, while approximately the same energy was spent in the treatment processes. Therefore, when considering the mass removal efficiency, these plasma reactors are more efficient at treating high concentration PFAS waters because they can remove more mass of PFAS for a given energy input. This finding could play an important role when implementing these plasma reactors into a practical treatment train for decomposing PFAS in contaminated waters.

### 4.4 Conclusions

Water samples with PFAS contamination were collected from two legacy sites and treated with plasma reactors. The percent removal was evaluated by quantifying the concentrations of PFAS before and after treatment, and the impacts of certain reactor control variables were assessed. There was little difference in PFOS removal percentage between the AC and ns-pulse power supplies, although the ns-pulse power supply deposits less power into the discharge by about a factor of 10 in the single jet experiments. In this sense, the ns-pulse power source may be considered more energy efficient, but it is worth noting that the AC power source can achieve similar percent removal of PFOS for the same treatment time and may be a more cost-effective power source for practical use. Regarding the feed gas, argon achieved slightly greater removal percentages of PFOS compared to air in the case of the plasma jets. Still, the fact that ambient air can be used in these reactors to remove significant amounts of PFAS is an important result, as it eliminates the need to transport and store argon as a consumable in the treatment process.

While the type of power source and feed gas had relatively minor impacts on the percent removal of PFOS, the plasma-liquid contact area was shown to be a significant variable. The dual jet configuration achieved approximately double the removal percentage of a single jet,

commensurate with the additional contact area for solvated electron mediated reduction processes. The packed-bed reactor further enhanced the contact area and achieved even greater PFOS removal percentage than the dual-jet reactor. Lastly, similar removal percentages were achieved for both waters, despite the higher starting PFAS concentrations in the Site 2 water, indicating an increase in mass removal efficiency when treating waters with high initial concentrations of PFAS with these plasma reactors. With this insight, plasma-induced decomposition of PFAS may be more effectively implemented into a practical treatment train in which the PFAS is first concentrated. It should also be noted that there are still possible unknown water quality influences that should be explored in future work, which might explain the improved degradation of PFHxS in the Site 2 samples.

## Chapter 5 Time-resolved PFAS Decomposition: Batch Kinetics

One important contribution of this thesis is to propose a new architecture for treating water in a flow-through configuration. Ideally, the effectiveness of the treatment at a minimum should faithfully recover the treatment efficacy observed in the batch process. This can be achieved if the system can be configured in a manner such that batch-mode kinetics are preserved; therefore, a comprehensive understanding of the batch-mode kinetics is needed. This chapter seeks to characterize the batch-mode kinetics of PFAS decomposition in groundwater to inform the scale-up approach to a continuous flow, or once-through, system.

To investigate the batch-mode kinetics, the concentrations of PFAS are measured as a function of treatment time. The resulting curves of concentration vs. time yields insight into the decomposition kinetics and should help answer some key questions. For example, what is the empirical order of the rate equation for PFAS removal? Additionally, how much treatment time is required to reduce these PFAS compounds to below EPA regulatory limits, and what are the energy costs to do so?

This chapter begins with a time-resolved high concentration PFOA decomposition test to provide some insight into the decomposition kinetics of PFOA in the packed-bed reactor and an initial energy efficiency estimate for PFOA decomposition (Section 5.1). Next, the DBD plasma jet reactor is revisited to time-resolve the PFAS decomposition in Site 1 groundwater (Section 5.2). After replacing most of the packed-bed reactor components that were exposed to the high concentration PFOA test, and thoroughly cleaning the remaining components, the Site 1

groundwater is treated with the goal of reducing the PFAS concentrations to below the Michigan maximum contaminate levels (Section 5.3) The goal was achieved for all PFAS except for PFOA, due to a contamination source within the reactor. Systematically eliminating and replacing reactor subcomponents revealed the source of the PFOA contamination to be a 3-D printed part used as the "showerhead" nozzle in the packed-bed reactor (Section 5.4). The challenges of this process highlight the ubiquity of PFOA, and follow-up tests were subsequently conducted to investigate PFOA decomposition in a contamination-free reactor.

### 5.1 Packed-bed Reactor High Concentration PFOA Decomposition

In addition to the groundwater sample tests, a spiked test was also carried out. Here, the goal was to assess the time evolution of PFAS decay. To investigate the decay behavior, deionized water samples were spiked with PFOA to achieve a concentration of approximately 5.7 ppm. Indeed, and lamentably, there are documented cases where the PFOA concentration in groundwaters has been even higher than this alarming value, and in this regard an initial PFOA concentration of 5.7 ppm still represents a relevant test point. Regardless, the high concentration also affords one the opportunity to study the effects of intermediates which could potentially serve as scavengers. PFOA was treated with the packed-bed reactor and the residual PFOA concentrations were measured as a function of treatment time. The concentration was reduced by 92% after a 1-hour treatment time at a power level of approximately 25 W with air as the working gas.

Interestingly, the data seem to show two types of rate behavior as can be seen in Figure 5.1. At early times there is a steep drop off in PFOA concentration (60%) followed by a more gradual decay. Compared to the relatively dilute solutions discussed previously in the µg/L and ng/L ranges, here the role of interfering intermediates may play a larger role in scavenging

reactive species such as solvated electrons and oxidative species. Future work should involve a full analysis of intermediates formed and their associated scavenging capacity.

For comparison, the degradation of PFOA via a number of advanced oxidation processes is shown in Figure 5.2 by Trojanowicz et al. which shows PFOA percent removal vs. treatment time at a starting concentration of 10 ppm.[114] Note the substantial differences in treatment time with the AOP methods requiring over triple the treatment time for comparable percent removal of PFOA using ozonation with simultaneous $TiO_2$-based photocatalytic decomposition compared to the packed-bed plasma treatment. With ozonation alone, at an ozone dosage of 25 mg/hr, only about 0.5% of the initial PFOA was decomposed after the 4 hr treatment time. While advanced oxidation is driven in the packed-bed reactor as well, the differences in removal over time suggests that plasma effects such as the solvation of the free electrons can lead to significant increases in the removal rate of PFOA.

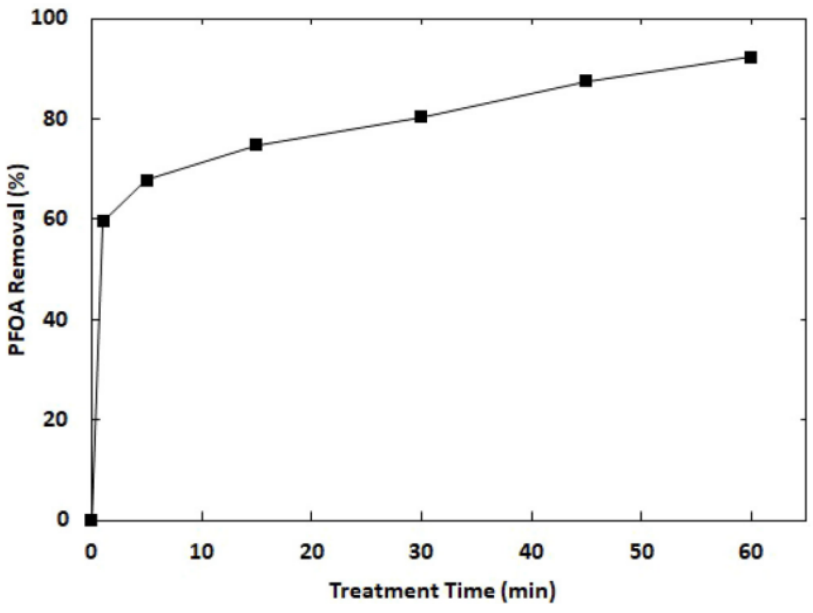


Figure 5.1 PFOA removal (%) vs. treatment time using the packed-bed reactor with the ns-pulsed power supply and ambient air as the working gas. The initial concentration of PFOA is 5.7 ppm.

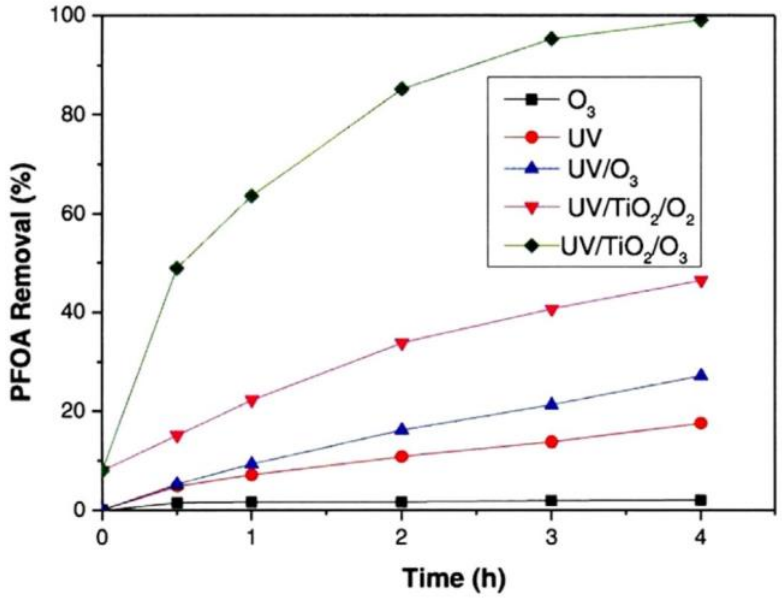


Figure 5.2 Advanced oxidation of PFOA from Trojanowicz et al.[114]

Water treatment systems such as advanced oxidation treatment trains featuring for example, photolysis via UV, UV-Ozone, or UV-hydrogen peroxide utilize predominantly electrical power to drive decomposition. A figure of merit that describes the decomposition efficiency of these systems is the Electrical Energy per Order.[115] The use of this parameter allows for direct comparison between this work and other PFAS studies featuring advanced reduction or advanced oxidation driven by electrical means including plasma methods.

The approach is particularly appropriate in assessing the power cost of treating dilute contaminant streams such as the ones explored in this work where the decomposition can be modeled as an effective first-order reaction. In short, the parameter is a measure of the power required to reduce the contaminant level one order of magnitude. The Electrical Energy per Order (EE/O, kWh/m$^3$) was calculated for the removal of PFOA based on the data in Figure 5.1 using Equation (5.1).

$$EE/O = \frac{P \times t \times 1000}{V \times 60 \times \log\left(\frac{C_i}{C_f}\right)} \quad (5.1)$$

Where $P$ in this case is the power discharged into the plasma (kW) calculated using Equation (4.1), $t$ is the treatment time (min), $V$ is the treated volume of water (L), and $C_i$ and $C_f$ are the initial and final pollutant concentrations, respectively. In this case, the concentrations refer to the amount of PFOA in the water (ppt). Based on the waveform analysis, a treated volume of 0.5 L, and the 92.3% removal of PFOA over the hour-long treatment time, the EE/O was estimated to be approximately 45 kWh/m$^3$. This value is of similar magnitude as those reported by Thagard and colleagues using the enhanced contact non-thermal reactor discussed in Section 2.4.3.[23], [24]

The values of EE/O for the removal of PFOS from the groundwater samples treated with the nanosecond pulse power supply (in Chapter 4) ranged from 93 to 196 kWh/m$^3$. These EE/O values for groundwater are higher than those for the deionized water spiked with PFOA likely due to the presence of multiple co-contaminants, normally occurring organic matter, and other scavengers of plasma-derived reactive species present in the groundwaters. PFOA and PFOS are also chemically different and may not have the same susceptibility to plasma treatment. Furthermore, none of the tests presented here were optimized in terms of EE/O, so far. Future work should involve power matching as well as the development of a comparative figure of merit which will include considerations such as plasma density and gas temperature, which are measures of how well power is being transferred to the plasma in the form of charged species production and losses to the gas via heating.

One of the challenges with calculating EE/O for plasma-based systems is that the waveforms can be difficult to interpret due to reflected power causing nonphysical voltage peaks

and oscillations. This uncertainty in the way the power supply quenches the applied pulse leads to some uncertainty in the discharge power calculation, and thus the EE/O estimation. Further studies are needed to account for these nonphysical waveform structures and to achieve more accurate estimates of the discharge power and EE/O value of the plasma treatment process.

### 5.2 Plasma Jet Groundwater Decomposition Kinetics

After running the high concentration PFOA decomposition kinetics test with the packed-bed reactor, it was discovered that there was a source of PFOA contamination that appeared to be derived from the reactor itself. Originally, it was not clear what the source of this contamination was; however, some of the possible sources included the Teflon (polytetrafluorethylene) thread seal tape used to seal the threaded plumbing connections, as well as residual PFOA stuck to the interior walls of the reactor from the previous high concentration test. Eventually, it was discovered that the main source of PFOA contamination was a 3-D printed component used for the "showerhead" nozzle which was made of an acrylic-based photopolymer; however, it took several tests to identify this component as the root cause of the contamination. These tests are described in Section 5.4.

While the packed-bed reactor was being re-built and tested to identify the source of PFOA contamination, the DBD plasma jet reactor was used to treat groundwater from Site 1 (see Table 4.1). The experimental set-up is described in Section 4.1.1, and the nanosecond pulse power supply (described in Section 4.2.2) is used to generate the plasma with air as the feed gas to the jets. The DC charging voltage was set to 450 V and the pulse repetition frequency was 2 kHz for the experiment presented in this section. The total air flow rate through the quartz tubes was 35 ± 2 SCFH air, and the reactor was operated in dual-jet mode.

Prior to treating the groundwater, the electrodes and quartz tubes were replaced to mitigate cross-contamination from the previous experiments. To test that there was not residual contamination in the DBD jet reactor, deionized water was treated for 30 min and 45 min using the DBD plasma jet operating conditions described above. These samples were analyzed by LC-MS/MS and all PFAS compounds tested were below the detection limits of the analysis, indicating that the DBD jet reactor was ready for groundwater testing.

Site 1 groundwater (500 mL) was treated using the DBD plasma jet with an average power of 93 ± 13 W (46 ± 7 mJ/pulse) for a total of 120 min. The temperature was monitored using a Fluke 87V true RMS multimeter with a type-K thermocouple (Fluke Corporation), and the reactor jar was placed in an ice bath approximately every 10 min to maintain the water temperature between approximately 20 and 30 °C.

Samples were collected throughout treatment to time-resolve the PFAS decomposition and gain insights into the batch-kinetics. The samples were analyzed for PFAS concentrations by LC-MS/MS, and the results are provided in Table 5.1 for perfluoroalkyl sulfonic acids (PFSAs) and Table 5.2 for perfluoroalkyl carboxylic acids (PFCAs). The number of carbons for each substance is listed as well as a comment summarizing the concentration behavior over time.

Table 5.1 Perfluoroalkyl sulfonic acid (PFSA) concentrations vs. treatment time for the DBD plasma jet reactor treatment of Site 1 groundwater. The water temperature was maintained between 20 and 30 °C. The uncertainty for these concentrations is estimated at ±10%. The maximum concentration in each column is denoted by boldface.

| Run Time (min) | [PFOS] ppt | [L-PFHpS] ppt | [PFHxS] ppt | [L-PFPeS] ppt | [PFBS] ppt |
|---|---|---|---|---|---|
| 0 | **175** | **8** | 212 | 30 | 44 |
| 2 | 147 | 7 | 225 | 29 | 41 |
| 5 | 148 | 7 | 208 | 30 | 44 |
| 10 | 118 | 7 | 227 | 34 | 53 |
| 20 | 78 | 6 | 233 | 36 | 59 |
| 30 | 72 | 7 | 253 | 40 | 61 |
| 40 | 76 | 6 | 237 | 39 | 64 |
| 50 | 51 | 5 | 230 | 41 | 64 |
| 60 | 47 | 5 | 228 | 43 | 73 |
| 90 | 31 | 4 | **270** | **51** | **84** |
| 120 | 25 | 2 | 174 | 42 | 83 |
| # carbons | 8 carbons | 7 carbons | 6 carbons | 5 carbons | 4 carbons |
| Comments | rapid decrease | gradual decrease | slight increase then decrease | slight increase then decrease | gradual increase |

Table 5.2 Perfluoroalkyl carboxylic acid (PFCA) concentrations vs. treatment time for the DBD plasma jet reactor treatment of Site 1 groundwater. The water temperature was maintained between 20 and 30 °C. The uncertainty for these concentrations is estimated at ±10%. The maximum concentration in each column is denoted by boldface.

| Run Time (min) | [PFNA] ppt | [PFOA] ppt | [L-PFHpA] ppt | [PFHxA] ppt | [PFPeA] ppt |
|---|---|---|---|---|---|
| 0 | **75** | 24 | 17 | 139 | 276 |
| 2 | 67 | 39 | 17 | 119 | 262 |
| 5 | 68 | 40 | 17 | 127 | 258 |
| 10 | 54 | 60 | 21 | 160 | 292 |
| 20 | 39 | 109 | 24 | 162 | 274 |
| 30 | 35 | 114 | 25 | 175 | 281 |
| 40 | 30 | **130** | 27 | 169 | 263 |
| 50 | 23 | 126 | 28 | 173 | 253 |
| 60 | 19 | 118 | 30 | 195 | 277 |
| 90 | 10 | 79 | **38** | **224** | **437** |
| 120 | 12 | 88 | 33 | 194 | 380 |
| # carbons | 9 carbons | 8 carbons | 7 carbons | 6 carbons | 5 carbons |
| Comments | gradual decrease | increase then decrease | gradual increase | gradual increase | delayed increase |

As can be seen from the tables, only the PFAS with the longest carbon chains show a significant decrease over time, namely PFOS (the 8 carbon PFSA) and PFNA (the 9 carbon PFCA). The other substances tend to show some level of increase before eventually decreasing, sometimes only decreasing by the final sampling time (120 min). This behavior is thought to be a result of larger chain PFAS decomposing to form shorter chain PFAS as by-products. Indeed, this behavior was observed in Section 4.3 (as negative percent removals of PFHxS), and has also been reported by Holsen et al. and Sales et al.[56], [113] Additionally, Singh et al. reported the trend that the concentrations of PFAS with fewer carbons (shorter chains) increased at early treatment times before decreasing with further treatment, suggesting a stepwise degradation in which larger chain PFAS can produce shorter chains in the decomposition process, with PFOA being the first byproduct of PFOS decomposition.[116] The data indicate that longer treatment times are necessary to significantly remove the shorter chain PFAS.

The concurrent decomposition and generation as by-products of longer chain PFAS decomposition makes analyzing the kinetics of the shorter chain substances complicated based on the data from this experiment. However, decomposition of the longest chain PFAS (PFOS and PFNA in this this groundwater) can by approximated by first-order decay.

The PFOS concentration vs. treatment time is plotted in Figure 5.3a. Since PFOS is the longest chain PFSA detected in the Site 1 groundwater, it does not appear to be produced during the treatment, only decomposed. In this case, the concentration vs. treatment time can be empirically approximated by first-order decomposition kinetics as expressed in Equation (5.2).

$$\frac{C}{C_0} = e^{-kt} \tag{5.2}$$

Where $C_0$ is the initial concentration of a substance, $C$ is the concentration at time $t$, and $k$ is the first-order rate constant. When plotted as the natural logarithm of $C/C_0$ vs. $t$, the slope of

the line is equal to *k*, as seen in Figure 5.3b. This is a useful check to gauge how well the data corresponds to first-order kinetics. In this case, the data points do not fall exactly on the trendline but do show a trend towards first-order decay behavior. Here, for PFOS, the first-order rate constant is estimated to be 0.016 $min^{-1}$.

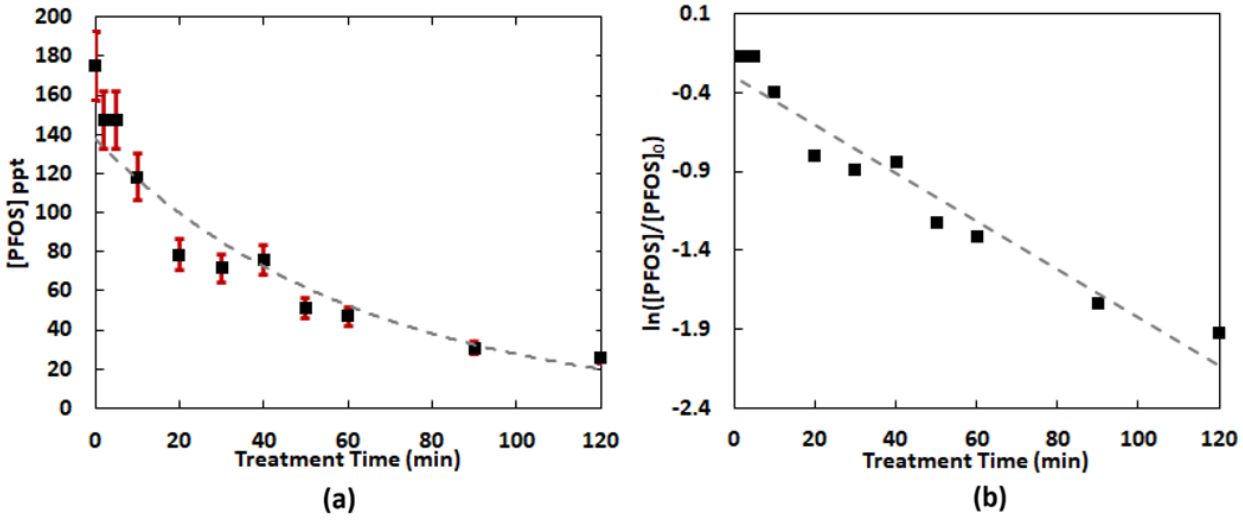


Figure 5.3 (a) PFOS concentration and (b) $\ln([PFOS]/[PFOS]_0)$ vs. treatment time with exponential decay trendlines (dashed gray lines).

Similarly, the PFNA concentration vs. treatment time is plotted in Figure 5.4a, and the natural logarithm of $[PFNA]/[PFNA]_0$ vs. treatment time is plotted in Figure 5.4b. Again, the data points deviate some from the exponential trendline, but appear to approximately follow first-order decay behavior with an estimated first-order rate constant of 0.017 $min^{-1}$ at a water temperature of 20 ± 1 °C. In this case, the observed first-order decay constants for PFOS and PFNA are remarkably similar.

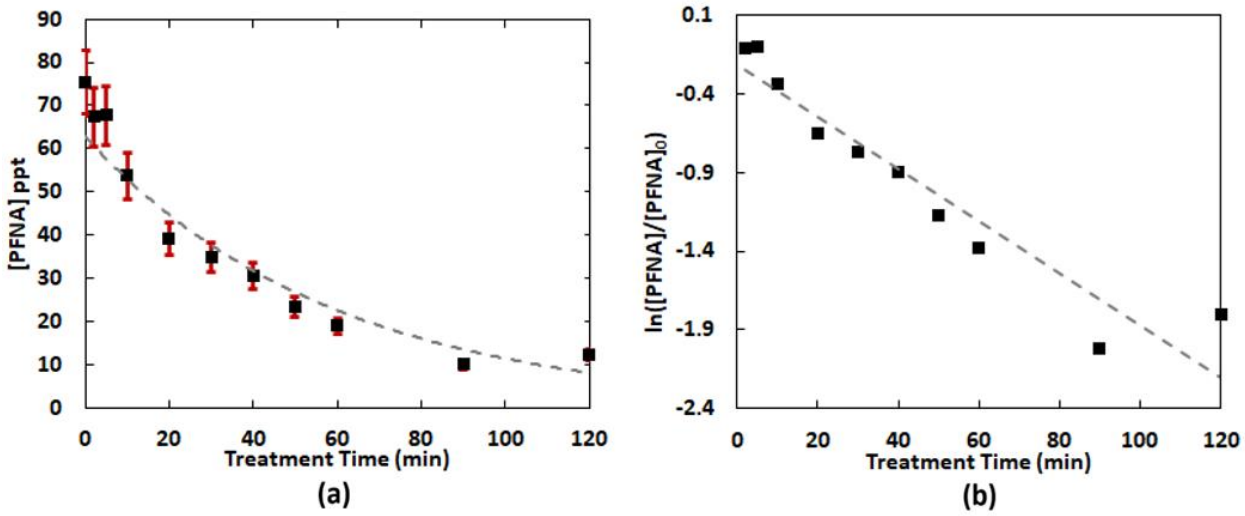


Figure 5.4 (a) PFNA concentration and (b) ln([PFNA]/[PFNA]$_0$) vs. treatment time with exponential decay trendlines (dashed gray lines).

It should be emphasized that this approximate exponential decay behavior observed for PFOS and PFNA does not necessarily indicate that the decomposition is governed by first-order reaction kinetics. At this point, it is simply a convenient way of empirically modelling the decay behavior and will be used to inform the scale-up analysis discussed in Chapter 7. Still, the production of short chain PFAS as by-products of longer chain PFAS decomposition presents an issue that must be addressed. The next section investigates this issue by treating the groundwater for a longer duration.

### 5.3 Packed-bed Reactor Long Duration Groundwater Treatment

Since the high concentration PFOA decomposition experiment presented in Section 5.1, the packed-bed reactor has been re-built to mitigate cross-contamination between the high concentration test and this relatively low concentration test using Site 1 groundwater. All subcomponents of the reactor were either been replaced or thoroughly cleaned. However, it will be discovered that there remained a source of PFOA contamination within the reactor that was

not related to the previous high concentration PFOA decomposition experiment, which will be discussed in Section 5.4.

For now, the goal of this long duration treatment is to decompose PFAS to below the maximum contaminant levels (MCLs) set by the Michigan Department of Environment, Great Lakes, and Energy (EGLE). These MCLs are summarized in Table 5.3 and include limits for PFNA, PFOA, PFOS, PFHxS, PFBS, and PFHxA. A MCL has also been established in Michigan for hexafluoropropylene oxide-dimer acid (HFPO-DA or GenX) at 370 ppt; however, this compound is not included in the EPA method development analyte list used for the LC-MS/MS analysis of PFAS concentrations, and thus was not quantified in this experiment.

Table 5.3 State of Michigan MCLs for six specific PFAS.

| [PFNA] ppt | [PFOA] ppt | [PFOS] ppt | [PFHxS] ppt | [PFBS] ppt | [PFHxA] ppt |
|---|---|---|---|---|---|
| 6 | 8 | 16 | 51 | 420 | 400,000 |

The packed-bed reactor described in Section 4.1.2 along with the nanosecond pulse power supply (from Section 4.2.2) is used to treat Site 1 groundwater. For this test, the water temperature is maintained within the range of 19 to 21 °C using an industrial chiller (Model CW-5200, OMTech Laser, Anaheim, CA, USA) connected to a copper cooling coil placed in the reactor's reservoir (i.e., mixing tank). Since this is a batch reactor, over time the reservoir temperature increases which may affect the chemical kinetics. By controlling the temperature of the reservoir, the temperature dependent reaction rate effects of elevated water temperatures can be mitigated. The PFAS decomposition is discussed in Section 5.3.1, followed by the water pH and electrical conductivity evolution throughout the treatment in Section 5.3.2. Lastly, the discharge voltage, current, and power is discussed in Section 5.3.3.

### *5.3.1 PFAS Decomposition*

Site 1 groundwater (500 mL) was treated with the packed-bed reactor excited by high-voltage nanosecond pulses for 7 hr at an average discharge power of 134 ± 14 W (67 ± 7 mJ/pulse). The DC charging voltage was set to 450 V with a pulse repetition frequency of 2 kHz, consistent with other tests presented in this thesis. The water was circulated through the reactor at a flow rate of 4.3 ± 0.2 L/min and maintained at a temperature of 20 ± 1 °C.

The concentration of PFOS decreased from its initial value of 165 ± 18 ppt with an observed first-order rate constant of 0.04 $min^{-1}$, shown in Figure 5.5a, and was removed to below the Michigan (MI) MCL within the first 1.5 hr of treatment. The natural logarithm of $[PFOS]/[PFOS]_0$ is shown in Figure 5.5b, suggesting that the decomposition is reasonably well approximated by first-order decay. After 3 hr of treatment, the PFOS concentration was near the detection limits of the LC-MS/MS analysis. Thus, the exponential trendline from 3 to 7 hr is somewhat arbitrary, in this case. Regardless, the calculated first-order rate constant of 0.04 $min^{-1}$ provides a reasonable estimate for the decay behavior at the early treatment times. One constraint in carrying out these tests is the relatively high cost of sample analysis on the LC-MS/MS system (approximately 350 USD/sample). Taking more data points in the first 1.5 hr of treatment would be recommended to better evaluate the PFOS decomposition kinetics.

The EE/O for PFOS decomposition in this experiment is estimated at 235 ± 25 kWh/$m^3$, compared to a value of 445 ± 65 kWh/$m^3$ in the DBD plasma jet decomposition test presented in Section 5.2. These values for EE/O may seem high, but they are still more competitive than most of the competing technologies, including persulfate, photochemical oxidation, sonolytic, sonochemical, and electrochemical processes (see Section 1.3). These tests were carried out to reduce PFAS concentrations which were already starting at trace amounts. The plasma approach

is most efficient when processing concentrated samples, as discussed earlier. Furthermore, the plasma treatments presented here were done using real groundwaters containing a host of PFAS, co-contaminants, and scavengers, while most research presents EE/O values for pristine waters spiked with PFOA, PFOS, or both. The treatment process has not yet been optimized for energy efficiency, so these initial reported EE/O values for plasma-driven PFAS decomposition may be significantly reduced, particularly if a concentration stage is added prior to the plasma treatment.

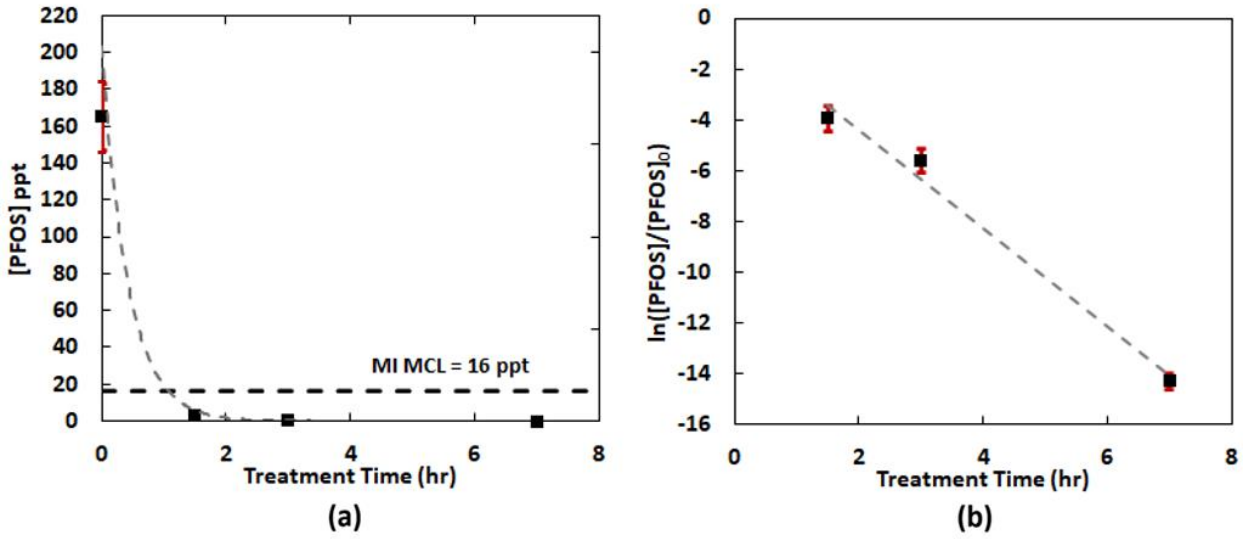


Figure 5.5 (a) PFOS concentration and (b) $\ln([PFOS]/[PFOS]_0)$ vs. treatment time with exponential decay trendlines (dashed gray lines).

The concentration of PFHxS vs. treatment time is provided in Figure 5.6a. Recall that in Section 5.2 the PFHxS concentration increased over the first 90 min of treatment before beginning to decrease. In this packed-bed reactor treatment, the PFHxS concentration has already decreased from its initial value of 426 ± 47 ppt to 62 ± 7 ppt in 90 min. This is attributed to both the enhanced contact area of the packed-bed reactor and the higher discharge power (by about a factor of 1.4).

It is still possible to fit an exponential decay curve to the data points. If the initial concentration data point is omitted, the decomposition behavior from 1.5 to 7 hr is well approximated by first-order decay, as seen in Figure 5.6b and by the orange solid curve passing through the last three data points in Figure 5.6a. Certainly, data should not be omitted to make it fit a particular decay behavior. This omission is only mentioned because after 1.5 hr of treatment, the PFOS concentration has already decayed to 3.2 ± 1.6 ppt. At this point, PFOS is not producing PFHxS as a decomposition by-product, and thus the source term for PFHxS is close to zero; thus, the PFHxS concentration vs. treatment time may be better approximated by first-order decay because the source of PFHxS (i.e., the decomposition of PFOS) has been mostly eliminated at this point. It is not clear that this is the case for other short-chain PFAS, but it would be interesting to explore this concept further in future research.

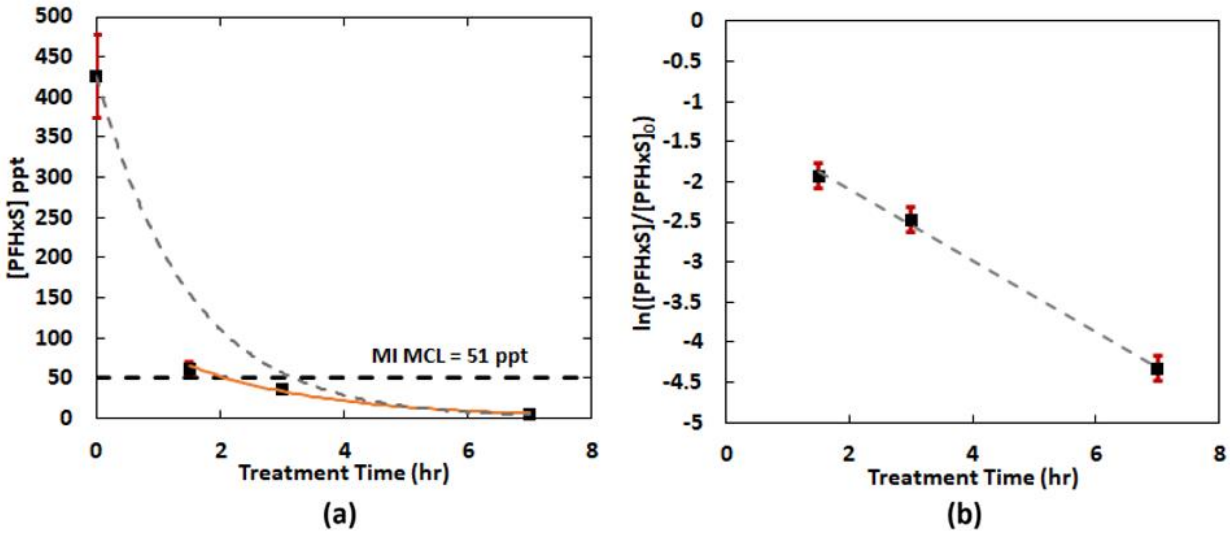


Figure 5.6 (a) PFHxS concentration and (b) $\ln([PFHxS]/[PFHxS]_0)$ vs. treatment time with exponential decay trendlines (dashed gray lines). The orange solid line in (a) crossing through the last three data points is an exponential curve for that omits the initial concentration ($[PFHxS]_0$).

Table 5.3 also lists MCLs for perfluorobutanesulfonic acid (PFBS) and perfluorohexanoic acid (PFHxA) at 420 and 400,000 ppt, respectively. The concentrations of

these compounds vs. time are provided in Figure 5.7. For both compounds, the concentrations initially increase over the first 1.5 hr of treatment, then decrease over the remaining 5.5 hr of treatment. This supports the hypothesis that the shorter chain PFAS require longer treatment times to start being removed. However, for both PFBS and PFHxA, the initial concentrations are already below the MI MCLs, and thus do not present a significant issue from a regulatory standpoint for this particular groundwater unless they are produced significantly as intermediates.

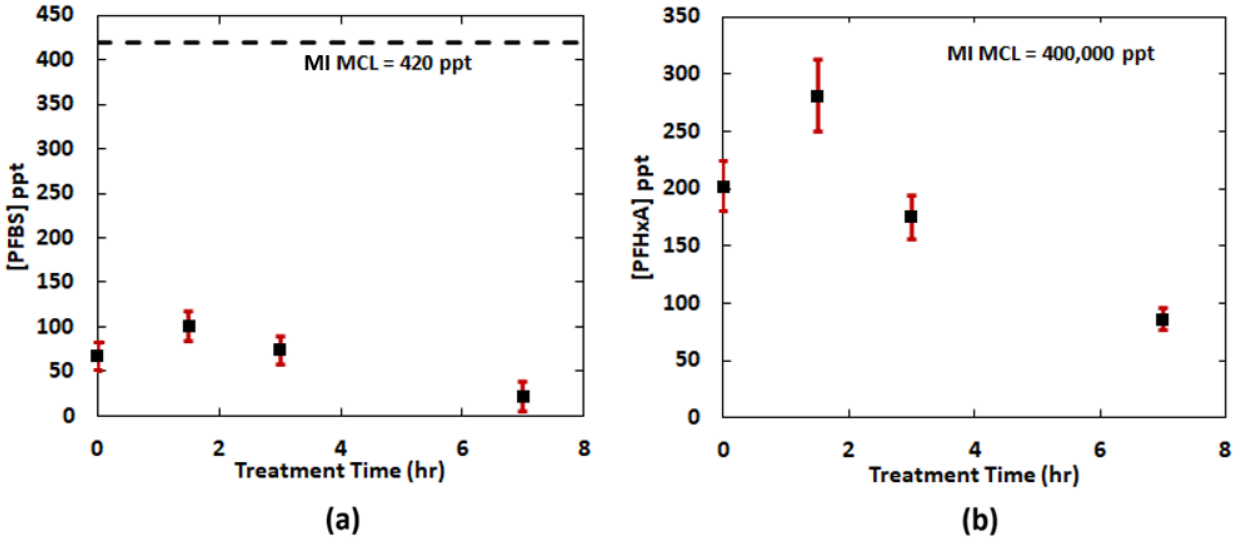


Figure 5.7 (a) PFBS concentration and (b) PFHxA concentration vs. treatment time.

On the other hand, PFNA starts at an initial concentration of 49 ± 5 ppt, roughly 8 times the MI MCL of 6 ppt. While PFNA does decay to a final concentration of 2 ± 1 ppt after 7 hr of treatment, the kinetics are not well approximated by first-order decay, contrary to the behavior observed in Section 5.2. It is not clear why PFNA appears to be more resistant to decomposition by the packed-bed reactor compared to the DBD jet reactor in these two treatments, but it might have to do with the gas temperature differences between the two reactor configurations.

The last compound to be addressed in Table 5.3 is PFOA. Indeed, PFOA has received perhaps the most attention regarding health concerns and regulations. The initial concentration of PFOA in the Site 1 groundwater was only 27 ± 4 ppt; however, the concentration increased to 79 ± 12 ppt after 1.5 hr of treatment. Instead of decreasing after an initial increase, as was observed in Table 5.2, the concentration appeared to continue increasing slightly over the remainder of the treatment time to a final value of 96 ± 14 ppt. Considering the uncertainty in these measurements, the PFOA concentration essentially levels off to an average value of 86 ± 13 ppt after 3 hr of treatment, thus suggesting a source of PFOA coming from within the reactor.

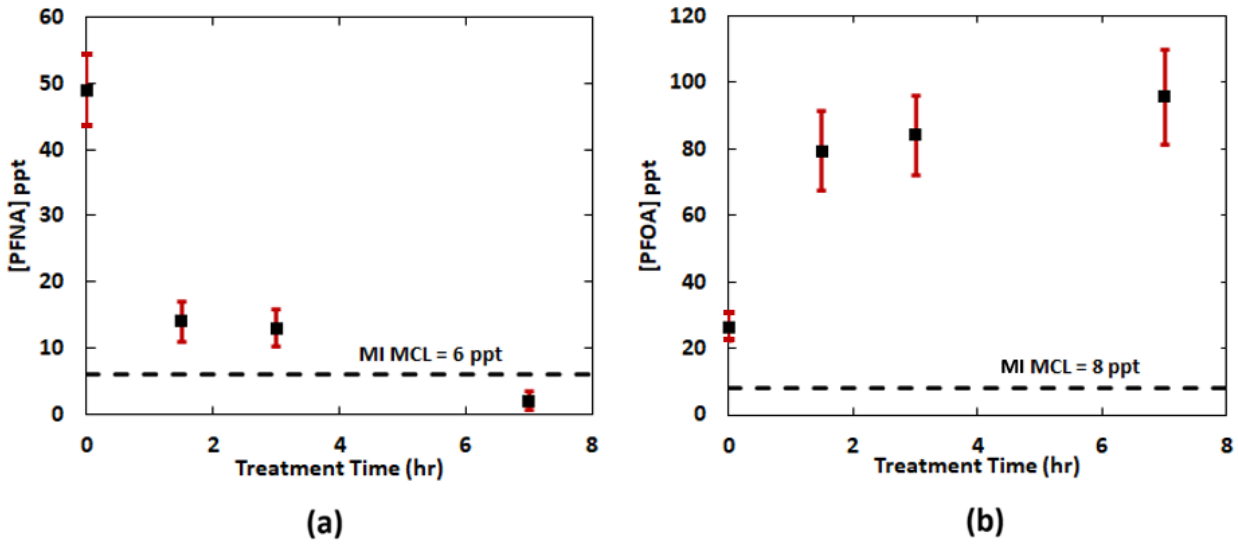


Figure 5.8 (a) PFNA concentration and (b) PFOA concentration vs. treatment time.

Consequently, identifying the remaining source of the PFOA required further testing and investigation, which will be discussed in Section 5.4. Nevertheless, this groundwater test with the packed-bed reactor has demonstrated the capability of plasma to decompose PFOS, PFHxS, and PFNA to below the MI MCLs. Meanwhile, PFBS and PFHxA can also be removed after a certain amount of treatment; however, these compounds were already below the MI MCLs in the

untreated groundwater, in this case. Next, the evolution of pH and electrical conductivity of the water throughout the 7 hr plasma treatment with the packed-bed reactor is discussed.

### 5.3.2 *pH and Electrical Conductivity*

The change in the pH of the water was monitored over the duration of the treatment and is shown in Figure 5.9a. The pH drops from an initial value of 7.59 ± 0.10 to a minimum value of 3.35 ± 0.07 after 1.5 hr. The pH then slowly drifts up over the next 5.5 hr to a final value of 4.41 ± 0.08. The error bars are too small to be seen on the plot, with the largest error being ±2.0%. The drop in pH with treatment time is expected as nitrogen species from the plasma diffuse into the water to form nitric and nitrous acids. The gradual increase in pH might be related to the presence of the copper cooling coil, as copper in contact with water has been reported to cause some increase in pH.[117]

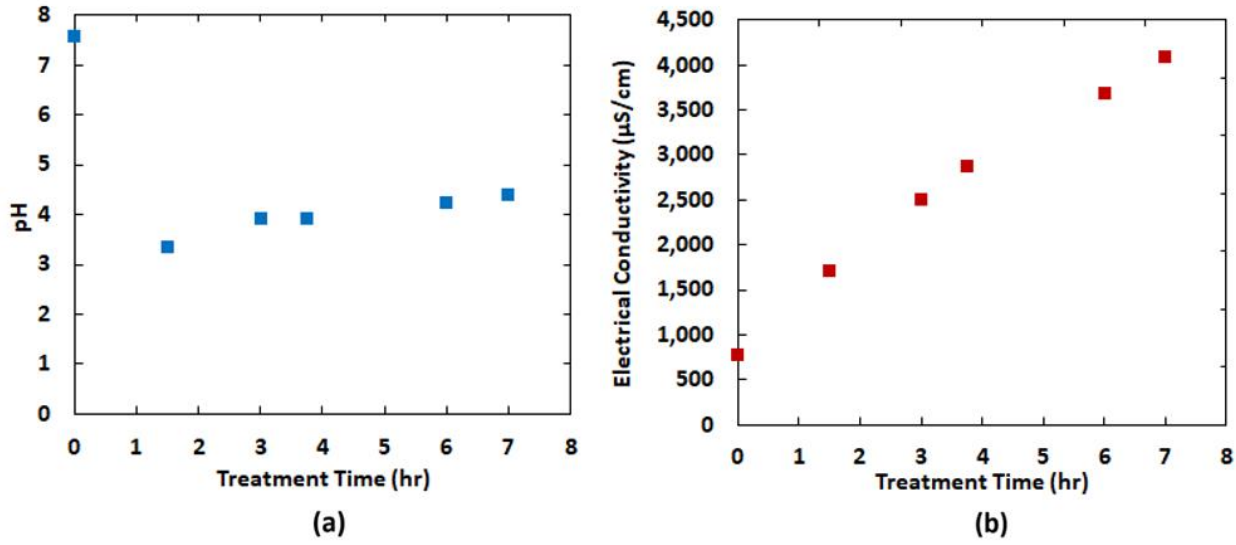


Figure 5.9 (a) Water pH and (b) electrical conductivity measured over the duration of the treatment time.

The change in the water electrical conductivity over the duration of the treatment is shown in Figure 5.9b. The conductivity starts at an initial value of 771 ± 8 µS/cm and increases

almost linearly to a final value of 4095 ± 41 µS/cm after 7 hr of treatment. The error bars are too small to be seen on the plot, with the largest error being ±1.1%. This increase in electrical conductivity of the water throughout the plasma treatment time can affect the voltage-current waveforms of the discharge, as shown in the next section.

### *5.3.3 Discharge Voltage, Current, and Power*

The discharge voltage and discharge current vs. time for typical nanosecond pulses are shown in Figure 5.10. It was observed that as the electrical conductivity of the water increased throughout the duration of the treatment, the peak voltages decreased from 10.9 ± 0.8 kV for an EC of 800 µS/cm to 8.5 ± 0.6 kV for an EC of 4,000 µS/cm. Contrariwise, the peak currents increased from 72 ± 3 A for an EC of 800 µS/cm to 102 ± 3 A for an EC of 4,000 µS/cm. The peak voltage and peak current vs. water electrical conductivity are summarized in Figure 5.11, and this behavior will be explored in more detail in Section 6.1.

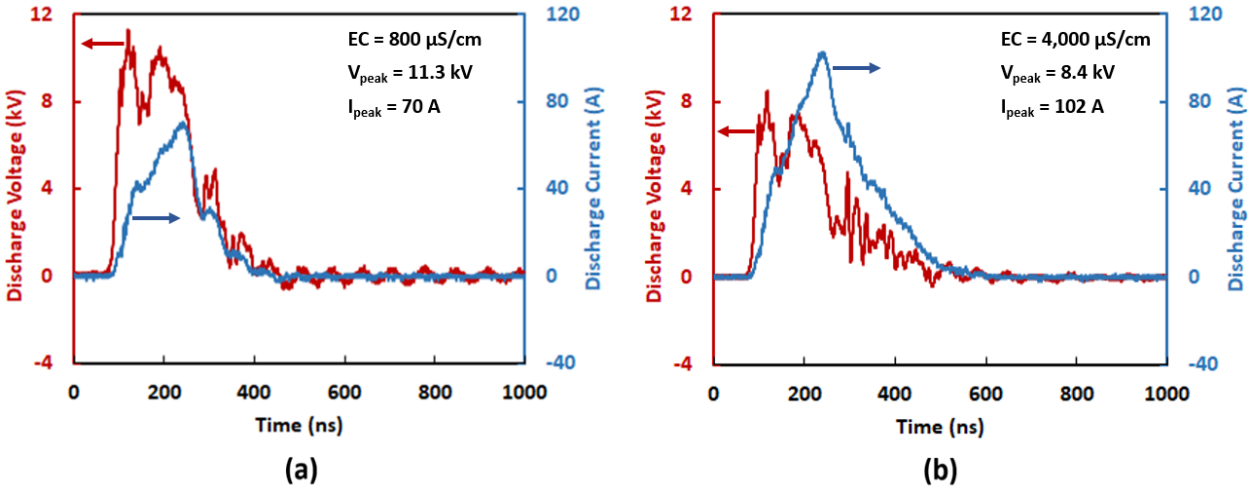


Figure 5.10 Discharge voltage and discharge current vs. time for (a) EC = 800 µS/cm, and (b) EC = 4,000 µS/cm.

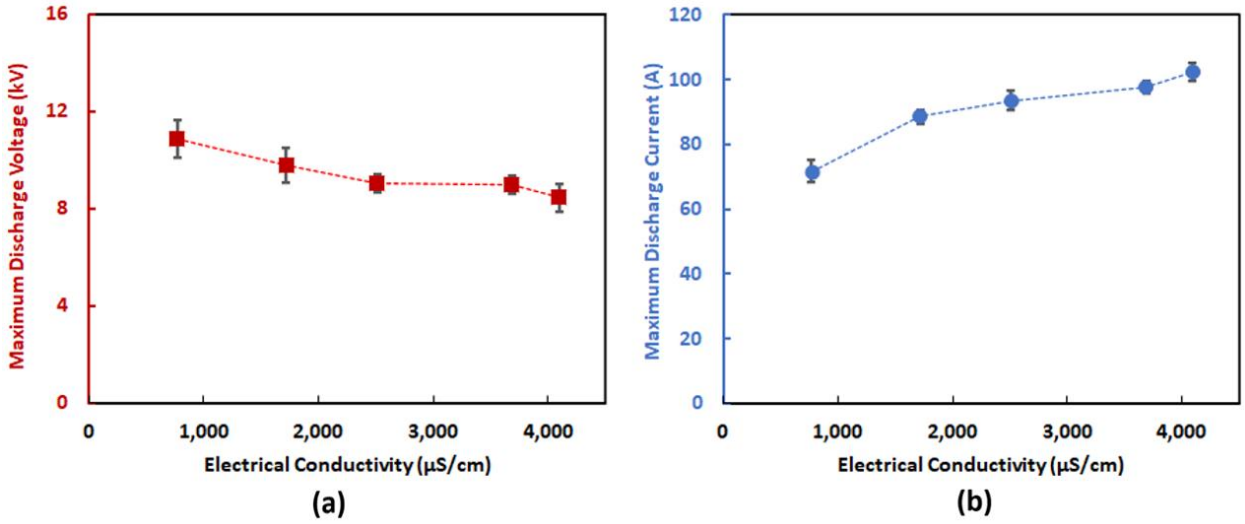


Figure 5.11 (a) Maximum discharge voltage vs. water EC, and (b) maximum discharge current vs. water EC.

Despite the trend of decreasing peak voltage and increasing peak current with increasing water electrical conductivity, the discharge power remains roughly constant at an average value of 134 ± 14 W. Since the energy per pulse is proportional to the discharge power, the same behavior is observed, with an average value of 67 ± 7 mJ/pulse. This trend of roughly constant discharge power with increasing water electrical conductivity will be explored further in Section 6.2.

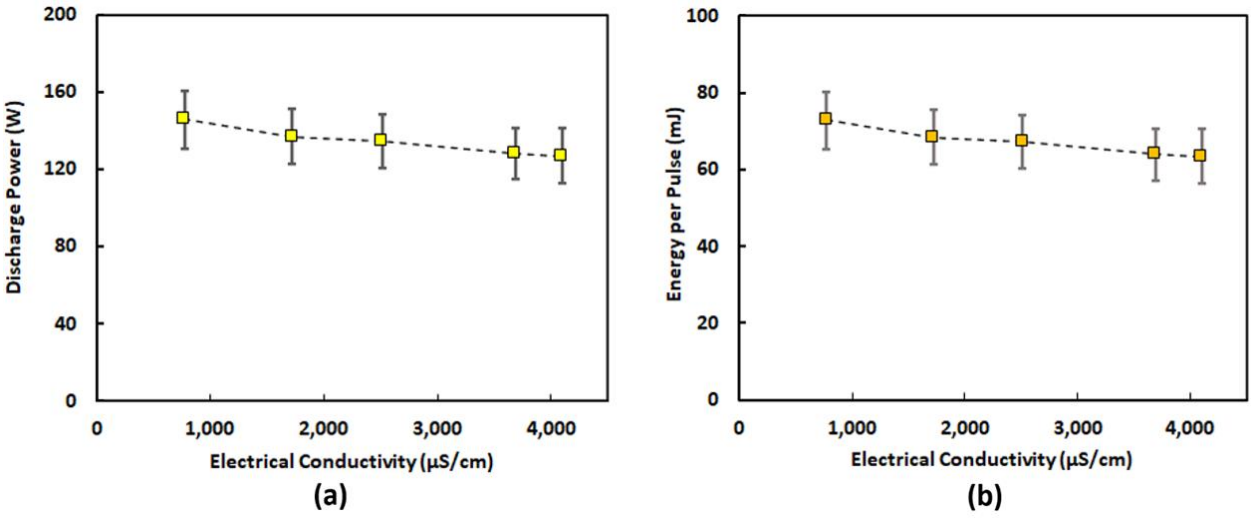


Figure 5.12 (a) Discharge power and (b) energy per pulse vs. water EC.

This long duration plasma treatment of Site 1 groundwater using the packed-bed reactor with ambient air as the working gas has demonstrated the capability to reduce PFAS to below MI MCLs, the PFOA contamination issue still needs to be resolved. While the obvious potential sources were accounted for (i.e., Teflon thread seal tape and residual contamination on the reactor walls), every subcomponent of the reactor with incomplete material information must be investigated. During this process, it became clear just how ubiquitous PFOA can be in a wide variety of products, including parts that are often used in contact with drinking water. Thus, researchers investigating PFAS remediation technologies must be extremely careful regarding the selection of parts and materials, lest they accidentally contaminate their experiments. Furthermore, water treatment experiments that do not measure PFOA concentrations may be unknowingly generating PFOA-contaminated waters.

### 5.4 Highlighting the Issue of PFOA Ubiquity

As seen in Figure 5.8b, the concentration of PFOA increases to some steady-state value during the 7 hr treatment, suggesting a source of PFOA contamination coming from within the

reactor. Two potential sources of PFOA contamination in the reactor considered first were the Teflon thread seal tape and the interior walls of the reactor's plumbing that had been exposed to high concentrations of PFOA during the test described in Section 5.1. To address this, all the reactor's original polyvinyl chloride (PVC) tubing was replaced with cross-linked polyethylene (PEX) tubing, and the threaded fittings were replaced with SharkBite fittings where possible.

Additionally, a new flow meter and a new wet-end kit for the pump were installed, as these components were exposed to PFOA during the high concentration test, as well. Any components that could not be completely replaced during this re-build process were thoroughly washed with Alconox cleaning detergent and placed in a warm ultrasound bath for approximately 20 min. The re-built packed-bed reactor was equipped with a new discharge region housing made from polyether ether ketone (PEEK). Any threaded connections in the reactor plumbing that could not be replaced were sealed with a silicone sealant, as opposed to using Teflon thread seal tape.

Before running more groundwater tests with the packed-bed reactor, several "blank" samples were generated by running deionized water through the reactor with the nanosecond pulse power supply set to the same settings as in the groundwater treatment from Section 5.3 (450 V DC charging voltage, 2 kHz pulse repetition frequency). These samples were then analyzed by LC-MS/MS as described in Section 3.3. If the PFOA contamination within the reactor had been eliminated, these blank samples should not have shown significant levels of PFOA (i.e., close to or below the detection limit of approximately 2 ppt).

Unfortunately, after 15 minutes of plasma treatment the PFOA concentration was measured at 175 ± 10 ppt, and after 30 minutes of plasma treatment the PFOA concentration rose to 345 ± 25 ppt. Clearly, there was still a significant source of PFOA contamination coming

from within the reactor. Thus, a series of tests were conducted to isolate the source of the contamination.

The plasma section of the packed-bed reactor was isolated from the reservoir, the pump, and the rest of the reactor's plumbing in the series of tests summarized in Table 5.4. First, a sample of deionized water (Milli-Q EMD Millipore) from the Engineering Research Building (ERB) was tested to ensure that the initial water used in the blank testing was not contaminated with PFOA. Next, water was circulated through only the packed-bed section of the rector, including the "showerhead" nozzle, the electrodes, and the PEEK discharge region housing. The reactor reservoir, plumbing, and pump were replaced with a Catalyst FH100X peristaltic pump (Cole Parmer, Inc., Vernon Hills, IL, USA) with silicone tubing. Simply circulating deionized water through this section of the reactor resulted in over 100 ppt of PFOA, indicating that this section of the reactor was a source of PFOA contamination.

Table 5.4 Packed-bed reactor Source Isolation (PBSI) test sample summary. Deionized (DI) water from the Engineering Research Building (ERB) was tested first to ensure that the starting water was not contaminated with PFOA. Samples PBSI-1, -2, and -3 involved flowing water through the packed-bed section (including the "showerhead" nozzle and the electrodes and housing), but the reactor reservoir, plumbing, and pump were replaced by a peristaltic pump with silicone tubing. [a] PBSI-4 included the same components as PBSI-3 except the heat shrink tubing covering the central electrode upstream of the discharge region was removed. [b] PBSI-5 did not include the nozzle or the electrodes. [c] PBSI-6 included the nozzle and central electrode, but not the outer electrode or the discharge region housing. Note that DI water rinsing occurred between samples PBSI-3 and PBSI-4. PBSI-HB confirmed that the silicone tubing did not leach PFOA. In all tests, 500 mL of DI water were circulated through the system.

| Sample ID | Sample Description | [PFOA] ppt |
|---|---|---|
| DI-ERB | DI water from ERB 1224 | 0 |
| PBSI-1 | Circulate water for 15 min, no plasma | 111 |
| PBSI-2 | Run with plasma for 30 min | 121 |
| PBSI-3 | Run with plasma for 60 min | 129 |
| PBSI-4 | Circulate DI water through packed-bed section, 30 min[a] | 18 |
| PBSI-5 | Circulate DI water through just the 'tee' for 30 min[b] | 16 |
| PBSI-6 | Circulate DI water through nozzle for 30 min[c] | 30 |
| PBSI-HB | Circulate DI water through pump hose (hose blank) | 0 |

Prior to generating Sample PBSI-4, the packed-bed section of the reactor was thoroughly rinsed with deionized water in attempt to remove any residual contamination from the subcomponent surfaces. Next, deionized water was circulated through the packed-bed section again, but the heat shrink insulation was removed from the central electrode, which insulate the electrode upstream of the discharge region to prevent parasitic losses to the water. This heat shrink insulation was made of an unknown material, and thus needed to be replaced. The rinsing and removal of the heat shrink insulation helped reduce the concentration of PFOA detected in the resulting "blank" sample but did not eliminate the contamination completely.

Next, deionized water was recirculated through just the tee-section of the packed-bed section (no nozzle or electrodes present), in sample PBSI-5. While the measured PFOA concentration for this sample was relatively low, about 16 ppt was still detected. In PBSI-6, the nozzle was added back to the packed-bed section along with the central electrode, but the outer electrode and housing was still absent from the circuit. The PFOA concentration increased in this sample to about 30 ppt, suggesting that the nozzle may be an issue.

Overall, the PBSI tests indicate that thorough rinsing with deionized water can help reduce the residual levels of PFOA in the reactor. However, it is not completely clear if removing the heat shrink insulation significantly impacted the PFOA contamination within the reactor. Still, at this point any subcomponents containing unknown materials should be replaced with PFAS-free alternatives. Indeed, the nozzle is made from a proprietary 3-D printed material, an acrylic-based photopolymer known as Visijet M3 Crystal. Due to the proprietary nature, the exact material formulation is not available, and it is not known whether PTFE has been added to aid in the extrusion process of the 3-D printing.

The next round of "blank" testing adds back all the reactor components that were removed from the PBSI tests (including the reservoir, pump, and plumbing), but the original heat shrink insulation has been replaced with a food grade heat shrink insulation made from acrylate olefin. The first set of samples in Table 5.5 involved circulating deionized water through the system (EIR-1 and EIR-2) and then running the plasma at typical treatment conditions (450 V DC charging voltage, 2 kHz pulse repetition frequency) for a total of 40 min (EIR-3 and EIR-4).

Again, the PFOA concentration increases to above 200 ppt; thus, replacing the unknown heat shrink insulation with an acrylate olefin insulator did not solve the contamination problem. The reactor was thoroughly rinsed with deionized water to prepare for the next round of testing in which the 3-D printed nozzle, shown in Figure 5.13a, was replaced by a PEEK nozzle of the same dimensions. A series of similar tests were performed. Deionized water was first circulated through the system for 20 min (PNR-1) and showed little traces of PFOA.

Table 5.5 Packed-bed reactor electrode insulation replacement (EIR) and printed nozzle replacement (PNR) test sample summary. Deionized (DI) water from the Engineering Research Building (ERB) was tested first to ensure that the starting water was not contaminated with PFOA. [a] The same batch of water was used for samples EIR-2 and -2. [b] The same batch of water was used for EIR-3 and -4. [c] The same batch of water was used for PNR-2, -3, and -4. Note that DI water rinsing occurred between samples EIR-4 and PNR-1. In all tests, 500 mL of DI water were circulated through the system.

| Sample ID | Sample Description | [PFOA] ppt |
|---|---|---|
| DI-ERB | DI water from ERB 1224 | 0 |
| EIR-1 | Circulate DI water for 20 min, no plasma[a] | 5 |
| EIR-2 | Circulate DI water for 40 min, no plasma[a] | 13 |
| EIR-3 | Run with plasma for 20 min[b] | 52 |
| EIR-4 | Run with plasma for 40 min[b] | 226 |
| PNR-1 | Circulate DI water for 20 min, no plasma | 2 |
| PNR-2 | Run plasma for 10 min[c] | 4 |
| PNR-3 | Let activated water sit overnight, then circulate 10 min[c] | 15 |
| PNR-4 | Run plasma for additional 10 min (20 min total)[c] | 12 |

Next, the plasma was run at typical treatment conditions for 10 minutes. At last, the PFOA concentration did not significantly increase (PNR-2). The plasma activated water was left to sit overnight to see how much PFOA, if any, would leach into the water. The PFOA concentration did increase by about 10 ppt, this might be attributed to the small amounts of PFOA being stuck to the reactor walls. It is difficult to get all the PFOA off during the deionized water rinses. In any case, the concentration is still relatively close to the detection limits of the LC-MS/MS analysis.

Then, the same water was treated for an additional 10 min with plasma, and the PFOA concentration did not increase any further. If the contamination source was still present, one would expect the PFOA concentration to notably increase, as was seen in the previous blank tests. It seems that the 3-D printed nozzle was the source of PFOA contamination throughout these tests, although it is possible that there were other sources originally that were eliminated through this systematic process. Indeed, the 3-D printed nozzle was present throughout all the previous testing. A follow-up test is planned to demonstrate that the reactor can remove PFOA to below MI MCLs now that the contamination source has been eliminated.



(a)



| | |
|---|---|
| Body Material | PVC Plastic |
| Ball Material | PVC Plastic |
| Seal Material | EPDM Rubber |
| Seat Material | PTFE Plastic |

(b)

Figure 5.13 (a) The 3-D printed "showerhead" nozzle that disperses the water into thin jet streams in the packed-bed reactor was found to be a significant source of PFOA contamination. (b) A PVC on/off valve for drinking water from McMaster-Carr with a polytetrafluoroethylene (PTFE) plastic seat.

This section is intended to serve as a word of caution to other researchers who are performing water treatment experiments. Many seemingly innocuous components contain PTFE, which can act as a precursor for PFOA. For example, the PVC on/off valve for drinking water from McMaster-Carr, shown in Figure 5.13b, contains a PTFE seat that may be exposed to water. Teflon thread seal tape is commonly used to prevent water leakage at threaded pipe connections, and many thermocouple probes have a PTFE insulation sleeve, which may be in contact with water if being used to monitor the water temperature during an experiment. More research should be conducted to evaluate how much PFOA leaches into water from these components containing PTFE, particularly when the water is acidic or contains reactive species.

## 5.5 Conclusions

This chapter extends upon the initial plasma source exploration study from Chapter 4 by investigating the batch-kinetics of PFAS decomposition. First, the packed-bed reactor treatment of deionized water spiked with 5.7 ppm of PFOA showed rapid degradation of PFOA (60%) in the first few minutes of treatment, followed by a more gradual decay for the remainder of the 60 min treatment. The Electrical Energy per Order was introduced as a figure of merit to describe the decomposition efficiency, and the EE/O value for this PFOA treatment was estimated at 45 $kWh/m^3$, which is competitive with other advanced PFAS treatment processes reported in literature.[23]

Next, Site 1 groundwater was treated with the DBD plasma jet reactor for 120 min and treated samples were analyzed at 10 different treatment times to investigate the decomposition kinetics. It was observed that the longest chain PFAS detected in the groundwater, PFOS and PFNA, were decomposed in a manner approximately commensurate with first-order kinetics; however, the shorter chain PFAS, such as PFHxS, showed a gradual increase for the first 90 minutes of treatment. This is thought to be due to production of PFHxS as a by-product of the decomposition of longer chain PFSAs, such as PFOS. Such behavior has indeed been reported elsewhere in literature.[56]

The Site 1 groundwater was also treated for a long duration (7 hr) with the goal of decomposing PFAS to below the MI MCLs. This was achieved for all compounds except for PFOA. The PFOA concentration vs. time suggested a contamination source within the reactor which was later identified. The decomposition of PFOS was again observed to follow approximately first-order decay with an EE/O of $235 \pm 25$ $kWh/m^3$. After 90 min of treatment the PFOS concentration was $3 \pm 2$ ppt, compared to the MI MCL of 16 ppt. After this point (90

min treatment), the remaining PFHxS concentration also decayed according to first-order kinetics, despite the expected increase in PFHxS concentration at the early treatment times. The PFNA decomposition did not match first-order decay, in this case, but was still removed to below the MI MCL (6 ppt). The electrical conductivity was observed to increase throughout the duration of the treatment, which was related to a decrease in peak discharge voltage and an increase in peak discharge current. Regardless, the discharge power (and energy per pulse) remained roughly constant throughout the treatment time.

Ultimately, a methodical approach involving elimination and replacement of reactor subcomponents identified a 3-D printed part as the source of the PFOA contamination. Removal of the 3-D printed part demonstrated that PFOA source was eliminated. This serves as a word of caution to other researchers who may be constructing reactors for the decomposition of PFAS. The selection of materials for reactor components is important, as Teflon (polytetrafluoroethylene or PTFE) is a material that can be found in many common components and can serve as a precursor to PFOA under certain conditions, such as high temperatures. Furthermore, 3-D printed materials often contain PTFE to aid in the extrusion process, and the heat at the printing nozzle may generate PFOA. This represents a potential hazard for the 3-D printer operators, and if parts containing PTFE or PFOA are used in systems intended to decompose PFAS, it is possible that they may act an unintended source of PFOA contamination.

## Chapter 6 Influence of Water Electrical Conductivity on Plasma Discharge Properties

It has been observed in this work and others that plasma treatment increases the electrical conductivity of the treated water, as charged species from the plasma and electrode materials are transferred to the water. Furthermore, different water matrices that may be encountered (i.e., from different contaminated sites) can have widely varying electrical conductivities. Thus, the purpose of the study presented in this chapter is to investigate how the plasma discharge properties change as the water conductivity changes over time and the implications for overall discharge efficiency.

Recall from Equation (3.4) that the electrical conductivity of the water directly impacts the charge relaxation time. As a result, increasing solution conductivity is generally associated with a change in plasma-water contact area related to shorter plasma streamer propagation lengths across the gas-liquid interface. The change in plasma volume can affect several physicochemical properties of the discharge.[118]–[121] Furthermore, since the water jets in the packed-bed reactor are part of the electrical circuit generating the plasma discharge, the water conductivity may influence discharge parameters such as the voltage and current waveforms, the deposited power and energy per pulse, the gas temperature, the plasma density (i.e., electron density), and the amount of energy that goes into heating the water.

This chapter systematically investigates the effects of water electrical conductivity on these discharge properties by adding sodium chloride to deionized water at varying amounts to generate water samples at electrical conductivities ranging between 4 µS/cm and 15,800 µS/cm,

which are then activated by plasma in the packed-bed reactor (described in Section 4.1.2). The lowest conductivity was simply deionized water (Milli-Q EMD Millipore) that had been re-circulated through the reactor, which had been previously rinsed thoroughly with deionized water to mitigate the effects of residual dissolved solids stuck to the internal walls of the reactor during the drying process between tests. Conversely, the highest conductivity was targeted at about 16,000 µS/cm.

This upper conductivity sample was chosen because the highest conductivity observed in the long duration groundwater treatment test (Section 5.3) was about 4,000 µS/cm; furthermore, recall that the studies performed in Chapter 4 indicated that concentrating the PFAS prior to plasma treatment may offer some benefit. Particularly, it was found that groundwater from both contaminated sites achieved similar percent removals of PFOS despite the significantly different starting concentrations, indicating that plasma treatments of highly concentrated PFAS contaminated waters can yield higher mass removal efficiencies.

The use of a membrane-based concentration stage (i.e., reverse osmosis) prior to plasma treatment could practically produce a concentration factor of about 4, hence an electrical conductivity of about 16,000 µS/cm is likely to be on the upper end of what might be expected for waters being treated by the packed-bed reactor. Meanwhile, the intermediate conductivities serve to offer some insight into the relationship between water electrical conductivity and the discharge properties being investigated.

Section 6.1 begins by analyzing the voltage and current waveforms to determine the peak voltages and peak currents achieved at varying water electrical conductivities. Next, those waveforms are integrated to estimate the power deposited into the discharge as well as the energy per pulse in Section 6.2. In Section 6.3, optical emission spectroscopy is used as a

plasma diagnostic to estimate how the gas temperature and plasma density of the discharge change as the water electrical conductivity increases. Section 6.4 addresses the amount of energy that goes into heating the water, and finally, Section 6.5 offers some concluding remarks regarding the conductivity study.

### 6.1 Voltage-Current Waveform Analysis

First, the voltage-current waveforms are investigated as a function of water electrical conductivity. To begin, 500 mL of the prepared waters at varying conductivities are added to the packed-bed reactor and re-circulated through the reactor plumbing at 4.2 ± 0.3 L/min for one minute. Next, power is supplied by the RCC NSP-5000 Series nanosecond pulser to generate a plasma in the discharge region. For all cases in this chapter, the DC charging power supply was set to 450 V and the frequency was set to 2 kHz.

The discharge voltage and discharge current for two different electrical conductivities are shown in Figure 6.1. The discharge waveforms shown for the low conductivity water of 4 µS/cm have a higher peak voltage and lower peak current ($V_{peak}$ = 17.9 kV and $I_{peak}$ = 36 A) compared to the higher conductivity of 4,350 µS/cm ($V_{peak}$ = 9 kV and $I_{peak}$ = 100 A), which is in agreement with the trends observed in Section 5.3. This decreasing peak voltage trend is likely due to increased potential losses to the water jets at higher electrical conductivities, while the increasing peak currents are likely due to increased current conduction capacity of the water jets.

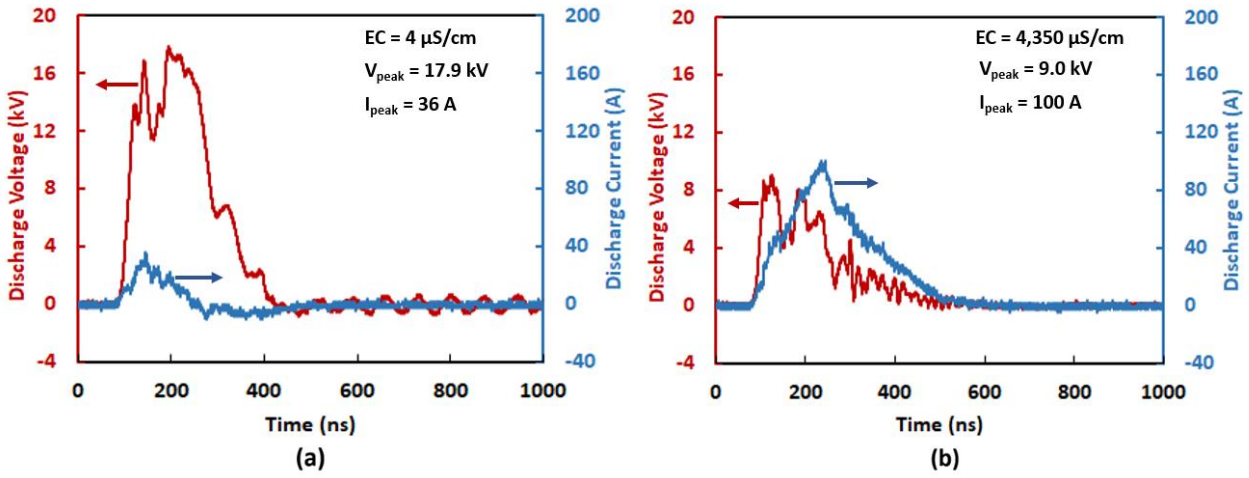


Figure 6.1 Discharge voltage and discharge current vs. time for (a) EC = 4 µS/cm, and (b) EC = 4,350 µS/cm.

The peak voltage and peak current (maximum discharge voltage and current) are extracted from the waveforms and plotted vs. the water electrical conductivity as shown in Figure 6.2a and Figure 6.2b, respectively. Again, the general trend of decreasing peak voltages and increasing peak currents with increasing water conductivity is observed. However, as EC increases beyond about 4,000 µS/cm, the peak voltages and currents appear to plateau around 9 kV and 100 A, respectively.

The large error bars seen for a water EC of 390 µS/cm are mostly a result of pulse-to-pulse variations in the discharge waveforms. This can be seen in Figure 6.3, in which peak voltage was found to vary between 11.9 and 15.2 kV ($V_{peak}$ = 13.1 ± 3.7 kV), while the peak current is 42 A for both waveforms. The maximum current recorded for a water EC of 390 µS/cm was 52 A (shown in Figure 6.5a), for a total reported value of $I_{peak}$ = 45 ± 12 A. In contrast, the waveforms collected at a water EC of 4,350 µS/cm, shown in Figure 6.4, are comparatively quite consistent between pulses with $V_{peak}$ = 9.0 ± 0.3 kV and $I_{peak}$ = 99 ± 3 A.

Some of the variations in waveforms that occur at a given conductivity may be associated with stochastic variation in the water jet structures (i.e., jet instabilities).

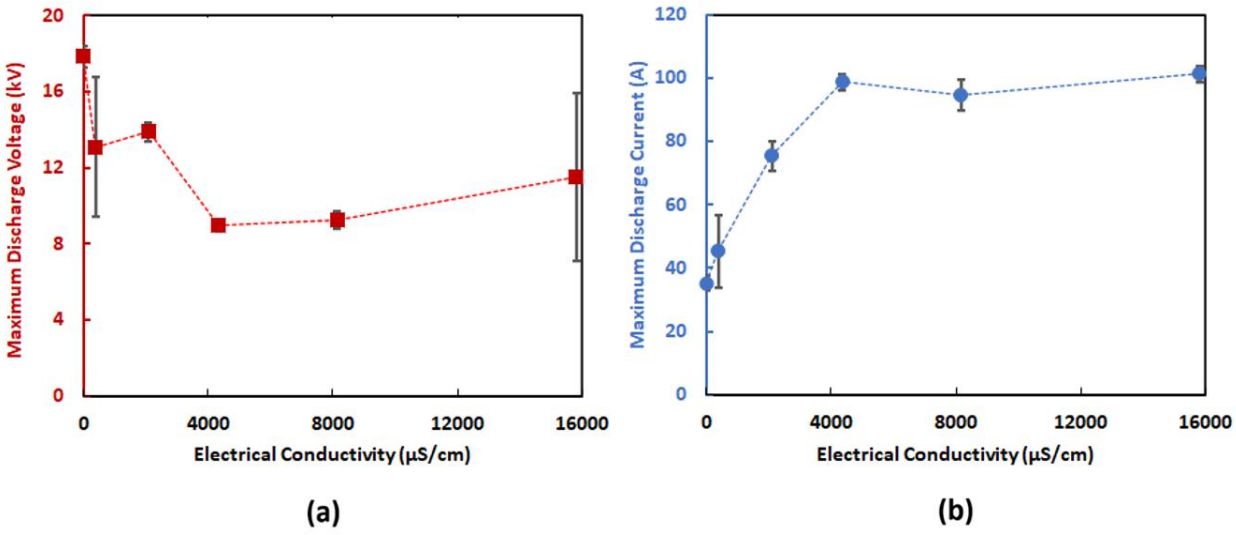


Figure 6.2 (a) Maximum discharge voltage vs. water EC, and (b) maximum discharge current vs. water EC.

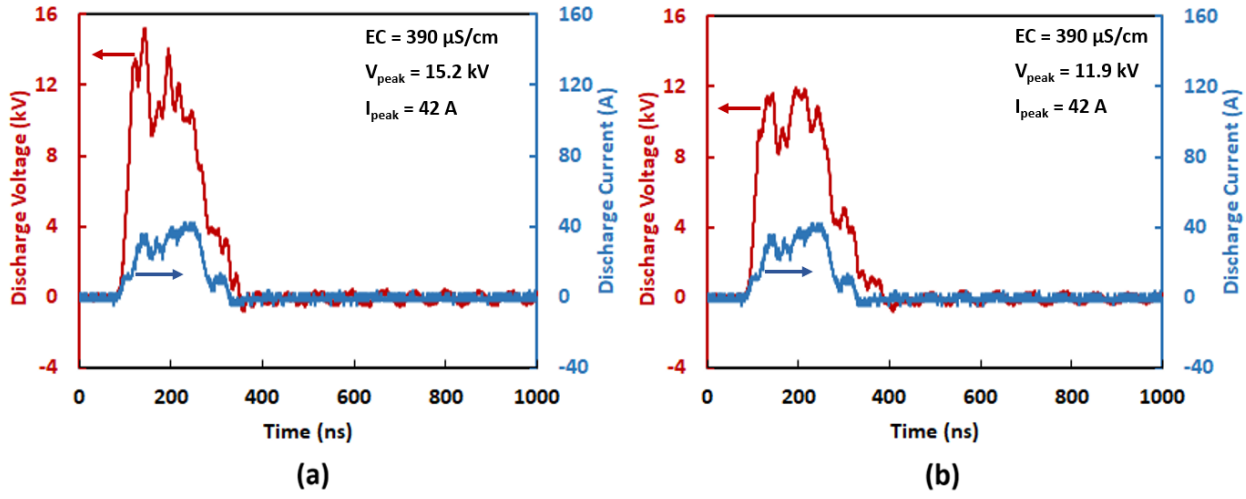


Figure 6.3 Discharge voltage and discharge current vs. time for (a) EC = 390 µS/cm, and (b) also EC = 390 µS/cm, showing the variation in voltage-current waveforms that can occur pulse-to-pulse for a given water EC and power supply inputs.

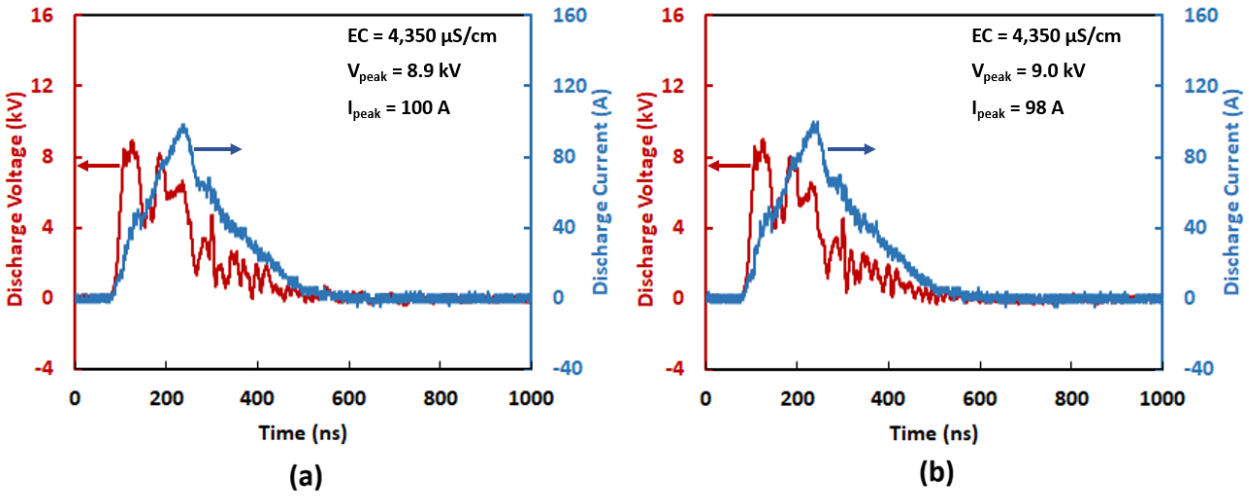


Figure 6.4 Discharge voltage and discharge current vs. time for (a) EC = 4,350 µS/cm, and (b) also EC = 4,350 µS/cm, showing the only small variations in peak voltage and peak current at around 9 kV and 100 A, respectively.

The pulse-to-pulse variation was observed to occasionally be even more pronounced, as seen in Figure 6.5, where the waveform shapes are significantly different. Note that these waveforms were collected at the same conditions (EC = 390 µS/cm), yet the pulse widths are considerably different, with the wider voltage pulse in Figure 6.5a having a pulse width of approximately 180 ns and the narrower voltage pulse in Figure 6.5b having a pulse width of about 70 ns. Additional analysis revealed that the "wide pulse" discharge mode results in pulse widths of 179 ± 5 ns, while the "narrow pulse" discharge produces pulse widths of 71 ± 10 ns. Furthermore, the peak current associated with the narrower voltage pulse is considerably higher ($I_{peak}$ = 122 A in Figure 6.5b compared to 52 A in Figure 6.5a) and continues to increase significantly after the voltage has dropped.

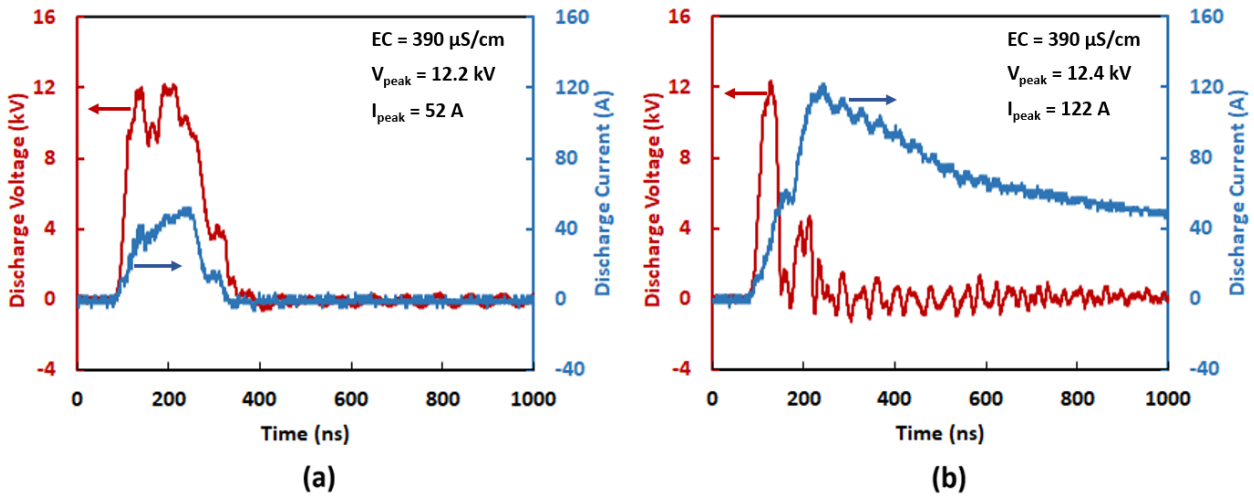


Figure 6.5 Discharge voltage and discharge current vs. time for (a) EC = 390 µS/cm, and (b) EC = 390 µS/cm, demonstrating two different discharge modes that can occur for a given water EC and power supply inputs; however, the narrow voltage pulse and high current waveform shown in (b) was observed to occur infrequently compared to the more stable and wider voltage pulse shown in (a).

Based on Figure 6.5, there appear to be two distinct discharge modes that can take place in the packed-bed reactor. Further research is needed to properly characterize these discharge modes and to identify the properties associated with each, as well as the conditions that affect the onset of each mode. Anecdotally, the narrow voltage pulse mode occurs more frequently at lower water electrical conductivities; however, this still needs to be quantified. Besides the pulse width and peak current differences, the "narrow pulse" discharge mode is also audibly louder and visually brighter (i.e., higher intensity sound and optical emission).

While understanding the differences between these two discharge modes in the packed-bed reactor requires further research, the hypothesis is that the shorter voltage pulse width of the "narrow pulse" discharge mode is associated with a pulsed transient spark type discharge. The sudden drop in voltage which is accompanied by the current increase is thought to be a result of a conductive plasma channel forming between the electrodes. The pulse width is not long enough to form a thermal arc, but it may still be associated with higher gas temperatures in the plasma

compared to the wider voltage pulse width discharge mode, which is thought to be pulsed corona type discharge.[122]

Since the “narrow pulse” discharge mode, thought to be a transient spark type discharge, occurred so rarely, it was omitted from the uncertainty analysis of the maximum discharge voltage and current, but this should be revisited in future work involving the analysis of much larger samples of voltage-current waveforms which could allow for a better understanding of the ratio of occurrence of each discharge mode.

Lastly, the large error bars on the peak discharge voltage at EC = 15,800 µS/cm are also associated with pulse-to-pulse variation, seen in Figure 6.6. Interestingly, the peak discharge current did not show the same variation ($V_{peak}$ = 11.5 ± 4.4 kV and $I_{peak}$ = 101 ± 3 A). The voltage waveform seen in Figure 6.6b appears to almost transition into the spark type mode, suggested by the large first voltage drop. If it were to continue dropping, this would yield a pulse width of about 73 ns, which is on the order of typical pulse widths of the “narrow pulse” discharge mode. However, after the voltage drops to 3 kV, it then increases to 6.6 kV before decaying for a final pulse width of 180 ns, commensurate with the “wide pulse” discharge mode. This may indicate a sort of hybrid discharge mode that, so far, has only been observed consistently at this high conductivity of 15,800 µS/cm.

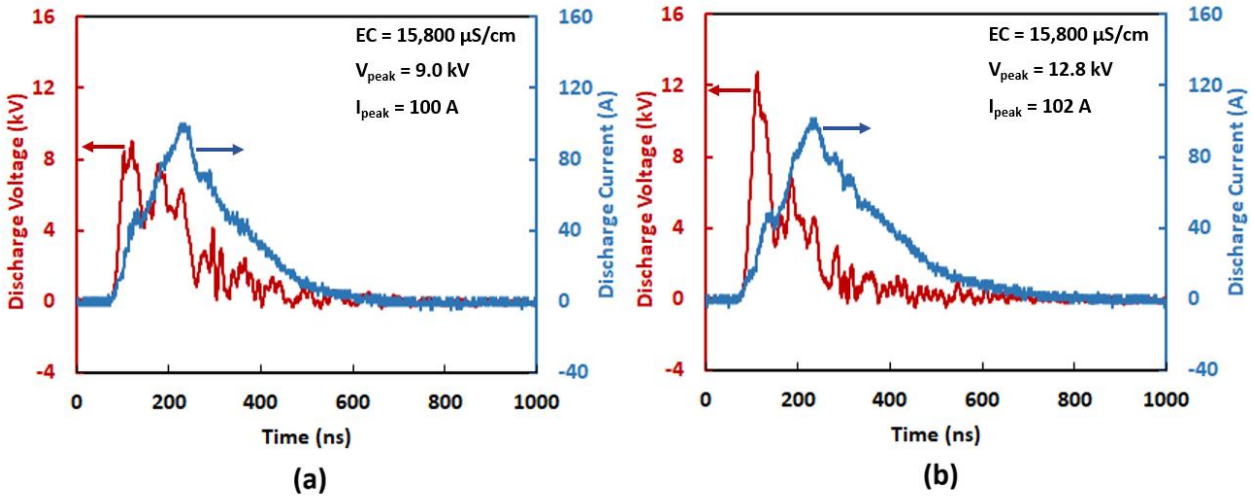


Figure 6.6 Discharge voltage and discharge current vs. time for (a) EC = 15,800 µS/cm, and (b) also EC = 15,800 µS/cm, demonstrating pulse-to-pulse variation that can occur for a given water EC and power supply inputs. In this case, the voltage waveform in (b) appears to almost transition into the spark type mode (large voltage drop), but the voltage increases again after the first drop and results in a similar pulse width overall as in (a). This may indicate a sort of hybrid discharge mode.

Again, more research is needed to properly quantify the ratios of each modes' occurrence as a function of the water electrical conductivity, and this will be a subject of future work. Still, this should be kept in mind when considering the OES experiments in Section 6.3 since light emitted from the plasma will need to be collected over many pulses to achieve the number of accumulations necessary to provide an adequate signal-to-noise ratio.

Unfortunately, it is not known exactly how many pulses during the time of light accumulation produce a particular discharge mode. Although quantitative data is not currently available, it was noticed that the "narrow pulse" discharge occurs relatively more frequently at very low conductivities and becomes increasingly rare as the EC increases beyond 200 µS/cm. One hypothesis is that the lower EC, and thus longer charge relaxation time, allows the plasma streamers to propagate further along the surface of the water jet structures in the packed-bed

reactor, making them more likely to form a conductive channel between the electrodes and form the spark. Additionally, water jet instabilities including turbulence effects may also play a role.

Indeed, the discovery that two distinct discharge modes are possible may be one of the most interesting results from this study and begs the question of how to control which discharge mode takes place for a given voltage pulse. If the discharge mode can be selected using reactor control variables such as flow rate or applied voltage, this could open new possibilities for tailoring the plasma discharge properties and the resulting plasma chemistry to target specific contaminants more effectively.

## 6.2 Discharge Power Analysis

The discharge power and energy per pulse over the range of electrical conductivities investigated is shown in Figure 6.7. The discharge power is calculated by integrating the voltage-current waveforms from the previous section according to Equation (4.1). The energy per pulse is calculated using the same equation, except the integral is not multiplied by the pulse frequency (i.e., $1/\tau$).

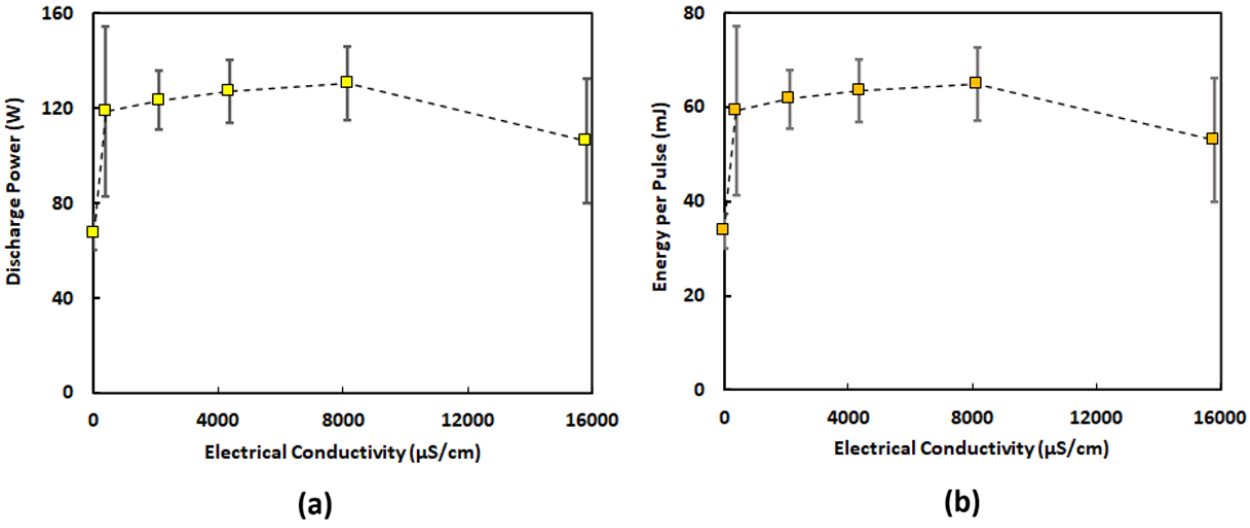


Figure 6.7 (a) Discharge power and (b) energy per pulse vs. water EC.

The values for discharge power are roughly constant between about 110 and 120 W, except for the very low EC of 4 µS/cm which has a discharge power of 67 ± 7 W. This is due to the relatively low peak current (35 ± 2 A), and that the current starts dropping from this peak value before the main voltage drop. An example of this can be seen in Figure 6.1a. Contrast that voltage-current waveform with that for an example at an EC of 390 µS/cm which also has a relatively low peak current (45 ± 12 A), but the current remains close to this maximum value for a longer duration of the pulse, as seen in Figure 6.3. The large error bars seen for EC = 390 µS/cm and EC = 15,800 µS/cm are once again due to the pulse-to-pulse variations in discharge waveforms and are proportionally larger due to the uncertainty propagation in the power calculation.

The energy per pulse, shown in Figure 6.7a, is directly proportional to the discharge power since the pulse frequency was kept constant at 2 kHz for all data points. The energy per pulse was calculated to be on average 55 to 60 mJ/pulse, except again for the low conductivity of EC = 4 µS/cm, which was 34 ± 4 mJ/pulse. Interestingly, despite the trend of decreasing peak voltage and increasing peak current with increasing water EC, the plasma discharge power remains roughly constant, and thus too does the energy per pulse. It seems that the changes in voltage-current waveform shapes do not necessarily impact the discharge power as much as was initially suspected. Indeed, the discharge power did not change significantly in the long duration packed-bed reactor treatment presented in Section 5.3 even though the water conductivity increased from about 800 to 4,000 µS/cm (see Figure 5.12).

## 6.3 Optical Emission Spectroscopy

As introduced in Section 3.6, optical emission spectroscopy (OES) involves collecting the light emitted from the plasma discharge, separating it based on the wavelength of light using a monochromator (i.e., spectrometer grating), and detecting the number of photons at each wavelength using an ICCD camera. Photon wavelength can be related to relative concentrations of certain species in the plasma discharge.

Furthermore, techniques may be used to analyze the collected spectra to estimate the gas temperature and plasma density of the discharge, which will be discussed in Section 6.3.1 and Section 6.3.2, respectively. It is to be noted that the plasma discharge being investigated is filamentary in nature, meaning that if the fiber optic is focused on the core of a plasma streamer, it would be expected to detect a higher gas temperature and plasma density than if it was focused on the outside of the streamer (glow region). This issue is mitigated to an extent by collecting light over hundreds or thousands of pulses to get the time-averaged emission.

Lastly, the pulse-to-pulse variations seen in the previous sections will still be present in this analysis, including the possibility of different discharge modes taking place during the light acquisition time. This is again partially mitigated by collecting light over many pulses, as well as by doing repeated tests at the same conditions and averaging the results. Regardless of these limitations, it is still possible to estimate reasonable gas temperatures and plasma densities in the discharge and may yield interesting information about the discharge behavior as the water conductivity changes. Indeed, this study represents the first OES experiments on the plasma discharge generated by the packed-bed reactor.

The experimental setup used in these experiments is shown in Figure 6.8. Both the nanosecond pulsed power supply and the gating of the spectrometer (ICCD) are triggered by a

signal/delay generator (Model 565, Berkley Nucleonics Corp., San Rafael, CA, USA) which generates a customizable voltage signal. The voltage signal triggering the power supply is converted to an optical pulse by a fiber-optic transmitter (FT-1). The ICCD gate width is set to 2 μs and is triggered about 400 ns prior to the onset of the voltage pulse to ensure that light from the entire plasma pulse is collected and time averaged. The collected spectra are recorded and saved to a computer for further analysis. Voltage and current waveforms are collected by the oscilloscope, along with the timing of the spectrometer gate ($S_{gate}$).

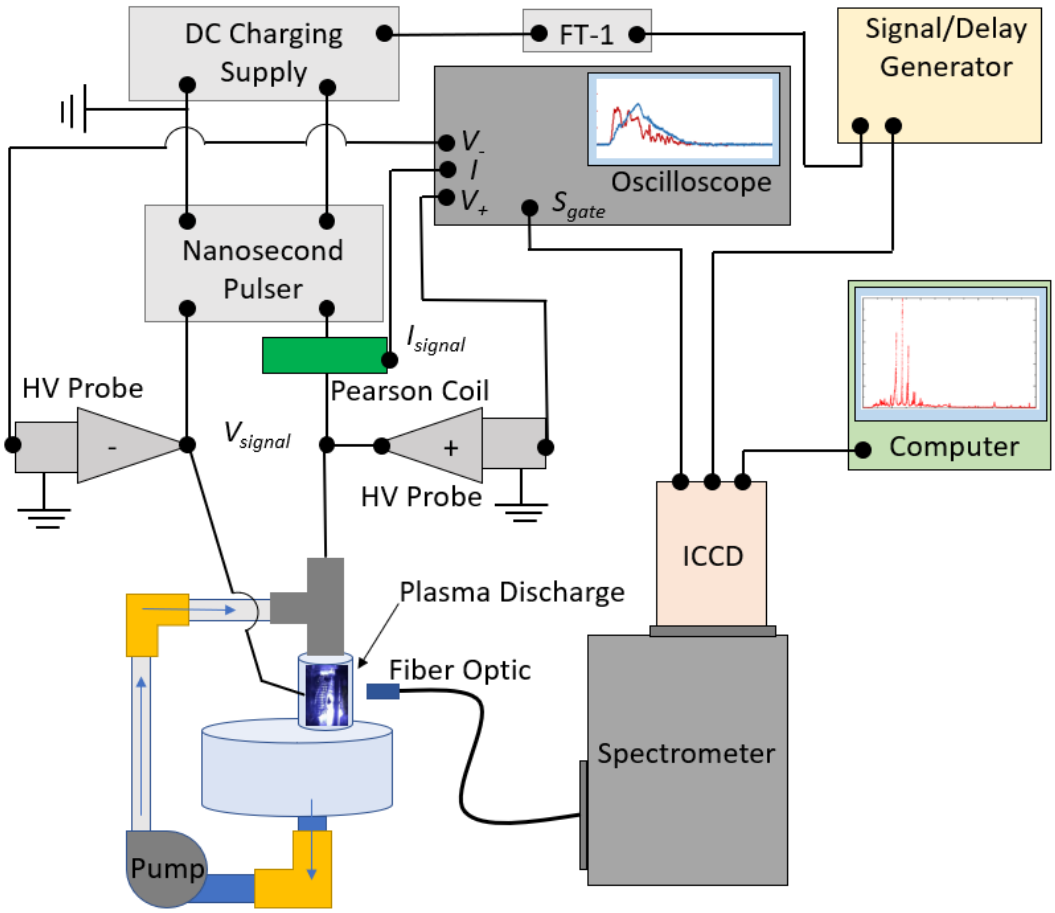


Figure 6.8 Experimental setup for optical emission spectroscopy using the packed-bed reactor.

Before discussing the gas temperature and plasma density calculations, refer to Figure 6.9 for a sample emission spectrum collected from the packed-bed reactor plasma discharge in contact with water at an EC of 200 µS/cm. In this case of relatively low EC, the most intense emission lines are in the ultraviolet (UV) range (200 – 400 nm), particularly in the short wavelength (high energy) UVC range (200 – 280 nm).

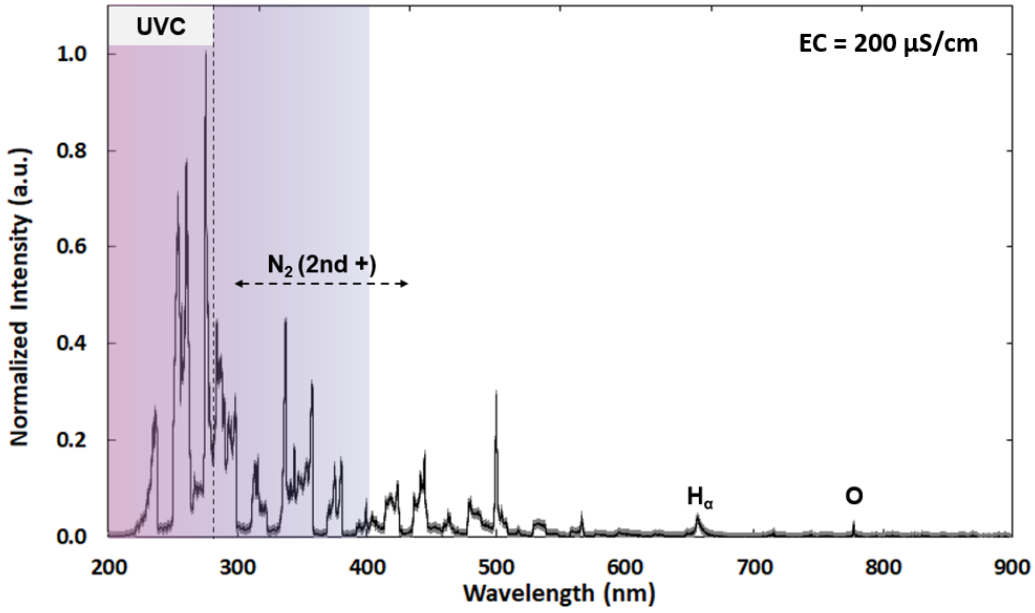


Figure 6.9 Sample emission spectrum from 200 to 900 nm collected from the plasma discharge in contact with water at EC = 200 µS/cm. The shaded region represents ultraviolet light (200 – 400 nm), with the high energy UVC light to the left of the dotted vertical line (200 – 280 nm). The wavelength range collected for analyzing the nitrogen second positive band (290 – 310 nm) is indicated, as well as the hydrogen alpha Balmer line (656.28 nm) used for the plasma density calculation. The oxygen line (777 nm) is also labeled.

Overall, the emission is largely dominated by nitrogen, as this is an air plasma (i.e., gas composition is approximately 78% nitrogen, 21% oxygen). Thus, the nitrogen second positive band is a good candidate for estimating the gas temperature since it has a relatively high intensity and very few interfering emission lines. More importantly, the nitrogen second positive band is well suited for gas temperature estimates because the rotational states are in equilibrium with the translational states. Meanwhile, the hydrogen alpha line ($H_\alpha$ at 656.28 nm) is mostly isolated

from other emission lines, making it a good candidate for estimating the plasma density. Lastly, the oxygen line at 777 nm is also labeled, which gives some insight into oxygen disassociation or production processes.

There is some level of continuum emission observed, particularly in the wavelength range from 200 to 500 nm. This is partly due to radiation from hydrogen molecules.[123] Additionally, to collect light from this wide wavelength range (200 – 800 nm), the spectrometer scans through the range collecting light in 10 nm increments, then splices the spectra together in a process called "step-and-glue." As a result, pulse-to-pulse variation may impact the shape of the full spectrum. Furthermore, at this relatively low EC of 200 µS/cm, the discharge is prone to produce both discharge modes discussed in Section 6.1, and this may affect the step-and-glue algorithm and the resulting glued spectrum.

Indeed, the high intensity of emission in the UV range is thought to be associated with the more intense spark type ("narrow pulse") discharge mode. Further evidence for this can be seen in Figure 6.10, in which the spectrum collected at the low water EC of 4 µS/cm (Figure 6.10a) is dominated by high-energy UVC radiation in the 200 – 280 nm wavelength range. Meanwhile, the spectrum collected at a significantly higher EC of 8,140 µS/cm (Figure 6.10b) is dominated by the nitrogen second positive band (300 – 400 nm) with relative low intensity emission occurring in the UVC range.

It was observed that during emission collection, the low water EC of 4 µS/cm the voltage-current waveforms were unstable and generated significantly more instances of the "narrow pulse" discharge mode. Meanwhile, the voltage-current waveforms at the high water EC of 8,140 µS/cm were very stable in the "wide pulse" discharge mode and was notably quieter and dimmer, in terms of sound and light emission. Comparing these two spectra indicates that

higher energy electrons are being generated in the low water EC case, which is related to the higher maximum discharge voltages observed at lower conductivities (as seen in Figure 6.2a), as well as the occurrence frequency of the "narrow pulse" (spark type) discharge mode, which has yet to be systematically quantified.

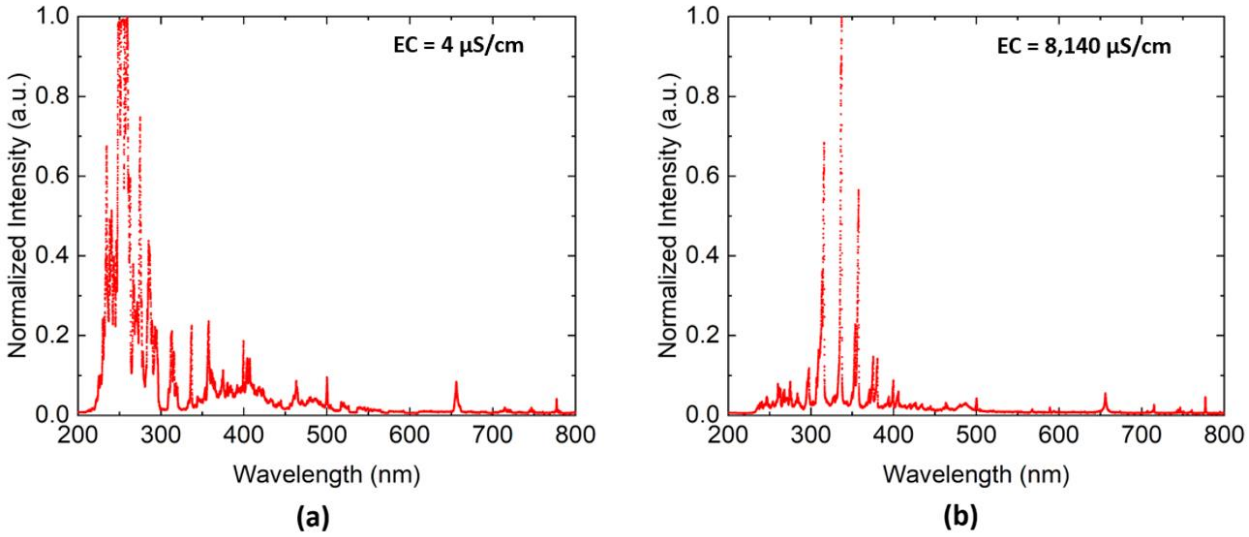


Figure 6.10 Emission spectra for (a) water EC = 4 µS/cm showing high intensity UVC emission (200 – 280 nm), and for (b) water EC = 8,140 µS/cm in which the emission is dominated by nitrogen in the 300 – 400 nm range.

These qualitative comparisons of the emission spectra at varying water conductivities may help to inform the interpretation of the gas temperature and plasma density calculations. The gas temperature calculations will be discussed next, as this value is required for the plasma density calculations.

### *6.3.1 Gas Temperature*

The gas temperature of the plasma refers to the temperature of the neutral species and is an important property as it impacts the rate constants for several chemical reactions in the plasma. Moreover, high gas temperatures (around 700 °C and above) may contribute to thermal decomposition of PFAS, as mentioned in Section 4.1. While non-equilibrium plasmas,

sometimes called cold plasmas, are generally associated with gas temperatures close to room temperature, the plasma discharges in the packed-bed reactor may be capable of reaching higher gas temperatures.

Here, the simulation software Specair Version 3.0 is used to simulate emission spectra for comparison with experimentally collected spectra. First, the gas composition is input as air with trace water vapor content, and the pressure is set to 1 atm. Next, the slit function (measured using 30 mW He-Ne laser, as described in Section 3.6) is uploaded to the software to account for instrumental broadening. The nitrogen second positive band transitions are selected for simulation, and temperatures are adjusted to find the best fit (i.e., smallest residual) to the experimental data. An example fit over the wavelength range 325 – 365 nm is shown in Figure 6.11 for a water EC of 15,800 µS/cm.

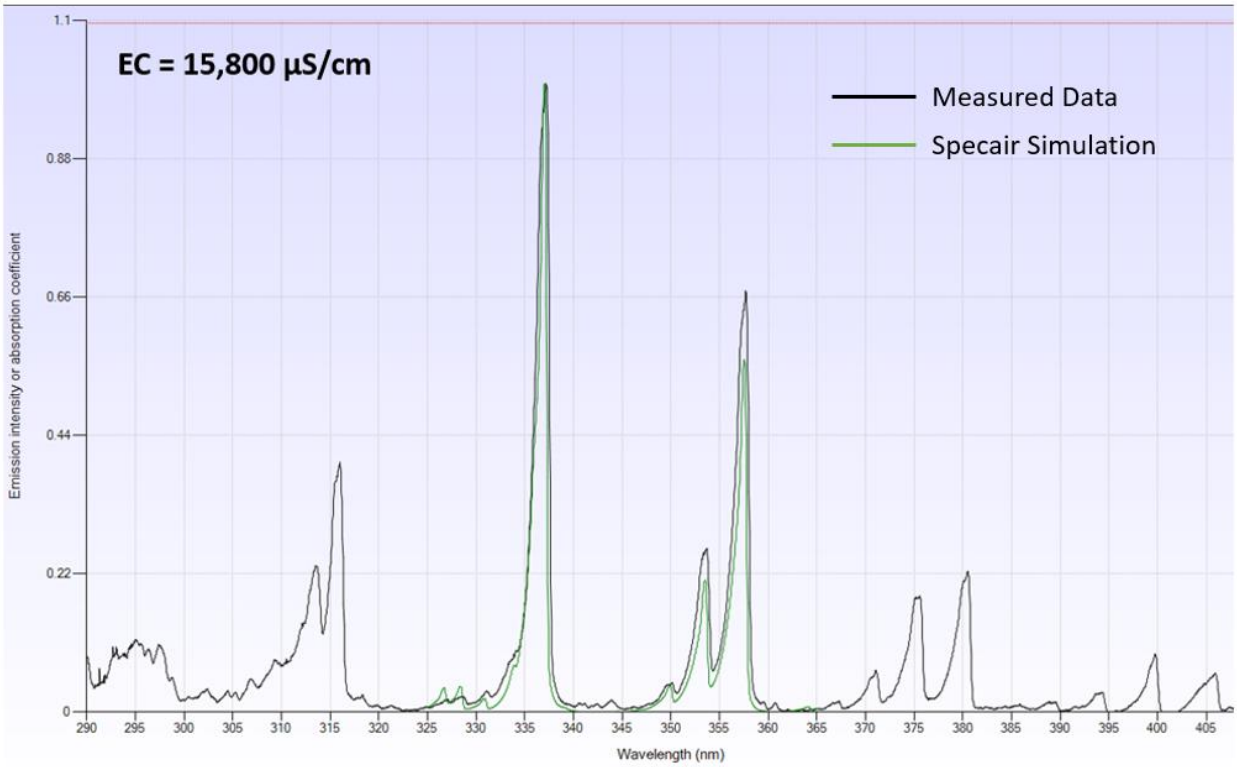


Figure 6.11 Specair simulated nitrogen second positive band (green) compared to the experimental data (black) at water EC = 15,800 µS/cm. The best fit (smallest residual) was found for the wavelength range of 325 – 365 nm. In this case, the gas temperature was estimated at 700 K.

Once the experimental spectrum is normalized and the baseline subtracted, the fitting procedure involves iteratively adjusting four temperatures: electronic, rotational, translational, and vibrational. The electronic, rotational, and vibrational temperatures determine the population of electronic levels, rotational levels, and vibrational levels, respectively, given a Boltzmann distribution at the respective temperature. The translational temperature refers to the classical thermodynamic temperature, which along with the input pressure determines the Doppler and collisional broadening widths and the overall population of molecules in the plasma.[124] For the example shown in Figure 6.11, the gas temperature was estimated at 700 K. For now, this represents an adequate first estimate of the gas temperature, and the same procedure will be used to estimate the gas temperatures of the plasma discharge at varying water electrical conductivities.

The experimentally determined gas temperature vs. water EC is provided in Figure 6.12. The gas temperature varies between about 600 K and 1,200 K. Interestingly, it seems to level out for the most part after about 4,000 µS/cm, which is about the same EC threshold beyond which peak voltage and peak currents level out, as discussed in Section 6.1. The cause of the variations at lower water conductivities is not completely clear, but it may again be related to variations in the discharge mode being captured by the spectrometer over the light accumulation period. The higher gas temperature estimated for the low EC of 4 µS/cm may indicate a higher occurrence frequency of the spark-type discharge mode, which is known to have gas temperatures on the order of 1,000 K.[122] The relatively large error bars make it difficult to identify trends in the data, if they in fact do exist; thus, repeating this experiment with a smaller spectrometer entrance slit width is recommended for future work.

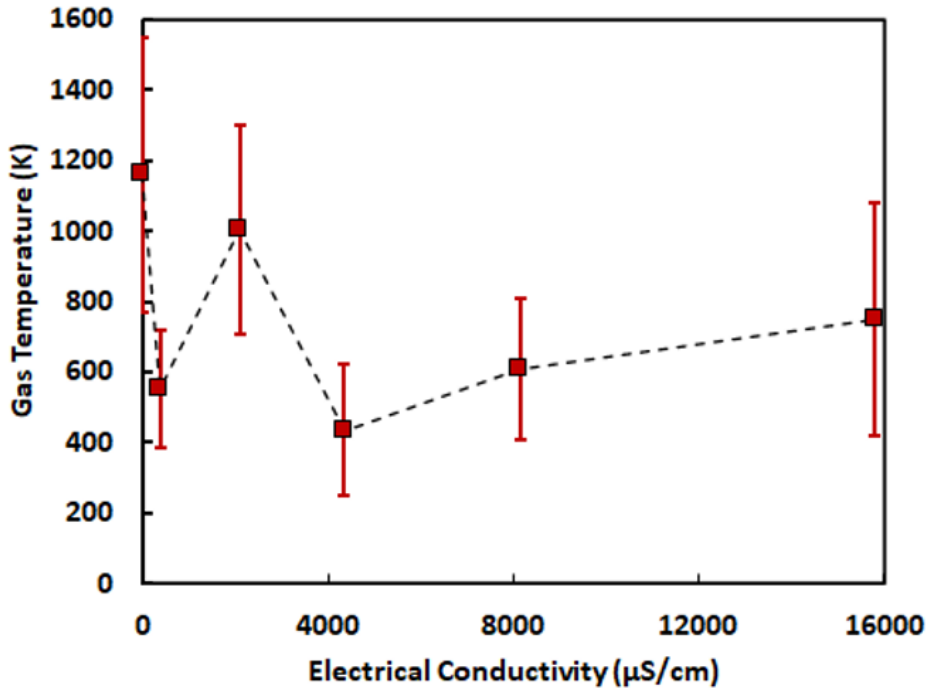


Figure 6.12 Experimentally determined gas temperatures vs. water EC.

While the gas temperature does not appear to be particularly dependent on the water EC, neither did the discharge power, so this result does seem reasonable. Additionally, the gas temperatures falling in the general range between 400 and 1200 K also seems reasonable for this type of discharge (or types of discharges). Moreover, the variation between experimental spectra even at the same water EC highlights some of the challenges related to these non-equilibrium discharges that are also affected by variations in the water jet structures, which play a role in the discharge configuration.

### *6.3.2 Plasma Density*

The plasma density, or electron density, of the discharge is thought to be an important parameter, particularly for the decomposition of PFAS. It has been well established that solvated

electrons ($e_{aq}^-$), are highly reactive in reduction reactions and are capable of cleaving carbon-fluorine bonds.[16], [125] Thus, when electrons from the plasma discharge become solvated, they are able to contribute to the de-fluorination and decomposition of PFAS.[108] For this reason, it is expected that higher plasma densities would lead to higher concentrations of solvated electrons, and thus enhanced rates of PFAS decomposition. However, the actual solvated electron density in water is not measured here. This section aims to determine how the plasma density changes in the packed-bed reactor discharge as the water conductivity increases.

The plasma density of the discharge is determined using the Stark broadening of the hydrogen-alpha ($H_\alpha$) line at 656.28 nm and was selected for its relatively high intensity and isolation from surround lines that would interfere in the analysis (aside from two low intensity nitrogen lines at 652 nm and 659.5 nm). First, the profile of the $H_\alpha$ line is assumed to fit to a Voigt profile, which is the convolution of a Lorentzian profile and a Gaussian profile. The full width at half maximum (FWHM) of the Voigt profile, $\Delta\lambda_V$, is related to Lorentzian and Gaussian profiles as expressed in Equation (6.1):

$$\Delta\lambda_V = \frac{\Delta\lambda_L}{2} + \sqrt{\left(\frac{\Delta\lambda_L}{2}\right)^2 + \Delta\lambda_G^2} \tag{6.1}$$

Where $\Delta\lambda_L$ is the FWHM of the Lorentzian shape profile and $\Delta\lambda_G$ is the FWHM of the Gaussian shape profile. The Doppler and instrumental broadenings contribute to the Gaussian shape profile according to Equation (6.2):

$$\Delta\lambda_G^2 = \Delta\lambda_{Doppler}^2 + \Delta\lambda_I^2 \tag{6.2}$$

Where $\Delta\lambda_{Doppler}$ is the FWHM of the Doppler broadening, and $\Delta\lambda_I$ is the FWHM of the instrumental broadening, which was measured to be 0.44 nm. The FWHM of the Doppler broadening for the $H_\alpha$ line can be found using Equation (6.3)[126]

$$\Delta\lambda_{Doppler} = 4.70 \times 10^{-4} T_{gas}^{1/2} \text{ (nm)} \quad (6.3)$$

Where $T_{gas}$ is rotational temperature estimated from the Specair simulation. Combining the Doppler and instrumental broadening contributions using Equation (6.2) gives the Gaussian contribution to the total the $H_\alpha$ line broadening. On the other hand, the Lorentzian shape profile consists of contributions from the van der Waals broadening and Stark broadening according to Equation (6.4).

$$\Delta\lambda_L = \Delta\lambda_{vdw} + \Delta\lambda_{Stark} \quad (6.4)$$

Where $\Delta\lambda_{vdw}$ is the FWHM of the van der Waals broadening, and $\Delta\lambda_{Stark}$ is the FWHM of the Stark broadening. The van der Waals broadening is calculated using Equation (6.5).[127]

$$\Delta\lambda_{vdw} = \frac{C}{T_{gas}^{0.7}} \text{ (nm)} \quad (6.5)$$

Where $C$ is a coefficient for the perturbing atom or molecule. In this case, we consider both air and water vapor as the perturbing molecules, for which the coefficients equal 3.6 and 4.1, respectively.[128], [129] Finally, the Stark broadening for the $H_\alpha$ line is given by Equation (6.6).[130], [131]

$$\Delta\lambda_{Stark} = 1.78 \times \left(\frac{n_e}{10^{23} \text{ m}^3}\right)^{0.67965} \text{ (nm)} \quad (6.6)$$

Where $n_e$ is the plasma density that is being solved for. Note that Equation (6.3) and Equation (6.6) have been derived specifically for the $H_\alpha$ line. If another line is being used for the plasma density analysis, such as the $H_\beta$ line, the coefficients in these expressions would be different.

From here, the FWHM of the Voigt shape profile is measured from the Voigt fit to the experimentally measured $H_\alpha$ line. An example of this Voigt fit to measured spectral data is shown in Figure 6.13 for a water EC of 4,350 µS/cm. The slight asymmetry of the of the $H_\alpha$ line

profile is likely due to a low intensity nitrogen emission line at 659.5 nm, and so this section of the $H_\alpha$ line profile was not prioritized in the fitted Voigt function.

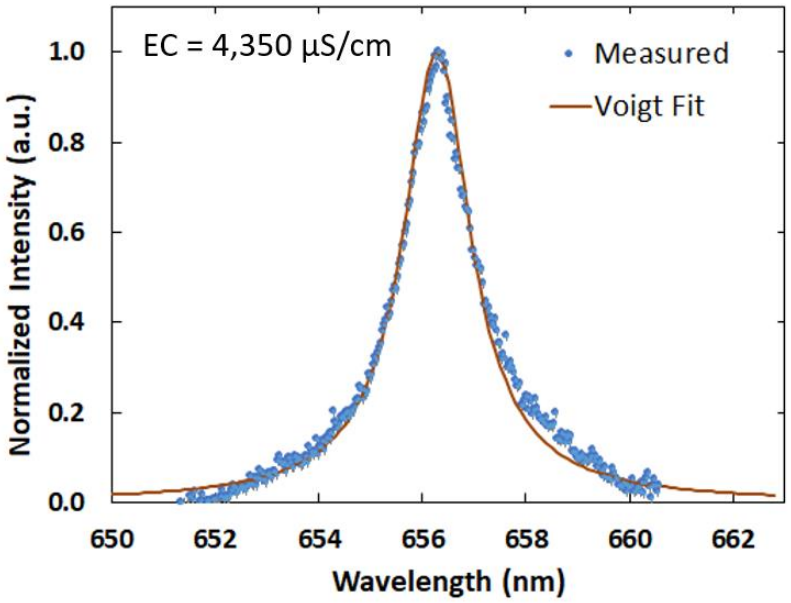


Figure 6.13 An example of a Voigt fit to experimentally measured data, in this case for a water EC = 4,350 µS/cm.

Now that the Gaussian contribution to the $H_\alpha$ line broadening has been determined from the Doppler and instrumental broadenings, and the FWHM of the Voigt profile as been determined from the measured data, the FWHM of the Lorentzian profile can be calculated from Equation (6.1). Then Equation (6.4) is used to calculate the Stark broadening contribution to the Lorentzian FWHM, since both $\Delta\lambda_{vdw}$ and $\Delta\lambda_L$ have been calculated. With the value for $\Delta\lambda_{Stark}$, the plasma density can be extracted from Equation (6.6).

The calculated plasma densities for different water conductivities are shown in Figure 6.14. At water conductivities of 400 µS/cm and above, the plasma density is roughly constant at about $(9 \pm 2) \times 10^{16}$ cm$^{-3}$. However, the low water EC of 4 µS/cm once again has a uniquely higher plasma density of $(14 \pm 3) \times 10^{16}$ cm$^{-3}$. An additional data point was collected at a water

EC of 200 µS/cm and was found to be in general agreement with the plasma density at a water EC of 4 µS/cm. The higher plasma densities measured at these low conductivities is attributed to the higher maximum discharge voltages that occur at the low conductivity and may also be related to the prevalence of the higher intensity spark type discharge mode.

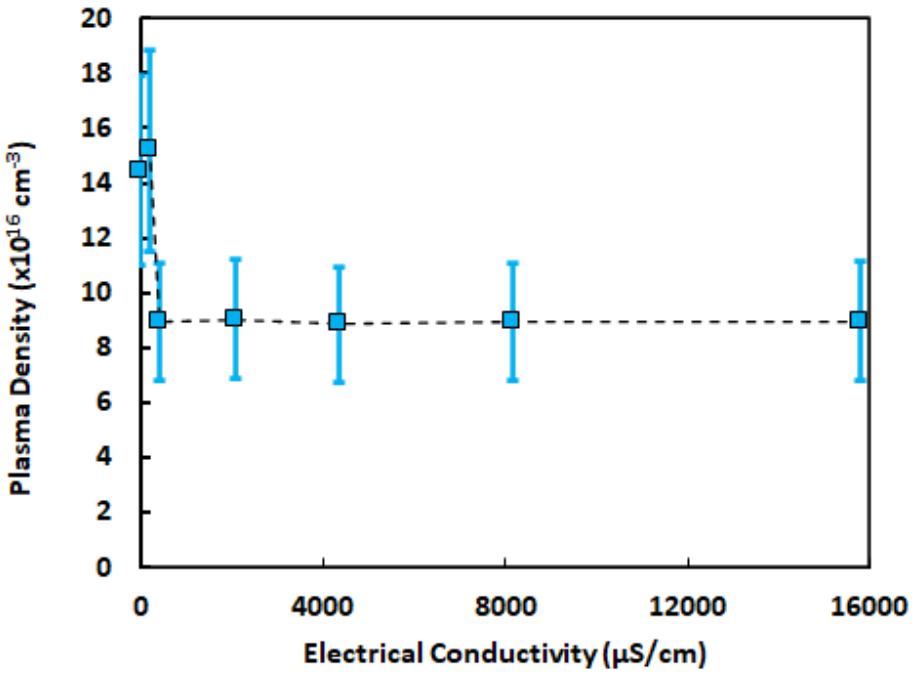


Figure 6.14 Experimentally determined plasma densities vs. water EC.

### 6.4 Water Heating

The energy that goes into heating the water was also investigated at a range of water electrical conductivities. For this experiment, waters of varying conductivities (adjusted again by adding NaCl to deionized water) were treated with the packed-bed reactor at the same flow rate and power supply conditions (4.2 ± 0.3 L/min, 450 V DC charging voltage, 2 kHz pulse repetition frequency) for a total of 4 min. The water temperature was measured before and after the treatment to calculate the energy transferred to the water as heat, *Q*, using Equation (6.7).

$$Q = mC_p(T_f - T_i) \tag{6.7}$$

Where $T_i$ is the initial water temperature, $T_f$ is the final temperature (after the 4 min plasma treatment), $m$ is the mass of water in the system, calculated by multiplying the volume of water in the system (0.5 L) by the water density at the average temperature, $(T_f - T_i)/2$, and $C_p$ is the specific heat capacity of water at the average temperature.

The total energy transferred as heat to the water over the 4 min treatment time, $Q$, is shown in Table 6.1, along with the energy per pulse that went into heating the water, $Q_{pp}$ (calculated by dividing $Q$ by the total number of pulses over the 4 min treatment). The EC shown in Table 6.1 is the average EC over the treatment time. While some heat losses via the reactor plumbing and some heat gain from the pump are expected, these contributions to energy transfer is assumed to be roughly equal for all conductivities over the 4 min treatment time, and thus was not corrected for in this experiment.

Table 6.1 Total energy over 4 min and energy per pulse added to the water as heat at varying water EC. The EC values listed in the tables are the average EC values over the treatment time.

| | Water Heating | |
|---|---|---|
| Conductivity, EC (µS/cm) | Energy over 4 min, $Q$ (kJ) | Energy per pulse, $Q_{pp}$ (mJ) |
| 250 | 15.9 ± 1.0 | 33.1 ± 2.0 |
| 400 | 21.4 ± 1.1 | 44.5 ± 2.3 |
| 2,300 | 23.9 ± 1.0 | 49.7 ± 2.2 |
| 4,500 | 24.5 ± 1.0 | 51.0 ± 2.1 |
| 8,600 | 24.7 ± 0.9 | 51.5 ± 1.8 |

As the water EC increases, the measured heat transfer to the water increases. This might be a result of increased current passing through the water jets at higher EC values leading to increased Joule heating; however, future research should be conducted to evaluate this theory. It is worth noting that there appears to be some plateauing effect here as well, in that the water heating for EC values of 2,300 µS/cm, 4,500 µS/cm, and 8,600 µS/cm are all very similar when

considering the uncertainties. Collecting data at more EC values could help to better assess the water heating behavior as a function of water conductivity.

### 6.5 Conclusions

The results from this chapter seem to indicate that water electrical conductivity is not directly related to certain plasma discharge properties, such as gas temperature and plasma density. Rather, the results seem to suggest that the gas temperature and plasma density may be more related to the discharge mode that occurs, which is in turn may be related to the water conductivity, at least to some extent. Despite the data showing a trend of decreasing peak discharge voltage and increasing peak discharge current with increasing water conductivity, the discharge power and energy per pulse appear to be roughly constant, except for the very low water EC of 4 μS/cm.

A possible explanation for the apparent independence of discharge properties on water conductivity, especially at the higher conductivities (EC ≥ 400 μS/cm), is that the plasma discharge forms under the conditions that are available to it, and the discharge properties are more closely related to the discharge mode that occurs. If a plasma streamer is able to form a conductive channel between the electrodes, then the discharge current rapidly increases while the discharge voltage suddenly drops, resulting in the spark-type ("narrow pulse") discharge mode. If this conductive channel is not formed, then the corona-type ("wide pulse") discharge mode forms. These two distinct discharge modes would be expected to have different plasma properties. The questions remain: what controllable variables determine which mode occurs for a given voltage pulse and what discharge properties (i.e., gas temperatures, plasma densities, and relative reactive species concentrations) are associated with each discharge mode?

The trend of lower peak discharge voltages at higher water conductivities is thought to be related to potential losses to the water jets, but it may also be that the threshold breakdown voltage is lower for higher water conductivities. Perhaps applying significant over-voltages can trigger a spark type discharge even at higher conductivities. Still, the electrical conductivity of the water does appear to contribute towards the likelihood of a certain discharge mode occurring and is likely related to the charge relaxation time and associated streamer propagation lengths. However, this may not be the only explanation for the variations in discharge properties under various conditions.

It would be interesting to take more data points between EC = 4 µS/cm and EC = 400 µS/cm to investigate if there are more direct relationships between water EC and plasma discharge properties in this low EC range. However, waters with low conductivities in this range are unlikely to be encountered in practical treatment applications. Groundwaters containing PFAS contamination would be expected to have electrical conductivities of at least 600 µS/cm, and likely higher. Particularly, if a concentration step is involved, the water EC would be increased roughly proportional to the concentration factor, so treating waters in the range of 4 – 400 µS/cm is not realistic to expect. Still, experiments in this low EC range could shed light on how conductivity is related to the type of discharge mode that is most likely to occur under a given set of conditions, and it is possible that there is a more direct relationship between EC and time-averaged discharge properties, such as gas temperature and plasma density, at low conductivities.

Certainly, further investigation into the natures of these observed discharge modes is needed. If the discharge modes could be isolated, such that only one occurs consistently, how different would the plasma properties be? For now, an investigation of the occurrence ratio of

each discharge mode at varying water conductivities would be a good place to start. Ideally, thousands of waveforms should be collected at each conductivity and analyzed in order to mitigate the effect of sampling bias that would have occurred in this study as the result of only analyzing a few waveforms for a given set of experimental conditions. That would allow one to quantify that there are 2 spark type discharges for every 1,000 corona type discharges at a certain EC, as an example. This ratio would be useful in analyzing and interpreting the discharge properties time-averaged over thousands of pulses.

Overall, the variables and controls that are available to shift the probability of achieving a specific discharge mode should be investigated in future work. Once significant control of the discharge mode is achieved, or at least the ratio can be quantified with some level of certainty, the actual impacts of the gas temperature and plasma density on decomposition efficiencies for PFAS should also be experimentally investigated in order to select reactor conditions that maximize performance and efficiency.

## Chapter 7 Packed-bed Reactor Scale-up Analysis

In Chapter 5, it was demonstrated that the packed-bed reactor is capable of decomposing PFAS to below the MI EPA MCLs. In particular, PFOS and PFHxS, the two most prevalent PFAS found in the Site 1 groundwater, are decomposed to below their respective MCLs (16 ppt and 51 ppt) within 3 hr of treatment. Furthermore, the energy requirements for this treatment are comparable or more competitive than most of the competing PFAS remediation technologies, even though the plasma treatment process has not yet been optimized for energy efficiency or scale-up.

Therefore, plasma treatment using the packed-bed reactor appears to be a promising emerging technology for the decomposition of PFAS in waters. However, the results presented in Chapter 5 are for laboratory-scale volumes (0.5 L) and is a recirculating batch treatment. When it comes to deploying a water treatment technology, typically a continuous flow configuration is highly preferred over batch treatment. Indeed, most existing water treatment systems deal with continuous flows (i.e., a certain water flow rate per minute, per day, etc.).

For an emerging water treatment technology to be adopted, the continuous flow criterion is highly advantageous and almost a requirement. This relates to the practicality of implementing a new technology into existing systems, such as wastewater treatment plants, but it also relates to the practicality of implementing a solution to deal with contaminated groundwaters (i.e., well waters). Groundwater wells have natural replenishment flows which generally set the maximum extraction rate (i.e., maximum flow rate that can be withdrawn

without drying out the well). This flow rate limit varies depending on the well, but in general, the maximum flow rate expected would be around 50 gallons per minute (gpm).

Indeed, the target flow rate for the treatment of Site 1 groundwater is about 40 – 45 gpm (57,600 – 64,800 gallons per day). If a plasma-based treatment system can accommodate a flow rate of 45 gpm (170 L/min) on a continuous flow basis, it should be able to treat a range of contaminated groundwater sites. Thus, as a demonstration pilot, the flow rate requirement for a practical, scaled-up system is assumed to be 170 L/min.

Beyond the practical capability of treating water on a continuous flow basis at flow rates up to 45 – 50 gpm, the scalability of the system is also important. Ultimately, scale up to municipality flow rates would be a key next step, without excessive equipment/infrastructure. Finally, the cost of treatment and the footprint of the treatment facility are also important.

The purpose of this chapter is to propose a treatment architecture amenable to continuous flow processing with the capability of treating relevant flow rates (up to 170 L/min). The hypothesis is that batch-mode kinetics (based on data from Chapter 5) can be used as a basis in the design of a continuous flow system provided that the input water receives an equivalent exposure to the plasma (i.e., the same power density or discharge power per volume of water being treated, and an equivalent number of passes through the plasma region for a given volume of water).

Section 7.1 proposes an architecture for converting the batch-mode packed-bed reactor into a continuous flow treatment configuration and provides a model for estimating the system size and performance based on the batch kinetics data. The approach is to use a series-parallel system of micro-reactors each with internal recirculation to achieve an equivalent plasma exposure, or an equivalent number of passes through the plasma section (plasma head) as the

water received in the batch-mode treatment, thus preserving the batch kinetics. The use of recirculation stages and the use of microreactors to achieve the desired treatment or synthesis goal is not new. Its currently an active area of research and application in chemical engineering.[132] Furthermore, a concentration stage can be used to reduce the total system size and should enhance the mass removal efficiency of the plasma treatment process.

### 7.1 Continuous Flow Architecture and Model

Broadly, the goal of this work is to convert a batch treatment process into a continuous flow treatment process. Whereas in a continuous flow reactor, the reactions typically take place either in a localized reaction zone with either a plug flow or a distribution of reaction zones over a distance to deliver the proper dose of reactive species to, the proposed architecture achieves the required treatment dose by recirculating water through the plasma "active zone" of a micro-reactor with rapid recirculation fitted to a well-sized detention tank.

In this case, plasma exposure (i.e., plasma-water contact area and contact time) is key. Figure 7.1 compares the distributed, conventionally implemented continuous flow system with the proposed plasma micro-reactor with internal recirculation of the water past the plasma discharge region. In the conventional approach, the most straightforward way to implement plasmas in a continuous flow system is to distribute the plasmas throughout the flow path (Figure 7.1a). The decomposition occurs primarily at the reaction zone where the plasma discharge is in contact with the water. Such a system can become prohibitively large and complex, particularly when scaling-up to higher flow rates, as several flow lines in parallel each containing a multitude of plasma applicators would be required to realize local treatment conditions faithful to that of a batch reactor. For this type of continuous flow system, the water passes by each plasma head only once, thus many plasma heads in series are required to achieve sufficient plasma exposure.

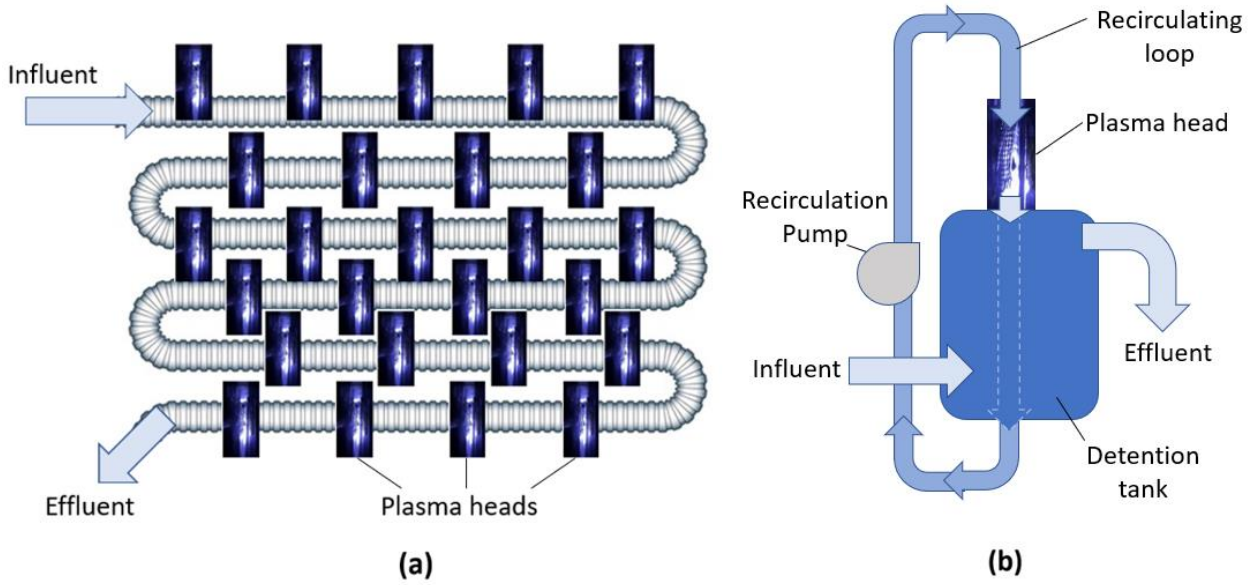


Figure 7.1 Comparison of (a) conventional continuous flow reactor and (b) the proposed plasma micro-reactor with internal recirculation.

On the other hand, through rapid recirculation as depicted in Figure 7.1b, similar plasma contact times can be achieved as in the distributed string of reactors but in a significantly more compact system. Here, fluid to be treated enters a detention tank sized to have a characteristic hydraulic detention time. Influent water is rapidly cycled through the plasma head so that the number of passes per unit time matches that was utilized in the batch reactor testing. This water then passes into the next cycler stage such that the requisite treatment is achieved after passing through a few micro-reactors in series, thus eliminating the multitude of reactors distributed over distance.

The performance of the proposed staged plasma micro-reactor treatment process can be estimated using the tanks-in-series model applied to a reactive system.[78] Mass balances for *n* number of tanks in series yield the following expression for a first-order reaction:

$$\frac{C_{n,out}}{C_0} = \frac{1}{(1+k\tau)^n} \tag{7.1}$$

Where $C_0$ is the initial contaminant concentration entering a series of $n$ reactors, $C_{n,out}$ is the contaminant concentration at the outlet of the series of reactors, $k$ is the first-order decay constant, and $\tau$ is the hydraulic retention time at each plasma stage. Equation (7.1) can be rearranged to solve for the value of $k\tau$ required to achieve a desired $C_{n,out}$ for a given $C_0$ and $n$.

$$k\tau = \sqrt[n]{\frac{C_0}{C_{n,out}}} - 1 \tag{7.2}$$

If a concentration stage is employed prior to the plasma treatment, then $C_0$ is replaced by $C_{conc} = C_0 \times CF$, where CF is the concentration factor achieved by the concentration stage, and $C_{conc}$ is the concentration of concentrate/reject stream of the membrane concentration stage. A schematic diagram of a continuous flow staged plasma treatment process with a membrane concentration stage is provided in Figure 7.2.

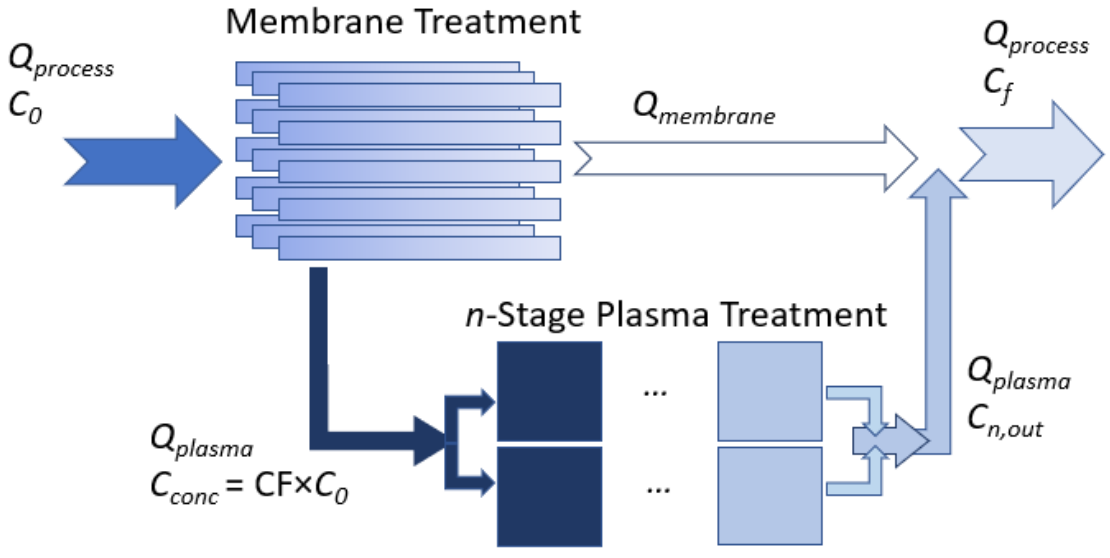


Figure 7.2 Schematic diagram of a continuous flow plasma treatment process with a membrane concentration stage (from T. Olson, personal communication).

For the analysis presented here, the following assumptions are made: (1) PFOS is the target compound, (2) PFOS undergoes first-order decay by plasma treatment, (3) the first-order rate constant for PFOS removal is 0.04 $min^{-1}$, (4) $n$ plasma reactors in series (stages) with $i$ parallel plasma process lines provide the desired level of treatment, (5) each reactor exhibits perfect mixing, (6) the influent concentration of PFOS without concentration is 200 ppt, (7) the permeate stream exiting the membrane treatment stage has a PFOS concentration of 0 ppt, and (8) the desired discharge concentration, $C_{des}$, is 12 ppt (75% of the MI MCL, 16 ppt). The rate constant for PFOS removal reflects that realized in the batch process experiment, and the 200 ppt is derived from measurements of the PFOS concentration in the groundwater at the Site 1 legacy well.

For a total process flow rate, $Q_{process}$, of 170 L/min, Table 7.1 provides the required values of $k\tau$ and $\tau$, as well as the required volume per tank, $V_{tank}$, and total tank volume ($V_{total} = n \times i \times V_{tank}$). The value for $C_{n,out}$ varies based on the concentration factor (CF) as a result of blending the membrane treatment permeate with the plasma treatment effluent, such that the final PFOS concentration exiting the system, $C_f$, is equal to the desired discharge concentration, $C_{des}$. As can be seen from the table, the total tank volume for the staged plasma treatment system can be reduced by concentrating the PFOS prior to the plasma treatment. Meanwhile, increasing the number of plasma reactors in series can also reduce total tank volume required, but comes at the cost of additional equipment (i.e., tanks, recirculation pumps, plasma).

Table 7.1 The required value of $k\tau$ and $\tau$, as well as the required volume per tank, $V_{tank}$, and total tank volume $V_{total}$ calculated using Equation (7.2) for varying values of concentration factor (CF) and number of plasma stages ($n$). Here, $q$ is the flow rate through an individual plasma stage unit, where $q = Q_{process}/(i \times CF)$ and $i = 2$ for all cases. The row in boldface (CF = 4, $n$ = 3) denotes the configuration depicted in Figure 7.3.

| CF | $n$ | $q$ (L/min) | $C_{conc}$ (ppt) | $C_{n,out}$ (ppt) | $k\tau$ | $\tau$ (min) | $V_{tank}$ (L) | $V_{tank}$ (gal) | $V_{total}$ (gal) |
|---|---|---|---|---|---|---|---|---|---|
| 1 | 3 | 85 | 200 | 12 | 1.55 | 38.9 | 3,303 | 872 | 5,229 |
| 1 | 4 | 85 | 200 | 12 | 1.02 | 25.5 | 2,169 | 572 | 4,578 |
| 2 | 3 | 42.5 | 400 | 24 | 1.55 | 38.9 | 1,652 | 436 | 2,615 |
| 2 | 4 | 42.5 | 400 | 24 | 1.02 | 25.5 | 1,084 | 286 | 2,289 |
| 3 | 3 | 28.3 | 600 | 36 | 1.55 | 38.9 | 1,101 | 291 | 1,743 |
| 3 | 4 | 28.3 | 600 | 36 | 1.02 | 25.5 | 723 | 191 | 1,526 |
| **4** | **3** | **21.3** | **800** | **48** | **1.55** | **38.9** | **826** | **218** | **1,307** |
| 4 | 4 | 21.3 | 800 | 48 | 1.02 | 25.5 | 542 | 143 | 1,144 |

The configuration shown in Figure 7.3 (CF = 4, $n$ = 3, $i$ = 2) was selected for further analysis due to its relatively small total tank volume (826 L) and number of tanks ($n \times i$ = 6 tanks). In this case, the total process flow rate of 170 L/min enters the membrane treatment stage with an initial PFOS concentration of 200 ppt. The membrane stage concentrates the PFOS by a factor of 4 and diverts water with a PFOS concentration of 800 ppt at a flow rate of 42 L/min to the 3-stage plasma treatment section with 2 parallel process lines. The water exiting the plasma treatment section contains a PFOS concentration of 48 ppt and is blended with the permeate from the membrane treatment to reach a final PFOS concentration of 12 ppt.[133]

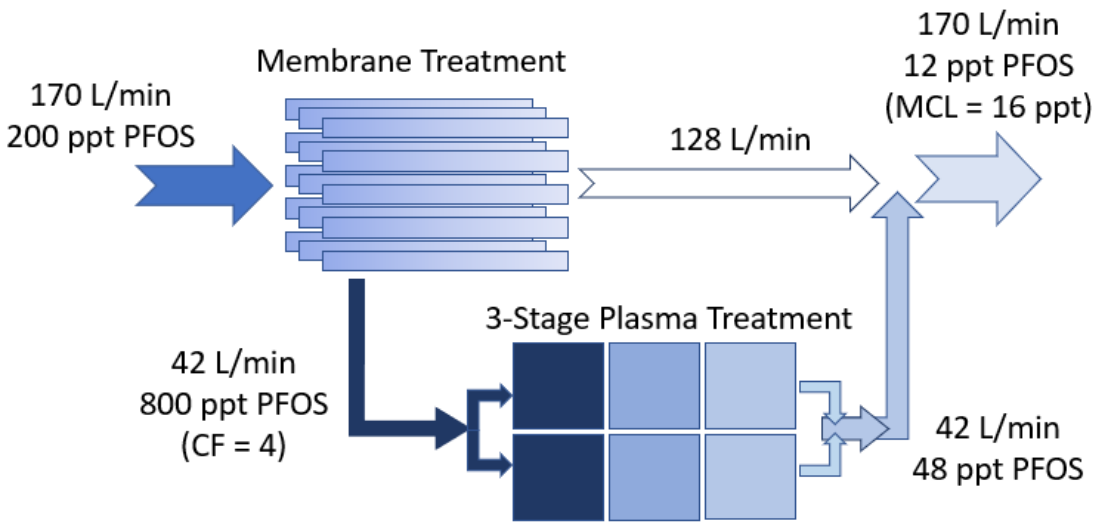


Figure 7.3 Schematic diagram of a continuous flow plasma treatment process with a membrane concentration stage for $Q_{process}$ = 170 L/min, CF = 4, $n$ = 3, $i$ = 2, and $C_{des}$ = 12 ppt PFOS.

Using this model and assumptions allows for the calculation of the PFOS concentration exiting each micro-reactor stage. For the model conditions described in Figure 7.3, these exit PFOS concentrations are shown in Figure 7.4. The PFOS concentration exiting the third plasma stage is $C_{3,out}$ = 48 ppt, which when blended with the membrane treatment permeate gives the desired $C_{des}$ = 12 ppt PFOS.

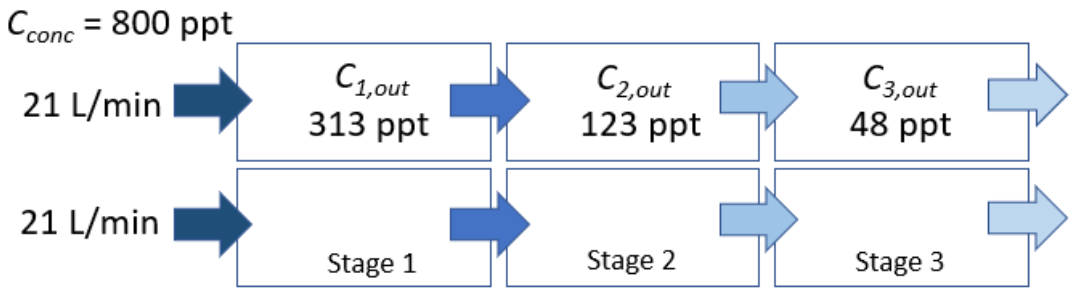


Figure 7.4 Concentration of PFOS exiting each stage of the plasma treatment process based on the model conditions described in Figure 7.3.

The plasma treatment process relies on the assumption that the water recirculates past the plasma active region the same number of times as in the batch treatments from which the first-order rate constant is estimated (i.e., equivalent plasma exposure and power density). This value is approximately 8 passes per min at 2 kHz pulse repetition frequency ($1.2\times10^5$ pulses per min). For an individual tank volume of 826 L, the recirculation flow rate would need to be 6,606 L/min (1,743 gal/min)! Thankfully, the required recirculation flow rate can be reduced by adjusting some of the micro-reactor variables.

For example, each tank can be affixed with multiple plasma heads, as illustrated in Figure 7.5 for the case of 6 plasma heads per tank. This essentially multiplies the plasma contact area that the water sees during each pass through the micro-reactor. As such, the required number passes per minute (based on a single plasma head) is divided by the number of plasma heads per tank, while the total number of pulses per minute is conserved.

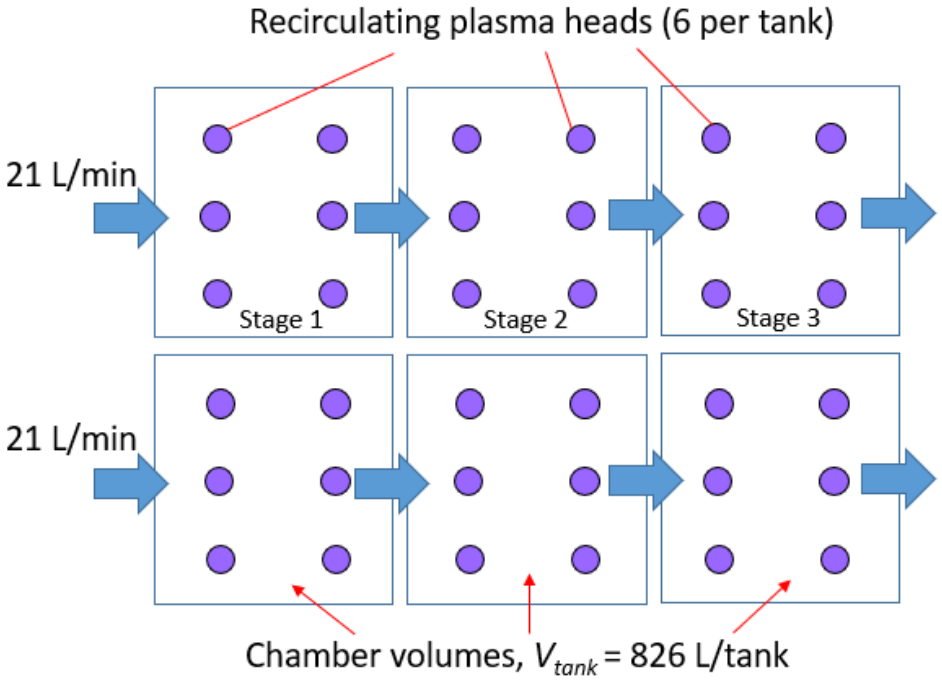


Figure 7.5 Schematic diagram of the 3-stage plasma treatment process with two parallel process lines based on the model configuration from Figure 7.3. Each tank has a volume of 826 L with 6 recirculating plasma heads per tank.

For the case of 6 plasma heads per tank, the required recirculation flow rate is reduced to 1,101 L/min (290 gal/min). The plasma power per micro-reactor will also increase proportional to the number of plasma heads, but this may prove worthwhile to avoid excessive recirculation flow rate requirements. It will be shown in Table 7.2 that high recirculation flow rates can consume a significant amount of power (e.g., 26 kW for a 6,606 L/min recirculation flow rate), and the proposed configuration requires six of these pumps (one per tank). Other strategies for reducing the recirculation flow rate, such as increasing the pulse repetition frequency, are discussed in Section 7.2 in the context of energy costs.

### 7.2 Energy Cost Assessment

Of course, for this continuous flow treatment configuration employing a membrane treatment concentration stage followed by a staged plasma treatment process to be competitive, the energy costs must be reasonable. This section estimates the energy costs associated with the plasma discharges, recirculation pumps, and the membrane concentration stage. The power consumed by the plasma discharges is assumed to be 130 W per plasma head, based on the measured discharge power from Section 5.3. The cost of energy is assumed to be 0.16 USD/kWh, throughout. For now, the cost of the membrane-based concentration is assumed to be 3.5 USD/kgal, and the power consumed by the recirculation pumps is estimated using the expression given in Equation (7.3).

$$P_h = \frac{Q_{recirc} \times p}{(3.6 \times 10^6 \times \eta)} \text{ (kW)} \tag{7.3}$$

Where $P_h$ is the hydraulic power (kW), $Q_{recirc}$ is the recirculation flow rate ($m^3$/hr) for one of the tanks in the staged plasma treatment process, $p$ is the differential pressure assumed to be 207 kPa, and $\eta$ is the pump efficiency, here assumed to be 87%.

Table 7.2 provides the energy cost estimates for powering the plasma heads ($E_{plasma}$), the recirculation pumps ($E_{pump}$), and the membrane concentration stage ($E_{membrane}$), along with the sum of these energy costs ($E_{total}$), once again based on the model configuration from Figure 7.3 ($Q_{process}$ = 170 L/min, CF = 4, $n$ = 3, $i$ = 2, and $C_{des}$ = 12 ppt PFOS). This is done first for the base case in which there is one plasma head per tank (6 total tanks, 6 total plasma heads). Then three possible energy cost enhancement options are considered, primarily based on reducing the energy costs associated with the recirculation pumps, which is related to the required number of passes per minute, $n_{pass}$, while maintaining an equivalent plasma exposure.

Table 7.2 Energy cost estimates for powering the plasma heads ($E_{plasma}$), the recirculation pumps ($E_{pump}$), and the membrane concentration stage ($E_{membrane}$), along with the sum of these, $E_{total}$. Here, $Q_{recirc}$ is the recirculation flow rate for a single tank, and $q_{recirc}$ is the recirculation flow rate through a single plasma head.

| | | Energy Cost Enhancement Options | | | |
|---|---|---|---|---|---|
| Variable | (units) | base case | # plasma heads/tank ($n_{ph}$) | pulse frequency ($f_p$) | contact area ($A_c$) |
| $f_p$ | (kHz) | 2 | 2 | 10 | 10 |
| $p_{plasma}$ | (W/head) | 130 | 130 | 650 | 650 |
| $n_{ph}$ | (#/tank) | 1 | 6 | 6 | 6 |
| $A_c/A_{c,0}$ | | 1 | 1 | 1 | 2 |
| $n_{pass}$ | (#/min) | 8.00 | 1.33 | 0.27 | 0.13 |
| $Q_{recirc}$ | (L/min) | 6,606 | 1,101 | 220 | 110 |
| $Q_{recirc}$ | (gpm) | 1,743 | 291 | 58.1 | 29.1 |
| $q_{recirc}$ | (L/min) | 6,606 | 184 | 36.7 | 18.4 |
| $q_{recirc}$ | (gpm) | 1,743 | 48.4 | 9.68 | 4.84 |
| $P_{plasma}$ | (kW) | 0.78 | 4.68 | 23.4 | 23.4 |
| $P_{pump}$ | (kW) | 157 | 26.1 | 5.22 | 2.61 |
| $E_{plasma}$ | (kWh/day) | 18.7 | 112 | 562 | 562 |
| $E_{plasma}$ | (kWh/kgal) | 0.29 | 1.74 | 8.69 | 8.69 |
| $E_{plasma}$ | (USD/kgal) | 0.05 | 0.28 | 1.39 | 1.39 |
| $E_{pump}$ | (kWh/day) | 3,759 | 626 | 125 | 62.6 |
| $E_{pump}$ | (kWh/kgal) | 58.2 | 9.70 | 1.94 | 0.97 |
| $E_{pump}$ | (USD/kgal) | 9.31 | 1.55 | 0.31 | 0.16 |
| $E_{membrane}$ | (USD/kgal) | 3.5 | 3.5 | 3.5 | 3.5 |
| $E_{total}$ | (USD/kgal) | 12.86 | 5.33 | 5.20 | 5.05 |

For the base case, there is only one plasma head per tank and the pulse repetition frequency is 2 kHz. This is directly based on the laboratory reactor experiments, from which the observed first-order rate constant for PFOS removal was approximately 0.04 $min^{-1}$ (the rate constant used in the model). In the batch-mode experiment, 0.5 L of water was recirculated through the system at approximately 4 L/min; hence, the treated volume of water passed through the plasma discharge region approximately 8 times per min ($n_{pass}$ = 8 passes/min). When the tank volume is scaled-up to 826 L/tank, the required recirculation flow rate becomes 6,606 L/min. For 6 pumps (1 pump/tank), the hydraulic power of the recirculation is estimated at 157 kW (9.31 USD/kgal). The energy cost of the recirculation pumps represents to 72% of the total energy cost. Clearly, it would be beneficial to find ways of decreasing the recirculation pumping costs.

The first enhancement option, which was already mentioned in Figure 7.5, is increasing the number of plasma heads per tank, $n_{ph}$. This increases the plasma contact area and the number of pulses per pass by the number of plasma heads, such that the total effective plasma contact area, $A_{c,total}$, is equal to the plasma contact area of a single plasma head, $A_c$, multiplied by the number of plasma heads per tank (i.e., $A_{c,total} = A_c \times n_{ph}$). In this way, the required number of passes of the volume through the plasma heads per minute is reduced by a factor of $n_{ph}/n_{ph,0}$, where $n_{ph,0}$ is the number of plasma heads in the base case (i.e., a factor of 6). Increasing the value of $n_{ph}$ from 1 to 6 decreases the total energy cost from 12.86 USD/kgal to 5.33 USD/kgal, a factor of nearly 2.5. While the plasma power increases proportionally to the number of plasma heads (4.68 kW for 6 heads/tank, total 36 heads vs. 0.78 kW for 1 head/tank, total 6 heads), this is offset by the reduced hydraulic power of the pumps.

Next, the pulse repetition frequency, $f_p$, and correspondingly the plasma discharge power per head, $p_{plasma}$, can be increased to further reduce the required $n_{pass}$ and recirculation flow rate per tank, $Q_{recirc}$. Here, it is assumed that the dose delivered per pulse is constant so that the rate of dose delivery can be increased greatly by simply increasing the frequency. In this case, the pulse repetition frequency is increased by a factor of 5 (from 2 kHz to 10 kHz), and the plasma discharge power per reactor head is assumed to increase commensurately from 130 W to 650 W. While the total volume of the water in each tank is recycled through the plasma discharge region fewer times per minute, the pulse frequency is increased to accommodate, such that a given slug of water passing through the staged plasma treatment system still receives the same number of pulses as in the base case. The level of treatment should be preserved, but the energy costs associated with the treatment, particularly the contribution from the recirculation pumps, can be decreased.

Lastly, it was observed during the packed-bed reactor batch-mode experiments that water jets do not necessarily remain separated throughout the entire length of the plasma discharge section (4.8 cm). Rather, the water jets tended to converge towards the bottom half of the discharge region and contact the central electrode resulting in power losses and a reduction to the maximum potential plasma contact area. If the pressure at the "showerhead" nozzle inlet can be optimized to sustain the water jet structures for the full length of the plasma discharge section, the plasma-water contact area per plasma head could be approximately doubled. This effect is included in the model through the ratio $A_c/A_{c,0}$, where $A_{c,0}$ is the contact area of the base case; thus, doubling the contact area via nozzle pressure optimization corresponds to $A_c/A_{c,0} = 2$ which further reduces the required value of $Q_{recirc}$ and the associated $E_{pump}$. After modeling these various enhancement factors, the total energy cost is estimated at 5.05 USD/kgal of water treated

(1.30 USD per thousand liters). At this point, the cost of the membrane-based concentration stage which is assumed to be a fixed cost of 3.5 USD/kgal accounts for 69% of the total energy cost.

Note that the assumption that the first-order rate constant can be preserved from the batch-mode treatment experiment and extended to continuous flow treatment by providing equivalent plasma exposure in the manner described here still needs to be validated. Additionally, the assumptions made to reduce the recirculation flow rate by increasing the number of plasma heads per micro-reactor tank, increasing the pulse repetition frequency, and increasing the plasma contact area by optimizing the pressure at the "showerhead" nozzle inlet also need to be tested. Validating or disproving the validity of these assumptions will be the subject of future work.

Furthermore, the plasma discharge power has not been optimized. Once the desired power supply conditions (i.e., output voltage and pulse repetition frequency) are selected for a particular discharge configuration, impedance matching between the power supply and the plasma load can be optimized to reduce reflected and wasted power. This will also be a subject of future work.

Finally, the issue of system size should be addressed. Here, the overall footprint of the proposed continuous flow staged plasma treatment system with upstream membrane-based concentration is mostly attributed to the size of the detention tanks. The plasma reactor heads and recirculation pumps can be fitted to these detention tanks to minimize the additional volume. Thus, the total system volume is estimated to be approximately 5 $m^3$. Even if the power supplies and instrumentation take up an additional 5 $m^3$ for a total volume of 10 $m^3$, this system could

potentially fit on a standard 10-ft truck having a volume of about 11 $m^3$, and it could certainly fit in a standard 40-ft shipping container (33 $m^3$ volume).

Overall, while a relatively simple treatment train consisting of a concentration stage followed by a series of plasma-water reactors could potentially treat contaminated well water such as that collected from Site 1 for approximately 5 USD/kgal of water treated at a relevant flow rate of 170 L/min (45 gpm), there are thousands of contaminated wells across the country, located in all 50 states and two territories.[134] Indeed, the concept of a mobile treatment unit capable of traveling between contaminated sites that uses a combination of concentration and destruction technologies is appealing and appears to be possible. Such a unit would likely be powered by a gas generator in the near term but potentially powered by solar energy in the future.

In many ways, the problem of PFAS contamination in groundwaters appears monumentally daunting, and it is. Still, water is a local resource and treating a few local groundwater wells, particularly those that are highly contaminated with PFAS, has the potential to make a significant difference in terms of the PFAS levels in that local community. Certainly, damage has already occurred, and PFAS has been detected in >98% of peoples' blood in the United States.[135], [136] Nevertheless, if a method for decomposing PFAS to less harmful chemicals is not implemented, these substances will presumably continue to bioaccumulate in the environment, and in humans, leading to increased occurrences of PFAS related health issues.

# Chapter 8 Summary and Future Work

In this dissertation, non-thermal plasma is investigated for the treatment of groundwaters containing PFAS contamination. Time-resolving the PFAS concentrations throughout the duration of treatment has provided insights into the batch-mode decomposition kinetics. As the electrical conductivity of the water increases with plasma treatment time, the discharge properties such as gas temperature, plasma density, and deposited power do not change substantially. Finally, a treatment architecture is proposed for converting the laboratory batch-mode treatment into a continuous flow process, and a model is presented to predict the treatment performance, system size, and energy costs based on data from the batch-mode kinetics experiments.

## 8.1 Summary

Chapter 1 provided a brief introduction to water resources and contaminants of emerging concern. While many of these contaminants can be mineralized using advanced oxidation processes, the strength of the carbon-fluorine bond found in PFAS resists decomposition by hydroxyl radical attack, for the most part. Several technologies exist or are emerging for the remediation of PFAS contamination in waters, but the most mature and feasible of these technologies currently fall into the category of absorptive/separative techniques which do not decompose PFAS to less harmful compounds. Instead, they merely move the PFAS into a concentrated media which then must be incinerated or isolated for long term storage, and thus runs the risk of reintroducing the contamination back into the environment if not properly

handled. Plasma-based treatment of PFAS contaminated waters has been introduced as a promising emerging technology for the cost-effective destruction of PFAS.

Chapter 2 provided a brief introduction to plasmas, with an emphasis on non-thermal plasmas in contact with liquids, primarily in the context of plasma-based water treatments (i.e., decomposition or mineralization of contaminants from waters by plasma action). While the use of plasma-liquid interactions for liquid processing and water treatment has shown great promise at laboratory scales, a principal challenge to realizing the successful commercialization of these plasma-based technologies is scaling up to commercially relevant throughputs. Thus far, this has not been achieved, but a few plasma-water reactor configurations have demonstrated capabilities towards treating pilot-scale volumes or flow rates. Among these are the early commercialization attempt by AquaPure and the recent field pilot reactor for PFAS remediation by DMax Plasma and Clarkson University.

In Chapter 3, an overview of the experimental methods used for evaluating plasma-based water treatment was provided, starting with the assessment of contaminant removal from waters and wastewaters. A case study highlighting the interference of hydrogen peroxide in standard chemical oxygen demand assessments was presented, intended to notify the plasma community that residual hydrogen peroxide from plasma treatment can affect the interpretation of this standard water quality metric. Next, the quantification of PFAS concentrations in water samples by liquid chromatography – tandem mass spectrometry is discussed, a measurement technique which was used extensively in Chapter 4 and Chapter 5. The equipment used for water property measurements such as electrical conductivity, pH, and temperature were provided, and titration and spectrophotometric techniques for the quantification of chemical species derived from the plasma treatment process were discussed. Lastly, an overview optical emission spectroscopy as

a plasma phase diagnostic was given, which was later used to estimate the gas temperature and plasma density of the packed-bed reactor discharge at a range of water conductivities.

In Chapter 4, two different plasma reactors were investigated for the decomposition of PFAS in waters. While the effects of feed gas (air vs. argon) and power source (AC vs. nanosecond pulsed) had relatively minor influence on the percentage of PFOS removed for a given treatment time, the geometric approach of increasing the plasma-water contact area offered by the packed-bed reactor was identified as a particularly promising configuration. Indeed, plasma treatment of water is recognized as primarily a surface treatment process in general, but particularly so for the decomposition of PFAS; thus, the contact area was identified as a critical reactor variable. This represents a general trend in plasma-water reactor performance: reactive species transfer from the plasma is limited by this contact area, and since decomposition of contaminants in water relies on reactive species transfer from the plasma to the water, optimizing the contact area is a key reactor design consideration, particularly for scale-up. Furthermore, similar removal percentages were achieved for both the high- and low-PFAS concentration waters, indicating that the mass removal efficiency of the plasma treatment is improved when treating high concentrations. As such, plasma-driven decomposition of PFAS may be more effectively implemented into a treatment train featuring an upstream concentration stage.

In Chapter 5, the initial plasma source exploration study from Chapter 4 was expanded upon by time-resolving the PFAS concentrations throughout the treatment time, thus offering insights into the batch-mode kinetics. First, a high concentration (5.7 ppm) spiked PFOA test demonstrated the packed-bed reactor's capability to cost-effectively decompose PFOA with an EE/O estimated at 45 kWh/m$^3$. Next, Site 1 groundwater was treated with the DBD plasma jet reactor for 120 min and the decomposition kinetics were analyzed by measuring the PFAS

concentrations at 10 points throughout the treatment. The longest chain PFAS compounds present in the groundwater sample, PFOS and PFNA, both decayed approximately according to empirical first-order kinetics. On the other hand, the shorter chain PFAS tended to increase during the early treatment times, which was also observed for PFHxS in Chapter 4. In addition, Site 1 groundwater was treated with the packed-bed reactor for a long duration in attempt to reduce the PFAS concentrations to below the MI EPA proposed maximum contaminant levels. This was achieved for all compounds except for PFOA. While the original high concentration PFOA test was successful, at low PFOA concentrations (starting around 25 ppt), a contamination source within the reactor prevented the PFOA from being decomposed to below the MI EPA limit of 8 ppt. This prompted a series of tests to systematically identify and eliminate any sources of PFOA contamination from within the reactor. Ultimately, the elimination of a 3-D printed nozzle component appeared to solve the contamination problem. A follow up test is being conducted to confirm that PFOA can be removed to below 8 ppt using the packed-bed reactor.

In Chapter 6, the effects of changes in water electrical conductivity on plasma discharge properties was investigated. While the voltage-current waveforms did show a general trend of decreasing peak voltage and increasing peak current with increasing water conductivity, the results indicated that the water conductivity does not directly affect certain discharge properties, such as deposited power, gas temperature, and plasma density as much as originally anticipated. Although the gas temperature and plasma density were calculated to be higher at a very low conductivity of 4 µS/cm, as the water conductivity increased above about 400 µS/cm the gas temperature and plasma density of the discharge remained roughly constant, considering the uncertainties in the measurements. This behavior might be related to the likelihood of a

particular discharge mode taking place. Indeed, one of the most interesting observations from this study was the occurrence of two distinct discharge modes. One is the typical pulsed corona discharge that is usually observed for waters with conductivities around that of tap water or higher (>700 µS/cm), and the other is a type of transient spark discharge which is generally only observed at low conductivities (<400 µS/cm). The spark-type discharge mode is thought to be associated with longer charge relaxation times at low water electrical conductivities, which allows plasma streamers to propagate further through the array of water jets and temporarily form a conductive channel between the electrodes, thus resulting in the sudden drop in voltage and simultaneous rise in current.

In Chapter 7, an architecture was proposed for converting the recirculating batch packed-bed reactor configuration into a continuous flow process featuring a series-parallel arrangement of packed-bed micro-reactors each having internal recirculation. To accompany the proposed architecture, a model based on the tank-in-series model applied to a reactive flow was developed using the observed first-order rate constant for the removal of PFOS from the long duration packed-bed treatment from Chapter 5. This model incorporates the concept of an equivalent plasma exposure as achieved in the laboratory packed-bed reactor experiment as a basis for estimating the required recirculation flow rates, based on the size of the detention tanks estimated from the tanks-in-series model. A simple treatment train featuring a membrane concentration stage prior to the plasma treatment and capable of removing an initial PFOS concentration of 200 ppt to below the MI EPA MCL of 16 ppt at a continuous flow rate of 170 L/min is provided. A cost assessment including energy costs incurred by the plasma, the recirculation pumps, and the concentration stage was conducted, and the base case cost estimate is about 13 USD/kgal of water treated. Energy cost enhancement options are proposed,

including increasing the number of plasma discharge sections per tank (plasma heads per tank), which is estimated to reduce the treatment cost to approximately 5 USD/kgal. This would make the proposed scaled-up continuous flow packed-bed reactor with membrane concentration stage competitive with the enhanced contact reactor field pilot system (from DMax Plasma and Clarkson University) that is currently estimated at 7.30 USD/kgal.

Finally, this chapter will present the proposed future work, followed by some concluding remarks regarding plasma-based remediation of PFAS and practical implementation considerations of plasmas for water treatment applications.

## 8.2 Future Work

Of course, some questions posed in this thesis have yet to be completely resolved, and indeed, many more questions have arisen throughout the course of the work presented here. This section will discuss two primary areas suggested for future research: (1) an investigation into the nature of the different discharge modes observed in Chapter 6 and potential control variables available for promoting the onset of a particular discharge mode, and (2) validating the proposed scale-up approach outlined in Chapter 7.

### *8.2.1 Understanding the Different Discharge Modes*

In Chapter 6, two distinct discharge modes were observed to occur in the packed-bed reactor. Interestingly, these two discharge modes could seemingly occur at the same conditions (i.e., same power supply inputs, water flow rate, and water properties such as electrical conductivity, pH, and temperature). Not only did the two discharge modes produce distinctive voltage-current waveforms (categorized by pulse width as “wide pulse” and “narrow pulse”), but they also produced unique observable characteristics.

Specifically, when running the packed-bed reactor with deionized water (conductivity around 4 μS/cm) the "narrow pulse" discharge waveform was noticeably more common compared to running at higher water conductivities, and the discharge was visually brighter and audibly louder. In general, it was observed that the "narrow-pulse" discharge mode occurred more frequently at low water conductivities (<200 μS/cm), and was quite rare at water conductivities greater than 400 μS/cm. Additionally, the waveforms as seen on the oscilloscope display were not stable, suggesting that both the "wide pulse" and "narrow pulse" discharges were occurring many times per second. On the other hand, at higher conductivities (>700 μS/cm), the discharge waveforms were mostly stable in the "wide pulse" mode. Evaluating the discharge mode occurrence frequency, or the ratio of "wide pulse" to "narrow pulse" discharges (in this case for a pulse repetition frequency of 2 kHz) at varying water conductivities should be investigated in future work.

Moreover, the nature of these discharge modes should be investigated further. What control variables are available to initiate the onset of a particular discharge mode? What are the characteristic gas temperatures, plasma densities, and discharge powers associated with each discharge mode? As proposed in Chapter 6, the "narrow pulse" discharge mode is thought to be associated with a spark-type discharge in which a plasma streamer navigates through the array of water jets to form a transient conductive channel.

The spark-type discharge would be expected to have higher gas temperatures, which might be advantageous for PFAS decomposition but may not be useful for the decomposition of other contaminants.[43], [112] While the water conductivity certainly appears to play a role in which discharge mode occurs (likely due to the charge relaxation time), other control variables

may be available, such as applied voltage and water flow rate (which would affect the Reynolds number and the water jet structures). This should be explored in future research.

### *8.2.2 Scale-up Approach Validation*

Perhaps the most important direction for future work is the validation of the architecture for scaling up the packed-bed reactor into a continuous flow treatment process that was proposed in Chapter 7. Indeed, the assumptions made regarding equivalent plasma exposure (i.e., plasma-water contact area, contact time, and power density) were intended to faithfully reproduce the treatment conditions applied in the batch-mode packed-bed reactor treatment. In practice, however, these assumptions still must be validated before proceeding with large-scale implementation.

This scale-up validation should be conducted in stages, rather than immediately attempting the pilot-scale flow rate (170 L/min) configuration presented in Chapter 7. For example, starting with a continuous process flow rate of 4 L/min (approximately the flow rate in the batch-mode treatment presented in Chapter 5) would seem a reasonable starting point for a laboratory-scale demonstration. If a system designed based on the proposed model can achieve the predicted decomposition performance at a continuous flow rate of 4 L/min, the next step would be a bench-scale test at 38 L/min (10 gpm).

These first two stages of approach validation could involve a 3-stage plasma treatment with a single process line; however, the detention tank volumes and recirculation flow rates would be adjusted to accommodate the total process flow rate. If the predicted performance is achieved at this increased flow rate, a pilot-scale project treating 170 L/min (45 gpm) would be warranted. Each step would involve added costs (for increasing detention tank volume, recirculation pump speed, and potentially the number of plasma heads per tank); however,

equipment could be re-used as the treatment system expands to accommodate higher process flow rates, thus mitigating added costs.

Finally, the issue of short-chain PFAS requires further research from a few standpoints. Short chain PFAS may prove to be similarly threatening from a public health standpoint. Unfortunately, our understanding of the actual health effects of exposure to PFAS of various carbon chain lengths lags behind the real impacts and the tolls taken on human lives. Thus, more research is needed to evaluate the health impacts of exposure to short-chain PFAS through drinking water supplies.

Additionally, the proposed continuous flow system from Chapter 7 is designed based on the removal of PFOS. To remove the shorter chain PFAS, longer treatment times may be necessary, which means larger detention tanks and higher recirculation flow rates. The addition of cationic surfactants such as cetrimonium bromide (CTAB) has been considered for improving the removal efficiency of PFOA, and has also been shown to improve the removal of short-chain PFAS.[39], [137] The addition of CTAB may be considered with the packed-bed reactor as well for improving the removal of short-chain PFAS.

### 8.3 Concluding Remarks

Overall, the PFAS decomposition studies presented herein further support the theory that non-thermal plasma reactors are currently one of the most promising technologies for the destruction of PFAS in contaminated groundwaters. The initial plasma source exploration study indicated that air can be used as a suitable alternative working gas to argon, which helps to reduce the system complexity and cost. Both AC and ns-pulsed power supplies can be used to attain similar percent removals of PFAS; however, the ns-pulsed discharge is more energy efficient by approximately a factor of 10. Plasma-water contact area has been identified as a

critical variable governing the PFAS decomposition performance, which is in alignment with the current understandings in the plasma-water reactor community. Furthermore, higher mass removal efficiencies can be achieved when treating waters with higher concentrations of PFAS. Thus, a concentration step prior to the plasma treatment appears to be a promising strategy for improving the cost-effectiveness of the treatment process.

The batch kinetic tests indicated that the long-chain PFAS can be empirically modeled by first-order decay. Notably, the two most prevalent PFAS found in the groundwater (PFOS and PFHxS) were removed to below the MI EPA MCLs within 90 minutes of treatment with the packed-bed reactor. These encouraging results should be disseminated through the proper channels such that they are noticed by state funding agencies. In the absence of enforceable federal regulations, the state agencies will likely be responsible for enforcing regulations to protect their citizens.

Although the water electrical conductivity increases throughout the plasma treatment duration, a separate test involving water samples spiked with NaCl at varying concentrations indicated that the plasma discharge properties do not change significantly with increasing water conductivity. Specifically, the plasma density, gas temperature, and discharge power remained approximately constant around $(9 \pm 2) \times 10^{16}$ $cm^{-3}$, 700 ± 250 K, and 120 ± 20 W, respectively. This would seem to suggest that this type of plasma treatment can be suitable for a range of waters at various conductivities that might be encountered.

Low water conductivities (<200 µS/cm) were associated with higher peak discharge voltages, higher electron densities and gas temperatures, and more intense UV emission. This is thought to be associated with a unique spark-type discharge that forms due to longer charge relaxation times and streamer propagation lengths associated with low water conductivities, thus

enabling a transient conductive channel to form between the electrodes. While these low water conductivities are not expected in natural groundwaters, the occurrence of this spark-type discharge is an interesting finding. Further investigation into the properties of this spark mode compared to the pulsed corona discharge mode is recommended for future work. It may be possible to leverage the reactor's ability to produce both discharge modes to enhance the treatment performance.

Finally, an architecture for converting the batch-mode plasma treatment into a scalable continuous flow configuration was proposed, along with a model for estimating the system size and performance based on the batch reactor kinetics. This architecture features membrane concentration of PFAS followed by a staged plasma micro-reactor treatment, each with internal water recirculation. The treatment cost for removing PFOS to below the MI EPA MCL was estimated to be approximately 5 USD/kgal operating at a continuous flow rate of 45 gpm.

This model assumes that plasma provides the treatment level necessary for meeting the MI EPA MCLs; however, it was observed that plasma is most efficient at decomposing PFAS when treating high concentrations. This may be used to inform other treatment train approaches to more cost-effectively address PFAS contamination. For example, plasma could be used to treat the concentrate stream from a reverse osmosis stage to a certain level. Then the effluent from the plasma stage may be sent through a GAC finishing stage to meet the required MCLs. In this way, plasma contributes to the decomposition of PFAS in a concentration range where it is most efficient, while at the same time lessening the load of PFAS that must be removed by the GAC filters, thus extending the filter lifetimes. Of course, many different treatment train approaches featuring a plasma-based PFAS destruction stage may be viable. This is one

example in which the burden of reaching low ppt concentrations is not delegated solely to the plasma stage.

Overall, several technical aspects regarding the engineering embodiment of any plasma-water reactor should be considered including (1) energy efficiency, (2) reactor lifetime and maintenance requirements, (3) processing volume or throughput, (4) an understanding of the toxicity of intermediates or by-products formed, (5) pre-treatment and post-treatment requirements, and (6) simplicity of the ancillary hardware. Beyond these technical design considerations, more practical aspects regarding implementation of a plasma-water reactor into a community should be considered, largely relating to stakeholder engagement. An example of a suggested planning and design process that connects engineering with sustained stakeholder participation from Guest et al. is provided in Figure 8.1.

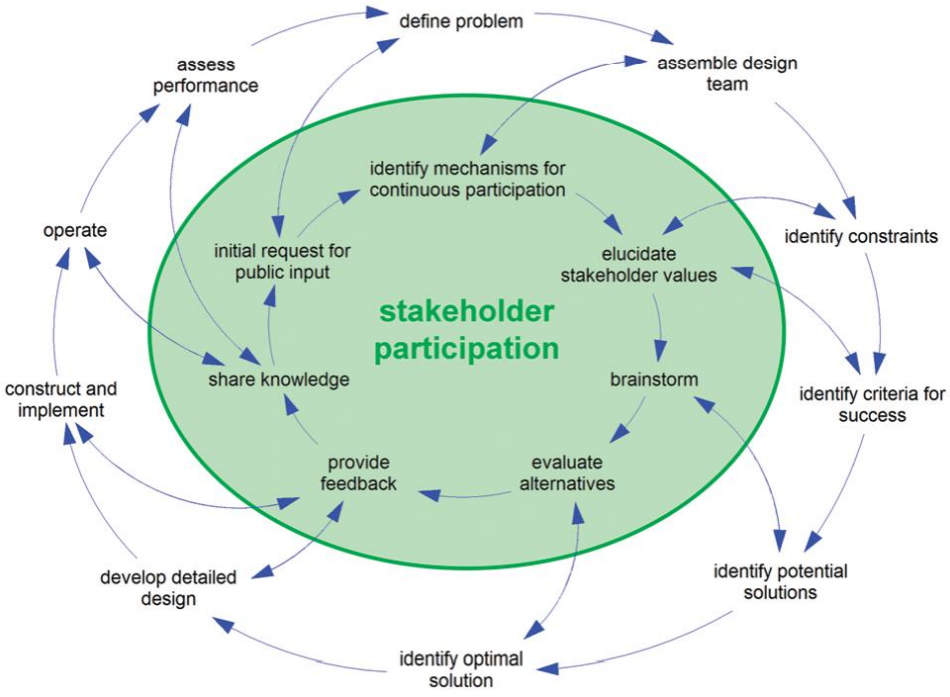


Figure 8.1 Example of a suggested planning and design process that connects engineering (outer loop) with sustained stakeholder participation (inner loop) from Guest et al.[138] The double-headed arrows connecting the technical design process with stakeholder participation represent workshops and engagement throughout the planning and design of a water treatment system.

It is important to prove to the community that plasma-based decomposition of PFAS works, not just promise that it will work. This process should involve participation from the stakeholders, including joint brainstorming sessions, community feedback, and knowledge sharing. An outreach component should also be included, in which the community can be taught about plasmas and how they can be used for environmental remediation efforts. The technology should be made accessible, and in the process, the community should be inspired to get involved. These strategies for stakeholder engagement should help ease the adoption process and improve outcomes throughout the implementation of a treatment system for addressing PFAS contamination in local groundwaters.

## Bibliography


[1] M. M. Mekonnen and A. Y. Hoekstra, “Four billion people facing severe water scarcity,” *Sci. Adv.*, vol. 2, no. 2, Feb. 2016, doi: 10.1126/sciadv.1500323.

[2] World Water Assessment Programme, “The United Nations World Water Development Report 2018,” New York, USA, 2018.

[3] A. Boretti and L. Rosa, “Reassessing the projections of the World Water Development Report,” *npj Clean Water*, vol. 2, no. 1, Dec. 2019, doi: 10.1038/s41545-019-0039-9.

[4] S. S. Ae, M. Carballa, A. E. Francisco, O. Ae, and J. M. Lema, “How are pharmaceutical and personal care products (PPCPs) removed from urban wastewaters?,” 2008, doi: 10.1007/s11157-008-9130-2.

[5] A. J. Ebele, M. Abou-Elwafa Abdallah, and S. Harrad, “Pharmaceuticals and personal care products (PPCPs) in the freshwater aquatic environment,” *Emerg. Contam.*, vol. 3, no. 1, pp. 1–16, Mar. 2017, doi: 10.1016/j.emcon.2016.12.004.

[6] P. C. Vandevivere, R. Bianchi, and W. Verstraete, “Treatment and reuse of wastewater from the textile wet-processing industry: Review of emerging technologies,” 1998.

[7] X. Jiang, S. Lee, C. Mok, and J. Lee, “Sustainable methods for decontamination of microcystin in water using cold plasma and UV with reusable TiO2 nanoparticle coating,” *Int. J. Environ. Res. Public Health*, vol. 14, no. 5, 2017, doi: 10.3390/ijerph14050480.

[8] H. Zhang, Q. Huang, Z. Ke, L. Yang, X. Wang, and Z. Yu, “Degradation of microcystin-LR in water by glow discharge plasma oxidation at the gas-solution interface and its safety evaluation,” *Water Res.*, vol. 46, no. 19, pp. 6554–6562, 2012, doi:

10.1016/j.watres.2012.09.041.

[9] Centers for Disease Control and Prevention, “2014 West Virginia Chemical Release,” 2014.

[10] J. Crook and R. Surampalli, “Water reclamation and reuse criteria in the U.S.,” *Water Sci. Technol.*, vol. 33, no. 10–11, pp. 451–462, 1996.

[11] Solarchem Environmental Systems, *The UV/oxidation handbook*. Markham, Ontario, Canada, 1994.

[12] E. M. Sunderland, X. C. Hu, C. Dassuncao, A. K. Tokranov, C. C. Wagner, and J. G. Allen, “A review of the pathways of human exposure to poly- and perfluoroalkyl substances (PFASs) and present understanding of health effects,” *Journal of Exposure Science and Environmental Epidemiology*, vol. 29, no. 2. Nature Publishing Group, pp. 131–147, 01-Mar-2019, doi: 10.1038/s41370-018-0094-1.

[13] D. O’hagan, “Understanding organofluorine chemistry. An introduction to the C–F bond,” *Chem. Soc. Rev.*, vol. 37, no. 2, pp. 308–319, Jan. 2008, doi: 10.1039/b711844a.

[14] J. L. Domingo and M. Nadal, “Human exposure to per- and polyfluoroalkyl substances (PFAS) through drinking water: A review of the recent scientific literature,” *Environmental Research*, vol. 177. Academic Press Inc., p. 108648, Oct-2019, doi: 10.1016/j.envres.2019.108648.

[15] S. E. Fenton *et al.*, “Per-and Polyfluoroalkyl Substance Toxicity and Human Health Review: Current State of Knowledge and Strategies for Informing Future Research,” *Environ. Toxicol. Chem.*, vol. 40, no. 3, pp. 606–630, 2021, doi: 10.1002/etc.4890.

[16] M. J. Bentel *et al.*, “Defluorination of Per- and Polyfluoroalkyl Substances (PFASs) with Hydrated Electrons: Structural Dependence and Implications to PFAS Remediation and

Management," *Environ. Sci. Technol.*, vol. 53, no. 7, pp. 3718–3728, 2019, doi: 10.1021/acs.est.8b06648.

[17] K. A. Barzen-Hanson *et al.*, "Discovery of 40 Classes of Per-and Polyfluoroalkyl Substances in Historical Aqueous Film-Forming Foams (AFFFs) and AFFF-Impacted Groundwater," 2017, doi: 10.1021/acs.est.6b05843.

[18] L. A. D'Agostino and S. A. Mabury, "Identification of novel fluorinated surfactants in aqueous film forming foams and commercial surfactant concentrates," *Environ. Sci. Technol.*, vol. 48, no. 1, pp. 121–129, 2014, doi: 10.1021/es403729e.

[19] U. S. E. P. A. (EPA), "EPA PFAS Action Plan: Program Update, February 2020," 2020.

[20] Michigan PFAS Action Response Team, "PFAS MCLs and Drinking Water," 2019. [Online]. Available: https://www.michigan.gov/pfasresponse/0,9038,7-365-95571_99970---,00.html.

[21] I. Ross *et al.*, "A review of emerging technologies for remediation of PFASs," *Remediation*, vol. 28, no. 2, pp. 101–126, Mar. 2018, doi: 10.1002/REM.21553.

[22] D. Lu, S. Sha, J. Luo, Z. Huang, and X. Zhang Jackie, "Treatment train approaches for the remediation of per- and polyfluoroalkyl substances (PFAS): A critical review," *J. Hazard. Mater.*, vol. 386, Mar. 2020, doi: 10.1016/j.jhazmat.2019.121963.

[23] C. Nau-Hix *et al.*, "Field Demonstration of a Pilot-Scale Plasma Reactor for the Rapid Removal of Poly- and Perfluoroalkyl Substances in Groundwater," *ACS ES&T Water*, vol. 1, no. 3, pp. 680–687, Jan. 2021, doi: 10.1021/acsestwater.0c00170.

[24] R. K. Singh *et al.*, "Rapid Removal of Poly- and Perfluorinated Compounds from Investigation-Derived Waste (IDW) in a Pilot-Scale Plasma Reactor," *Environ. Sci. Technol.*, vol. 53, p. 11375−11382, 2019, doi: 10.1021/acs.est.9b02964.

[25] Y. C. Lee, S. L. Lo, P. Te Chiueh, Y. H. Liou, and M. L. Chen, “Microwave-hydrothermal decomposition of perfluorooctanoic acid in water by iron-activated persulfate oxidation,” *Water Res.*, vol. 44, no. 3, pp. 886–892, 2010, doi: 10.1016/j.watres.2009.09.055.

[26] M. J. Chen, S. L. Lo, Y. C. Lee, and C. C. Huang, “Photocatalytic decomposition of perfluorooctanoic acid by transition-metal modified titanium dioxide,” *J. Hazard. Mater.*, vol. 288, pp. 168–175, Jan. 2015, doi: 10.1016/j.jhazmat.2015.02.004.

[27] H. Moriwaki, Y. Takagi, M. Tanaka, K. Tsuruho, K. Okitsu, and Y. Maeda, “Sonochemical decomposition of perfluorooctane sulfonate and perfluorooctanoic acid,” *Environ. Sci. Technol.*, vol. 39, no. 9, pp. 3388–3392, 2005, doi: 10.1021/es040342v.

[28] C. E. Schaefer *et al.*, “Electrochemical treatment of perfluorooctanoic acid and perfluorooctane sulfonate: Insights into mechanisms and application to groundwater treatment,” *Chem. Eng. J.*, vol. 317, pp. 424–432, 2017, doi: 10.1016/j.cej.2017.02.107.

[29] L. Jin, P. Zhang, T. Shao, and S. Zhao, “Ferric ion mediated photodecomposition of aqueous perfluorooctane sulfonate (PFOS) under UV irradiation and its mechanism,” *J. Hazard. Mater.*, vol. 271, pp. 9–15, Apr. 2014, doi: 10.1016/j.jhazmat.2014.01.061.

[30] B. R. Locke, M. Sato, P. Sunka, M. R. Hoffmann, and J. S. Chang, “Electrohydraulic discharge and nonthermal plasma for water treatment,” *Industrial and Engineering Chemistry Research*, vol. 45, no. 3. pp. 882–905, 01-Feb-2006, doi: 10.1021/ie050981u.

[31] C. Roth, G. Oberbossel, E. Buitrago, R. Heuberger, and P. Rudolf Von Rohr, “Nanoparticle synthesis and growth in a continuous plasma reactor from organosilicon precursors,” *Plasma Process. Polym.*, vol. 9, no. 2, pp. 119–134, 2012, doi: 10.1002/ppap.201100180.

[32] T. Shirafuji *et al.*, “Functionalization of multiwalled carbon nanotubes by solution plasma

processing in ammonia aqueous solution and preparation of composite material with polyamide 6," *Jpn. J. Appl. Phys.*, vol. 52, no. 12, 2013, doi: 10.7567/JJAP.52.125101.

[33] Y. Yang, H. Kim, A. Fridman, and Y. I. Cho, "Effect of a plasma-assisted self-cleaning filter on the performance of PWT coil for the mitigation of mineral fouling in a heat exchanger," *Int. J. Heat Mass Transf.*, vol. 53, no. 1–3, pp. 412–422, Jan. 2010, doi: 10.1016/j.ijheatmasstransfer.2009.09.015.

[34] H. N. Phong Vo *et al.*, "Poly-and perfluoroalkyl substances in water and wastewater: A comprehensive review from sources to remediation," *Journal of Water Process Engineering*, vol. 36. Elsevier Ltd, p. 101393, Aug-2020, doi: 10.1016/j.jwpe.2020.101393.

[35] Z. Song, H. Tang, N. Wang, and L. Zhu, "Reductive defluorination of perfluorooctanoic acid by hydrated electrons in a sulfite-mediated UV photochemical system," *J. Hazard. Mater.*, vol. 262, pp. 332–338, Nov. 2013, doi: 10.1016/j.jhazmat.2013.08.059.

[36] J. Cui, P. Gao, and Y. Deng, "Destruction of Per- and Polyfluoroalkyl Substances (PFAS) with Advanced Reduction Processes (ARPs): A Critical Review," *Environmental Science and Technology*, vol. 54, no. 7. American Chemical Society, pp. 3752–3766, Apr-2020, doi: 10.1021/acs.est.9b05565.

[37] J. E. Foster, "Plasma-based water purification: Challenges and prospects for the future," *Phys. Plasmas*, vol. 24, no. 5, p. 55501, 2017, doi: 10.1063/1.4977921.

[38] M. Saleem *et al.*, "Comparative performance assessment of plasma reactors for the treatment of PFOA; reactor design, kinetics, mineralization and energy yield," *Chem. Eng. J.*, vol. 382, p. 123031, Feb. 2020, doi: 10.1016/j.cej.2019.123031.

[39] R. K. Singh *et al.*, "Removal of Poly-and Per-Fluorinated Compounds from Ion Exchange

Regenerant Still Bottom Samples in a Plasma Reactor," *Cite This Environ. Sci. Technol*, vol. 54, 2020, doi: 10.1021/acs.est.0c02158.

[40] J. E. Foster, S. Mujovic, J. Groele, and I. M. Blankson, "Towards high throughput plasma based water purifiers: Design considerations and the pathway towards practical application," *Journal of Physics D: Applied Physics*, vol. 51, no. 29. Institute of Physics Publishing, p. 293001, Jun-2018, doi: 10.1088/1361-6463/aac816.

[41] A. Fridman, *Plasma Chemistry*. Cambridge University Press, 2008.

[42] A. Fridman and L. A. Kennedy, *Plasma Physics and Engineering*. Milton: Taylor & Francis Group, 2020.

[43] A. Fridman, A. Chirokov, and A. Gutsol, "Non-thermal atmospheric pressure discharges," *J. Phys. D. Appl. Phys.*, vol. 38, no. 2, pp. 1–24, 2005, doi: 10.1088/0022-3727/38/2/R01.

[44] S. Samukawa *et al.*, "The 2012 plasma roadmap," *J. Phys. D. Appl. Phys.*, vol. 45, no. 25, p. 253001, 2012, doi: 10.1088/0022-3727/45/25/253001.

[45] P. Bruggeman and C. Leys, "Non-thermal plasmas in and in contact with liquids," *J. Phys. D. Appl. Phys.*, vol. 42, no. 5, 2009, doi: 10.1088/0022-3727/42/5/053001.

[46] G. Zhu, Y. Peng, B. Li, J. Guo, Q. Yang, and S. Wang, "Biological removal of nitrogen from wastewater," *Rev. Environ. Contam. Toxicol.*, vol. 192, pp. 159–195, 2008, doi: 10.1007/978-0-387-71724-1_5.

[47] A. F. Yong Yang, Young L. Cho, *Plasma discharge in liquid : water treatment and applications*. Boca Raton, FL: CRC Press, 2012.

[48] Z. C. Liu *et al.*, "Physicochemical processes in the indirect interaction between surface air plasma and deionized water," *J. Phys. D. Appl. Phys.*, vol. 48, no. 49, 2015, doi: 10.1088/0022-3727/48/49/495201.

[49] J. Lai and J. E. Foster, “Time-resolved imaging of streamer formation inside gaseous bubbles in liquids,” *J. Phys. D. Appl. Phys.*, vol. 53, no. 2, p. 025206, Oct. 2019, doi: 10.1088/1361-6463/ab4c9d.

[50] W. Tian, K. Tachibana, and M. J. Kushner, “Plasmas sustained in bubbles in water: Optical emission and excitation mechanisms,” *J. Phys. D. Appl. Phys.*, vol. 47, no. 5, 2014, doi: 10.1088/0022-3727/47/5/055202.

[51] B. S. Sommers and J. E. Foster, “Plasma formation in underwater gas bubbles,” *Plasma Sources Sci. Technol.*, vol. 23, no. 1, p. 10, 2014, doi: 10.1088/0963-0252/23/1/015020.

[52] N. K. Kaushik *et al.*, “Cold atmospheric plasma and gold quantum dots exert dual cytotoxicity mediated by the cell receptor-activated apoptotic pathway in glioblastoma cells,” *Cancers (Basel).*, vol. 12, no. 2, 2020, doi: 10.3390/cancers12020457.

[53] B. Haertel, T. von Woedtke, K. D. Weltmann, and U. Lindequist, “Non-thermal atmospheric-pressure plasma possible application in wound healing,” *Biomol. Ther.*, vol. 22, no. 6, pp. 477–490, 2014, doi: 10.4062/biomolther.2014.105.

[54] G. Isbary *et al.*, “Successful and safe use of 2 min cold atmospheric argon plasma in chronic wounds: Results of a randomized controlled trial,” *Br. J. Dermatol.*, vol. 167, no. 2, pp. 404–410, 2012, doi: 10.1111/j.1365-2133.2012.10923.x.

[55] P. J. Bruggeman *et al.*, “Plasma-liquid interactions: A review and roadmap,” *Plasma Sources Sci. Technol.*, vol. 25, no. 5, 2016, doi: 10.1088/0963-0252/25/5/053002.

[56] A. J. Lewis *et al.*, “Rapid degradation of PFAS in aqueous solutions by reverse vortex flow gliding arc plasma,” *Environ. Sci. Water Res. Technol.*, vol. 6, no. 4, pp. 1044–1057, 2020, doi: 10.1039/c9ew01050e.

[57] M. A. Malik, “Water purification by plasmas: Which reactors are most energy efficient?,”

*Plasma Chem. Plasma Process.*, vol. 30, no. 1, pp. 21–31, 2010, doi: 10.1007/s11090-009-9202-2.

[58] E. E. Kunhardt, "Generation of large-volume, atmospheric-pressure, nonequilibrium plasmas," *IEEE Trans. Plasma Sci.*, vol. 28, no. 1, pp. 189–200, 2000, doi: 10.1109/27.842901.

[59] G. R. Stratton, C. L. Bellona, F. Dai, T. M. Holsen, and S. M. Thagard, "Plasma-based water treatment: Conception and application of a new general principle for reactor design," *Chem. Eng. J.*, vol. 273, pp. 543–550, 2015, doi: 10.1016/j.cej.2015.03.059.

[60] I. Even-Ezra, A. Mizrahi, D. Gerrity, S. Snyder, A. Salveson, and O. Lahav, "Application of a novel plasma-based advanced oxidation process for efficient and cost-effective destruction of refractory organics in tertiary effluents and contaminated groundwater," *Desalin. Water Treat.*, vol. 11, no. 1–3, pp. 236–244, 2009, doi: 10.5004/dwt.2009.807.

[61] J. Foster, B. S. Sommers, S. N. Gucker, I. M. Blankson, and G. Adamovsky, "Perspectives on the interaction of plasmas with liquid water for water purification," *IEEE Trans. Plasma Sci.*, vol. 40, no. 5, pp. 1311–1323, 2012, doi: 10.1109/TPS.2011.2180028.

[62] J. E. Foster, G. Adamovsky, S. N. Gucker, and I. M. Blankson, "A comparative study of the time-resolved decomposition of methylene blue dye under the action of a nanosecond repetitively pulsed dbd plasma jet using liquid chromatography and spectrophotometry," *IEEE Trans. Plasma Sci.*, vol. 41, no. 3, pp. 503–512, 2013, doi: 10.1109/TPS.2013.2245426.

[63] J. E. Foster and M. C. Garcia, "Promise of nonthermal plasmas in addressing emerging environmental and health problems: Present and future," *Phys. Plasmas*, vol. 29, no. 6, p. 060601, Jun. 2022, doi: 10.1063/5.0083766.

[64] S. J. and T. D., “Method 537.1: Determination of Selected Per- and Polyfluorinated Alkyl Substances in Drinking Water by Solid Phase Extraction and Liquid Chromatography/Tandem Mass Spectrometry (LC/MS/MS),” Washington DC, 2018.

[65] C. Volk, L. Wood, B. Johnson, J. Robinson, H. W. Zhu, and L. Kaplan, “Monitoring dissolved organic carbon in surface and drinking waters,” *J. Environ. Monit.*, vol. 4, no. 1, pp. 43–47, 2002, doi: 10.1039/B107768F.

[66] *Standard Methods for the Examination of Water and Wastewater*, 15th ed. Washinton, D.C., USA: American Public Health Association, Water Environment Federation, 1999.

[67] G. F. Sawyer, C.N.; McCarty, P.L.; Parkin, *Chemistry for Environmental Engineering and Science*, 5th ed. New York, USA: McGraw-Hill, 2003.

[68] J. . Norton, *Standard Methods for the Examination of Water and Sewage*, 9th ed. Washington, D.C.: American Public Health Association, 1946.

[69] D. Carreres-Prieto, J. T. García, F. Cerdán-Cartagena, and J. Suardiaz-Muro, “Wastewater quality estimation through spectrophotometry-based statistical models,” *Sensors*, vol. 20, no. 19, pp. 1–29, Oct. 2020, doi: 10.3390/s20195631.

[70] Nepal Agricultural Research Council, *A handbook of Soil Science*. Khumaltar, Lalitpur, Nepal: Khumaltar: Soil Science Division, 2015.

[71] S. Prahl, “Oregon Medical Laser Center - Methylene Blue Data.” [Online]. Available: http://omlc.org/spectra/mb/.

[72] J. H. Sharp, “Total organic carbon in seawater — comparison of measurements using persulfate oxidation and high temperature combustion,” *Mar. Chem.*, vol. 1, no. 3, pp. 211–229, Sep. 1973, doi: 10.1016/0304-4203(73)90005-4.

[73] P. C. Vandevivere, R. Bianchi2, and W. Verstraete1, “Review Treatment and Reuse of

Wastewater from the Textile Wet-Processing Industry: Review of Emerging Technologies," 1998.

[74] E. Lee, H. Lee, Y. K. Kim, K. Sohn, and K. Lee, "Hydrogen peroxide interference in chemical oxygen demand during ozone based advanced oxidation of anaerobically digested livestock wastewater," *Int. J. Environ. Sci. Tech*, vol. 8, no. 2, pp. 381–388, 2011.

[75] S. N. Gucker, J. E. Foster, and M. C. Garcia, "An investigation of an underwater steam plasma discharge as alternative to air plasmas for water purification," *Plasma Sources Sci. Technol.*, vol. 24, no. 5, 2015, doi: 10.1088/0963-0252/24/5/055005.

[76] G. Ni, G. Zhao, Y. Jiang, J. Li, Y. Meng, and X. Wang, "Steam Plasma Jet Treatment of Phenol in Aqueous Solution at Atmospheric Pressure," *Plasma Process. Polym.*, vol. 10, no. 4, pp. 353–363, Apr. 2013, doi: 10.1002/PPAP.201200155.

[77] I. Talinli and G. K. Anderson, "Interference of hydrogen peroxide on the standard cod test," *Water Res.*, vol. 26, no. 1, pp. 107–110, 1992, doi: 10.1016/0043-1354(92)90118-N.

[78] K. J. H. and G. T. John C. Crittenden, R. Rhodes Trussell, David W. Hand, *MWH's Water Treatment: Principles and Design*, Third. John Wiley & Sons, Inc., 2012.

[79] A. F. Rusydi, "Correlation between conductivity and total dissolved solid in various type of water: A review," *IOP Conf. Ser. Earth Environ. Sci.*, vol. 118, no. 1, 2018, doi: 10.1088/1755-1315/118/1/012019.

[80] F. M. Brown E, Skougstad M, "Methods for collection and analysis of water samples," 1960.

[81] O. Pedersen, T. D. Colmer, and K. Sand-Jensen, "Underwater photosynthesis of submerged plants – recent advances and methods," *Article*, vol. 4, no. 1, 2013, doi:

10.3389/fpls.2013.00140.

[82] F. Tampieri, M.-P. Ginebra, and C. Canal, “Quantification of Plasma-Produced Hydroxyl Radicals in Solution and their Dependence on the pH,” *Cite This Anal. Chem*, vol. 93, p. 3670, 2021, doi: 10.1021/acs.analchem.0c04906.

[83] M. Hayashi, “Temperature-electrical conductivity relation of water for environmental monitoring and geophysical data inversion,” 2004.

[84] P. Wardman, “Fluorescent and luminescent probes for measurement of oxidative and nitrosative species in cells and tissues: Progress, pitfalls, and prospects,” *Free Radic. Biol. Med.*, vol. 43, no. 7, pp. 995–1022, Oct. 2007, doi: 10.1016/J.FREERADBIOMED.2007.06.026.

[85] A. Hickling, *The mechanism of electrode processes in aqueous solutions*, vol. 3, no. 2. 1949.

[86] A. T. Bullock, “Electron spin resonance detection of spin-trapped radicals formed during the glow-discharge electrolysis of aqueous solutions,” *J. Chem. Soc.*, vol. 76, pp. 648–653, 1980.

[87] G. M. Rosen, B. E. Britigan, H. J. Halpern, and S. Pou, “Free Radicals: Biology and Detection by Spin Trapping,” p. 482, 1999.

[88] C. Lagercrantz, *Spin trapping of some short-lived radicals by the nitroxide method*, vol. 75, no. 22. 1971.

[89] H. Tresp, M. U. Hammer, J. Winter, K. D. Weltmann, and S. Reuter, *Quantitative detection of plasma-generated radicals in liquids by electron paramagnetic resonance spectroscopy*, vol. 46, no. 43. 2013.

[90] P. Lukes, M. Clupek, V. Babicky, I. Sisrova, and V. Janda, “The catalytic role of tungsten

electrode material in the plasmachemical activity of a pulsed corona discharge in water," *Plasma Sources Sci. Technol.*, vol. 20, no. 3, pp. 34011–34022, 2011, doi: 10.1088/0963-0252/20/3/034011.

[91] M. J. Kirkpatrick and B. R. Locke, "Effects of Platinum Electrode on Hydrogen, Oxygen, and Hydrogen Peroxide Formation in Aqueous Phase Pulsed Corona Electrical Discharge," 2006, doi: 10.1021/ie0511480.

[92] M. Anbar and H. Taube, "Interaction of Nitrous Acid with Hydrogen Peroxide," *J. Am. Chem. Soc.*, vol. 76, no. 24, pp. 6243–6247, 1954.

[93] G. M. Eisenberg, "Colorimetric Determination of Hydrogen Peroxide," *Ind. Eng. Chem. - Anal. Ed.*, vol. 15, no. 5, pp. 327–328, May 1943, doi: 10.1021/i560117a011.

[94] P. Lukes, "Plasma Sources Science and Technology Aqueous-phase chemistry and bactericidal effects from an air discharge plasma in contact with water: evidence for the formation of peroxynitrite through a pseudo-second-order post-discharge reaction of H 2 O 2 and HNO 2," 2014, doi: 10.1088/0963-0252/23/1/015019.

[95] P. Szakálos, G. Hultquist, and G. Wikmark, "Corrosion of copper by water," *Electrochem. Solid-State Lett.*, vol. 10, no. 11, pp. 63–67, 2007, doi: 10.1149/1.2772085.

[96] G. Stando, P. M. Hannula, B. Kumanek, M. Lundström, and D. Janas, "Copper recovery from industrial wastewater - Synergistic electrodeposition onto nanocarbon materials," *Water Resour. Ind.*, vol. 26, p. 100156, Dec. 2021, doi: 10.1016/J.WRI.2021.100156.

[97] C. Peng, Y. Liu, J. Bi, H. Xu, and A. S. Ahmed, "Recovery of copper and water from copper-electroplating wastewater by the combination process of electrolysis and electrodialysis," *J. Hazard. Mater.*, vol. 189, no. 3, pp. 814–820, May 2011, doi: 10.1016/J.JHAZMAT.2011.03.034.

[98] S. A. Al-Saydeh, H. El-Naas, and S. J. Zaidi, “Copper removal from industrial wastewater: A comprehensive review,” 2017, doi: 10.1016/j.jiec.2017.07.026.

[99] C. Yubero, M. S. Dimitrijević, M. C. García, and M. D. Calzada, “Using the van der Waals broadening of the spectral atomic lines to measure the gas temperature of an argon microwave plasma at atmospheric pressure,” *Spectrochim. Acta Part B At. Spectrosc.*, vol. 62, no. 2, pp. 169–176, Feb. 2007, doi: 10.1016/J.SAB.2007.02.008.

[100] G. R. Stratton, F. Dai, C. L. Bellona, T. M. Holsen, E. R. V. Dickenson, and S. Mededovic Thagard, “Plasma-Based Water Treatment: Efficient Transformation of Perfluoroalkyl Substances in Prepared Solutions and Contaminated Groundwater,” *Environ. Sci. Technol.*, vol. 51, no. 3, pp. 1643–1648, Feb. 2017, doi: 10.1021/acs.est.6b04215.

[101] D. Palma *et al.*, “PFAS degradation in ultrapure and groundwater using non-thermal plasma,” *Molecules*, vol. 26, no. 4, Feb. 2021, doi: 10.3390/molecules26040924.

[102] K. H. H. Aziz *et al.*, “Degradation of perfluorosurfactant in aqueous solution using non-thermal plasma generated by nano-second pulse corona discharge reactor,” *Arab. J. Chem.*, vol. 14, no. 10, Oct. 2021, doi: 10.1016/j.arabjc.2021.103366.

[103] A. Mahyar *et al.*, “Development and Application of Different Non-thermal Plasma Reactors for the Removal of Perfluorosurfactants in Water: A Comparative Study,” *Plasma Chem. Plasma Process.*, vol. 39, no. 3, pp. 531–544, 2019, doi: 10.1007/s11090-019-09977-6.

[104] F. Xiao *et al.*, “Thermal Stability and Decomposition of Perfluoroalkyl Substances on Spent Granular Activated Carbon,” *Environ. Sci. Technol. Lett*, vol. 7, p. 350, 2020, doi: 10.1021/acs.estlett.0c00114.

[105] T. Y. Campbell, C. D. Vecitis, B. T. Mader, and M. R. Hoffmann, “Perfluorinated

surfactant chain-length effects on sonochemical kinetics.," *J. Phys. Chem. A*, vol. 113, no. 36, pp. 9834–42, Sep. 2009, doi: 10.1021/jp903003w.

[106] W. A. Maza *et al.*, "Nanosecond transient absorption studies of the pH-dependent hydrated electron quenching by HSO3-," *Photochem. Photobiol. Sci.*, vol. 18, no. 6, pp. 1526–1532, 2019, doi: 10.1039/c9pp00063a.

[107] C. Richmonds *et al.*, "Electron-transfer reactions at the plasma-liquid interface," *J. Am. Chem. Soc.*, vol. 133, no. 44, pp. 17582–17585, Nov. 2011, doi: 10.1021/JA207547B/SUPPL_FILE/JA207547B_SI_001.PDF.

[108] P. Rumbach, D. M. Bartels, R. M. Sankaran, and D. B. Go, "The solvation of electrons by an atmospheric-pressure plasma," *Nat. Commun.*, vol. 6, 2015, doi: 10.1038/ncomms8248.

[109] J. E. Foster, B. Weatherford, E. Gillman, and B. Yee, "Underwater operation of a DBD plasma jet," *Plasma Sources Sci. Technol.*, vol. 19, no. 2, p. 25001, Jan. 2010, doi: 10.1088/0963-0252/19/2/025001.

[110] R. Brandenburg, "Dielectric barrier discharges: Progress on plasma sources and on the understanding of regimes and single filaments," *Plasma Sources Sci. Technol.*, vol. 26, no. 5, p. 053001, 2017, doi: 10.1088/1361-6595/aa6426.

[111] J. Foster, B. Sommers, B. Weatherford, B. Yee, and M. Gupta, "Characterization of the evolution of underwater DBD plasma jet," *Plasma Sources Sci. Technol.*, vol. 20, no. 3, Jun. 2011, doi: 10.1088/0963-0252/20/3/034018.

[112] N. Merino, Y. Qu, R. A. Deeb, E. L. Hawley, M. R. Hoffmann, and S. Mahendra, "Degradation and Removal Methods for Perfluoroalkyl and Polyfluoroalkyl Substances in Water," *Environ. Eng. Sci.*, vol. 33, no. 9, pp. 615–649, Sep. 2016, doi: 10.1089/ees.2016.0233.

[113] R. K. Singh, S. Fernando, S. F. Baygi, N. Multari, S. M. Thagard, and T. M. Holsen, "Breakdown Products from Perfluorinated Alkyl Substances (PFAS) Degradation in a Plasma-Based Water Treatment Process," *Environ. Sci. Technol.*, vol. 53, no. 5, pp. 2731–2738, Mar. 2019, doi: 10.1021/acs.est.8b07031.

[114] M. Trojanowicz, A. Bojanowska-Czajka, I. Bartosiewicz, and K. Kulisa, "Advanced Oxidation/Reduction Processes treatment for aqueous perfluorooctanoate (PFOA) and perfluorooctanesulfonate (PFOS) – A review of recent advances," *Chemical Engineering Journal*, vol. 336. Elsevier B.V., pp. 170–199, Mar-2018, doi: 10.1016/j.cej.2017.10.153.

[115] J. R. Bolton, K. G. Bircher, W. Tumas, and C. A. Tolman, "Figures-of-merit for the technical development and application of advanced oxidation technologies for both electric- and solar-driven systems," *Pure Appl. Chem.*, vol. 73, no. 4, pp. 627–637, Apr. 2001, doi: 10.1351/pac200173040627.

[116] R. K. Singh, S. Fernando, S. F. Baygi, N. Multari, S. M. Thagard, and T. M. Holsen, "Breakdown Products from Perfluorinated Alkyl Substances (PFAS) Degradation in a Plasma-Based Water Treatment Process," *Environ. Sci. Technol.*, vol. 53, no. 5, pp. 2731–2738, Mar. 2019, doi: 10.1021/acs.est.8b07031.

[117] V. B. P. Sudha, S. Ganesan, G. P. Pazhani, T. Ramamurthy, G. B. Nair, and P. Venkatasubramanian, "Storing drinking-water in copper pots kills contaminating diarrhoeagenic bacteria," *J. Heal. Popul. Nutr.*, vol. 30, no. 1, pp. 17–21, 2012, doi: 10.3329/jhpn.v30i1.11271.

[118] K. R. Stalder, J. Woloszko, I. G. Brown, and C. D. Smith, "Repetitive plasma discharges in saline solutions," *Appl. Phys. Lett.*, vol. 79, no. 27, p. 4503, Mar. 2002, doi: 10.1063/1.1429752.

[119] S. Mededovic and B. R. Locke, “Primary chemical reactions in pulsed electrical discharge channels in water,” *J. Phys. D. Appl. Phys.*, vol. 40, no. 24, p. 7734, Nov. 2007, doi: 10.1088/0022-3727/40/24/021.

[120] B. R. Locke and S. M. Thagard, “Analysis and review of chemical reactions and transport processes in pulsed electrical discharge plasma formed directly in liquid water,” *Plasma Chem. Plasma Process.*, vol. 32, no. 5, pp. 875–917, 2012, doi: 10.1007/s11090-012-9403-y.

[121] I. Kornev, F. Saprykin, and S. Preis, “Stability and energy efficiency of pulsed corona discharge in treatment of dispersed high-conductivity aqueous solutions,” *J. Electrostat.*, vol. 89, pp. 42–50, Oct. 2017, doi: 10.1016/J.ELSTAT.2017.07.001.

[122] A. Fridman, *Plasma Chemistry*. New York, USA: Cambridge University Press, 2008.

[123] K. Fantz, U ; Schalk, B ; Behringer, “Calculation and interpretation of the continuumradiation of hydrogen molecules,” 2000.

[124] SpectralFit S.A.S., “Specair User Manual Version 3.0,” 2012.

[125] H. Park, C. D. Vecitis, J. Cheng, W. Choi, B. T. Mader, and M. R. Hoffmann, “Reductive Defluorination of Aqueous Perfluorinated Alkyl Surfactants: Effects of Ionic Headgroup and Chain Length,” doi: 10.1021/jp807116q.

[126] A. Y. Nikiforov, C. Leys, M. A. Gonzalez, and J. L. Walsh, “Electron density measurement in atmospheric pressure plasma jets: Stark broadening of hydrogenated and non-hydrogenated lines,” *Plasma Sources Sci. Technol.*, vol. 24, no. 3, May 2015, doi: 10.1088/0963-0252/24/3/034001.

[127] A. Rodero and M. C. García, “Gas temperature determination of non-thermal atmospheric plasmas from the collisional broadening of argon atomic emission lines,” *J. Quant.*

*Spectrosc. Radiat. Transf.*, vol. 198, pp. 93–103, Sep. 2017, doi: 10.1016/J.JQSRT.2017.05.004.

[128] C. O. Laux, T. G. Spence, C. H. Kruger, and R. N. Zare, "Optical diagnostics of atmospheric pressure air plasmas," *Plasma Sources Sci. Technol.*, vol. 12, no. 2, pp. 125–138, May 2003, doi: 10.1088/0963-0252/12/2/301.

[129] P. Bruggeman, D. Schram, M. Á. González, R. Rego, M. G. Kong, and C. Leys, "Characterization of a direct dc-excited discharge in water by optical emission spectroscopy," *Plasma Sources Sci. Technol.*, vol. 18, no. 2, p. 025017, Mar. 2009, doi: 10.1088/0963-0252/18/2/025017.

[130] M. A. Gigosos, M. Á. González, and V. Cardeñoso, "Computer simulated Balmer-alpha, -beta and -gamma Stark line profiles for non-equilibrium plasmas diagnostics," *Spectrochim. Acta - Part B At. Spectrosc.*, vol. 58, no. 8, pp. 1489–1504, Aug. 2003, doi: 10.1016/S0584-8547(03)00097-1.

[131] A. Y. Nikiforov, C. Leys, M. A. Gonzalez, and J. L. Walsh, "Electron density measurement in atmospheric pressure plasma jets: Stark broadening of hydrogenated and non-hydrogenated lines," *Plasma Sources Sci. Technol.*, vol. 24, no. 3, p. 034001, Apr. 2015, doi: 10.1088/0963-0252/24/3/034001.

[132] G. Dong *et al.*, "Advanced oxidation processes in microreactors for water and wastewater treatment: Development, challenges, and opportunities," *Water Res.*, vol. 211, p. 118047, Mar. 2022, doi: 10.1016/j.watres.2022.118047.

[133] V. Franke, M. Ullberg, P. McCleaf, M. Wålinder, S. J. Köhler, and L. Ahrens, "The Price of Really Clean Water: Combining Nanofiltration with Granular Activated Carbon and Anion Exchange Resins for the Removal of Per- And Polyfluoralkyl Substances (PFASs)

in Drinking Water Production," *ACS ES&T Water*, vol. 1, no. 4, pp. 782–795, 2021, doi: 10.1021/acsestwater.0c00141.

[134] Environmental Working Group, "PFAS Contamination in the U.S. (June 8, 2022)," 2022. [Online]. Available: https://www.ewg.org/interactive-maps/pfas_contamination/#about.

[135] R. C. Lewis, L. E. Johns, and J. D. Meeker, "Serum biomarkers of exposure to perfluoroalkyl substances in relation to serum testosterone and measures of thyroid function among adults and adolescents from NHANES 2011–2012," *Int. J. Environ. Res. Public Health*, vol. 12, no. 6, pp. 6098–6114, 2015, doi: 10.3390/ijerph120606098.

[136] E. M. Sunderland, X. C. Hu, C. Dassuncao, A. K. Tokranov, C. C. Wagner, and J. G. Allen, "A review of the pathways of human exposure to poly- and perfluoroalkyl substances (PFASs) and present understanding of health effects," *Journal of Exposure Science and Environmental Epidemiology*, vol. 29, no. 2. Nature Publishing Group, pp. 131–147, Mar-2019, doi: 10.1038/s41370-018-0094-1.

[137] Y. F. Li, W. Y. Chien, Y. J. Liu, Y. C. Lee, S. L. Lo, and C. Y. Hu, "Perfluorooctanoic acid (PFOA) removal by flotation with cationic surfactants," *Chemosphere*, vol. 266, p. 128949, Mar. 2020, doi: 10.1016/j.chemosphere.2020.128949.

[138] J. S. Guest *et al.*, "A new planning and design paradigm to achieve sustainable resource recovery from wastewater," *Environ. Sci. Technol.*, vol. 43, no. 16, pp. 6126–6130, Aug. 2009, doi: 10.1021/ES9010515/SUPPL_FILE/ES9010515_SI_001.PDF.

[139] J. Groele and J. Foster, "Hydrogen Peroxide Interference in Chemical Oxygen Demand Assessments of Plasma Treated Waters," *Plasma*, vol. 2, no. 3, pp. 294–302, Jul. 2019, doi: 10.3390/PLASMA2030021.

[140] J. R. Groele, N. Sculley, T. M. Olson, and J. E. Foster, "An investigation of plasma-driven

decomposition of per- and polyfluoroalkyl substances (PFAS) in raw contaminated ground water," *J. Appl. Phys.*, vol. 130, no. 5, p. 053304, Aug. 2021, doi: 10.1063/5.0039264.